# Development of molecular targeted imaging methods for detection of lung metastasis and angiogenesis




Stavros Melemenidis

Linacre College

University of Oxford

2014

Thesis submitted for the degree of Doctor of Philosophy

# Abstract

The focus of this thesis is the development of two molecularly targeted imaging methods, in both cases based on contrast agents encompassing micron-sized microparticles of iron oxide (MPIO). MPIO are obligate intravascular agents and as presented in this thesis the half-life in the blood circulation is < 1min.

In the first approach described in the thesis, the overall goal was to detect metastasis in mouse lungs, very early in metastatic development, by targeting vascular cell adhesion molecule 1 (VCAM-1) using conjugates of an anti-VCAM-1 antibody and 1 μm MPIO (VCAM-MPIO). In Chapter 3, I demonstrate specific retention of VCAM-MPIO in the vasculature of a lung metastasis model, and also the very short blood half-life of the contrast agent; both of which suggest the potential for *in vivo* detection. In Chapter 4, I show that whilst the bound VCAM-MPIO do not sufficiently dephase the signal obtained with the bright lung MRI approaches used (hyperpolarized $^{3}$He/$^{129}$Xe or $^{19}$F MRI), it is possible to sensitively detect the presence of lung metastases *in vivo* using radiolabelled VCAM-MPIO ($^{89}$Zr-DFO-VCAM-MPIO) in combination with PET imaging.

The overall goal of the second approach described, was to detect and characterize tumour angiogenesis by targeting $\alpha_v\beta_3$-expressing endothelium *in vivo*, using a conjugate of cyclic penta-peptides c(RGDyK) and 2.8 μm MPIO [c(RGDyK)-MPIO]. To this end, I demonstrate in Chapter 5 that c(RGDyK)-MPIO specifically binds to $\alpha_v\beta_3$-expressing endothelium in subcutaneous tumours and yields quantifiable contrast effects on $T_2$*-weighted MRI. Furthermore, I have implemented in this approach gadolinium DCE imaging, providing dynamic vascular information.

To date there is no reported detection method for pulmonary metastasis at the micrometastastic stage, as presented in this thesis. Translation of this method into clinic could allow for earlier therapeutic intervention and, thus, more effective treatment. The angiogenesis characterization imaging method presented here may provide a sensitive approach for the characterization of heterogeneity in tumour angiogenesis/vascularity and monitoring of anti-angiogenic therapies.



“I would like to dedicate this work to the most important element behind this thesis. To all of my lady mice, with the greatest respect.”

# Acknowledgements

The years I spend working on my DPhil in Oxford University they have been the most interesting years of my life and I have to admit that working on my DPhil it has been extremely fun and pleasant. One key element behind this wonderful experience has been my primary supervisor, Professor Nicola R Sibson who allowed me to be myself. I can only hope that in my future career I will gain her qualities as a scientist and as a person. Thank you Niki, it has been a pleasure working with you.

I would also like to thank my group colleagues, the Sibson's, for being my family here in Oxford and all of the people from RRI that help me to feel at home.

# Table of Contents

**Abstract** ..... **i**

**Acknowledgements** ..... **v**

**Table of figures** ..... **xiii**

**Chapter 1 – Introduction** ..... **1**

**1.1 How common is cancer?** ..... **1**

1.1.1 Cancer diagnosis ..... 1

1.1.2 Cancer mortality rates ..... 2

1.1.3 Cancer and metastasis ..... 3

**1.2 Development of solid carcinomas** ..... **4**

1.2.1 DNA damage – DNA repair – DNA mutation ..... 4

1.2.2 Neoplasia ..... 4

1.2.3 Tumour heterogeneity ..... 5

1.2.4 Tumour stroma and microenvironment ..... 6

1.2.5 Tumour vasculature ..... 7

**1.3 Hallmarks of cancer** ..... **8**

1.3.1 Tumour angiogenesis ..... 8

1.3.1.1 Integrins ..... 9

1.3.1.2 RGD ..... 10

1.3.2 Metastasis ..... 13

1.3.2.1 Seed and soil ..... 13

1.3.2.2 Dissemination of pre-malignant cells ..... 14

1.3.2.3 Pre-metastatic niche ..... 14

1.3.2.4 Endothelial tumour cell adhesion and extravasation ..... 15

1.3.2.5 Circulating cancer cells and disseminated dormant tumour cells ..... 16

**1.4 Molecularly targeted imaging** ..... **17**

1.4.1 Imaging of Angiogenesis ..... 17

1.4.1.1 MRI vascular measurements and detection of angiogenesis ..... 18

1.4.1.1.a MRI intravascular contrast agents ..... 18

1.4.1.1.b Dynamic Contrast Enhanced MRI ..... 19

1.4.1.1.c Molecularly targeted Gd-based moieties ..... 19

1.4.1.1.d Superparamagnetic iron oxide ..... 20

1.4.1.1.e Diffusion-Weighted MRI ..... 20

1.4.1.2 PET and SPECT ..... 21

1.4.1.3 Contrast enhanced Ultrasonography (US) ..... 22

1.4.1.4 Contrast enhanced Computed Tomography (CT) ..... 23

1.4.2 Imaging of Metastasis ..... 24

1.4.2.1 PET and SPECT ..... 25

1.4.2.2 Molecular MRI for detection of metastasis ..... 26
1.4.2.3 Diffusion-Weighted MRI ..... 27
**1.5 Aims of thesis ..... 27**

**Chapter 2 – Materials & Methods ..... 29**
**2.1 Chemicals and solutions ..... 29**
2.1.1 Chemicals ..... 29
2.1.2 Substrates ..... 29
2.1.3 Buffers ..... 29
**2.2 Cell lines and tissue culture ..... 30**
2.2.1 Tumour cell lines and culture mediums ..... 30
2.2.2 Cell culture and incubation ..... 30
2.2.3 Cell revival ..... 30
2.2.4 Cell storage ..... 31
2.2.5 Cell suspension ..... 31
2.2.6 Cell preparation for injections ..... 31
**2.3 Animal work ..... 31**
2.3.1 Mouse strains ..... 31
2.3.2 Pulmonary metastasis model ..... 31
2.3.3 Subcutaneous carcinoma model ..... 32
2.3.4 Lung harvest ..... 32
2.3.5 S.c. tumour harvest ..... 32
2.3.6 Tissue management ..... 33
**2.4 Injectable agents ..... 33**
2.4.1 VCAM- or rat IgG-MPIO conjugation ..... 33
2.4.2 Cyclo[-RGDfK-]- or cyclo[-RADfK-]-MPIO conjugation ..... 33
**2.5 Antibodies ..... 34**
2.5.1 Antibodies for immunohistochemistry ..... 34
2.5.2 Antibodies for immunofluorescence ..... 35
**2.6 Imaging ..... 35**
2.6.1 Magnetic resonance imaging ..... 35
2.6.1.1 In vivo HP gas lung MRI ..... 35
2.6.1.1.a Instrumentation ..... 35
2.6.1.1.b HP Gas Production and Delivery ..... 36
2.6.1.1.c Animal preparation ..... 36
2.6.1.1.d MRI sequences ..... 36
2.6.1.2 In vivo $^{1}$H MRI ..... 36
2.6.1.2.a Instrumentation ..... 36
2.6.1.2.b Animal tumour models ..... 37
2.6.1.2.c Experimental protocol ..... 37
2.6.1.2.d MRI sequences ..... 37
2.6.1.2.e MRI dataset handling ..... 38
2.6.1.2.f MRI dataset segmentation ..... 38
2.6.2 *In vivo* whole body dynamic PET and CT ..... 39

**Chapter 3 – *Ex vivo* specific targeting of pulmonary VCAM-1 activated endothelium..41**
**3.1 Introduction.....41**
**3.2 Methods.....42**
3.2.1 General inflammation and initial pulmonary metastasis mouse models.....42
3.2.2 *Ex vivo* binding of VCAM-MPIO on LPS inflamed endothelium.....42
3.2.3 Optimisation of MPIO (iron) concentration.....43
3.2.4 Optimisation of pulmonary metastatic mouse model.....43
3.2.5 Biological clearance of MPIO.....44
3.2.6 *Ex vivo* binding of VCAM-MPIO on pulmonary micrometastases associated inflamed endothelium.....45
**3.3 Results.....45**
3.3.1 *Ex vivo* binding of VCAM-MPIO on LPS inflamed endothelium.....45
3.3.2 Initial studies of *ex vivo* binding of VCAM-MPIO in metastasis-bearing lungs...47
3.3.3 Optimization of injected MPIO (iron) dose.....49
3.3.5 Identification of optimal time point post-VCAM-MPIO administration for imaging.....52
3.3.6 *Ex vivo* quantitation of VCAM-MPIO retention in metastatic mouse model.....53
**3.4 Discussion.....56**

**Chapter 4 – *In vivo* specific targeting of pulmonary metastasis induced VCAM-1 activated endothelium.....59**
**4.1 Introduction.....59**
**4.2 Methods.....61**
4.2.1 *In vivo* HP gas lung MRI.....61
4.2.1.1 Animal Preparation.....61
4.2.1.2 HP Gas Production and Delivery.....62
4.2.1.3 Imaging.....62
4.2.2 *Post mortem* $^{19}$F-labelled gas and liquid lung imaging.....62
4.2.2.1 Fluorinated gases.....62
4.2.2.2 Fluorinated liquids.....63
4.2.3 [$^{89}$Zr]-DFO-VCAM- or [$^{89}$Zr]-DFO-IgG-MPIO synthesis.....63
4.2.4 *In vitro* binding of [$^{89}$Zr]-DFO-VCAM-MPIO.....64
4.2.4.1 Radioimmunoassays with rVCAM-1.....64
4.2.4.2 Radioimmunoassays with HUVECs.....64
4.2.5 *Ex vivo* biodistribution of MPIO.....65
4.2.6 *Ex vivo* autoradiography.....65
4.2.7 *In vivo* binding of [$^{89}$Zr]-DFO-VCAM-MPIO.....65
**4.3 Results.....67**
4.3.1 HP gases lung MRI.....67
4.3.2 *Post mortem* imaging of lungs with fluorinated gases and liquids.....69
4.3.2.1 Fluorinated gases.....69
4.3.3 *In vitro* binding of [$^{89}$Zr]-DFO-VCAM-MPIO.....71
4.3.4 *In vivo* PET imaging of [$^{89}$Zr]-DFO-VCAM-MPIO.....73
4.3.5 *Ex vivo* Biodistribution of [$^{89}$Zr]-DFO-VCAM-MPIO.....76

4.3.6 Lung autoradiography....78
**4.4 Discussion....81**
**Chapter 5 – *In vivo* MRI characterisation of angiogenesis in s.c. tumour models....85**
**5.1 Introduction....85**
**5.2 Materials and Methods....87**
5.2.1 RGD-MPIO Synthesis....87
5.2.2 Assessment of peptide-loading....87
5.2.3 RGD-MPIO binding in vitro....88
5.2.4 Animal tumour models....88
5.2.5 In vivo experimental protocol....89
5.2.6 In vivo Magnetic Resonance Imaging....91
5.2.7 MRI data analysis....91
5.2.7.1 Static $T_2$*-Weighted dataset....91
5.2.7.1.a Hypointensity Volumes....91
5.2.7.1.b Mean Intensities....92
5.2.7.1.c $T_2$* relaxation times....92
5.2.7.2 DCE MRI....96
5.2.8 Histological analysis....96
5.2.9 Biological blood clearance protocol....98
5.2.10 Determination of blood relaxivity....98
5.2.11 Synthesis of dextran coated NPIO....98
**5.3 Results....99**
5.3.1 In vitro binding studies....99
5.3.2 Biological clearance of micro- and nano sized iron oxide particles from blood circulation....101
5.3.3 Quantification of c(RGDyK)-MPIO binding in vivo....103
5.3.3.1 Hypointensity volumes....103
5.3.3.2 Mean tumour intensity....110
5.3.3.3 $T_2$* relaxation times....112
5.3.3.4 Size grouping for colorectal model....114
5.3.3.4.a Hypointensity volumes....114
5.3.3.4.b Mean tumour intensity....115
5.3.3.4.c $T_2$* relaxation times....115
5.3.4 DCE MRI....119
5.3.5 Comparison of MPIO analysis with DCE MRI....120
5.3.6 Immunohistochemistry (IHC) and immunofluorescence (IMF)....121
5.3.6.1 Quantitative assessment of IHC and IMF....122
5.3.6.2 Quantitation of MPIO binding from IHC....122
**5.4 Discussion....125**
5.4.1 Comparison of MPIO based agents with NPIO or smaller molecules....125
5.4.2 Binding characteristics....126
5.4.3 MPIO induced contrast effect....126
5.4.4 Quantitative analyses....128

5.4.4.1 Hypointensity volumes ..... 128
5.4.4.2 Mean tumour intensities and $T_2$* relaxation times ..... 132
5.4.4.3 Comparison of MRI quantitation methods ..... 133
5.4.4.4 Comparison of MRI with IHC quantitation ..... 136
5.4.4.5 Control peptide c(RADyK) ..... 137
5.4.5 Concomitant DCE ..... 137
**5.5 Conclusions ..... 138**

**Chapter 6 – Discussion ..... 141**
**6.1 MPIO *vs.* NPIO ..... 141**
**6.2 Pulmonary micrometastasis detection ..... 141**
**6.3 Detection of multi-organ micrometastasis ..... 142**
**6.4 Characterisation of angiogenesis in subcutaneous tumours ..... 143**
**6.5 Future directions ..... 144**
6.5.1 Micrometastasis detection targeting VCAM-1 ..... 144
6.5.2 Angiogenesis detection targeting $\alpha_v\beta_3$ ..... 145
**6.6 Concluding remarks ..... 145**

**Bibliography ..... 147**

**Abbreviations ..... 177**

# Table of figures

Figure 1.1. Cancer UK statistics ..... 2
Figure 1.2. Cancer worldwide statistics ..... 2
Figure 2.1. VCAM-MPIO ..... 34
Figure 2.2. Cyclic(RGDyK)-MPIO ..... 34
Figure 3.1. General inflammation mouse-model ..... 43
Figure 3.2. Initial metastatic mouse-model ..... 44
Figure 3.3. Optimised metastatic mouse-model ..... 44
Figure 3.4. VCAM-MPIO binding on activated endothelium ..... 46
Figure 3.5. VCAM-MPIO binding on initial metastatic model ..... 48
Figure 3.6. Non-specific retention at high iron concentration ..... 48
Figure 3.7. Representative number and size of metastases using initial mouse model ..... 49
Figure 3.8. Optimisation of injectable iron concentration ..... 50
Figure 3.9. Representative number and size of metastases using optimised mouse model ..... 51
Figure 3.10. Biological clearance half-life for 1.08 μm MPIO ..... 52
Figure 3.11. Specific binding on micrometastasis ..... 54
Figure 3.12. Specific binding on VCAM-1 activated ..... 55
Figure 3.13. Quantitation of VCAM-MPIO on metastasis model ..... 56
Figure 4.1. [$^{89}$Zr]-DFO-VCAM-MPIO ..... 64
Figure 4.2. *In vivo* PET protocol ..... 66
Figure 4.3. *In vivo* HP gas imaging ..... 67
Figure 4.4. Confirmation of successful administration of contrast agents ..... 68
Figure 4.5. Colocalisation of VCAM-MPIO and micrometastases in lungs ..... 68
Figure 4.6. *Post mortem* $^{19}$F gas MRI ..... 69
Figure 4.7. *Post mortem* $^{19}$F liquid MRI ..... 70
Figure 4.8. Testing binding specificity of [$^{89}$Zr]-DFO-VCAM-MPIO ..... 72
Figure 4.9. Representative PET dynamic analysis ..... 74
Figure 4.10. Mean activity uptake of lung, blood, liver and kidney over time ..... 75
Figure 4.11. PET static analysis for lungs ..... 75
Figure 4.12. Biological clearance determined from PET ..... 76
Figure 4.13. Biodistribution of [$^{89}$Zr]-DFO-VCAM-MPIO ..... 77
Figure 4.14. Autoradiography of lung tissue ..... 79
Figure 4.15. Correlation of [$^{89}$Zr]-DFO-VCAM-MPIO with micrometastasis ..... 80
Figure 4.16. VCAM-1 activated vessel with no apparent metastasis on tissue section ..... 81
Figure 4.17. Figure 2 as presented in Branca *et al*, 2010 ..... 83
Figure 4.18. Figure 4 as presented in Branca *et al*, 2010 ..... 84

Figure 4.19. Imperfect HP $^{3}$He ventilation-inflation on the cranial lobe, from a control group .....84
Figure 5.1. Schematic diagram of the *in vivo* experimental MRI protocol.....90
Figure 5.2. Methodology of estimating MPIO-induced hypointense voxel .....93
Figure 5.3. Categorization and interpretation of positive hypointensce volumes.....94
Figure 5.4. Schematic diagrams of MRI analysis methodology.....95
Figure 5.5. Schematic diagram of IHC analysis .....97
Figure 5.6. *In vitro* c(RGDyK)-MPIO binding on $\alpha_v\beta_3$ activated HUVECs .....100
Figure 5.7. Biological clearance of unbound MPIO *vs.* unbound NPIO from the blood circulation. .....102
Figure 5.8. MPIO structure .....103
Figure 5.9. Hypointensity volume ratio results for melanoma derived tumours .....106
Figure 5.10. Hypointensity volume ratio results for colorectal derived tumours .....107
Figure 5.11. 3D reconstructions of hypointesity volumes of the melanoma derived tumours .....108
Figure 5.12. 3D reconstructions of hypointesity volumes of the colorectal derived tumours .....109
Figure 5.13. Mean tumour intensity results for both subcutaneous mouse models.....111
Figure 5.14. Mean tumour $T_2$* relaxation times for both subcutaneous mouse models.....113
Figure 5.15. Subcutaneous tumour volumes.....114
Figure 5.16. Hypointensity volume ratios for size restricted sub-groups of colorectal derived tumours .....116
Figure 5.17. Mean tumour intensities for size restricted sub-groups of colorectal derived tumours .....117
Figure 5.18. Mean tumour $T_2$* relaxation times for size restricted sub-groups of colorectal derived tumours .....118
Figure 5.19. DCE MRI results and their correlations with tumour volume, for colorectal derived tumours .....120
Figure 5.20. Correlation of MRI analyses with tumour volume, for the colorectal derived tumours .....121
Figure 5.21. Demonstration of specific binding of c(RGD)-MPIO on tumour vasculature, by IF and IHC .....123
Figure 5.22. Quantitation of specific binding of c(RGD)-MPIO on tumour vasculature, assessed from IHC treated sections .....124
Figure 5.23. Schematic representation of the dephasing magnitude of a single MPIO, within a cube of water based molecule.....128
Figure 5.24. 1$^{st}$ theoretical example of underestimated MPIO-induced hypointensities in the volumetric analysis .....130
Figure 5.25. 2$^{nd}$ theoretical example of underestimated MPIO-induced hypointensities in the volumetric analysis .....131
Figure 5.26. Schematic diagram illustrating the relationship between MPIO density and signal intensity reduction.....132
Figure 5.27. Outline of all paired analyses for c(RGDyK)-MPIO treated groups, for all implemented MRI analyses .....134

Figure 5.28. Outline of all paired analyses for c(RADyK)-MPIO treated groups, for all implemented MRI analyses ..... 135
Figure 5.29. Outline of all un-paired analyses for c(RGDyK)-MPIO treated groups, for all implemented MRI analyses ..... 136

# Chapter 1 – Introduction

## 1.1 How common is cancer?

### 1.1.1 Cancer diagnosis

Cancer can develop at any age but its frequency correlates with aging and is most common amongst older people. Since the mid-1970s, the overall cancer incidence rates in the UK have increased by one third, with incidence rates in women increasing by 23% and by 43% in men. In the UK alone, during 2011 more than 331,000 new incidences of cancer were diagnosed, a daily average of approximately 900 individual diagnoses or one every two minutes. The risk of cancer development up to the age of 50 is 1 in 20 for women and 1 in 35 for men, while more than a third of all cancer cases are diagnosed in people over 75 years old. Less than 1% of all cancer occurs in children aged up to 14, and a further 1% in teenagers and young adults aged between 15 and 24 years old. Taking in to account these incidence rate differences amongst age groups, the rates can be normalised according to age (age standardisation). The UK age-standardised (AS) rates for 2011 showed that there are 376 new cancer cases for every 100,000 women, 427 for every 100,000 men, or 396 new cases per 100,000 for mixed gender population (Figure 1.1) [1].

On a larger scale, for the year 2012, the annual cancer diagnosis rate for Europe was estimated to be 3.4 million. For the same year, worldwide 14.1 million new cancer cases were reported, with more than half of them encountered in developing countries. Worldwide the cancer incidence for women was 47% and for men 53%, and the World AS incidence rates show that there are 165 new cancer cases for every 100,000 women in the world, and 205 for every 100,000 men (Figure 1.2) [2].

The World statistics have to be interpreted taking into consideration the very inhomogeneous data source. The frequencies of cancer worldwide show big variations, owing to roughly speaking two factors: the development of the medical infrastructure in each individual country, including medical reliability; and the life-style of each population and how much this deviates from healthy standards. Consequently, the rates of cancer incidence per country population are higher in developing countries but more than 50% of all cancer diagnoses worldwide are recorded in the less developed countries [3].

The most common cancer in the UK amongst women is breast cancer, followed by lung and colorectal cancer, and for men, prostate, followed by lung and colorectal. Although worldwide lung cancer is the most common among men, followed by prostate and colorectal [3, 4]. From Cancer Research UK statistical reports men are 14% more likely to get cancer than women [5].

| ALL CANCERS COMBINED | Males | Females | Persons | Country | Year[4] |
|---|---|---|---|---|---|
| Number of new cases per year[1] | 167,487 | 164,000 | 331,487 | UK | 2011 |
| Incidence rate per 100,000 population[2] | 426.5 | 376.2 | 396.2 | | |
| Number of deaths per year | 83,711 | 75,467 | 159,178 | UK | 2011 |
| Mortality rate per 100,000 population[2] | 200.9 | 146.7 | 169.9 | | |
| One-year survival rate[1,3] | 66.7% | 74.1% | 70.4% | England & Wales | 2010-2011 |
| Five-year survival rate (predicted)[1,3] | 49.3% | 59.2% | 54.3% | | |
| Ten-year survival rate (predicted)[1,3] | 45.8% | 53.7% | 49.8% | | |

1. Excluding non-melanoma skin cancer 2. European age-standardised 3. Adults diagnosed
4. Latest statistics available

**Figure 1.1. Cancer UK statistics.** Cancer Research UK statistics for the year 2011. Table shows cancer incidence rates, mortality rates and survival rates for males, females or combined gender UK population.

| CANCER WORLDWIDE STATISTICS | Males | Females | Persons | Country | Year[2] |
|---|---|---|---|---|---|
| Number of new cases per year | 7,427,148 | 6,663,001 | 14,090,149 | Worldwide | 2012 |
| Incidence rate per 100,000 population[1] | 205.4 | 165.3 | 182.3 | | |
| Number of deaths per year | 4,653,132 | 3,547,898 | 8,201,030 | Worldwide | 2012 |
| Mortality rate per 100,000 population[1] | 126.3 | 82.9 | 102.4 | | |

1. World age-standardised 2. Latest estimates available

**Figure 1.2. Cancer worldwide statistics**. Cancer Research UK statistics for the year 2012. Table shows cancer incidence rates and mortality rates for males, females and combined gender World population.

### 1.1.2 Cancer mortality rates

With respect to cancer related mortality rates, during 2011 in the UK, approximately 159,000 cancer related deaths were recorded, an average of 430 people per day or 2 deaths every 3 minutes due to cancer. From all deaths, more that 50% occurred in elders, aged 75 years and over. With respect to gender, approximately 75,400 (47%) of cancer related deaths were amongst women and 83,700 (53%) amongst men. The UK AS mortality rates for 2011, estimates that 234 in 100.000 women and 269 in 100.000 men died from cancer (Figure 1.1) [6].

Worldwide, approximately 8.2 million cancer related deaths were recorded, with 3.5 million (43%) female cases and 4.7 million (57%) male cases. According to the AS mortality rates,

there are 83 cancer deaths for every 100,000 females and 126 cancer deaths for every 100,000 men (Figure 1.2) [7].
In the UK the type of cancer responsible for the most deaths amongst men is lung cancer (23%), followed by prostate (13%), colorectal (8.5%), oesophageal (6%) and pancreatic cancer (5%). For women, the most deadly cancer is also lung (21%), followed by breast (21%), colorectal (9%), ovarian (6%) and pancreatic cancer (5%) [6].
Overall in the UK, men are not only 14% more likely to get cancer than women, but also 37% more likely to die from it [5]. This inequality in tumour incidences vs. mortality is reflected also in the world statistics.

### 1.1.3 Cancer and metastasis

In the UK, cancer is the cause of over 25% of all deaths in the country, and more than 1 in 3 people are estimated to develop a type of cancer during their lifespan. According to Cancer Research UK public survey, "Cancer is the number one fear for the British public, feared ahead of debt, knife attack, Alzheimer's disease and losing job" [1].
These statistics present cancer as a single incident, allowing ease of understanding in the wider public. However, it is well appreciated that the mobility of a primary cancer to a distant organ is responsible for over 90% of all cancer related deaths [8], a process known as metastasis. This fact alone splits the perspective of the disease into two categories in terms of clinical treatment; primary and secondary malignancy. It appears that over the past 100 years great improvements have been made in the survival rates from primary cancer, but evidently less progress has been made towards diagnosing early and treating metastatic progression. This highlights our poor understanding of the mechanisms, that underlie the metastatic phenotype of the cells, the synergy of the cancer cells and healthy cells within the tumour microenvironment and the selective properties of some certain types of cancer cells for particular organs (Seed and soil).
Therefore, the number one fear for the UK population is undoubtedly metastasis. It is clear that by unravelling the secrets of metastatic mechanisms, the mortality rates worldwide will decrease dramatically.
The work described in this thesis focuses on the development of molecular imaging techniques, with the aim of volumetrically characterising tumour vascularity or to detect metastasis early in the process of the disease. Angiogenesis and metastasis are cancer phenotypes that are strongly related. Therefore, it is essential to include in this introduction the journey of a healthy cell through its transformation and development into a solid carcinoma tumour. Furthermore, the development of vasculature in solid tumours will be described, in order to provide background to the angiogenic phenotype and metastatic mechanisms.

## 1.2 Development of solid carcinomas

### 1.2.1 DNA damage – DNA repair – DNA mutation

The human body is an astonishing network of approximately 200 types of different cells. These cells compose a variety of structural and functional organs. The estimated number of cells in a 30-year-old young adult, weighing 70 kg and a height of 1.72 cm is $3.72x10^{13}$ [9]. The maintenance of the human body requires cell proliferation, with exceptionally accurate DNA replication. The parent cell will duplicate the DNA code (genome), approximately 6 x $10^9$ nucleotides, which must be successfully copied and passed on to the daughter cell in order to preserve genomic stability. Since the day of birth and throughout the life of a human, cells of the human body encounter numerous lesions on their DNA structure, known as DNA damage. DNA damage is the result of endogenous factors attacking the chromosomes, such as reactive oxygen species or cell replication errors, and exogenous factors, like radiation, hydrolysis, toxins (plants), man-made chemical (carcinogenics) and viruses. The DNA damage can be either base related molecular lesions or DNA strand related lesions, such as single and double strand breaks. In order to sustain genomic stability, the cell has multiple and specific DNA repair mechanisms, which are remarkably efficient in correcting DNA damage, with a rate of thousand to a million molecular lesions per day. If the cell replicates with unrepaired damage in the DNA code, this error will be inherent to all future generations of this cell, a process known as mutation. In order to ensure genomic stability, the ultimate defence of a cell is to enter programmed cell death [10].
However, despite the impressively sophisticated cell defence mechanisms, mutations are natural occurring processes that accumulate during the life span of an organism. Therefore, the number of mutations increases with aging, as a result of poorer performance of DNA repair and cumulative exposure to exogenous factors. The fact that the DNA of normal cells shows a significantly low number of mutations, whilst a cancer cell shows a substantial number of mutations, does not support the theory that malignancy is a linear process of mutation accumulation. It has been proposed that mutations on DNA domains such as oncogenes and tumour suppressor genes, which are important for the maintenance of genomic stability, could be responsible for a phenotype that significantly increases the rate of mutations; the mutator phenotype [11, 12]. Inevitably, some cascades of mutations will enable the cell to bypass the organ's regulatory processes, known as a malignant phenotype. The malignant phenotype will continue proliferative signalling within the cell, and if the cell survives the organism's natural defence mechanisms, will divide unregulated. This process is known as neoplasia and leads to the growth of neoplasms.

### 1.2.2 Neoplasia

Neoplasms or tumours may be of benign, pre-malignant (carcinoma in situ) or malignant phenotypes. Benign neoplasms contain cells that lack the ability to invade the surrounding tissue and grow regulated surrounded by a fibrous sheath of connective tissue, like a mole (nevi). Pre-malignant neoplasms are morphologically altered tissues, but their cells also lack

the ability to invade the surrounding tissue. However, a neoplasm with pre-malignant phenotype has cells associated with a high rate of mutation accumulation [12]. A malignant neoplasm will have cells that develop phenotypes with migratory characteristics and has the potential to spread to the surrounding tissues. This is the most fearsome and devastating aspect of the neoplastic development since malignant cells can disseminate from its primary site to distant organs, by entering the blood stream, a phenomenon called metastasis. The term cancer encompasses a very broad group of diseases involving unregulated cell growth, which is organ and cell-type specific. Malignant neoplasms are more frequent in rapid proliferating tissues like endothelial and epithelial cells [13], and these subsets are known as carcinomas. The rest of the cancers derived from slower growing tissues result in melanomas, sarcomas, neuro-ectodermal tumours and leukaemia. Leukaemia may be an exception because leukemic cell proliferation could be very rapid.

### 1.2.3 Tumour heterogeneity

Cancer is known as the disease of any type of cell, where a cascade of mutations can lead to a phenotype involving unregulated cell growth. Since there are approximately 200 distinct types of cells in the human body, the number of human cancer subtypes are at least as many as the number of cell-types. The nature of the disease is apparently far more complex if we consider that two identical malignant cells will not create the same neoplasm in two individual patients, owing to further variations in the initial clone and different microenviromental stimuli.

In the 1930s, when tumours were still assumed to be monoclonal, scientists tried to determine the number of neoplastic cells required to induce certain types of cancer in rodents. For murine carcinoma and sarcoma the number was estimated to be 100,000 neoplastic cells whilst for lymphoid and myeloid leukaemia anything from a single neoplastic cell to 100 was required [14]. Although the morphological heterogeneity in solid tumours has been observed from the start of the 20$^{th}$ century, it was not until the late 70's that scientists started isolating different clones from a single tumour. Studies on the ability of clones, derived *in vitro* from a single parent culture of murine malignant melanoma, to form metastatic colonies, demonstrated in 1977 that the parent tumour is heterogeneous and that a highly metastatic tumour cell variant sub-population pre-exist in the parental population [15]. The same year, another group submitted relevant data on the heterogeneity of tumours to Cancer Research but the authors found difficulty in challenging the conventional idea that tumours are monoclonal [16]. The study was presented with more novel results and was published the following year in the same journal [17]. Subsequent studies on biological and phenotypic diversity of tumours established the theory of heterogeneous tumours [16, 18, 19].

Technological advancements in the field of genomics allowed studies showing that tumours, leukemic or solid, quite frequently display substantial intra-tumour heterogeneity in virtually all distinguishable phenotypic features: cellular morphology; gene expression including the expression of cell surface markers; growth factors and hormonal receptors; metabolism; motility. Thus, angiogenic, proliferative, immunogenic or metastatic phenotypes of a tumour are not global characteristics, but rather local tumour characteristic [20, 21]. Such evidence

highlighted the need for a theory to explain the phenotypic diversities present in the subpopulations within tumours.

The cancer stem cell (CSC) concept has been suggested as an explanation for the heterogeneity of cancer cells [22]. A few years earlier, it was demonstrated that malignant teratocarcinoma cells could spontaneously differentiate into mature benign cells [23]. However, for many years CSC was not identified. The concept emerged as a mainstream idea in 1994, when a phenotypically distinct subset of human acute leukemia cells ($CD34^{+}CD38^{-}$) where shown to reconstitute the disease upon transplantation into immundeficient mice, whilst the rest of the leukemic cells lacked this ability [24]. The first solid tumour CSC was reported almost ten years later, as the $CD44^{+}CD24^{-}$ subset of human breast cancer cells [25]. However, the identification of CSCs for solid tumours was not widely accepted [26]. According to the CSC theory, out of the total number of tumour cells only a minor fraction are CSCs. CSCs have both the ability to self-renew and to differentiate into non-stem cells. The product of abnormal differentiation of the CSCs will in fact be the majority of the tumour volume. Thus, CSCs are responsible for the maintenance and proliferation of tumours [20, 21].

An alternative theory is that of phenotypic plasticity, where it is believed that the majority of the tumour cells can be viewed as CSCs. Their ability to self-renew and proliferate varies according to microenviromental stimuli (cues) and cell-autonomous stochastic mechanisms. The great influence of microenviroment was illustrated by the observation that teratocarcinoma cells can contribute morphologically to normal cells, when injected in to normal blastocysts [27]. To date there is extensive evidence that microenviroment has a profound effect on the phenotype of tumour cells and can promote phenotypic malignancy and tumour progression [28].

### 1.2.4 Tumour stroma and microenvironment

Solid tumours are heterogeneous and abnormal cell masses, composed of malignant cells with various phenotypes, and in order to survive and proliferate (tumourigenesis) they must recruit healthy cells as active participants. These recruited cells comprise the tumour associated stroma. Stroma, (from Greek στρῶμα, meaning "layer, bed") refers to the connective and supporting framework of a biological tissue or organ. Thus, we can categorise tumours volumes into two distinct sub-groups of cells, the tumour and the stromal cells. The structure of the tumour stroma will vary with organ and cell-type of malignant cells. The basement membrane interposes between the stromal cells and the tumour cells, but it can be interrupted in carcinomas, whilst in other types of cancer, tumour cells may interact directly with stromal elements. The stromal cells of solid tumours can be grouped into three general categories: the matrix synthesis components such as fibroblasts, myofibroblasts and histiocytes; the connective tissue elements, such as matrix components fibronectin, interstitial collagens, elastin, glycosaminoglycans; and the inflammatory cells, primarily lymphocytes and macrophages [29, 30]. Malignant cells can initiate crucial changes in the microenvironment, which eventually will deceive the anti-tumorigenic mechanisms through a

favourable cross-talk between recruited cells, which promote matrix remodelling, cell growth and, ultimately, development of vascular networks [31].
Vasculature is a requirement for the growth of all solid tumours, since in order to proliferate they will need structural mechanisms for nutrition supply, oxygen supply (vasculature) and waste discharge (lymphatic system) [29]. Tumours would not be able to grow more than 1-2 mm without new vasculature [32] and can be categorised as vascular or non-vascular tumours, depending on whether they do or do not contain endothelial cells, pericytes and smooth muscle cells. The cells of the tumour vasculature, therefore, are also stromal cells. An intense constant cross talk exists between neoplastic, immune and non-epithelial cells, and the tumour microenvironment is characterised as acidic, hypoxic and containing a lot of growth factors. The presence of tumour vasculature, which is quite chaotic in structure, will enhance the heterogeneity of the tumour microenvironment [20]. The role and functions of stromal cells have been extensively summarised according to their role in different tumour phenotypes [33]; hallmarks of cancer.

### 1.2.5 Tumour vasculature

The tumour circulatory system is distinctly different from normal tissue counterparts [29, 34]. The circulatory system interconnects all organs in the body, through lymphatic and blood circulation, and plays an important role in the communication between distant organs. This thesis will be focusing entirely on blood vasculature, the endothelial cells and their cell surface molecules, since the contrast agents used for this work are obligate intravascular agents owing to their size.
In the first instance, the formation of the vasculature is known as neovascularisation and mediated through two processes known as vasculogenesis and angiogenesis. Vasculogenesis refers to the formation of new blood vessels when there are no pre-existing blood vessels, whilst angiogenesis refers to formation of blood vessels from pre-existing vessels. Vasculogenesis is the onset of vascularisation, which occurs to a great extent during embryogenesis, and angiogenesis is a later process following vasculogenesis [35].
Tumour blood vessels lack architecture and hierarchy patterns, they have heterogeneous vascular density, they are irregularly spaced and their structure is markedly tortuous. Furthermore, these vessels are disorganised in shape, hyperpermeable to micromolecules, often lack pericytes and display arteriovenous shunting [36, 37]. Tumour endothelial cells show a 30 to 40-fold greater proliferation rate than that of normal tissue endothelial cells [38, 39]. This complex of abnormalities results in poor functionality of the vasculature and inconsistent blood flow. The lymphatic vasculature appears in advanced primary cancers with poor functional lymphatic capillaries. The lymphatic endothelial cells do not have tight connections between them and vessels are more leaky. The poor lymphatic circulation cannot regulate the micro/macromolecular fluids and in combination with the extra volume of tumour growth is responsible for the significant increase in interstitial pressure. The lymphatic vessels are constrained from the interstitial pressure, reducing even further their normal function, and there is little or no functional lymphatic system inside tumours [34, 40].

Tumour vessels can be categorized according to their structure and function in to six groups: mother vessels normal-appearing capillaries, glomeruloid microvascular proliferations, vascular malformations, feeding arteries, and draining veins [36, 37].

## 1.3 Hallmarks of cancer

So far, we have described the requirements for cells to gain a cancerous phenotype (the cause) and their development as structural solid carcinomas (the structure). The multistep process of tumourigenesis, the complexity of the tumour microenvironment and the diversity of neoplastic diseases can be organised and classified according to different stages of primary neoplastic disease or else according to the tumour pathology. For the great majority of different cancers, during neoplastic development, tumours acquire capabilities to alter their phenotypes. These capabilities include self-sufficiency in growth signals to sustain proliferation, insensitivity to anti-growth signals by evading growth suppressors, resistance to cell death by evading apoptosis, limitless replication potential enabling replicative immortality, inducing and sustaining angiogenesis, and ultimately promotion of tumour invasion and metastasis. These six different capabilities were proposed by Hanahan and Weinberg in 2000 as the hallmarks of cancer, with remarkable appreciation [41]. More recently, the same authors reviewed this proposal and suggested two additional hallmarks of cancer. The first involves the ability to reprogramme cellular energy metabolism in order to support continuous cell growth and proliferation. The second involves the escape of cancer cells from the natural defence of the immune system [42]. Evading immune destruction is not well understood and seems to possibly share some common mechanisms with the process of stromal cell recruitment from malignant neoplasms. It is remarkable how the same defence mechanisms of an organism can be manipulated to switch against itself, and awaits further research to shed more light on these mechanisms.
This thesis will expand on two of the hallmarks of cancer, angiogenesis and metastasis, and the potential to image these processes during tumour development.

### 1.3.1 Tumour angiogenesis

The term angiogenesis, etymologically, is a Latin portmanteau from two Greek nouns; *angeion* (ἀγγεῖον) stands for vessel, and *genesis* (γένεσις) for birth. Angiogenesis is a vital process in growth and development, and also for wound healing including granulation tissue formation. Though angiogenesis is a healthy process, tumour growth and metastasis are also angiogenesis-dependent. The first study concerning tumour angiogenesis dates back to 1968, when Greenbatt and Shudi performed transfilter diffusion studies on hamsters using a transparent chamber technique [34, 43]. In 1971, Folkman first highlighted the essential role of angiogenesis in tumour growth and proposed the term tumour angiogenesis factor (TAF) [32, 44].
In the early development of tumours there is no vasculature and the tumour volume results from pre-vascular neoplasia, as a result mostly of metaplasia and dysplasia due to abnormal

stimuli: physiological or chemical. In this phase of tumour development no cells with angiogenic phenotype are evident, or their number is insignificant. In this phase, tumour growth is restricted to a volume of few $mm^3$, owing to nutrition deprivation and lack of oxygenation, and the tumour may enter a dormant phase. When the number of cells with angiogenic phenotype exceeds a certain threshold then the tumour microenvironment becomes angiogenic, blood vessel growth is activated and the tumour neoplasm becomes malignant. The shift in the balance from anti-angiogenic towards pro-angiogenic factors is termed the "angiogenic switch" [45]. The trigger ocdf this angiogenic switch depends on tumour type and local microenvironment, and is regulated by numerous pro-angiogenic and anti-angiogenic determinants. The pro-angiogenic factors include groups of molecules such as vascular endothelial growth factor (VEGF) family, fibroblast growth factor (FGF) family, platelet-derived growth factor (PDGF), transforming growth factor-β (TGF-β), insulin-like growth factor, angiopoietins, and several chemokines. Anti-angiogenic factors include thrombospondin-1, angiostatin, endostatin and matrix metalloproteinases (MMPs) [46].
VEGF isoforms and the associated receptors are crucial mediators of blood vessel growth and well-studied signalling pathways of angiogenesis [47]. In 1993, it was first shown that a monoclonal mouse anti-human VEGF had great inhibitory growth effect *in vivo*, when administered to mice with variant tumour cell lines [48]. Subsequently, 4 years later, the humanised VEGF isoform was patented (Bevacizumab) and entered Phase I clinical trials [49]. Unfortunately, although anti-VEGF therapies have been successful in reducing tumour growth in mice, at the clinical level the results, to date, have not been very impressive [50, 51]. Imaging of angiogenesis has been considered using antibodies against VEGF receptor 2 using monoclonal VEGF isoforms or recombinant antibodies, showing that is possible to image angiogenesis, characterise expression of VEGFR-2, monitor drug delivery and/or monitor angiogenic changes due to therapy [52-57].
Another, well defined angiogenesis molecular target has been found in the integrin family, the integrin $\alpha_v\beta_3$. The advantage of this target is that, as we will see in the following paragraphs, it can be targeted with a small tripeptide sequence Arg-Gly-Asp (RGD), which is considerably smaller than a full antibody. The primary benefit of using only the specific binding sequences, is that this readily allows for chemical synthesis and experimental alterations of the structure to increase specificity and/or affinity. Furthermore, with regards to synthesizing molecularly targeted contrast agents, a greater loading efficiency can be achieved with these smaller molecules on the surface of the reagent's vehicle (e.g. MPIO), which may increase binding efficiency.

#### *1.3.1.1 Integrins*

Angiogenesis is dependent on adhesive interaction of vascular cells. Endothelial cell adhesion molecules and cell-surface receptors, known as integrins, mediate dynamic interactions between the cell and the extracellular matrix molecules and play an important role in organising the cytoskeleton. The term integrin was introduced in 1986 and, in vertebrates, the integrin family has at least 18 alpha ($\alpha_1$-$\alpha_{11}$, $\alpha_{IIb}$, $\alpha_D$, $\alpha_E$, $\alpha_L$, $\alpha_M$, $\alpha_V$ and $\alpha_X$) and 8 beta ($\beta_1$- $\beta_8$) subunits, which combine to 24 distinct homologue αβ heterodimers, the integrins. Alpha

subunits are approximately 150 to 180 kDa long, beta subunits about 90 kDa and an integrin has length approximately 280 Å [58, 59].
Integrins are molecules located partly on the cell surface and partly within the cytoplasm (transmembrane molecules), possessing a small cytoskeleton domain (cytoplasmic tail) and an extracellular domain (head). The extracellular domain of an integrin recognizes extracellular matrix (ECM) components, like proteins or counter receptors on adjacent cells and the cytoskeleton domain induces a transduction signal inside the cell. Consequently, information from the ECM environment is transmitted within the cell (outside-in signalling) [60, 61]. Interestingly enough, integrins can also induce signal transduction from inside the cell towards the surface of the cell (inside-out signalling) [62]. Through integrins, cells can modulate gene expression and the cell cycle, as well as regulating the cytoskeleton and activation of kinase signalling cascades [63, 64].
Integrins are involved in various biological activities through the transmission and receiving of molecular signals that regulate cell attachment, cell proliferation [65-68] and cell migration [69-72]. Furthermore, integrins also regulate tumour invasion, angiogenesis and metastasis [73-80].
A short list of key mediator integrins in tumour proliferation and metastasis will include [81]: $\alpha_v\beta_3$, also known as vitronectin receptor, is most well studied from the entire family and is expressed on activated endothelial cells, as well as some tumour cells [82]; $\alpha_v\beta_5$ also recognizes vitronectin and adenovirus ligands and is expressed primarily on fibroblasts and epithelial cells; $\alpha_2\beta_1$, also refer to as VLA-2, recognizes collagen and laminin ligands; $\alpha_5\beta_1$ or VLA-5 and also refer to as fibronectin receptor recognizes fibronectin and proteinases [83], $\alpha_6\beta_1$ or VLA-6, also known as laminin receptor recognizes laminin; $\alpha_6\beta_4$ also recognizes laminin and is expressed on epithelial cells.
$\alpha_v\beta_3$ and $\alpha_v\beta_5$ have been found to be especially critical for angiogenesis, as well as being important mediators of metastasis and invasion [81, 84, 85]. $\alpha_v\beta_3$ has been extensively studied and characterized as a marker of angiogenic vascular tissue, owing to its strong expression on activated endothelial cells and certain tumour cells, but only weakly on the non-activated endothelial cells and non-malignant tissue [86]. $\alpha_v\beta_3$, together with several other integrins recognizes the amino acid tripeptide sequence RGD. RGD was first observed in fibronectin and later on in many ECM components. On this basis it was concluded that the RGD sequence serves as a primary cell recognition motif [87-92]. However, the receptor-ligand activation was not fully understood until the 3D crystal structure of the extracellular domain of $\alpha_v\beta_3$ was reported [93] and, shortly afterwards, the structure of the $\alpha_v\beta_3$-RGD complex [94].

#### *1.3.1.2 RGD*

In 1976, fibroblast surface-associated glycoprotein was classified as fibronectin [95, 96]. Fibronectins have been observed to be major extracellular matrix (ECM) proteins and soon gained attention as a key element for cell surface interactions [97]. Studies have focused on the cell attachment site of fibronectin and in 1983, the cell attachment binding side of fibronectin was identified, sequenced and reproduced by peptide synthesis [98-100]. Further

narrowing down of the synthesis led to a four amino acid sequence Arg-Glys-Asp-Ser [101]. The RGD motif was found to be present in other ECM ligand binding sites and was soon assumed to be a prominent recognition sequence, involved in cell anchoring and in bi-directional integrin signalling pathways [102-104].

Studies on cell growth and morphology in tissue culture lead to the isolation of serum spreading factor, in 1980, which was later classified as vitronectin [105-107]. Studying further the cell-attachment binding domain of vitronectin, the RGD motif was again identified to be present. Although both fibronectin and vitronectin receptors recognize the RGD peptide sequence, they show mutually exclusive reactivities [82, 108, 109]. Vitronectin receptor, later known as $\alpha_v\beta_3$, found to be expressed on endothelial cells and was described first as a homologous αβ heterodimer. It was reported that the cell-attachment binding site of the alpha subunit contained the amino acid residues responsible for cell attachment and a correlation between vitronectin expression and cell adhesiveness was demonstrated. In 1990, evidence suggested that $\alpha_v\beta_3$ also has binding amino acid residues on the beta subunit. Furthermore, it was suggested that both discrete amino-terminal domains contribute to the structure of the ligand binding domain of the integrin. Thus, the binding domains are spatially and functionally linked [110]. In the same year, $\alpha_v\beta_5$ was purified and it was found that although $\alpha_v\beta_3$ binds to vitronectin, fibrinogen, von Willebrand factor and fibronectin, $\alpha_v\beta_5$ binds preferentially to vitronectin. Immunological comparison showed that $\beta_3$ and $\beta_5$ were distinct immunologically, whilst $\alpha_v$ was identical in both integrins, indicating an architectural difference at the ligand-binding site of these related integrins [110]. Also, in the same year, the angiogenic inhibitory effect of a polymeric peptide based on RGD was also reported [111]. RGD recognition is not spread through all the integrins and RGD is non-functional to a number of proteins, which leads to the idea that integrin receptors recognise a distinct conformational space within the amino acid sequence. All of this extensive focus on cell attachment mechanisms demonstrated that RGD, especially in the chemical structure found in vitronectin, has high specificity for $\alpha_v\beta_3$ and its inhibitory function has a dramatic effect on angiogenesis related pathology. Inevitably, this very small amino acid sequence has been flagged as a superior angiogenesis marker and a very promising molecule for therapeutic and diagnostic implementations in cancer.

Arg-Gly-Asp-Ser was the minimal structure recognized in fibronectin and consequently, Arg-Gly-Asp-Ser-based backbone-cyclised hexa- and penta-peptides were synthesized as antagonists for various proteins [82, 101, 112-117]. Concerning $\alpha_v\beta_3$-vitronectin inhibitory integrin interaction, the hexa-peptides showed little or no effect, whilst the penta-peptides did. More specifically, cyclic penta-peptides containing Arg-Gly-Asp-Phe-Val were synthesized, with 5 different backbone conformations by introducing a single D-amino acid and 4 L-amino acids, and tested for their vitronectin inhibitory activity. The peptide with the D-amino acid residue in Phe, *cyclo*(-Arg-Gly-Asp-[D-Phe]-Val) or *cyclo*(-RGDfV-), was selected as having displayed a 100-fold improved, compared to Arg-Gly-Asp-Phe-Val, inhibitory capacity for vitronectin. This conformation has been tested as an angiogenesis inhibitor, in models of implanted human tumour cell lines into chick embryos, with remarkable anti-angiogenic effect [86]. Modification of *cyclo*(-RGDfV-) by substituting Gly with Ala resulted in a homologue peptide *cyclo*(-RADfV-) with dramatically reduced binding characteristics and specificity for $\alpha_v\beta_3$, and has been used as control homologue [113, 117,

118]. The latter study also highlighted the importance of the Gly peptide in the sequence, for affinity to $\alpha_v\beta_3$ and $\alpha_{IIb}\beta_3$. At the same time, the differences in the binding activities of the different peptide sequences for $\alpha_v\beta_3$ and $\alpha_{IIb}\beta_3$, highlighted the importance of the 3D conformation of the binding side. The cyclic conformation of the most specific and active peptides have Arg and Asp oriented around Gly and it was concluded that a constrained cyclic peptide can mimic the conformation necessary for receptor binding more closely than a flexible linear peptide [113]. It has also been suggested that the distance between the $C_\beta$ of Arg and Asp plays a crucial role in the adhesion of the ligand. As measured by NMR spectroscopy, a distance between Arg and Asp in the range of 0.75-0.85 nm increases binding for $\alpha_{IIb}\beta_3$ ,whilst a distance below 0.67 nm enhances binding to $\alpha_v\beta_3$ [117, 119].

Subsequent improvement of *cyclo*(-RGDfV-) resulted in a very potent vitronectin antagonist. The introduction of $N^\alpha$ methylation of an amino acid residue in the backbone, constrained the conformation further, mimicking very closely the receptor conformation of $\alpha_v\beta_3$. The $N^\alpha$ methylation of the Val amino acid showed outstanding affinity for $\alpha_v\beta_3$ (0.58 $IC_{50}$ in mM) and negligible affinity for $\alpha_{IIb}\beta_3$ (860 $IC_{50}$ in mM), however, the compound was also found to have high affinity for $\alpha_v\beta_5$ and $\alpha_5\beta_1$ (11.7 and 13.2 $IC_{50}$ in mM). The compound was developed under the code EMD121974, by Merck KGaA (Damstadt) and given the name cilengitide [120-122]. Cilengitide entered phase II clinical trials in non-small lung cancer in 1999 [123] and in combination with gemcitabine for pancreatic cancer [124]. Later clinical studies of cilengitide increased exponentially, with various cancer therapy designs related to $\alpha_v\beta_3$-vitronectin inhibition: e.g. Phase I trials in recurrent malignant glioma [125] and in patients with advanced solid tumours [126].

Recent studies have investigated the effects of di-N-methylation of the backbone on the binding activity and specificity. Through binding affinity assays against $\alpha_v\beta_3$, $\alpha_v\beta_5$, $\alpha_5\beta_1$ and $\alpha_{IIb}\beta_3$, the possible combinations of di-methylating the 5 amino acids were screened. Di-methylations in D-V [c(-R-G-**D**-f-**V**)] and f-V [c(-R-G-D-**f**-**V**)] proved to be the most selective for $\alpha_v\beta_3$, with negligible binding to $\alpha_5\beta_1$, $\alpha_v\beta_5$ and $\alpha_{IIb}\beta_3$. Although the selectivity for $\alpha_v\beta_3$ was almost perfected, the binding affinity decreased by 10- and 50-fold for c(-R-G-**D**-f-**V**) and c(-R-G-D-**f**-**V**), respectively, (5.9±2.5 $IC_{50}$ in nM and 36.2±8.1 $IC_{50}$ in nM), compared to cilengitide [c(-R-G-D-f-**V**)] (0.65±0.07 $IC_{50}$ in nM) [122].

Since the introduction of the D-Phe in 1994, *cyclo*(-RGDfV-) was already a very promising compound for the synthesis of $\alpha_v\beta_3$ targeted molecular imaging. However, one problem with this conformation is that in order to conjugate any spacer the peptide requires a spacer-anchor unit, without which the peptide loses its activity characteristics. Immobilization of the fourth-amino group of the RGD sequence suggested that Val does not play an important role in the activity characteristics of the sequence [127]. Consequently, these observations, led to the substitution of Val with Lys (amino acid symbol K) and screening showed significant differences in specificity or affinity compared to Val containing peptide, making c(RGDfK), the ideal candidate for synthesizing probes for angiogenesis imaging [128].

### 1.3.2 Metastasis

The ability of tumours to gain metastatic characteristics and spread to distant organs is described as another hallmark of cancer. Yet, the full mechanisms underlying the ability of individual cells or tumours to metastasise are not fully understood. Metastasis is currently the biggest challenge of clinical cancer research. Metastasis, from the Greek, meta (next) and stasis (placement) means displacement, a term proposed by Jean Claude Recamier in 1829 [129].

#### *1.3.2.1 Seed and soil*

In 1889, Paget retrospectively studied 735 breast cancer autopsies and concluded that there is an emerging pattern as to the preference of circulating tumour cells (seeds), from a specific primary tumour site, for certain host organs (soil) [130]. On this basis, he proposed the hypothesis of "seed and soil", contradicting a previously suggested theory that metastasis could be simply explained by the mechanical arrest of CTC cell emboli in the vasculature [131]. However, by 1928, the latter hypothesis has gained evidence based on the mechanical circulatory patterns between the primary site and the host organ [132]. Consequently, it took many years before the seed and soil hypothesis regained interest [133] as further evidence suggested that mechanical circulatory patterns alone are not sufficient to explain the metastatic signatures [134, 135]. It is accepted, however, that the mechanical circulation factor does contribute to a certain extent to the delivery of cancer cells to specific organs [136] but to date our understanding of the relative contributions of these two hypotheses remains unclear.

Although metastasis will vary in characteristics according to the metastatic cell-type and host organ, the steps required for development of metastatic phenotype can be assumed to be approximately the same amongst solid carcinomas. Metastasis is a complex and rate-limited multi-step process and has been demonstrated since the 1970s to be a very inefficient process [137]. It has been further demonstrated that although 80% of the total number B16F1 murine melanoma cells, injected intraportally into murine liver, will survive and extravasate by day 3, only 1 in 40 will form micrometastases and only 1 in 100 will form macrometastases [138]. A metastatic cell requires distinct properties in order to be able to successfully migrate and initiate disease in a distant organ. More specifically, a metastatic cell from a primary neoplasm, in order to develop into a macrometastasis in a distant organ, must: (1) lose cellular adhesion; (ii) increase invasive characteristics; (iii) enter the circulatory system or else intravasate; (iv) survive in the microenvironment of circulation; (v) adhere to endothelial cells at the distant site; (vi) exit the circulatory system or extravasate; (vii) migrate in the organ parenchyma and survive the host organ microenvironment and; (viii) activate proliferation and initiate a micrometastatic colony. Each of these steps could be an individual chapter, but the aim of the following paragraphs is to describe the new strong concepts and insights in the metastasis field that have shaped the direction of research in recent decades.

#### *1.3.2.2 Dissemination of pre-malignant cells*

The ability of cancer cells to gain metastatic phenotype has been assumed for decades to be a very late stage process in the development of malignant neoplasms. In 2008, a study showed that untransfected mouse mammary cells, which have been engineered to express inducible oncogenic transgenes, once injected into the circulation can bypass transformation at the primary site and induce metastastic pulmonary lesions upon immediate or delayed oncogene induction [139]. In the same year, further studies were published in which pre-malignant cells were shown to have the potential to disseminate systemically from early alterations in certain genes. This study used a transgenic model in which human ductal carcinoma cells from premalignant human gland were transplanted into mice and the number of disseminated cells and their karyotypic abnormalities were found to be very similar to the clinical profiles of the equivalent metastatic patients. They concluded that dissemination of cells can occur at early, pre-invasive, stages and that these cells can frequently account for metachronous metastasis [140]. These findings suggest that non-metastatic cells can leave a primary site early in neoplastic development and diverge genetically in a distant organ's microenvironment. How early and in which cases are questions yet to be further defined. However, it is worth mentioning that a 1 cm breast carcinoma ($10^9$ cells) is approximately 10 years old, with at least 30 doubling times of 130 days each [141].

#### *1.3.2.3 Pre-metastatic niche*

In 2005, a ground-breaking experiment contributed to a marked change in the way we see metastatic disease and introduced the concept of a pre-metastatic niche [142]. It was shown that tumour cells could mobilise normal bone marrow derived cells (BMDCs) in order to migrate to certain regions (organ parenchyma) and form clusters. These clusters seemed to prepare the host's local microenvironment for the arrival of tumour cells, creating a pre-metastatic niche. In that study wild type mice were irradiated in order to eliminate the healthy bone marrow cells, and were transplanted with green tagged bone marrow-derived haematopoetic progenitor cells expressing VEGFR-1. Two mammary tumour red-tagged cell lines were used for this experiment with different and well-defined metastatic aggressiveness, and they were inoculated subcutaneously 4 weeks after BMDC transplantation. Prior to inoculations with tumours cells, the BMDCs mobility was minimal. After inoculation, the mobility of BMDCs remain minimal until day 8, at which point migration of BMDCs was observed and cluster formation by day 16. At 18 days post inoculation the first tumour cells were found to co-localise with pre-established BMDC clusters and these cells where the ones that established metastases. It was shown that the BMDC cluster formation correlated with tumour metastatic destination, since the tumour model is organ specific. Impressively enough, when conditioned media from the melanoma cells (MCM) alone was inoculated subcutaneously, this could also initiate BMDC mobilisation and cluster formation. Subcutaneous administration of MCM also enhanced the number of melanoma cells arrested in lungs, one day after tumour cells were injected intravenously, compared to mice treated with unconditioned media. Moreover 4 days later, the size and the frequency of nodules in

the lungs were augmented by MCM. These findings suggests that a pre-metastatic niche, established from VEGFR1$^+$ haematopoetic progenitors, plays an important role in the regulation of metastasis and importantly that the regulation is driven by soluble factors released from the tumour cells known as exosomes.
In the same study, it was highlighted that the BMDC clusters were VEGFR-1, VLA-4 ($\alpha_4\beta_1$), MMP9 and Id3 gene expression positive. By either blocking VLA-4, disrupting the VEGFR-1 pathway with MMP9 or by using Id3 knock out mice, a remarkable reduction in the haematopoietic progenitor cluster and metastasis formation was observed. The expression of MMP9 and its association with VLA-4, as well as its association with VEGRF-1 had previously been reported [143, 144]. Investigating the VLA-4 molecular mechanism, these authors observed increased expression of fibronectin in the metastatic niche, suggesting that fibronectin upregulation increased the adhesion of BMDCs. The role of VEGFR-1$^+$ progenitors cells was investigated *in vitro* and it was concluded that these cells promote adherence and growth of tumour cells. In response to this conclusion, a commentary was published by a different group showing VEGFR-1-activity-independent metastasis formation [145] although issues relating to relevance of the model used remain [146].

#### *1.3.2.4 Endothelial tumour cell adhesion and extravasation*

Tumour cells travel to distant sites via the blood circulation with exception of the lymph nodes. The lymphatic route will carry tumour cells to lymph nodes and, subsequently, to the haematogenous circulation [40, 147]. In order for a tumour cell to extravasate (exit the intravascular space) through the vascular endothelial layers, the tumour cell will have to slow down and eventually stop on the luminal endothelium.
There are different findings as to how tumour cell arrest occurs on endothelial cells. Mechanical occlusion, owing to the size of the tumour cell or cluster of cells, which is supported by the fact that within a few minutes of intravenous injection, tumour cells lodge in a capillary bed (223,333,353-359). An additional route for tumour cell arrest could be through micro-emboli within a capillary bed, following coagulation of tumour cells with platelets. Although tumour cells are bigger than platelets and neutrophils, they are in the circulation for significant amount of time. The tumour cells can produce haemostatic factors, release inflammatory cytokines and express adhesion proteins to bind to platelets. These routes are not mutually exclusive and may have significant overlap. The third possibility assumes that tumour cells can mimic the behaviour of leukocytes and express endothelial adhesion receptors, roll on the vasculature, slow down and finally adhere firmly. All three ways have been observed in preclinical and clinical studies in a variety of tumour types.
The leukocyte adhesion and extravasation route, however, also gives an insight into how tumour cells penetrate the endothelial wall, although the two mechanisms may not involve the same cell adhesion molecules. Circulating leukocytes recognize inflamed or activated endothelial cells and will arrest in these areas followed by extravasation through the vascular wall. The leukocyte adhesion and extravasation process has been reported since 19$^{th}$ century [148, 149]. However, it was not until the 1990s that the process was described as a multi-step process [150, 151]. This initial adhesion cascade has been described as a three-step process;

(i) the selectin mediated rolling, (ii) chemokine-triggered activation and (iii) integrin-dependent arrest, without including transendothelial migration. A decade of research has shed light into the structure and signalling events that underlie integrin activation [152, 153] and the classical three-step cascade has more recently been updated with the addition of further steps, including extravasation; slow rolling, adhesion strengthening, intraluminal crawling, paracellular and transcellular migration [154]. Leukocyte rolling is primarily mediated by L-selectin ,P-selectin and E-selectin, which interact with P-selectin glycoprotein ligand 1 (PSGL1). L-selectin is expressed on most leukocytes, whilst P- and E-selectin are most commonly found on inflamed endothelial cells [155, 156]. Integrins $\alpha_4\beta_1$, $\alpha_4\beta_7$ [157] and $\alpha_L\beta_2$ [158] and their associated ligands VCAM-1, MADCAM-1 and ICAM-1 from the immunoglobulin family participate in leukocyte and lymphocyte rolling and mediate firm adhesion. Chemokines and other chemoattractants also mediated firm adhesion via activation of the leukocytes or lymphocytes, thereby increasing integrin affinity [159, 160].

#### *1.3.2.5 Circulating cancer cells and disseminated dormant tumour cells*

Circulating tumour cells (CTCs) were first described by Thomas Ashworth in 1869, in his case study report entitled "A case of cancer in which cells similar to those in the tumours were seen in the blood after death". The work of Paget in 1889 expanded on the idea that these CTCs end up in certain organs, and furthermore, that CTCs (seeds) show specific preference to favourable organs (soil). The presence of isolated CTCs in the bone marrow has been classified with a different name and these cells are known as disseminated tumour cells (DTCs). CTCs and DTCs are two different steps in the metastatic process and their detection has given rise to clinical diagnostic interest. The detection of these cells is of particular interest with respect to the elucidation of metastatic processes and many techniques have been developed that aim to isolate this significantly small population of cells. However, some critical issues exist with these detection methods, including accuracy, quantification, relevance to mechanism and new cancer targets.

In patients without signs of overt metastases (M0) it has been observed that there are dormant CTCs in the vascular and lymphatic circulation, as well as DTCs in the bone marrow. CTCs and DTCs have become the subject of intense studies over the past 10 years, to assess the clinical relevance of these cells with respect to prognosis of metastasis or primary tumour relapse after surgical operation [161]. The findings of CTCs and DTCs to date are not entirely in accord, but there are certain types of tumours at the M0 and M1 for which these cells show significant clinical relevance [161, 162]. The presence of CTCs in a patient has been found to be associated with metastatic relapse and/or associated with reduced survival rate in patients with M0 prostate [161], colorectal [163], breast [164] and lung [161] cancer. In the case of M1 stage metastatic prostate, breast and colorectal cancer the CTCs correlate significantly with clinical prognosis [165] which can also be explained from the macrometastatic tumour burden [166].

For patients with M0 breast cancer the detection of DTCs in bone marrow is a validated marker of prognosis [167] but not for M1 breast cancer staging [162]. In contrast, for lung and prostate cancer the detection of DTCs vary with regards to prognostic relevance [168]and

for colorectal cancer no prognostic benefits has been found. The preclinical and clinical findings do not yield homogeneous results with regards to the mechanisms of dormancy in DTCs, but it has been shown that most of the DTCs detected are in the G0 phase of the cell cycle [169]. Overall, metastatic breast cancer seems to have the most coherent prognostic benefits from detection of CTCs and DTCs at the M0 stage, and this has lead to a new staging (TNM) subclass of M0 for breast cancer patients with detected CTCs and/or DTCs, cM0($i^+$) [170].

## 1.4 Molecularly targeted imaging

Experimental imaging, broadly speaking, is defined as the interpretation of any measurement of an object into a direct or indirect visualization of the object, or the object's behaviour or properties, and has been the founding stone for modern experimental science. The best examples of this analogy are the fields of biological sciences and medicine, which would have been almost impossible to evolve to today's understanding and quality without the continuous advancement of physics and technology. Until the discovery of the conventional imaging technologies, which took place during the first 50 years of the past century [X rays, Crystallography, Fluorescence Microscopy, Ultrasonography (US), Computed Tomography (CT), Magnetic Resonance Imaging (MRI), Positron Emission Tomography (PET) and Single Photon Emission Computed Tomography (SPECT)] immunology was the only tool for imaging tissues *ex vivo*. Conventional imaging modalities have improved only in quality (acquisition speed, resolution and accuracy) over the past 60 years, and not in the fundamental science behind their technologies. However, many distinctly different imaging approaches have emerged from the same fundamental technologies, owing to radical changes in methodology and identification of new targets for imaging. Molecularly targeted imaging is one of the methodologies that can be implemented for currently widely used imaging modalities and there is significant research is underway towards this aim.
As our understanding of the tumour microenvironment allows for verification of major molecular pathways, and furthermore, provides insight into important key molecules in the development of cancer, the attempt to image them is inevitable. Molecularly targeted imaging is a radical shift in the existing worldwide used modalities and it will inevitably contribute in our future deeper understanding of the tumour microenvironment.

### 1.4.1 Imaging of Angiogenesis

Extensive pre-clinical research, since 1970, has focused on anti-angiogenic therapies for solid tumour treatment, which has led to numerous clinical trials. To date the conventional clinical method for the characterisation of new vessel formation is through histological analysis of biopsies. This invasive technique cannot provide information for the entire tumour volume and is insufficient for a complete understanding of tumour physiology, owing to the inhomogeneity of the majority of solid tumours. It is apparent, therefore, that non-invasive *in*

*vivo* imaging methods, that accurately evaluate the extent of angiogenesis, are needed for cancer therapy management.
Recently it has become clear that molecular targeted imaging has the potential to evaluate and characterise tumour vasculature, both prior to and in response to therapy, providing non-invasive, repeatable measurements. Furthermore, the choice of biological markers and the type of modality can either assess the functional integrity of tumour vasculature or the molecular pathways involved in its regulation and response to therapy.
In the following paragraphs the most interesting advances of clinical and pre-clinical molecular imaging techniques for tumour blood volume measurements and detection of tumour angiogenesis expression, using contrast enhanced methodology for MRI, PET, SPECT, US and CT, will be discussed. Optical imaging has superior sensitivity but its clinical applications are limited by penetration depth, therefore, this method will not be discussed.

#### *1.4.1.1 MRI vascular measurements and detection of angiogenesis*

Nuclear magnetic resonance (NMR) is the framework of the MRI applications. NMR is a physical phenomenon, which describes how specific nuclei (e.g. $^{1}H$, $^{2}H$, $^{3}He$, $^{19}F$, $^{13}C$, $^{129}Xe$) when placed inside a static magnetic field are able to emit and absorb electromagnetic radiation, at specific resonance frequency related to the strength of the magnetic field. Historically, NMR it was first described from Isidor Rabi in 1938, in a publication with title "A new method of measuring nuclear magnetic moment", and in 1944 he received the Nobel Prize in Physics for his contribution to science.

##### 1.4.1.1.a MRI intravascular contrast agents

Conventional $^{1}H$ MRI, which uses the $^{1}H$'s in the water abundant body, is widely available in the clinic and doesn't use harmful radiation. As an imaging modality stands out from the rest for its high spatial resolution (submillimeter range) and its superior soft tissue contrast. However, MRI lacks of sensitivity and the $^{1}H$ MRI has orders of magnitude lower sensitivity than optical imaging and radionuclide imaging. With the aim to improve the sensitivity and contrast of MRI, paramagnetic and superparamagnetic contrast agents have been developed in order to enhance the contrast on $T_1$– and $T_2$ –Weighted $^{1}H$ MRI. Paramagnetic Gadolinium ($Gd^{3+}$; positive contrast agent) significantly reduces $T_1$ relaxation times and paramagnetic and superparamagnetic iron oxides (negative contrast agent) significantly reducing $T_2$ relaxation time [171-174]. However, in principle, either type of contrast agent reduces both $T_1$ and $T_2$ parameters. $Gd^{3+}$ has been implemented in the clinic but the iron oxides and their suitability for clinical use is being evaluated in clinical trials [175, 176].

#### 1.4.1.1.b Dynamic Contrast Enhanced MRI

Dynamic contrast imaging of blood flow is a functional technique (does not target molecular biomarkers) but provides information on the vascular permeability and laminar blood flow (diffusion and perfusion). Tumour vasculature usually has abnormal blood flow compared to normal vascularised tissues. DCE MRI using paramagnetic gadolinium ions ($Gd^{3+}$; OMNISCAN) and is a standard clinical technique for detection of vascularised abnormal tissues using $T_1$-Weighted sequenscies. $Gd^{3+}$ ions can also be chelated to low molecular weight ligands, such as diethylenetriaminepentacetic acid or ethylenediaminetetraacetic acid (Gd-DTPA or Gd-EDTA) and therefore provide stronger local contrast. Syntheses of these Gd-based low molecular weight molucules are reasonably cheap and they show low toxicity. However, although the method is fairly sensitive, the dynamic nature of the acquisition comes with the cost of spatial resolution (clinical 1.5 $mm^3$) [177].

#### 1.4.1.1.c Molecularly targeted Gd-based moieties

Binding of only few gadolinium complexes to molecular targets cannot provide a sufficiently high signal-to-noise ratio. In order to improve the contrast, $Gd^{3+}$ complexes are very often loaded onto nanocarriers in a multivalent configuration [178, 179]. The first study that demonstrated molecular MRI was performed in 1998 and aimed to detect angiogenesis by targeting $\alpha_v\beta_3$, using antibody-coated paramagnetic cross-linked liposomes with a high payload of gadolinium (containing 30 % $Gd^{3+}$ chelate-labelled lipid) and a mean size of 300-350 nm in diameter [178]. This seminal paper was a proof of concept study and the techniques used were poorly developed at the time, while later work by other investigators has advanced this work tremendously. The study was repeated 5 years later with peptomimetic instead of the antibody against $\alpha_v\beta_3$ conjugated on the Gd-based nanoparticles [179], which can be more efficient than an antibody due to its multivalent configuration, which seems to increase affinity. After 2 hours of intravenous administration into rabbits with squamous cell carcinoma, regions of tumour angiogenesis were detectable by MRI. Work in mice-bearing subcutaneous tumours using similar paramagnetic Gd nanocarriers conjugated to anti-integrin $\alpha_v\beta_3$ peptidomimetic was able to characterise the angiogenic phenotype in early melanoma [180], whilst $\alpha_5\beta_1(\alpha_v\beta_3)$-targeted nanocarriers have enabled 3D maps of angiogenesis in xenographs to be constructed [181]. Again, to enable sufficient contrast accumulation, MRI assessments were performed 2 h post-administration of the contrast agent, owing to the limited binding efficiency at earlier time points. Other endeavours for improving MRI sensitivity for tumour angiogenesis imaging include developing $Gd^{3+}$-containing micelles, liposomes, or high-density lipoprotein-like nanoparticles. Work in mice bearing subcutaneous tumours with RGD-liposomes containing fluorescence dies have been able to reduce the time of MRI assessment post-administration to 35 minutes, with sufficient $T_1$-W contrast to characterise angiogenesis [182, 183]. In that work, there was evidence that unbound nanoparticles had extravasated from the vasculature [182, 183], but this was considered insignificant for $T_1$-W imaging of the nanoparticles, owing to the relatively small contrast effect of the Gd.

#### 1.4.1.1.d Superparamagnetic iron oxide

As we seen previously, small leakage of $T_1$ contrast agent do not pose significant problem of unspecific binding but an equivalent leakage of $T_2$ contrast agents of iron oxides would have cause significant non-specific contrast on $T_2$-W imaging. For example, specific targeting of tumour angiogenesis has been demonstrated using RGD-USPIO conjugates (< 100 nm) [184], in squamous cell carcinoma-bearing subcutaneous xenographs. One limitation that was identified was the tendency for passive extravasation and accumulation, thereby diminishing molecular specificity, as also found in tumour xenograft models implanted with non–small cell lung cancer cells [185]. In contrast, micron-sized particles (< 500 nm) do not passively extravasate and furthermore it has been previously shown that 1 μm diameter iron oxides are not internalised by either endothelial cells or peripheral immune cells (e.g. macrophages) during the period between injection and imaging [186]. A further limitation of nano-scale particles for MRI is their relatively long blood half-life, which increases background contrast effects and greatly reduces the binding-specific contrast at short time frames after administration. As I am going to demonstrate in the following Chapters, the half-life of micron-sized particles in the blood is considerably shorter (< 1min). It has been previously demonstrated that this clearance occurs primarily through the liver and spleen, with minimal retention in non-target organs (e.g. kidney, lungs, brain), but the role of complement in this process cannot be excluded. In common with previously described molecular imaging approaches [186-195], it has been shown empirically that specific MPIO binding to target is sufficient to attain effective contrast. In imaging vascular inflammation using a particle targeting vascular cell adhesion molecule-1 (VCAM-1) it has been previously shown that specific binding has occurred within 20 minutes of administration and that this was maintained at a constant level for at least 60 minutes [188]. Hence, in the work presented in this Thesis, both methods have used the rapid clearance of the micron-sized particles (MPIO pharmacokinetics) as a beneficial parameter that allows for quick MRI acquisition after administration of the contrast agent, without undesired background from circulating iron oxides as seen in the application of the nano-scale counterparts. Furthermore, the fact that these large particles are oblidged intravascular agents makes them suitable for targeting endothelial biomarker, ensuring that there is no leakage of the agent owing to leaky tumour vasculature.

#### 1.4.1.1.e Diffusion-Weighted MRI

DW-MRI does not require contrast agent and can provide molecular information by allowing mapping of the diffusion process of molecules, mainly water, in biological tissues, *in* vivo. Recently, there has been as interest in using this technique as a clinical biomarker for response to therapy [196-199]. DW-MRI determines the apparent diffusion coefficient (ADC) of tissue water, which varies in the tumour microenvironment owing to factors such as tumour hypercellularity and vasogenic edema [196]. It has been shown that the increase of ADC in the tumours correlates with positive treatment response and concerning early

vascular assessment of vascular tumour therapy DW-MRI can be superior to DCE-MRI [199, 200].

#### *1.4.1.2 PET and SPECT*

Positron emission tomography (PET) and single photon emission computed tomography (SPECT), both are modalities that can provide 3D whole body *in vivo* imaging. Both modalities are based on a functional method where injection or inhalation of radiation-emitting radionuclides (tracers) are required, providing information on the molecular pathways with high sensitivity and specificity. The two modalities using different type of nuclear emitters (beta and gamma or only gamma radiation) and are based on different philosophy of detection (time of flight or angle of incidence), whilst using the same reconstruction method (filtered backprojection). Preparation of PET isotopes require tedious radiochemistry and convenient nearby cyclotron and radiopharmaceutical facilities, hence, it is an expensive imaging application. In addition the radioisotopes for PET imaging, which have the safest radiation, are very short lived [fluoride-18 ($^{18}$F), $T_{1/2}$ = 109 min; carbon-11 ($^{11}$C), $T_{1/2}$ = 20 min]. In contrary SPECT radiochemistry is easily available, has lower cost and the radioisotopes produced have significantly longer half-life [metastable technetium-99 ($^{99m}$Tc), $T_{1/2}$ = 6 h or iodine-123 ($^{123}$I), $T_{1/2}$ = 13 h].
PET has the advantage to operate without the need of collimation, therefore, shows greater sensitivity than SPECT, detecting pM *vs.* nM concentrations of the tracer. To measure the directly emitted gamma-radiation, collimators gate the bulk of rays in order to define the angle of incidence, which leads to low detection efficiency [201]. Nonetheless, owing to this superior sensitivity both modalities can be operated in the clinic with low risk radiation exposure and no physiological effect on the patient. One great advantage of the radionuclide imaging is that allows for dynamic monitoring of these tracers and probes can be engineered in order to investigate the biodistribution and pharmacokinetics of these agents for the purpose of imaging and therapy delivery [202, 203]. PET and SPECT suffer from poor spatial resolution in the sub-millimeter range (PET, 2-5 mm *vs.* SPECT, 5-15 mm). However, development on collimation engineering has provided a new technology of collimation for SPECT that has increase the resolution SPECT imaging. Multi-pinhole collimator for SPECT (pinhole-SPECT) can offer a trade of; field of view for resolution, with preserved sensitivity. Therefore, pinhole-SPECT is not suitable for whole body clinical imaging but is ideal for small animal imaging with resolution ranging from 0.3-2 mm [204, 205].
$^{15}$O-labelled water has been the first radiolabelled PET tracer for cancer patients, aiming to identify and quantify blood flow and tissue perfusion in tumours [206] and monitor response to chemotherapy [207]. This method is considered as the gold standard for blood flow measurements; nonetheless, studies only functional changes due to alterations of volume distribution of radiolabeled water within the tumor tissue. At the current development of PET and SPECT imaging of angiogenesis there is great interest on specific biomarkers of angiogenesis, including VEGF and its receptors and adhesion molecules like integrins [208-211]. This permits a molecular evaluation of the dynamic processes of tumor angiogenesis and can correlate the uptake of the agent with the biomarkers expression. One of the most

popular molecules for imaging VEGF expression is bevacizumab, which is a monoclonal antibody and its recombinant has been humanized [212]. Bevacizumab can inhibit VEGF receptor 1 and 2 and it can bind to all isoforms of human VEGF having affinity in the nanomolar concentration. Bevacizumab has been used for molecular pre-clinical PET imaging with various isotopes; $^{89}$Zr [213, 214], $^{64}$Cu [215, 216], and $^{124}$I [217]. However, only $^{89}$Zr-bevacizumab has made it to clinical trials with breast cancer patients [214]. Bevacizumab has also been labeled with indium-111 ($^{111}$In), which has 67 h half-life, for SPECT imaging. $^{111}$In-bevacizumab has been used in subcutaneous implanted human tumours in mice and showed comparable uptake characteristics for the tumours and organs compared to $^{89}$Zr-bevacizumab [218]. The specificity of the agent was further evaluated *in vitro* and *in vivo* [219, 220] and later used in the clinic for melanoma patients, where the uptake and the VEGF expression from biopsy showed significant correlation [221].
Concerning $\alpha_v\beta_3$ integrin as biomarker of angiogenesis, [$^{18}$F]-galacto-RGD was the first RGD agent to be used in clinical trials for imaging. It is a glycosylated RGD molecule which is more hydrophilic than cyclic RGD [162], therefore, has increased renal excretion compared to cyclic RGD; excreted predominantly via the hepatobiliary route [163, 164]. $^{18}$F-Galacto-RGD radiotracer enabled the visualization of $\alpha_v\beta_3$-integrin expression successfully in patients with squamous cell carcinoma of head and neck with good tumor to background ratios. The fact that $^{18}$F-FDG-images of the glucose metabolism were not closely related to those of $\alpha_v\beta_3$-Integrin expression indicated an important angiogenesis specific benefit of information obtained by the use of the integrin specific radiotracer [222]. Maraciclatide is a cyclic RGD-based molecule (diamine dioxime-Lys-Cys-Arg-Gly-Asp-Cyc-Phe-Cys- polyethylene glycol) that has been developed into a SPECT agent (GE Healthcare; $^{99m}$Tc-maraciclatide) [223]. Pre-clinical evaluations of the biodistribution of the agent have shown that $^{99m}$Tc-maraciclatide is stable in the blood and is predominantly accumulating to liver and kidneys. $^{99m}$Tc-maraciclatide is being evaluated in the clinic [224, 225].

#### *1.4.1.3 Contrast enhanced Ultrasonography (US)*

Ultrasound imaging is inexpensive, portable and has convenient penetration for the human body, thus, permits real-time anatomical and functional imaging. Ultrasonography is limited in field of view and resolution but is being used for operative guidance [226] and is suitable for intravascular imaging, with particular suitability for cardiac diagnostics; echocardiography [227]. Recently developed microbubbles for US, made out of various gases, have been the most favourable intravascular ultrasonic contrast agent and has been used for molecular imaging of angiogenesis, inflammation and thrombosis [228]. The outer layer of the microbubbles can be engineered by certain chemistry methods in order to allow conjugation of ligands for *in vivo* molecular targeting [229-231].
The first reports of *in vivo* ultrasound molecular imaging of tumour angiogenesis using microbubbles were published in 2003 [232, 233], demonstrating dynamic contrast enhanced US in glioma brain tumours (intracerebrally injected U87MG human glioma cells into athymic nude rats; imaged in 2 and 4 weeks) and in subcutaneous matrigel plug mouse models (heparin and FGF-2 enriched martigel plugs subcutaneously injected in C57BL6

mice) using microbubbles (3–4 μm in diameter) targeted to integrin $\alpha_v\beta_3$ or integrin $\alpha_v$ respectively. Thereafter, improved methods have been reported for detection of angiogenesis and for monitoring response in anti-angiogenic therapies [228].
This molecular imaging modality is convenient and suitable for pre-clinical imaging, providing great sensitivity. However, most pre-clinical molecular ultrasound imaging studies have been utilize microbubbles that have a streptavidin, avidin, or biotin moiety incorporated into the lipid shell via a polyethylene glycol (PEG) arm for conjugation of the ligand via a strept(avidin)-biotin chemistry, which is toxic to humans. Apart from toxicity, streptavidin has been reported to mediate non-specific adhesion to endothelial cells via interactions with endogenous fibronectin [234], and furthermore, the administration of streptavidin [235] or streptavidin-antibody conjugates [236] resulted in elevated plasma levels of human anti-streptavidin antibodies in the clinical investigation of radioimmunotherapies for tumour treatment. The studies on the development of covalent conjugation of cRGD onto microbubbes for *in vivo* targeting of angiogenesis reporting absence of acute toxicity after intravenous administration of these agents in mice [237]. A second limitation of molecular US is the field of view and the restriction to 2D perspective. To this end, development of the proof of principal 3D *in vivo* molecular ultrasound imaging, including volumetric analysis of inter- and intra-animal targeting, provides a thorough way of characterizing angiogenesis and will be a more robust assessment technique for the future [238, 239].

#### *1.4.1.4 Contrast enhanced Computed Tomography (CT)*

X-ray 3D computed tomography is a non-invasive widely available imaging modality. The nature of the detection (contrast between bone, tissue and air) as wells as the speed of acquisition makes modern CTs the most useful tool in hospitals today and one of the best modalities for structural imaging of lungs, which are undoubtedly a constant challenge for the rest of clinically available modalities. However, the soft tissue contrast of CT is very poor and concerning visualisation of blood vessels, conventional CT cannot distinguish between vessels and surrounding tissues (same X-ray absorbance range).
CT contrast agents like small molecules of iodinated contrasts agents are available for pre-clinical *in vivo* CT imaging. This type of contrast agent when used in conventional CT with only slices per rotation (flat-panel Volumetric CT; fpVCT) can depict vessels with 150-200 μm resolution [240, 241] and enable longitudinal studies with minimum anaesthesia exposure (acquisition within few seconds) [242, 243]. When higher doses of iodine or barium containing contrast agent were administrated, 40 to 50 μm vessels could be visualised with great sensitivity. Blood pool agents like colloidal polydisperse eXia 160$^{TM}$ can prolong the circulation of the contrast agent and diffuse more slowly from blood vessels to extracellular space, hence, can be used to improve the resolution and contrast over time. Contrast enhanced micron resolution CT (micro-CT) required high doses of blood pool contrast agent and the prolonged high radiation necessary to achieve higher resolution is suitable only for preclinical applications [244-247].
Very recently, a great interest has been focusing on gold nanoparticles (GNP) owing to its great optical properties, non-toxic biocompatibility *in vivo* and suitability for conjugation of

ligands on its surface [248-251]. The X-ray absorption is depended on the atomic number and electron density of the material and whilst currently used iodine has (53 and 4.9 g/cm3) gold has (79 and 19.32 g/cm), therefore, provides much higher X-ray absorption and stronger contrast on CT. Although GNP provide high degree of flexibility in terms of functional groups for coating and targeting, to date there are no attempts to image angiogenesis by targeting $\alpha_v\beta_3$ or equivalent biomarker for angiogenesis. GNP, like blood pool agents, have prolonged circulation in the blood. The basic strategy implemented for GNP with CT have been the passive targeting, for detection of subcutaneous tumours taking advantage of the progressive permeation through transendothelial pore of tumour blood vessels (EPR effect) [252]. Coating of GNP with ligands which target biomarkers expressed in tumour cells has been shown to provide 1.6-fold increase in active tumour targeting [253]. GNP can also be used for photothermal therapy, owing to their suitable optical characteristics and inevitably the focus of research and development has been in creating multifunctional GNP probes that aim to monitor and enhance radiation therapy [254]. To this end, $^{177}$Lu-labeled GNP have been coated with cyclo-RGDfK peptides for molecular targeted anti-angiogenic radiotherapy [255]. Concerning CT detection of angiogenesis using targeted GNP to an angiogenesis biomarker, the method will have to tackle significant drawbacks. The resolution of CT forbids single GNP detection, therefore, the accumulation of GNP per voxel should be significantly high. In addition, the fact that the particles are subject of the extravasation via EPR effect will increase the non-specific binding for endothelial targeting biomarkers. Potentially, micron-sized gold particles could provide a solution since, as will be outlined in the following chapters, the micron-sized particles are obliged intravascular agents and their volume will provide significantly improved attenuation of X-rays.

### 1.4.2 Imaging of Metastasis

To date, detection of lymphatic or vascular mediated metastasis, at very early stages of the process remains a significant limitation in pre-clinical and clinical practice. Metastasis in the clinic can be detected with various modalities but in the macroscopic level because there is no available technique that allows detection of micrometastatic colonies smaller than 1-2 mm. Macroscopic metastasis in the clinic is classified as M1 stage and is the most life-threatening aspect of cancer development with very low survival expectancy owing to reoccurrence of the disease. Concerning primary breast tumours, over the past decades the treatment outcome has been improved owing to the advancement in techniques for early detection, surgical removal and targeted therapy. Nevertheless, the mortality rates of breast cancer are still high owing primarily to metastatic disease, with lung, brain, bone and liver being the most common organs for distant dissemination [256, 257]. The sensitivity of the currently available clinical diagnostic non-invasive imaging methods is of the order of subcentimetre, leaving micron-sized metastasis undetected upon metastatic screenings. The metastatic clinical staging of the breast cancer (TNM model), which has been very poorly classified, is reflecting this sensitivity setback. Patients with metastasis are clinically classified as single staging group, M1 patients, irrespective of whether they have just a single metastatic colony or many metastatic colonies or metastases in more than one organ and as a

consequence they receive the same cancer metastasis treatment. Patients with undetected metastasis are all classified as M0 patients and without invasive biopsy there is no means of knowing if the patient has metastatic development, events of extravasation or micrometastasis, during which treatment could be crucial. Lack of early detection of metastatic processes has as a consequence that clinical therapy is often beyond the point of effective intervention. Significant advantages might be gained if improvements could be made to staging.

Concerning radiotherapy, it has been demonstrated that irradiation of subcutaneous tumours can promote tumour self-seeding, where tumour cells circulate and they are re-seeded to the same subcutaneous tumour in mice. It is suggested that tumour microenvironment (TME) plays important role in the tumour self-seeding mechanism [258]. Furthermore, vascularisation plays crucial role in the self-seeding mechanism and because micrometastasis has no or significantly less vascular density compared to macrometastasis [259] if small metastatic lesions (50-200 μm cross sectional diameter) can be detected before they establish metastatic tumour microenvironment (recruitment of healthy cells from host organ) then is believed that therapy could be more beneficial and possibly improve the therapeutic survival expectancy. There is a need for a method that allows for specific and high-resolution imaging, which can characterise invasion and micrometastasis.

The lack of molecularly specific and sensitive imaging methods that allow monitoring of cell-biological events late at the invasion-metastasis cascade limits our understanding for the mechanisms and key molecular pathways that mediate the successful metastatic development. On the same lines of thinking, molecularly targeted imaging approaches provide a tool to study the mechanisms underline the late invasion-metastasis events, prior to detectable development of macroscopic metastasis, such as extravasation and micrometastasis formation. Optical bioluminescence imaging has offered a tool for investigating these processes with outstanding specificity but is limited by its tissue penetration for clinical practise, and for this reason will not be discussed further. In the following paragraphs, research on metastasis pre-clinical and clinical detection, as wells as recent advances in the field, will be discussed.

#### *1.4.2.1 PET and SPECT*

Diagnosis of lymphatic metastasis in the sentinel node (SLN) is detrimental upon choice of cancer therapy treatment, and therefore, imaging methods that can accurately define diseased lymph nodes are of a great importance for the stratification of treatment. Standard diagnosis of lymph node metastasis is based on the assessment of the size or the morphology of the lymph nodes, and therefore, variety of conventional structural imaging can be employed; US, MRI, CT [260]. However, these conventional approaches are not molecular sensitive and cannot provide information on the molecular level without contrast agents, with the exception of DW-MRI, which is going to be discussed later. PET has a great importance in lymph node imaging primarily with the glucose analogue $^{18}$F-FDG and although is functional and not molecularly targeted, has great sensitivity for abnormal glycolytic cell metabolism; $^{18}$F-FDG is avidly taken up by cells with increased rates of glycolysis and is phosphorylated to $^{18}$F-

FDG-6P. The method is limited to detect macrometastases and is more efficient for lessions > 1 cm, whilst PET-CT is not efficient identifying malignant lymph nodes in the mediastinum [261].
SPECT with the use of cationic lipophilic radiotracers [$^{99m}$Tc-tetrofismin, $^{99m}$Tc-methoxyisobutylisonitrile], which are conventionaly used for standard practise scintimammography, might have the potential to evaluate the preoperative axillary lymph node status in patients with breast cancer with higher efficiency than current used scintimammography. If pinhole collimators are employed in such clinical evaluations it has been suggested that micrometastasis might be detected [262]. $^{111}$In-bevasizumad has been used for first time in clinical trials for detection of liver metastasis from colorectal cancer [263]. However the uptake of the agent did not correlate with the expression of VEGF levels from the biopsies and it has been suggested that $^{111}$In-bevacizumab uptake might not be influenced by some secreted isoforms of VEGF [220]. $^{99m}$Tc-maraciclatide has also been considered in a clinical study as a probe for detection of metastasis [264]. The study concluded that $^{99m}$Tc-maraciclatide for brain and lung metastasis has the potential to detect metastasis for breast and lung primary cancer, whilst detection of bone and liver metastasis was poor.

#### *1.4.2.2 Molecular MRI for detection of metastasis*

The use of superparamagnetic particles in lymph node metastasis has been suggested as more accurate assessment of lymph node screening. Certain types of USPIO [265] are not taken up by metastatic lymph nodes and it was suggested that this contrast enhanced MRI lymph labelling technique can provide a more accurate assessment for lymphatic metastasis compared to standard clinical lymphography, allowing also for whole body screening [266, 267]. It has been demonstrated in pre-clinical studies that use of USPIO for the detection of specific lymph node metastasis in prostate, testicular and renal cancer is possible [176, 268, 269]. However, the technique is limited to detection of macrometastatic lessons. Concerning molecularly targeted MRI using labelled USPIO with biological ligands is challenging and has inherent limitations of low target valency and long half-life of blood, which reduces binding specific contrast effects.
Alternatively, the micron-sized iron oxide particles presented in this Thesis are proposed as high valency molecular probes for molecular MRI and with rapid biological clearance. VCAM-1 is overexpressed on brain endothelium during metastatic development. Thus, on the basis of the early upregulation of VCAM-1 in the metastatic seeding process, VCAM-1 has been considered previously as target for detection of micrometastasis in the brain using a molecularly targeted MRI agent, VCAM-MPIO [270]. By targeting the metastasis induced VCAM-1 activated endothelium in the brain, bound VCAM-MPIO were able to dephase the signal from the brain on *in vivo* $T_2$*-weighted MRI, providing a sensitive and specific endothelial biomarker of micrometastatic colonies. This proof of principal study has the limitation that used magnetic microparticles that are incompatible with clinical practise owing to their toxicity. However, there is development of multimeric biodegradable micron-

sized particles synthesized from smaller iron oxide biodegradable nanoparticles that makes the clinical translation of this method a realistic possibility.
In the work which will be outlined in the 3rd and 4th Chapter of this Thesis, a molecularly targeted method for detection of micrometastasis in the lungs, using monoclonal anti-VCAM-1 labelled micron-sized iron oxides (1.08 μm in diameter), will be described.

#### *1.4.2.3 Diffusion-Weighted MRI*

Studies with DW-MRI, have shown that the ADC measurement of benign lesions is higher than of malignant lesions, in breast and prostate cancer [271, 272]. The method does not use contrast agent and is comparable to FGD-PET/CT, which is used in the clinic for detection of systemic metastasis. DW-MRI can also be performed as a whole body (WB) imaging technique to cover all possible site of metastasis. WB DW-MRI has been used for detection of malignancy in patients and showed highly sensitive and specific detectability, which is relevant to FDG-PET/CT [273]. Work also on brain metastases showed that DW-MRI pose technical advantages over FGD-PET/CT [273, 274]. Concerning micrometastasis in the brain, studies have shown that DW-MRI can detect differences in ADC when blood brain barrier (BBB) is still intact, thus, cannot be detected with DCE-MRI [275, 276]. Furthermore, DW-MRI as an alternative systemic screening for skeletal metastasis compared to FDG-PET/CT [277] and $^{99m}$Tc-phosphonate scintillography has shown that the MR-based method has revealed higher specificity and sensitivity for early detection of skeletal metastases [278, 279]. Given the excellent soft tissue contrast and resolution of MRI, DW-MRI appears to be a very promising technique for detection of small micometastatic lessions.

## 1.5 Aims of thesis

Based on the unmet needs described above the primary aims of this thesis were to develop two intravascular molecular imaging agents, for pre-clinical *in vivo* detection of (i) lung micrometastasis and (ii) tumour angiogenesis. These agents were constructed on an iron oxide platform with diameter in the micrometre size range (Microparticles of Iron Oxide - MPIO), and in the case of lung metastasis a dual PET/MRI agent was created.

Within these overall aims I have specifically tested the following hypotheses:

Chapter 3

1. VCAM-MPIO bind to VCAM-1 on activated pulmonary endothelium.
2. Retention of VCAM-MPIO in metastasis bearing lungs is specific to micrometastasis induced expression of endothelial VCAM-1.

Chapter 4

1. Specific retention of VCAM-MPIO on micrometastasis bearing lungs can be detected using bright lung MRI.
2. Specific retention of radiolabeled VCAM-MPIO on micrometastasis bearing lungs can be detected by PET *in vivo* imaging.

Chapter 5

1. Conjugation of a cyclic penta-peptide c(RGDyk) to MPIO does not affect its binding affinity and specificity to $\alpha_v\beta_3$.
2. Binding of c(RGDyK)-MPIO is detectable by $T_2$* weighted MRI *in vivo* within a short time-frame after administration.
3. The *in vivo* contrast effect of c(RGDyK)-MPIO can be used as a quantitative measure of tumour angiogenesis.
4. The *in vivo* contrast effect of c(RGDyK)-MPIO can be used to provide spatial information on $\alpha_v\beta_3$ expression.

# Chapter 2 – Materials & Methods

## 2.1 Chemicals and solutions

### 2.1.1 Chemicals

Sodium dihydrogen orthophosphate dihydrate (S/3760/53), di-sodium hydrogen orthophosphate (Sorrenson's salt) (S/4440/60), sucrose (S/8600/60), tris-hydrochloride (BPE153-1), sodium chloride (BP358-212), magnesium chloride (M/0600/53), calcium chloride (C/1500/50), iso-Pentane (99+%) (P/1030/08), propan-2-ol (P/7490/17), ethanol (99.8%) (E/0650DF/17), methanol (99.9%) (M/4000/17), Hydrochloric acid (H/1200/PB17), Boric Acid (B/3800/60), HEPES (H3375-100G) and triton X-100 (BP151-500) were obtained from Fisher Scientific (Loughborough, UK). Paraformaldehyde (PFA) (15,812-7), manganese chloride (M3634-500G),l-lysine monohydrochloride (L5626), zinc chloride (208086), (-)-tetramisole hydrochloride (L9756), ethylenediaminetetraacetic acid (EDTA) (E5134), Sodium hydroxide (7169-500G), Hydrogen peroxidase (H1009-500ML) and glutaraldehyde (G5882) were obtained from Sigma-Aldrich (Gillingham, UK). Sodium metaperiodate (27986.235), sodium azide (10369) and sulfuric acid (191695E) were obtained from VWR International (Lutterworth, UK). Phosphate buffered saline (PBS) (Dulbecco A) tablets (BR0014G) were obtained from Oxoid (Basingstoke, UK).

### 2.1.2 Substrates

3,3,5,5'-tetramethylenediamine (TMB) (BA-9500, e-Bioscience UK Ltd). 3M Sulfuric acid was diluted down from initial high concentration with Q-H2O. Neutravidin-horseradish peroxidase (HRP) (P8250-50KU, Sigma Aldrich, UK). Ophenylenediamine hydrochloride (OPD) (P6787, Sigma Aldrich, UK). Methanol with 1% of hydrogen peroxide solution [solution - 30% (w/w)] used for quenching the peroxidases in immunohistochemistry or for immunofluorescence P-buffer with 1% of hydrogen peroxide [solution - 30% (w/w)].

### 2.1.3 Buffers

TS buffer (TS): 20 mM Tris-HCl pH 7.5, 150 mM NaCl, 1 mM $CaCl_2$, 1 mM $MgCl_2$, and 1 mM $MnCl_2$. TSB buffer (TSB): TS + 1% BSA . Tris-NaCL buffer (TNB): 1M Tris-Cl (pH 7.5), 5M NaCl. 0.1M Phosphate buffer (P): 0.1 M $NaH_2PO_4$, 0.2M $NaHPO_4$, pH 7.4. Phosphate buffered saline (PBS): 10 mM $Na_2HPO_4$ pH 7.5, 150 mM NaCl. Phosphate buffered saline with Tween-20 (PBST): 10 mM $Na_2HPO_4$ pH 7.5, 150 mM NaCl, and 0.01% Tween-20. Phosphate-Citrate buffer (PC): 24 mM sodium citrate, 50 mM $Na_2HPO_4$ pH 5.0,

0.012% $H_2O_2$. Carbonate buffer (CARB): 15 mM of $Na_2CO_3$, 35 mM $NaHCO_3$, pH 9.6. 0.1 M sodium borate buffer (SB): 0.1M $H_3BO_3$, 5M NaOH, pH 9.5. 3M ammonium sulphate in phosphate buffer (ASPB): 3M $(NH_4)_2SO4$, 0.1M PB buffer, pH 7.4. 3M ammonium sulphate in sodium borate buffer (ASSB): 3M $(NH_4)_2SO_4$, 0.1M SB buffer, pH 9.5. Storing buffer (STOR): PBS + 0.1% NaN3. Storing buffer with BSA (STORB): PBS + 0.1% $NaN_3$ + 0.1% BSA w/v. Washing buffer (WASH): PBST + 0.1% BSA. Blocking buffer (BLOCK): PBST + 0.5% BSA. 1M HEPES buffer (HEPES): 1M $C_8H_{18}H_2O_4S$.

## 2.2 Cell lines and tissue culture

### 2.2.1 Tumour cell lines and culture mediums

4T1 murine mammary carcinoma (ATCC, Teddington, UK) [17, 280] transfected with a plasmid promoting the expression of EGFP [281] and MC-38 murine colon carcinoma cells (ATCC, Teddington, UK) were grown in Dulbecco's Modified Eagle Medium (DMEM) (PAA, Yeovil, UK) containing 10% v/v (25 mmol/L) glucose and supplemented with 1% v/v (200 mmol/L) L-glutamine (PAA) and 10% v/v fetal bovine serum (FBS, BioSera, Ringmer, UK). B16F10 murine melanoma cells (ATCC, Teddington, UK) were grown in a modified medium, as stated above, with additional 1% v/v (0.1 mmol/L) nonessential amino acids (PAA, Yeovil, UK) and 1% v/v (1 mmol/L) sodium pyruvate (PAA, Yeovil, UK). Human Unbiliant Vascular Cells were grown in Lonza Medium with Bullet-kit2.

### 2.2.2 Cell culture and incubation

All cells were grown in tissue culture flasks of 75 cm² (Corning Life Sciences) in at least 12 ml of appropriate complete medium. Cells were grown in an incubator with a humidified atmosphere at 37 ºC at 5% $CO_2$. The cells were allowed to grow until 90% confluence and were periodically tested for mycoplasma infection (Lonza Rockland Inc, MycoAlert Mycoplasma Detection Kit).

### 2.2.3 Cell revival

Cells were thawed from storage with first rapid dilution of the cell suspension in pre-warmed complete medium. For HUVECs only, the solution was seeded to appropriate flasks without any centrifusion, while for all the rest of the cell lines, then solution was centrifuged (4 min at 1200 rpm at 4 °C) and cell pellet was re-suspended in complete medium, before seeded into appropriate flasks.

### 2.2.4 Cell storage

A million cells were re-suspended in 1ml of 90% FBS and 10% DMSO (Sigma Aldrich, UK) and aseptically sealed in cryo-vials (Sigma Aldrich). For short time storage cells were placed in a freezing container (Sigma Aldrich) and stored at -80ºC. For long-term storage cryo-vials were stored in liquid nitrogen container at -199 Celsius (VWR international Jencons).

### 2.2.5 Cell suspension

Cell culture flasks were first washed with pre-warmed PBS buffer (3x with 12 ml) and then incubated for 2-5 min with 3 ml of Trypsin 0.05% with EDTA (GIBCO). The following cell suspension was then diluted in pre-warmed medium and centrifuged (4 min at 1200 rpm at 4 °C).

### 2.2.6 Cell preparation for injections

After re-suspension in pre-warmed PBS buffer, the cell concentration was measured using the Nucleocounter NC-100 (Chemometec) as per manufacturer's instructions. The appropriate dilution was calculated for the live cell fraction and cell suspensions for injection were prepared in PBS buffer. The cells were transported in 1.5 ml eppendrof tubes (Fisher Scientific).

## 2.3 Animal work

### 2.3.1 Mouse strains

All mouse strains used were house in individually ventilated cages with food and water provided *ad libitum.* All experiments were performed in accordance with the U.K. legal requirements "under the Animals (Scientific Procedures) Act 1986" and ethical guidelines defined by the wider research community for University of Oxford.
C57BL/6 (C57BL/6N) and BALB/c (BALB/cOlaHsd and BALB/cAnNCr) mice were purchased from Harlan and Charles River Laboratories. For each experiment, female mice between the ages of 6-10 weeks were included.

### 2.3.2 Pulmonary metastasis model

4T1-GFP tumour cells ($5x10^5$, $1x10^5$ or $5x10^4$ cells) were injected intravenously into the lateral tail vein of BALB/c's. At specific times after tumour cell injection (day 7, 10, 14)

mice were killed and lungs harvested as described below. The tissue was fixed by immersion in 4% PFA for 24 h and cryo-protected in 30% sucrose (S9378, Sigma Aldrich, UK) for 48 h.

### 2.3.3 Subcutaneous carcinoma model

C57Bl/6 mice were anesthetised with 2-3% isoflurane (IsoFlo) in $O_2$ and injected subcutaneously in the right upper flank with either $5x10^4$ B16F10 murine melanoma cells or $5x10^4$ MC-38 colon carcinoma cells in 100 µl sterile PBS[1]. Tumours were allowed to grow for either 21 days, to achieve tumour volumes < 400mm$^3$ or for 28 days to achieve tumour volumes > 400mm$^3$.

### 2.3.4 Lung harvest

At the specified time-points, animals were terminated with lethal injection of 0.2 ml of pentobartbital, 2:1 dilution in water. Each mouse was tracheotomised and a 24-gauge cannula was inserted and subsequently firmly tightened with a suture knot. For the studies where blood perfusion was required, the left auricle of the heart was pierced and pre chilled at 4°C PBS with 0.04% Heparin sodium (25,000 I.U./ml, Wockhardt, Wrexham, UK) was infused into the right ventricle of the heart, followed by a cut on the right aorta. The infusion was achieved with gravitation force by locating the heparinised PBS container approximately one meter above hearts level. Further, the lungs were removed and inflated with pre chilled at 4°C 4% PFA through the previously inserted cannula. The lungs were left in 4% PFA overnight and then incubated with 30% sucrose (Fisher Scientific) PBS solution at 4ºC for 48 h, which was changed at 24 h.

### 2.3.5 S.c. tumour harvest

At specified time-points animals were sacrificed by lethal i.p. injection of 0.2 ml pentobartbital: 2:1 dilution in water. The perfusion of the blood was performed through the opposite cardiac route, right ventricle and left aorta, with pre-chilled (4 °C) PBS containing $4e10^{-5}$ % v/v heparin sodium (Greiner BioOne). Perfusions were performed using a perfusion pump (505L, Watson Marlow, Falmouth, UK). The carcinomas were excised and embedded in optimum cutting temperature compound (OCT-Tissue Tek, VWR International Ltd, Lutterworth, UK) and frozen with isopentane and dry ice. Consequently, the tissues were cut onto SuperFrost Plus positively coated slides (J1800AMNZ, Thermo Scientific), using a Leica CM1900 cryostat (Leica Microsystems). The samples were kept on -20 °C.

[1] Cell lines were a generous gift from Carlos Arteaga, Vanderbilt Univ., USA.

### 2.3.6 Tissue management

The tissue was snapped frozen using cryospray (Agar Scientific) and sectioned using a cryostat microtome at an optimal thickness of 10 μm. The organs were sectioned in a sequential manner as follows: three sections from different locations of the organ were placed on one positively charged slide (Fisher scientific). These were then left to air-dry at least overnight at 37 ºC and further stored at -20 ºC.

## 2.4 Injectable agents

### 2.4.1 VCAM- or rat IgG-MPIO conjugation

Synthesis of VCAM-MPIO was carried out with MyOne™ Tosylactivated MPIO, 1.08 μm diameter MPIO (65501, Invitrogen, Life Technologies Ltd, UK) and rat anti-mouse VCAM-1 antibody (1510-01, Cambridge Bioscience, Cambridge, UK). 50 μl of MPIO solution is equal to 5mg of particles, estimated $5\times10^9$ particles, and all conjugations were performed in 5 mg protocols. 50 μl of solution was transferred to 1.5 ml tube and MPIO were suspended with a neodymium magnet (12320D, DynaMag™, Spin Magnet, Invitrogen, Life Technologies Ltd, UK) for 5 minute. The supernatant was removed and the particles were washed with 0.1 M sodium borate buffer, pH 9.5, by repeating the suspension. The particles were incubated with 400 μl rat anti-mouse VCAM-1 antibody, 400 μL of 0.1 M sodium borate buffer (pH 9.5) and 400 μl 1M ammonium sulphate (pH 9.5), vortexing at 1000 rpm for 24 hours at 37 °C. The antibody solution was removed and replaced with blocking buffer and vortex at 1000 rpm overnight at 37 °C to block any unbound tosyl sites. The beads were washed and then stored on a vortexing shaker (1000 rpm) at 4 °C prior to use, suspended in STORB buffer containing sodium azide and BSA. For long term storage beads were suspended in STOR buffer, without BSA (Figure 2.1).

### 2.4.2 Cyclo[-RGDfK-]- or cyclo[-RADfK-]-MPIO conjugation

Synthesis of RGD-MPIO was carried out with M270™ Amide, 2.8 μm diameter MPIO (14307D, Invitrogen, Life Technologies Ltd, UK) and cyclo[-RGDfK-] peptide (provided from Dr Shawn Chen – NIH, CS bio, Menlo Park, CA). 166 μl of MPIO solution, as provided from the company is equal to 5mg of particles ($3.4 \times 10^8$ MPIO). The MPIO were washed repeatedly in SB buffer and then incubated with 400 μl rat anti-mouse VCAM-1 antibody (1510-01, Cambridge Bioscience, Cambridge, UK), 400 μl of SB buffer and 400 μl ASSB buffer, vortexing at 1000 rpm for 24 hours at 37 °C. The antibody solution was removed and replaced with BLOCK buffer and vortex at 1000 rpm overnight at 37 °C to block any unbound tosyl sites. The beads were washed and then stored on a rolling shaker at 4 °C prior to resuspended in STOR buffer. (Figure 2.2).

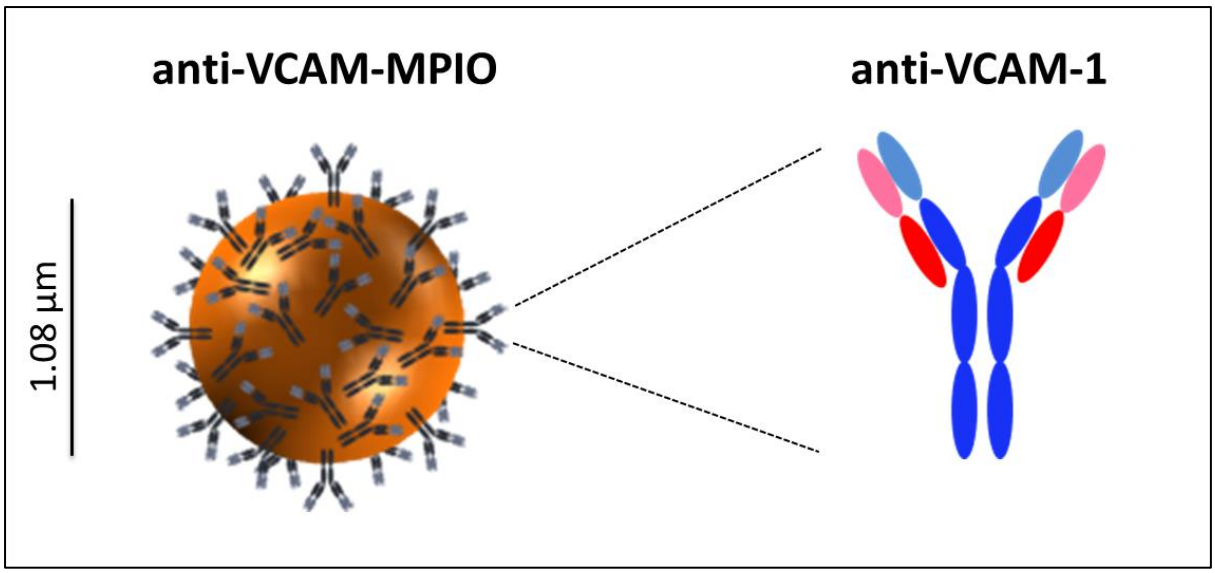



**Figure 2.1. VCAM-MPIO.** Schematic representation of the VCAM-MPIO assembly (not to scale).

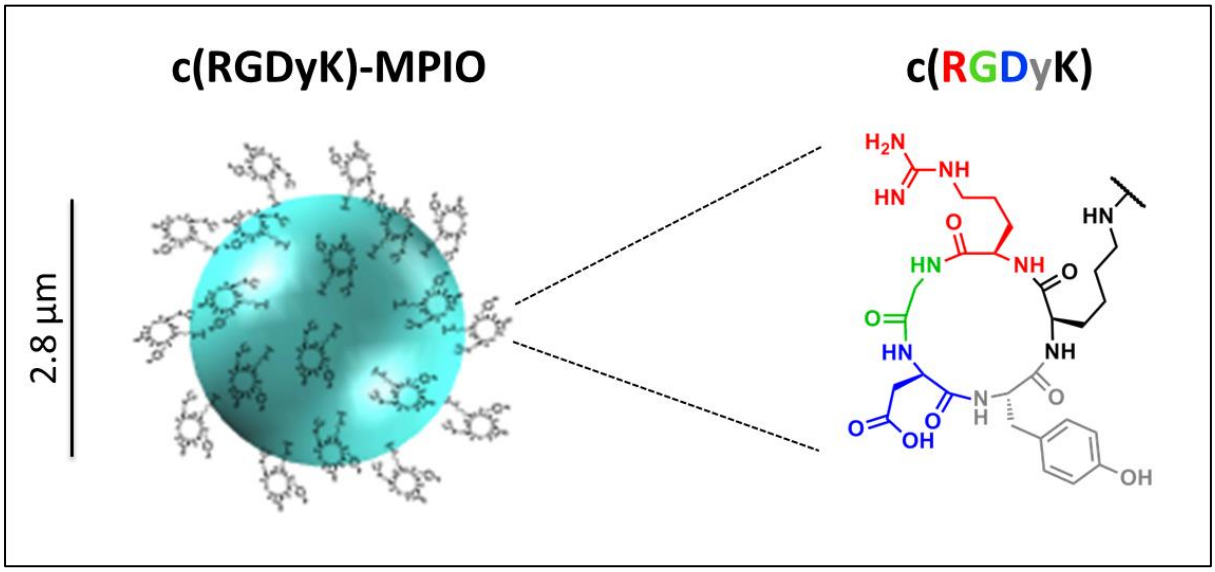



**Figure 2.2. Cyclic(RGDyK)-MPIO.** Schematic representation of cyclic(RGDyK)-MPIO assembly (not to scale).

## 2.5 Antibodies

### 2.5.1 Antibodies for immunohistochemistry

For expression of VCAM-1 on pulmonary vasculature, lung tissues were stained with DAB: primary rat anti-VCAM-1 (1/500; 1510-01, Cambridge Bioscienses, UK) and secondary horse anti-rat biotynilated (1/100; BA-4001, Vector Lab, UK). For expression of PECAM on subcutaneous tumour vasculature, tissues were stained with DAB: primary rabbit CD-31

polyclonal antibody (1/100; ab32457, Abcam UK), secondary biotonylated anti-rabbit (1/500; BA-1000, Vector Lab, UK.
In order to confirm the specificity of the secondary antibodies (staining negative control), a slide was stained using the same procedure where the primary antibody had been omitted. Instead the tissue was incubated with PBS alone.

### 2.5.2 Antibodies for immunofluorescence

S.c. tumour tissues assessed for co-localisation of $\alpha_v$ and $\beta_3$, for expression of $\alpha_v\beta_3$, with fluorescence microscopy: $\alpha_v$ using rat CD-51 primary antibody (1/100; LS-C57970), secondary biotonylated anti-rat and fluorophore Cy3, $\beta_3$ using rabbit CD-61 monoclonal primary antibody (1/50; ab75872, EP2417Y, Abcam UK) and secondary AMCA anti-rabbit IgG (H+L) (CI-1000, Vector Lab, UK). ). In order to confirm the specificity of the secondary antibodies (staining negative control), a slide was stained using the same procedure where the primary antibody had been omitted. Instead the tissue was incubated with TNB alone.

## 2.6 Imaging

### 2.6.1 Magnetic resonance imaging

A scout image was acquired to position the centre of the subqutaneous tumours or *ex vivo* samples in the centre of the magnet and to enable positioning of volumes and slices for further imaging protocols. A manual shim was completed prior to the start of imaging.

#### *2.6.1.1 In vivo HP gas lung MRI*

2.6.1.1.a Instrumentation

*In vivo* HP gas MRI was performed at the Center for In Vivo Microscopy, Duke University. The images were acquired on a 2T horizontal 30-cm horizontal bore magnet (Oxford Instruments, Oxford, England) equipped with 18 G/cm shielded gradients (Resonance Research), controlled by a console (EXCITE, version 12.0; GE Healthcare, Milwaukee, Wis). The scanner was interfaced to the dual-tuned (85.1/64.8 MHz) birdcage coil (5.5 × 3.5 cm) using a separate integrated transmit/receive switch with 31-dB gain preamplifier (Nova Medical) for the $^{1}$H or $^{3}$He frequency. For $^{129}$Xe imaging the system was interface to a dual-tuned (85.1/23.66 MHz) birdcage coil (5.5 x 3.5 cm). These frequencies were created by modifying the intrinsic 63.86 MHz frequency of the scanner to either 85.1 MHz for $^{1}$H, 64.8 MHz for $^{3}$He or 23.66 MHz for $^{129}$Xe using an up–down converter (Cummings Electronics Labs, North Andover, Mass).

2.6.1.1.b HP Gas Production and Delivery

Isotopically enriched (85% $^{129}Xe$) xenon was hyperpolarized in a 1% Xe, 10% $N_2$, 89% He mixture (Linde Electronics and Specialty Gases Inc., Stewartsville, NJ), by spin exchange optical pumping using a prototype commercial polarizer (model 9800, MITI, Durham, NC) and extracted from the buffer gases in a liquid nitrogen. Following cryogenic accumulation, HP $^{129}Xe$ (polarization ~10%) was thawed into 150 ml Tedlar bags (Jensen Inert Products, Coral Springs, FL) housed inside a Plexiglas cylinder. This cylinder was then pressurized to 3.5 psig, and HP $^{129}Xe$ was delivered to the mice using the custom ventilator, as described previously [282]. $^{3}He$ was polarized using the same polarizer, but with the cartridge removed and replaced with a $^{3}He$ specific unit. $^{3}He$ was polarized overnight at 10 atm to 30%-40% polarization, then cooled, dispensed, and delivered in the same manner as $^{129}Xe$.

2.6.1.1.c Animal preparation

Mice were prepared following procedures approved by the Duke University Institutional Animal Care and Use Committee. Prior to MRI experiments, animals were anesthetized by intraperitoneal injection of 75-mg/kg sodium pentobarbital (Nembutal, Lundbeck, Inc., Deerfield, IL) and tracheotomised with an 18-G catheter (Abbocath, Hospira, Inc., Lake Forest, IL) to provide an airtight seal for mechanical ventilation. Anesthesia was maintained with periodic injections of sodium pentobarbital (25 mg/kg) administered via an indwelling 22-G IP catheter. Animals were ventilated (75% $N_2$ and 25% $O_2$) at a rate of 100 breaths/minute on an HP-gas compatible, constant-volume mechanical ventilator [282] using a tidal volume of 0.20 ml. During HP gas MRI acquisition, HP gases replaced the $N_2$ in the breathing gas mixture, while the $O_2$ concentration was held constant. During MRI acquisitions, the ventilation rate was reduced to 75 breaths/minute (140-ms inhalation period, a 360-ms breath-hold and a 300-ms period of passive exhalation) to accommodate a longer mechanical breath-hold.

2.6.1.1.d MRI sequences

Ventilation imaging was achieved using a 3D radial sequence (views = 2501, views per breath = 4, TR = 20 ms, flip angle = 30°, matrix = 64×64×64, FOV = 2.5 cm, acquisition BW = 8 kHz), with a non-selective, 500-μs, 3-lobe sinc pulse and 8-kHz excitation bandwidth. The echo time was selected to be 0.384 ms (minimum, for maximum overall signal), 4 ms or 8 ms, to allow for increased detection of local magnetic field inhomogeneities. For $^{3}He$, the scan parameters were views = 10001, views per breath = 10, TR = 15 ms, flip angle = 20°, matrix = 128×128×128, FOV = 2.5 cm and acquisition BW = 31.25 kHz.

### *2.6.1.2 In vivo $^{1}H$ MRI*

2.6.1.2.a Instrumentation

*Ex vivo* lung MRI, *post mortem* fluorinated gas and liquid MRI, MR relaxometry and *in vivo* subcutaneous tumour MRI were performed at Radiobiology Research Institute, Oxford University. The images were acquired at a 4.7T 30 cm horizontal bore magnet (Agilent

Technologies, Santa Clara, CA, USA) using a 25 mm quadrature birdcage $^{1}H$ coil (Rapid Biomedical, Wurzburgy, Germany).

#### 2.6.1.2.b Animal tumour models

Female, C57Bl/6 mice (n = 26; Charles River, UK) were housed in ventilated cages with a 12-hour light / dark cycle and controlled temperature (20-22°C), fed normal chow and given water *ad libitum*. 7-10 week old mice were anesthetised with 2-3% isoflurane (IsoFlo) in $O_2$ and injected subcutaneously in the right upper flank with either 5 x $10^4$ B16F10 mouse melanoma cells (n = 10), or 5 x $10^4$ MC-38 mouse colon carcinoma cells (n = 16) in 100 µl sterile PBS. Tumours were allowed to grow for either 21 days to achieve tumour volumes < 400 $mm^3$ (n =20), or 28 days for tumour volumes > 400 $mm^3$ (n = 6). All experiments were approved by the UK Home Office.

#### 2.6.1.2.c Experimental protocol

For imaging, mice were anaesthetised with 2-3% isoflurane in room air and a tail vein cannulated for contrast agent administration. Anaesthesia was maintained with 1-2% isoflurane in room air thereafter. Core temperature was monitored and maintained at 36 °C with a homeothermic system (Harvard Instruments, Edenbridge, Kent, UK). Respiratory gating was achieved using a pressure balloon, placed in contact with the chest, that was interfaced to a signal processing unit (MP150 unit, Biopac Inc, California, USA) and trigger control unit (DTU200, Biopac Inc).
For each animal, a $T_2$*-weighted 3D dataset was acquired prior to contrast agent administration and again 30 min after injection. After the initial acquisition, the coil was removed from the magnetic field with the cradle at fixed position, while anesthesia and monitoring was maintained. The contrast agent was administered intravenously while the mice remained within the coil to enable co-registration of pre- and post-contrast images. Mice were injected with 100 µl of either c(RGDyK)-MPIO or the control c(RADyK)-MPIO at a concentration of 4 mg Fe/kg body weight. Dynamic contrast enhanced (DCE) MRI was performed at the end of each imaging protocol with 30 µl gadolinium-DTPA (Omniscan; 0.5 mmol/ml) injected intravenously during the scan.

#### 2.6.1.2.d MRI sequences

For detection of MPIO, a respiratory-gated, fat-suppressed, 3D multi-gradient echo, $T_2$*-weighted acquisition was performed with TE = 3.33, 7.82, 12.31 and 16.8 ms; TR = 40ms; nominal flip angle = 16°; field of view (FOV) 54 x 27 x 27 mm giving an isotropic resolution of 150 $\mu$m. For DCE MRI, a respiratory-gated 3D gradient echo, $T_1$-weighted acquisition was performed with TE = 0.55 ms, TR = 1.1 ms, nominal flip angle = 5°, FOV = 54 x 27 x 27 giving an isotropic spatial resolution of *ca.* 412 $\mu$m in a scan time of

*ca.* 10 s/frame. 100 frames were acquired with contrast agent infused (Omniscan, 30 $\mu$L) over the duration of frame 11/100. Respiratory gating to eliminate residual motion artefacts, whilst maintaining constant $T_1$-weighting throughout the scans, was achieved by only acquiring data during the respiratory plateau period [283]. $B_1$ inhomogeneity was corrected for using a respiratory-gated implementation of the Actual Flip angle Imaging technique [284] performed with TE = 0.59, TR = 20, 100 ms, nominal flip angle = 60°, covering the same FOV as the DCE scan, but at half the resolution in each of the phase encode directions, to give a spatial resolution of *ca*. 400 x 800 x 800 μm in a scan time of approximately 4 min. $T_1$ was estimated using the same scan parameters as for the DCE acquisition, but with an array of flip angles (1-6°) in a scan time of approximately 1 min. Both $B_1$ correction and $T_1$ mapping were performed prior to the DCE scan to avoid confounding arising from gadolinium washout.

#### 2.6.1.2.e MRI dataset handling

The MRI datasets were extracted as NIfTI files with file extension *.nii*. Each file contains different parameters, e.g. dual file (*.hdr* & *.img*) or single file (*.nii*) storage. One of the parameters is the image file with file extension .img, which affine coordinate definitions relating to voxel index (*i, j, k*) to spatial location (*x, y, z*). This file also stores vector-valued dataset over a fourth dimensional domain, where in our data set the fourth dimension is the time of acquisition (i.e. 4 echo times: $t_{echo}$ = 3.33, 7.82, 12.31, 16.8ms). Each voxel stores a grey intensity level which correlates with the magnetization $M(t_{echo})$ per pixel at the time of the echo. For $T_2$ measurements, as the echo is getting longer the echo the single to noise decreases. The 4-D data set were visualised with imaging software ImageJ (Image Processing and Analysis in Java). The grey scale images appear as 2-D images, which can be manually interchanged in the third dimension (stack files). They can also interchange through the $4^{th}$ dimension (hyperstack files).

#### 2.6.1.2.f MRI dataset segmentation

The images were segmented with ITK-Snap v2.4.0 (http://www.itksnap.org) [285]. Each mouse is associated with a pair of data sets, pre- and post-contrast agent treatment. Although the software provides semi-automated segmentation function the images have been segmented manually. This is due to low resolution and the nature of the tumours (i.e. edema, necrosis, fat), which makes the borders of balk tumour volume with the surrounding tissue not well defined. Consequently, for the same reason, the manually segmented tumours of different pairs might not have the same tumour differentiation criteria. However, important aim of the segmentation was to keep the tumour differentiation criteria for each pair the same. In order to improve the definition of the images and enhance segmentation accuracy, the four echoes have been averaged using MATLAB v7.11.0.584 (2010b) (Mathworks, Cambridge, UK). Except tumour volumes, muscle volumes were segmented located near the tumour and

also bladder volumes. The segmented files were saved as NifTI files of the same size as the original image.

### 2.6.2 *In vivo* whole body dynamic PET and CT

PET and CT imaging was performed using the Inveon PET/CT system (Siemens Preclinical Solutions). Mice with pulmonary metastases (section 2.3.2) were used through out. Mice were anesthetized with 3% isofluorane mixed with room air, and subsequently anaesthesia was maintained with 1-2% isofluorane until termination. Metastasis-bearing mice were injected with either [$^{89}$Zr]-DFO-VCAM-MPIO or [$^{89}$Zr]-DFO-IgG-MPIO (1.6 mg/kg iron concentration and 5 MBq activity per injection; n=4 per group). As further controls, naïve mice were injected with either [$^{89}$Zr]-DFO-VCAM-MPIO or [$^{89}$Zr]-DFO-VCAM (n=4 per group).

Throughout each imaging session, mice were maintained at 37 °C and respiration rate was monitored (60-100 respirations/minute). Mice were placed supine, head first, in the imaging cradle and a cannula was inserted into the lateral tail vein. CT based attenuation correction (continuous rotation, 220 degrees, 120 steps, 65 kV, 500 μA, 200ms exposure time, 3072 x 2048 matrix, binning of 4, 3 bed positions with 28.45% overlap) was performed before each PET emission scan. The latter CT acquisition was also used for anatomical referencing. Both histogramming and image reconstruction was conducted with the Inveon Acquisition Workplace software (IAW, version 1.5). For all compounds, 1-hour whole-body dynamic acquisitions were acquired. Following the attenuation CT-scan, the PET emission data acquisition (3600 s, Zr-89, 3.432 ns timing window, 511 keV photpeak energy level, 350 – 650 keV energy level discrimination) was initiated and the radiotracer injected via the tail vein cannula. Data were histogrammed in 24 time frames (15x 20s, 7x 300s, 2x 600s) with a span of 3 and a ring difference of 79. Global deadtime correction and Fourier rebinning was applied to all data sets.

The dynamic histograms were reconstructed using a 2-dimensional filtered backprojection (2D-FBP) algorithm, a Ramp projection filter, a 0.5/mm Nyquist projection cutoff value, no zoom and a matrix size of 128x128x159 (sagittal x coronal x transversal). Image analysis was performed using the Inveon Research Workplace software (IRW, version 4.2).

# Chapter 3 – *Ex vivo* specific targeting of pulmonary VCAM-1 activated endothelium

## 3.1 Introduction

It has been suggested that the mechanisms of tumour cell extravasation are similar to the multi-step process of leukocyte extravasation, which has been characterised very well at a molecular level. However, the molecules and processes involved in leukocyte extravasation and tumour cell extravasation may not be exactly the same. For example, although leukocyte extravasation is a normal process and causes only temporary changes in endothelial integrity, tumour cell extravasation can cause irreversible damage to the endothelial structure. Further, the site of extravasation may differ between the two; arteriole, capillary or venule [286]. At the same time, it has been shown that tumour cells can form clusters with leukocytes and, consequently, use the leukocyte extravasation process to cross the endothelial layer with them. Thus, the processes and molecules involved in tumour cell extravasation are undoubtedly complicated, and likely vary according to primary tumour type, metastatic site and immunological factors.

Interactions of the very late antigen 4 (VLA-4 or integrin $\alpha_4\beta_1$) with VCAM-1 are important for leukocyte activation and arrest on the activated endothelium during an inflammatory response [154]. VLA-4/VCAM-1 interactions have also been shown to play an important functional role in the transmigration of both murine [287] and human [288] melanoma cells. Many tumor cells express VCAM-1 and its ligand, and increased VCAM-1 expression on the cerebral vasculature has been reported in murine models of brain metastasis using breast cancer cell lines [195, 289]. Increased expression of VCAM-1 has also been reported in pulmonary metastasis experimental models [290]. In both studies, VCAM-1 was upregulated early in metastatic development and inhibition of VCAM-1/VLA-4 interactions significantly reduced metastatic colony formation, indicating an important role in metastasis seeding. Induction of VCAM-1 in the lungs, as a consequence of tumour cell attachment, has been shown to be dependent on tumour clot formation [290]. Importantly, VCAM-1 is not highly expressed constitutively on either brain or lung endothelium. Thus, on the basis of the early upregulation of VCAM-1 in the metastatic seeding process, VCAM-1 has been considered as target for detection of micrometastasis in the brain using a molecularly targeted MRI agent, VCAM-MPIO [195]. By targeting the metastasis induced VCAM-1 activated endothelium in the brain, bound VCAM-MPIO were able to dephase the signal from the brain on $T_2$*-weighted MRI, providing a sensitive and specific biomarker of micrometastatic colonies.

Considering the successful detection of early metastasis in the brain by targeting VCAM-1 and the previous work showing VCAM-1 expression in the pulmonary vasculature early in

metastasis formation, it was hypothesised that if the expression of VCAM-1 is sufficient in the lungs, VCAM-MPIO should also bind to metastasis-activated pulmonary endothelium. Although proton MRI of lungs is not possible owing to the low proton density of the lung tissue, it was further hypothesised that alternative imaging approaches, including bright lung MRI and PET imaging would provide a viable *in vivo* detection method (as discussed in Chapter 4).
This chapter will focus on the first hypothesis, using *ex vivo* assessment of a systemic inflammation mouse model and a pulmonary metastatic mouse model, to determine whether VCAM-MPIO binding is (a) specific to inflamed vessels in the lung and (b) sufficient for potential *in vivo* detection.

## 3.2 Methods

### 3.2.1 General inflammation and initial pulmonary metastasis mouse models

BALB/c mice were injected intraperitoneally with LPS (0.5 mg/ml). At 2 h post i.p., the signs of systemic inflammation are evident (hunched posture, piloerection) and at 4 h post i.p. marked VCAM-1 expression is evident on the microvasculature of the lungs upregulates strong VCAM-1 expression (Couch Y, DPhil Thesis, Oxford University).

### 3.2.2 *Ex vivo* binding of VCAM-MPIO on LPS inflamed endothelium

LPS injected mice were injected i.v. with either VCAM- or IgG-MPIO, at 4 h post i.p., and terminated 1 h post i.v. of the contrast agent (Figure 3.1). Mice were perfused intracardially with heparinised pre-chilled PBS and the lungs inflated with pre-chilled 4% PFA. Subsequently, lungs were excised and post-fixed in 4% PFA for 24 h at 4 °C, followed by 48 h incubation in 30% sucrose at 4 °C. Lungs were snap-frozen and cryo-sectioned at 14 µm thickness and stored at -20 °C until immunohistochemical analysis. Sections were stained for VCAM-1 with DAB and nucleus definition with hematoxylin. Naïve mice were injected with the same dose of VCAM- or IgG-MPIO, as control samples, and lungs were excised and treated as previously described.
In order to quantify the binding of VCAM-MPIO against IgG-MPIO, 9 representative lung sections, stained for VCAM-1 were chosen from each animal and the number of particles associated with 81 positive stained vessels were counted manually under bright field microscopy (3 slides per animal x 3 sections of lung tissue each x 3 vessels per lung section x 3 animals per group = 81). Clumps of particles were counted as a single count when they were clumped.

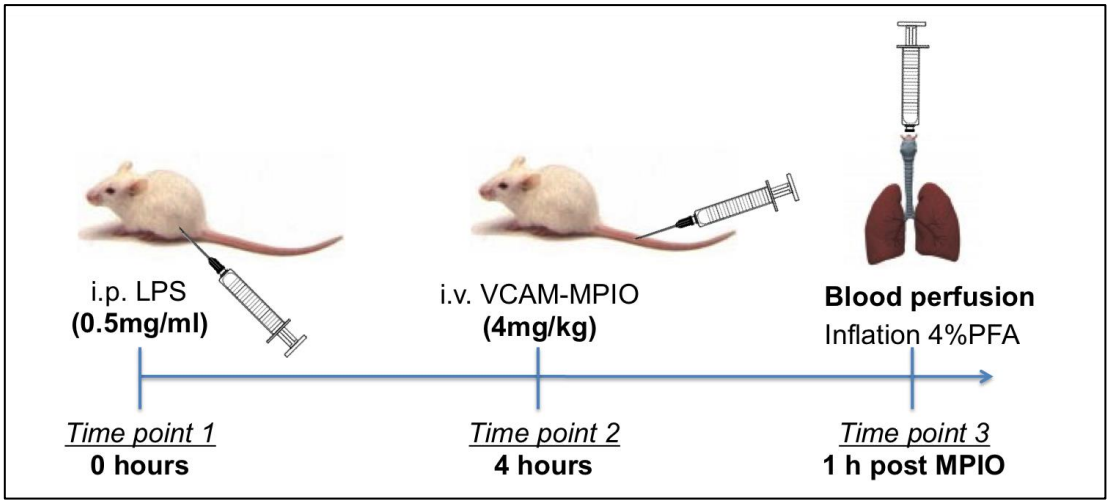



**Figure 3.1. General inflammation mouse-model.** Schematic representation of the general inflammation mouse model experimental protocol.

### 3.2.3 Optimisation of MPIO (iron) concentration

Naive mice were injected with a range of iron concentrations (0.05, 0.07, 0.1, 0.2, 0.4, 1.5 and 2 mg/kg per injection) and were terminated at 1 h post-VCAM-MPIO. The lungs were treated as previously described (section 3.2.2) and following sucrose incubation, were embedded in PBS + 1% agarose in a 25 ml falcon tube. Subsequently, the samples were MRI scanned overnight at 4.7T using a 25 mm coil and a GE3D $T_2$* weighted sequence. The optimum dose of MPIO was identified, by determining the concentration of particles that minimized non-specific retention in healthy lung tissue, as determined from the absence of susceptibility effects on the $T_2$* weighted images.

### 3.2.4 Optimisation of pulmonary metastatic mouse model

The pulmonary metastasis model previously used for VCAM-1 work involved BALB/c mice injected intravenously with $5x10^5$ 4T1-GFP cells and terminated at 7 days post injection (Figure 3.2). Initial studies using this model raised a number of issues; (i) large number of micrometastatic colonies per lung and (ii) large cross sectional area of metastatic colonies, shifting away from the scope of early detection of metastasis. Therefore, in order to optimize the size and number of metastases per lung, BALB/c mice were injected i.v. (tail vein) with either $5x10^3$ or $5x10^4$ 4T1-GFP cells and terminated at either 7 or 10 days post-injection (n=3/group). The lungs were treated as previously described (Section 3.2.2) and assessed histologically for the number of lung metastases per animal and expression of VCAM-MPIO. This optimum pulmonary metastasis model was used for all further *ex vivo* or *in vivo* experiments (Figure 3.3).

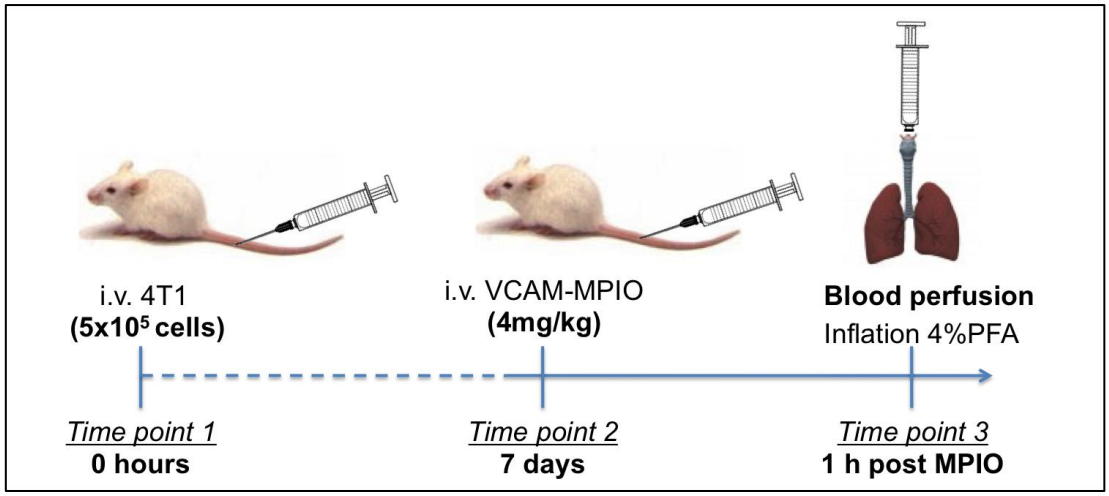



**Figure 3.2. Initial metastatic mouse-model.** Schematic representation of the metastatic model experimental protocol, as previously used from pulmonary VCAM-1 work (Ferjancic *et al*, 2010).

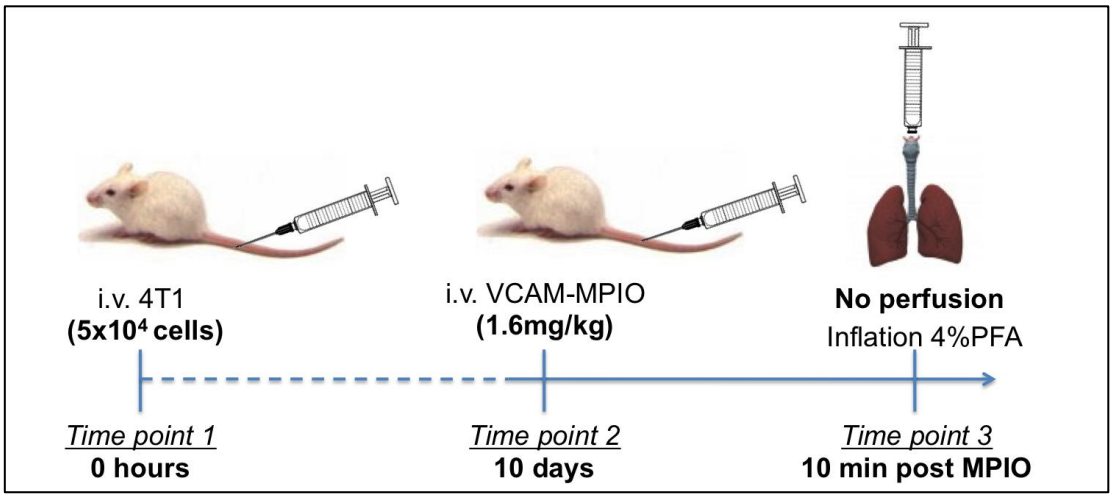



**Figure 3.3. Optimised metastatic mouse-model.** Schematic representation of the optimised metastatic mouse model experimental protocol.

### 3.2.5 Biological clearance of MPIO

Naïve mice were anesthetised with 2-3% isoflurane in $O_2$ and injected i.v. with 4mg/kg of 1.08 μm diameter BSA-MPIO (negative control; MPIO with blocked active tosyl groups). At different time points after administration of MPIO, mice underwent a thoracotomy followed by cutting of the inferior vena cava and aorta below the lungs to allow the blood to pool inside the thoracic cavity. Blood was collected with a syringe containing 5 μl of heparin sodium (25,000 I.U./ml, Wockhardt, UK). For early time points, surgery was performed prior to injection of particles, leaving the diaphragm intact. Time points studied were: 10, 20, 30, 40, 50, 60, 120, 180 and 240 s after MPIO injection (n = 1 per time point). Blood samples were also collected from a naïve mouse. Blood samples were oxygenated by incubation with $O_2$ gas in a sealed tube on a rolling platform for 5 min. Samples were set into agar by mixing

blood and 1% agarose solution in PBS, both at 40.5 °C, in a 1:1 ratio, to a final volume of 300 µl, in a 500 µl microcentrifuge tube. Set samples were stored at 4 °C. $T_2$ relaxivity measurements were made at 4.7 T, within 24 h, using an array of 100 µs hard 90° and 180° pulses, TR = 1000 ms, 2000 complex points and 8 averages. Blood half-life was determined from the fitted one phase decay curves, constrained to a plateau at the average naive blood sample value (baseline).

### 3.2.6 *Ex vivo* binding of VCAM-MPIO on pulmonary micrometastases associated inflamed endothelium

Metastases baring animals or naïve animals were injected with 1.6 mg/kg of either VCAM-MPIO or IgG-MPIO and terminated at 10 min, 1 h, and 3 h post injection of administration of the agents (n=5 per group). Lung tissues were treated as previously described (section 3.2.2). Representative sections were chosen across the lung sample (15 sections) and fixed size fields of view (45 per lung sample), centred on a single metastatic colony, were chosen. The metastases and vessels were manually segmented and the number of adherent MPIO was manually counted using bright field microscopy. From these data the number of MPIO per metastatic area and MPIO per inflamed vessel was calculated. The level of non-specific retention was determined from equivalent fields of view in naïve animals injected with VCAM-MPIO or IgG-MPIO. In order to compare the non-specific retention in naïve animals with the non-specific retention in metastasis-bearing animals, a further 45 fields of view per metastasis-bearing lung, chosen from a metastasis-free part of the lung section, were also assessed for MPIO binding.

## 3.3 Results

### 3.3.1 *Ex vivo* binding of VCAM-MPIO on LPS inflamed endothelium

Positive binding of VCAM-MPIO to inflamed pulmonary vessels was initially confirmed *ex vivo*. As proof of principal, a mouse model of general inflammation (LPS model) was used and inflamed pulmonary vessels assessed immunohistochemically for binding of VCAM-MPIO compared to IgG-MPIO on the activated endothelium (n=3 per group; Figure 3.4). In LPS treated mice, VCAM-MPIO administration resulted in strong binding of MPIO to activated endothelium (Figure 3.4 A), whilst little or no retention was observed following IgG-MPIO administration (Figure 3.4 B). Naïve mice injected with either VCAM-MPIO or IgG-MPIO showed no retention on the endothelium (Figure 3.4 C-D). Administration of VCAM-MPIO showed significantly greater retention on inflamed endothelium compared to IgG-MPIO (Figure 3.4 E; $P < 0.0001$). Since the particles at this dose showed significant clumping, quantitative assessment of the particles was performed counting clumps as a single event and, thus, the absolute number of particles measured does not reflect the real number of

bound particles. If the particles were assessed as individual particles, the number of VCAM-MPIO per inflamed vessel would be much greater.

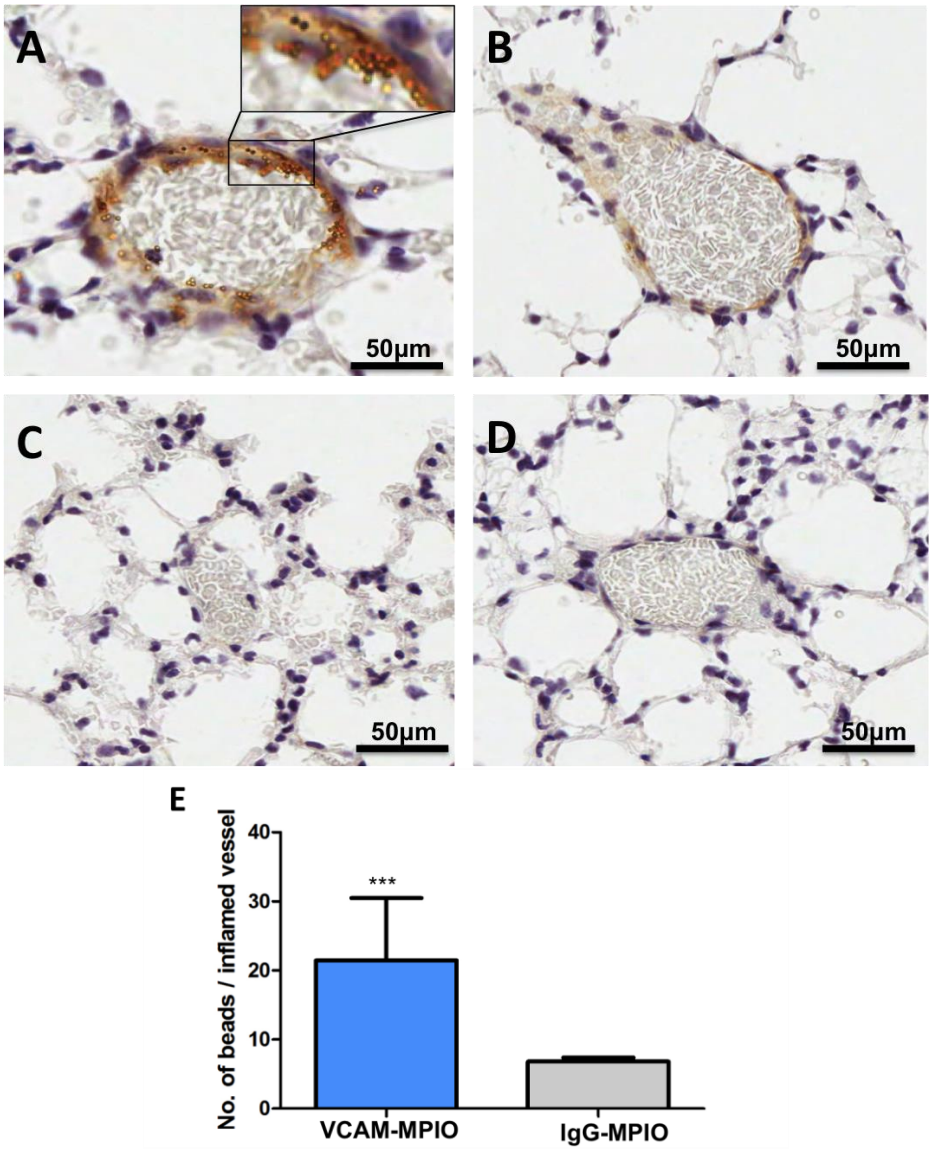



**Figure 3.4. VCAM-MPIO binding on activated endothelium.** (A-D) Bright field micrographs of lung tissue acquired from mice stained immunohistochemically for CD31 expression (brown) and nuclei (blue). (A-B) Lung tissue from LPS treated mice, showing VCAM-1 activated vessels, injected with VCAM-MPIO (A) or IgG-MPIO (B). A large number of VCAM-MPIO were evident on activated endothelium (enlarged picture; A), whilst no retention was seen for IgG-MPIO (B). (C-D) Lung tissue from naïve mice injected with VCAM-MPIO (C) or IgG-MPIO (D). No retention of MPIO was seen in either case. (E) Graphs showing quantitation of VCAM-MPIO binding per VCAM-1-positive vessel compared to IgG-MPIO in lungs tissue acquired from LPS treated mice (81 vessels per animal, n=3; $P<0.0001$).

### 3.3.2 Initial studies of *ex vivo* binding of VCAM-MPIO in metastasis-bearing lungs

Following demonstration of the specific binding of VCAM-MPIO in inflamed lungs, a metastatic model previously developed in the group [290] was used. In this model, retention of the injected tumour cells in the pulmonary capillary bed induces metastatic colonies within 7 days, as previously shown [290]. Mice were injected at this time point with VCAM-MPIO, terminated 1 h post-injection and lung sections stained immunohistochemically for VCAM-1 expression (Figure 3.5). From the IHC data, it was observed that MPIO were found on vessels in the periphery, but not the core, of the metastatic colonies (Figure 3.5 red arrows). Inflamed pulmonary arterioles close to the metastases were also found to contain a significant number of MPIO, but these were all phagocytosed by immune cells (neutrophils and/or macrophages; Figure 3.5, green arrows). This observation raised concerns as to non-specific binding or retention since these MPIO-laden macrophages have essentially becoming multi-MPIO mobile targets. These findings indicated a need to optimise the time point of binding assessment before cells can start engulfing MPIO (see Section 3.3.5). A further consideration that these initial studies raised was the possibility that with transcardial perfusion with PBS the MPIO experience strong hydraulic forces, leading to enhanced clump formation and dislocation of MPIO-laden neutrophils and/or macrophages either from another organ to the lungs or from another part of the lung. Both of these eventualities would result in misleading histological representation. As a result of these concerns, in all following studies animals were not transcardially perfused with PBS.

Consistent observation of single MPIO or MPIO aggregates within the pulmonary microvasculature, that were not associated with VCAM-1 expression, in both metastasis-bearing and naïve mice (Figure 3.6 A-D) raised a further concern of non-specific retention and, consequently, increased background signal for future *in vivo* imaging. It was hypothesized that a reduction in injected iron concentration would reduce or eliminate this effect (see Section 3.3.3). Finally, the large number of metastatic colonies found in this model (5-15 per lung section; Figure 3.7 A) and their large cross sectional area (249.87 ± 88.84 μm diameter; Figure 3.7 B), also suggested that the model should be optimized to produce fewer and smaller metastatic colonies thus enable discrete and accurate quantitation of individual colonies as well as healthy tissue (see Section 3.3.4).

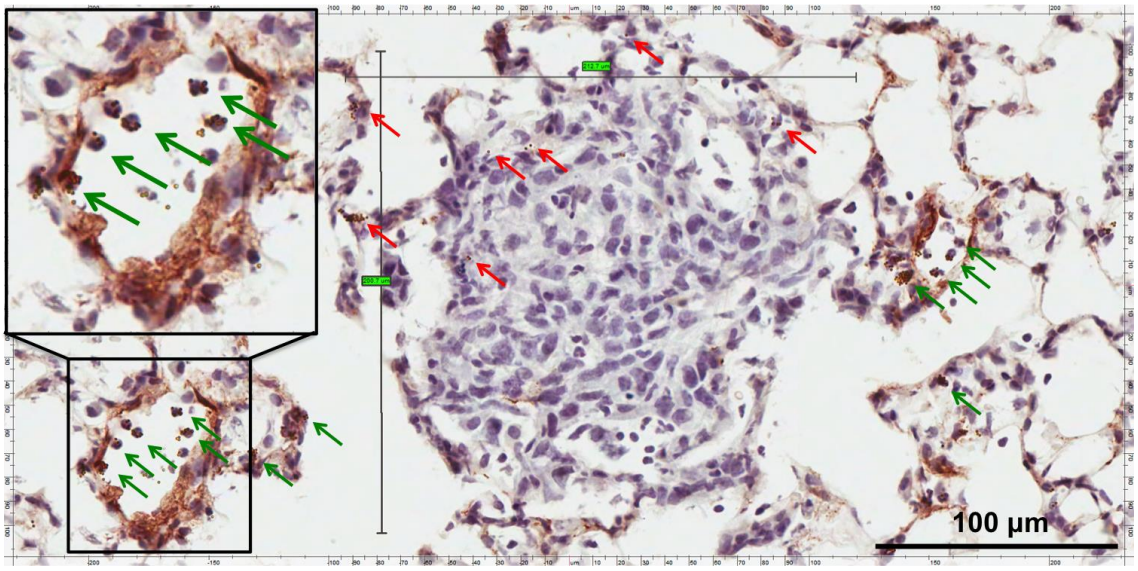



**Figure 3.5. VCAM-MPIO binding on initial metastatic model.** Lung tissue acquired from original metastatic mouse model ($5x10^5$ cells; day 7) 1 h post-injection of VCAM-MPIO, stained immunohistochemically for VCAM-1 (brown) and nuclei (blue). Figure shows a micrometastasis (200 µm cross section diameter) in which VCAM-MPIO are visible at the periphery of the tumour colony (red arrows), co-localising with endothelial VCAM-1 expression, which reflects the inflamed microvasculature. VCAM-MPIO are also seen in the VCAM-1 expressing arterioles nearby, where VCAM-MPIO appears to be taken up by phagocytic cells (neutrophils and macrophages; enlarged picture, green arrows).

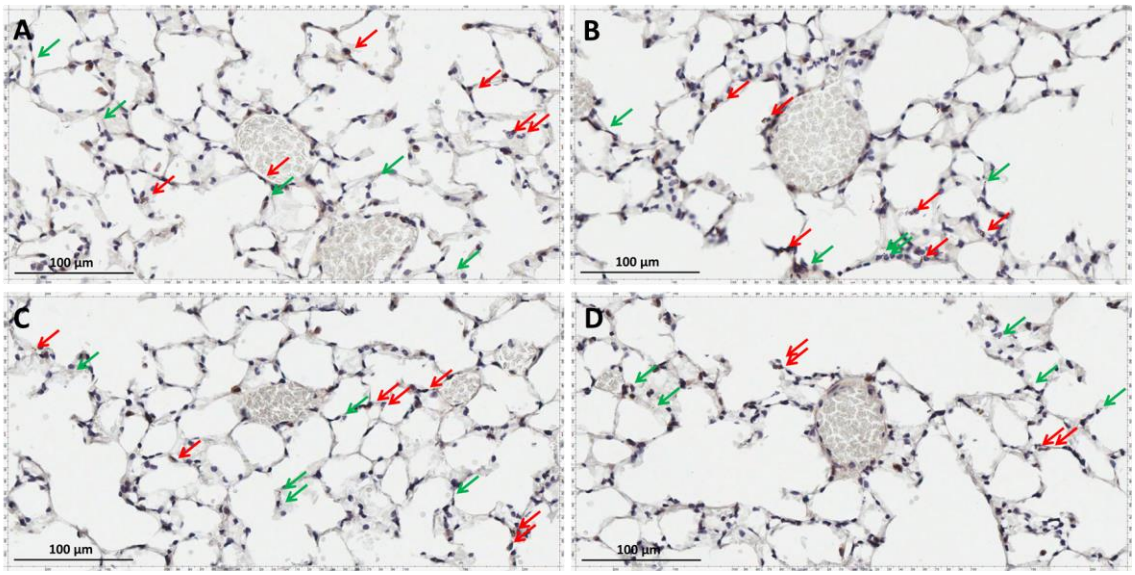



**Figure 3.6. Non-specific retention at high iron concentration.** Bright field micrographs from lungs tissue acquired from metastasis-bearing mice as previously used from pulmonary VCAM-1 work (Ferjancic *et al*, 2010) (A,B) or naïve mice (C,D), injected with VCAM-MPIO (A,C) or IgG-MPIO (B,D) at 4 mg/kg of iron concentration as previously used from brain VCAM-1 work (Serres *et al*, 2012). (A,B) Representative fields of view chosen away from metastatic colonies. Consistent non-specific retention of single MPIO (green arrows) or MPIO aggregates (red arrows) was seen at the specified iron concentration.

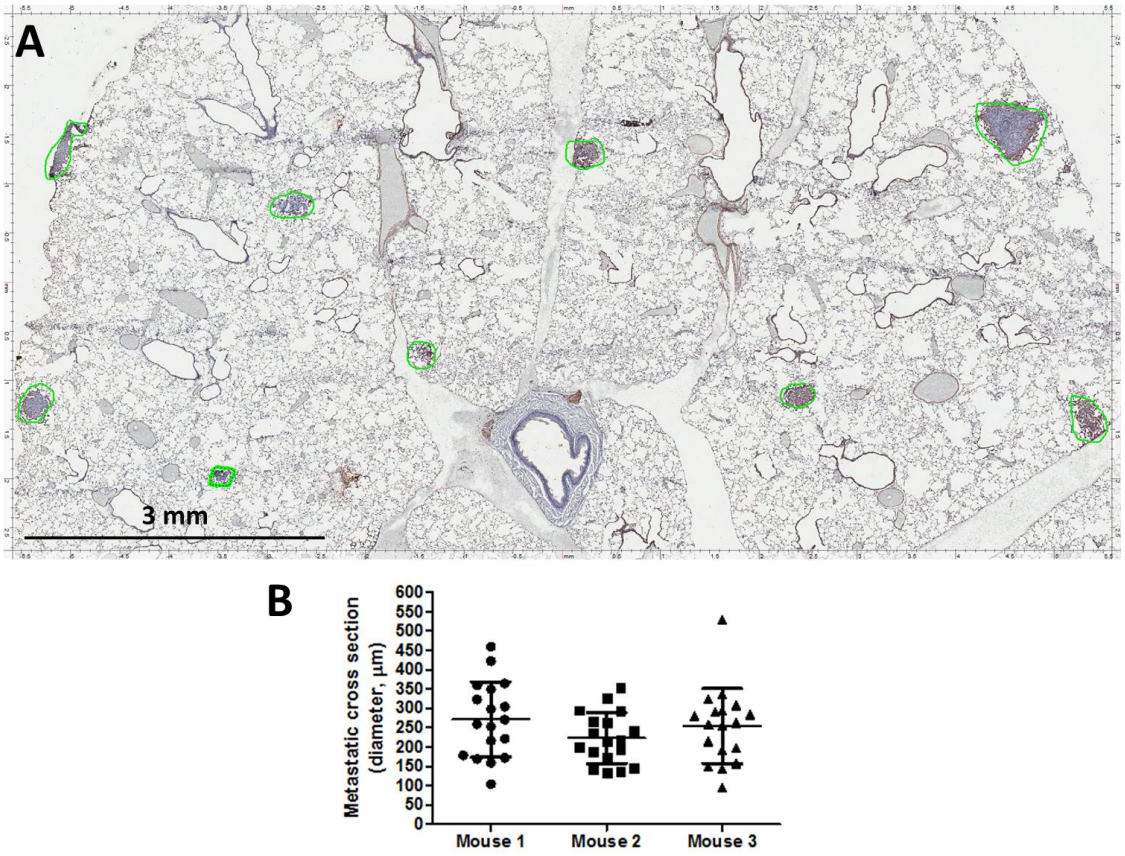



**Figure 3.7. Representative number and size of metastases using initial mouse model.** (A) Bright field micrograph from lungs tissue acquired from metastasis-bearing mice as previously used from pulmonary VCAM-1 work (Ferjancic *et al*, 2010). Representative lung tissue section showing large number of metastatic colonies (green circumferences) per lung section. (B) Vertical scatter plots showing metastatic cross sectional diameter from pulmonary micrometastases assessed from mice intravenously injected with $5x10^5$ 4T1-GFP cells on day 7 (mean ± SD, 249.87 ± 88.84 µm; n=18 per mouse).

### 3.3.3 Optimization of injected MPIO (iron) dose

The optimum injected concentration of particles per animal was investigated by ex vivo MRI assessment of $T_2$* relaxation of 4% PFA-inflated lungs from naïve mice injected intravenously with a range of MPIO concentrations (4.0, 3.0, 2.0, 1.5, 1.0, 0.5 and 0 mg iron per kg body mass; Figure 3.8 A-G respectively). The degree of hypointensity in the lungs decreased rapidly as a function of dose reduction, from 4 to 1.5 mg/kg (Figure 3.8 A-D). At a dose of 1.5 mg/kg the number of detectable hypointensities was minimized; Lower doses (Figure 3.8 E-F) were comparable with control lungs from non-injected mice (Figure 3.8 G). Subsequently, VCAM-MPIO and IgG-MPIO at the dose of 1.5 mg/kg were injected in LPS treated (positive control) and naïve mice (n=1/group) and lungs underwent $T_2$* weighted assessment. Data from LPS treated mouse injected with VCAM-MPIO (Figure 3.8 H) confirmed that the dose is adequate for retention at inflamed pulmonary vasculature, while

the controls, naïve injected with VCAM-MPIO (Figure 3.8 I) or IgG-MPIO (Figure 3.8 K) confirmed minimal background. LPS treated mice injected with IgG-MPIO (Figure 3.8 J) showed lower number/volume of hypointensities compare to LPS treated mice injected with VCAM-MPIO. However, when more LPS treated mice were repeated, it was found that inflamed lungs injected with VCAM-MPIO did not always show a greater degree of hypointensities than IgG-MPIO injected mice. It is possible that the systemic inflammation can affect inflation of the lungs and data from LPS treated mice from the same groups were consistently different. Consequently, the data were not quantified.

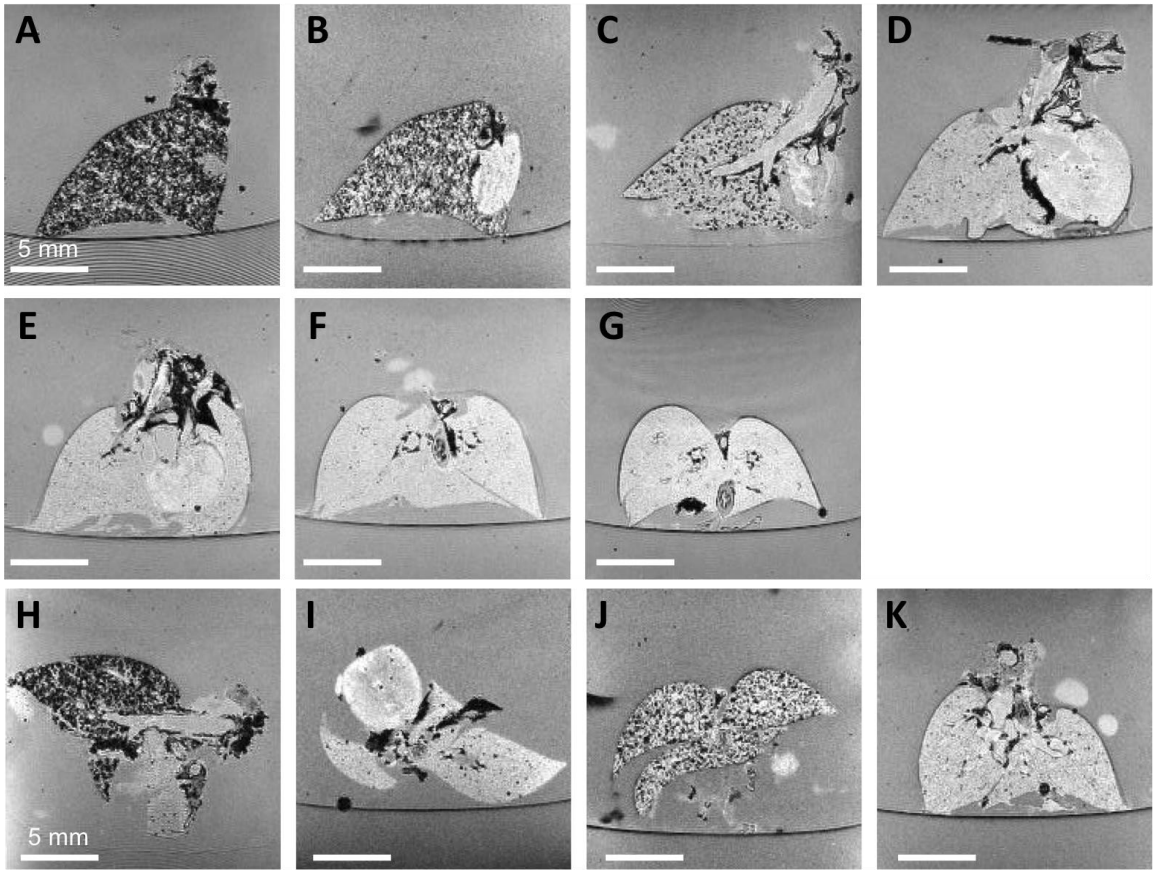



**Figure 3.8. Optimisation of injectable iron concentration.** (A-K) $T_2$*-weighted images of 4% PFA-inflated lungs, embedded in PBS+1% agarose. (A-F) Lungs acquired from naïve mice injected with various concentrations of VCAM-MPIO (4.0, 3.0, 2.0, 1.5, 1.0, 0.5 mg iron per kg body mass; respectively) or no injection (G). Hypointensities, owing to negative susceptibility effect of MPIO, from non-specific retention, are seen to reduce with iron concentration dilution. (D-F) Iron concentrations with no visible hypointensities, comparable with lungs not containing MPIO (G). (H,J) Lungs acquired from LPS treated mice and injected with optimum iron dose (1.5 mg/kg) of VCAM-MPIO (H) or IgG-MPIO (J). (I,K) Naïve animal injected with of VCAM-MPIO (I) or IgG-MPIO (K). A greater number/volume of hypointensities was seen in the LPS treated mouse injected with VCAM-MPIO (H) than any of the controls (I-K).

### 3.3.4 Optimisation of the pulmonary metastatic mouse model

Development of the original model to obtain the optimal number and size of metastases in the lungs was assessed immunohistochemically in mice injected i.v. with either $5x10^3$ or $5x10^4$ and terminated at two different time points, 7 or 10 days post injection (n=3 per group). Injection with $5x10^3$ cells did not yield detectable metastases at either day 7 or 10. In contrast, animals injected with $5x10^4$ showed a small number of pulmonary metastases per lung section at both time points. At day 10 the number of pulmonary metastases per lung section was between 0 and 5, and these metastases had an average cross-sectional diameter of 130.92 ± 49.96 µm (Figure 3.9 A-B). Staining of lung sections, from mice injected with $5x10^4$ cells at 10 days, for VCAM-1 expression confirmed the presence of inflamed pulmonary vasculature at this stage of the disease (Figure 3.9 A, enlarged area). Lungs acquired at 10 days from animals injected with $5x10^4$ cells were identified as ideal for further experiments, since the lungs were found to have sparse metastases (0-5 micrometastases per section) and VCAM-1 expression was confirmed on microvasculature associated with metastases. Consequently, this model was used for all future experiments.

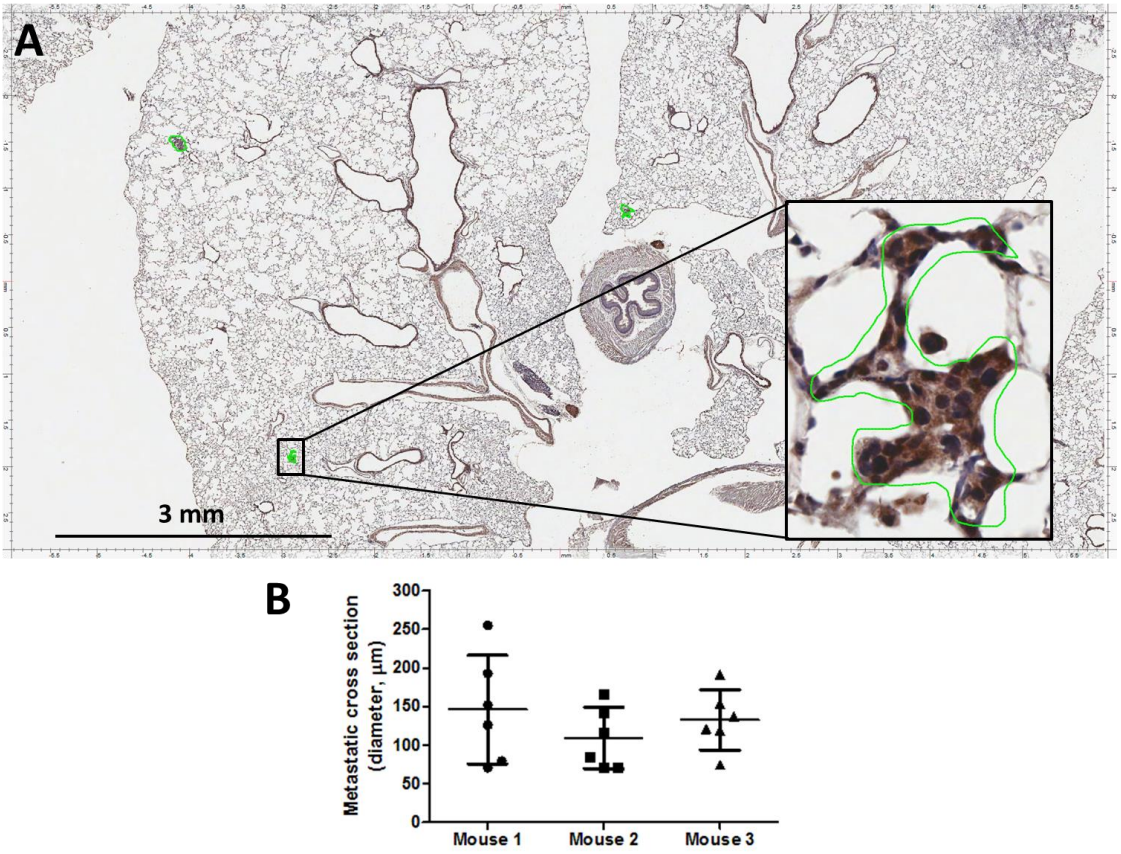



**Figure 3.9. Representative number and size of metastases using optimised mouse model.** (A) Bright field micrograph from lungs tissue acquired from optimised metastatic mouse model. Representative lung tissue section showing small number of metastatic colonies (green circumferences) per lung section. (B) Vertical scatter plots showing metastatic cross sectional diameter from pulmonary micrometastases assessed from mice intravenously injected with $5x10^4$ 4T1-GFP cells on day 10 (mean ± SD, 130.92 ± 49.96 µm; n=6 per mouse).

### 3.3.5 Identification of optimal time point post-VCAM-MPIO administration for imaging

In order to minimize the phagocytosis observed at 1 h post-intravenous injection of VCAM-MPIO (Figure 3.10), earlier time points after injection were investigated. Since a major factor for retention of MPIO would be the half-life of the circulating MPIO the biological clearance from the circulation was investigated. To this end, blood samples were collected from naïve mice injected with BSA-blocked MPIO at a dose of 4mg/kg iron dose[2]. The half-life of the MPIO clearance from blood was determined from $T_2$ relaxivity measurements of blood samples (see section 3.2.5) acquired at different time points (10, 20, 30, 40, 50, 60, 120, 180 and 240 s) post BSA-MPIO administration. $T_2$ relaxation rates were plotted as a function of time (Figure 3.10) and the half-life of MPIO in the blood was determined from the decay curve. The MPIO concentration in the blood decreased exponentially with time and the half-life of MPIO in the circulation was estimated to be 39.86 s (K = 0.017 $s^{-1}$, Y0 = 47.80 Hz; Figure 3.10).

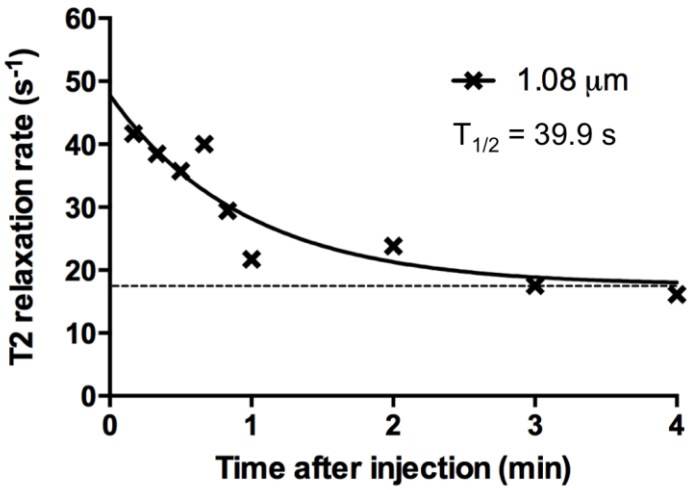



**Figure 3.10. Biological clearance half-life for 1.08 μm MPIO**. Graphs showing the decay curve of the biological clearance of 1.08 μm diameter MPIO from circulation, at a constant dose of 4mg of iron per kg of body weight over time after injection. Graph shows $T_2$ relaxivity values of blood samples at different time points after administration of 1.08 μm MPIO. The clearance half-life was calculated to be 39.86 s (K = 0.017 $s^{-1}$, Y0 = 47.80 Hz). Curve is fitted as a single phase exponential decay constrained to a plateau at the average naïve blood sample values (baseline; dashed lines).

[2] This dose of iron was much higher than the optimised dose determined from section 3.3.3 but was used because it did not pose problems to the conclusion of the experiment and would provide essential information for the general work performed with MPIO as a group (Experimental Neuroimaging Group).

### 3.3.6 *Ex vivo* quantitation of VCAM-MPIO retention in metastatic mouse model

In this study the optimal dose of VCAM-MPIO (1.5 mg/kg) was injected i.v. into mice with pulmonary metastases. Figure 3.11 A shows lung tissue stained with hematoxyin (blue), in which a representative size micrometastasis can be seen associated with an arteriole, containing red blood cells (grey). A great number of particles are evident in the metastasis microvasculature (Figure 3.11 B). Injections of the control agent did not show IgG-MPIO retention within the vasculature of metastatic colonies (Figure 3.12 A), despite clear VCAM-1 expression as confirmed immnunohistochemistry (Figure 3.12 B). Specific binding of VCAM-MPIO was clearly demonstrated on partially activated endothelium, where particles were bound only to the VCAM-1 expressing part of the vessel (Figure 3.12 C). Subsequently, quantitation of the MPIO retention in the targeted and control groups was performed and compared with the equivalent groups of mice terminated at 3 hours post-administration of the contrast agent (n = 5 per group). The number of VCAM-MPIO associated with the micrometastasis colonies was found to be consistently and significantly higher than the number of IgG-MPIO at 10 min post-injection (VCAM-MPIO vs. IgG-MPIO per micrometastatic $\mu m^2$ ± SD, $1.19 \times 10^{-3} \pm 7.40 \times 10^{-4}$ vs. $4.41 \times 10^{-5} \pm 6.23 \times 10^{-6}$; P = ns), also significantly greater than the number of either VCAM-MPIO or IgG-MPIO at 3 h post-injection (VCAM-MPIO vs. IgG-MPIO per micrometastatic $\mu m^2$ ± SD, $7.26 \times 10^{-5} \pm 1.45 \times 10^{-5}$ vs. $8.02 \times 10^{-6} \pm 3.11 \times 10^{-6}$; Figure 3.13 A). The number of particles per unit μm of inflamed endothelium (not capillaries) at 10 min post-VCAM-MPIO injection was significantly greater than following control IgG-MPIO injection (VCAM-MPIO vs. IgG-MPIO per vessel μm ± SD, $9.80 \times 10^{-3} \pm 1.20 \times 10^{-3}$ vs. $4.45 \times 10^{-4} \pm 3.33 \times 10^{-4}$; P < 0.0005) and also significantly higher than both the targeted and control particles found at 3 h post-administration (VCAM-MPIO vs. IgG-MPIO per vessel μm ± SD, $1.54 \times 10^{-3} \pm 1.48 \times 10^{-3}$ vs. $1.18 \times 10^{-4} \pm 1.03 \times 10^{-4}$; compared to VCAM-MPIO at 10 min P < 0.0005; Figure 3.13 B). The non-specific retention, quantified from FOV that did not contain metastatic colonies, in each group was compared with FOV of from naïve animals injected either with targeted or control agent. Although VCAM-MPIO injected mice showed a significantly greater number of particles present per $\mu m^2$ of tissue over the IgG-MPIO in all groups (P < 0.05; Figure 3.13 C) the amplitude of retention was comparable to the basal retention of the control agent at 10 min post-injection per $\mu m^2$ of micrometastatic area (Figure 3.13 A; dashed line). Thus, in all groups minimal non-specific retention was observed.

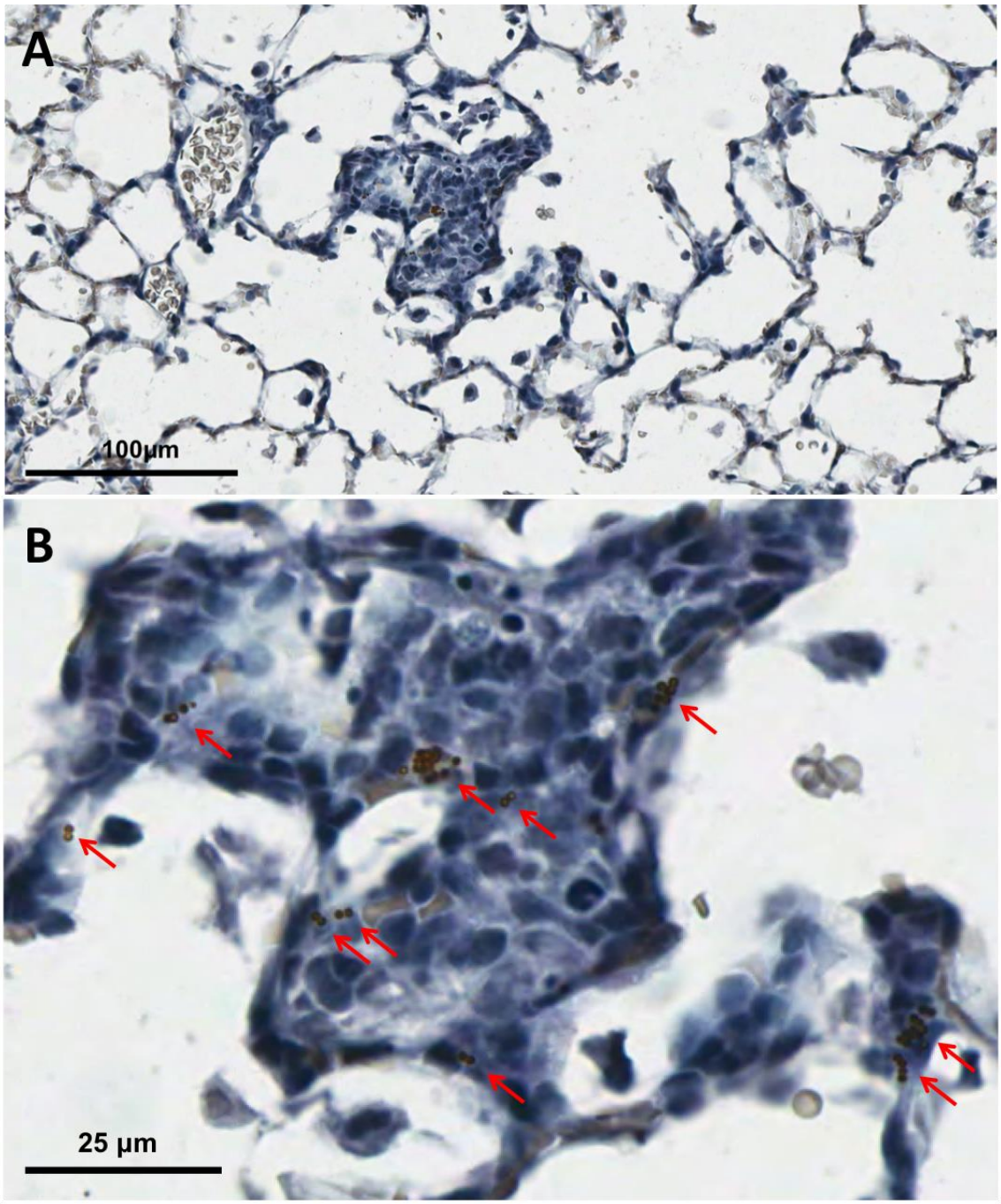



**Figure 3.11. Specific binding on micrometastasis.** Lung tissue acquired from the metastatic mouse model ($5x10^4$ cells; day 10) 10 min post-intravenous injection of VCAM-MPIO, stained for nuclei (blue) and not perfused (red blood cells are seen as grey). (A) Micrograph showing representative size micrometastasis (100 µm cross-section diameter) next to an arteriole. A substantial number of MPIO are associated with the metastasis microvasculature (B; red arrows).

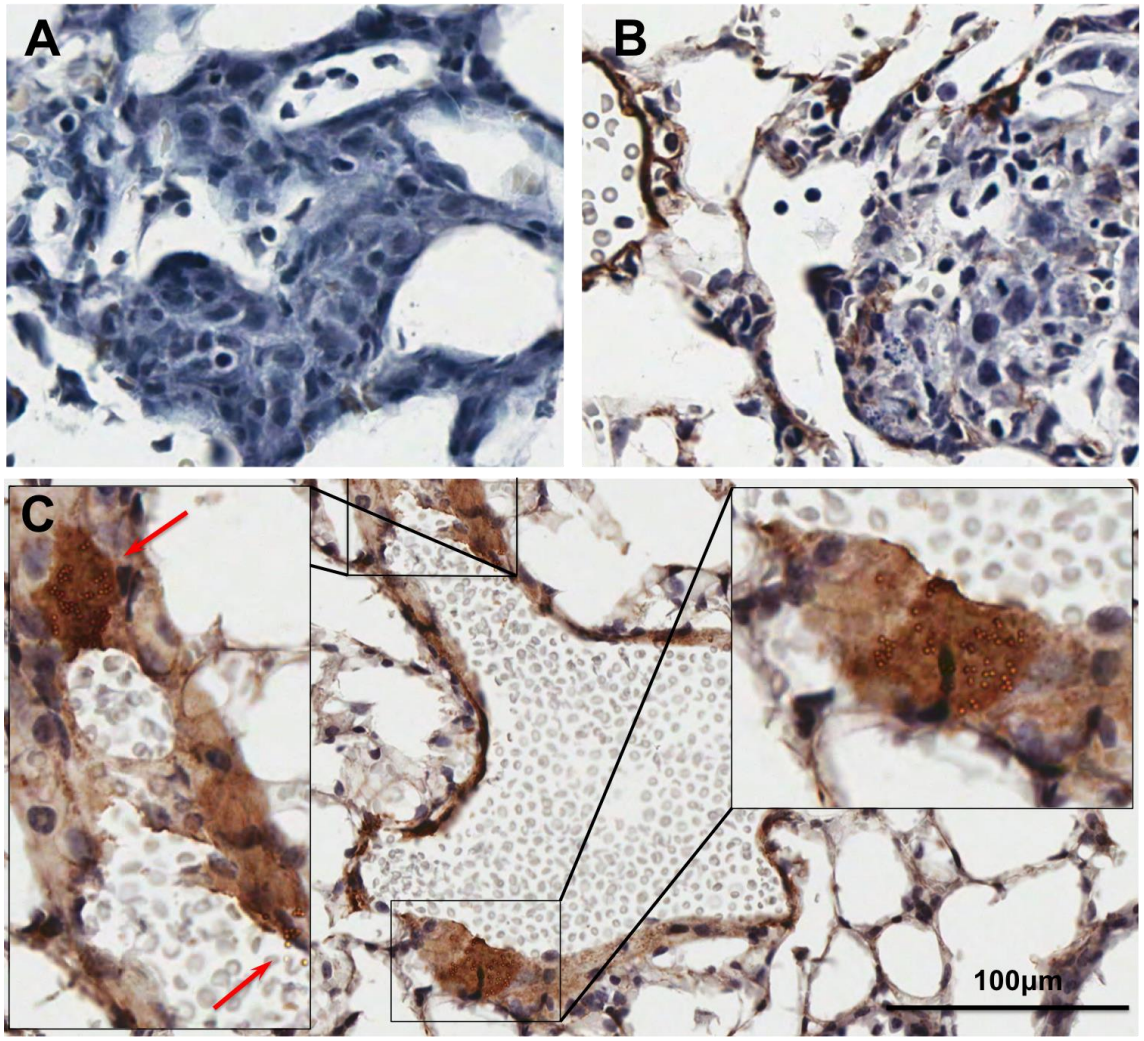



**Figure 3.12. Specific binding on VCAM-1 activated.** Lung tissue acquired from the metastatic mouse model ($5x10^4$ cells; day 10) 10 min post-intravenous injection of IgG-MPIO, without blood perfusion. (A) Tissue stained only for nuclei (blue), to allow for particle contrast (MPIO are evident as glass-brown on bright field microscopy). (B) Consecutive lung tissue section also stained for VCAM-1 expression (brown). No MPIO are seen associated with the micrometastasis following control IgG-MPIO injection. (C) Lung tissue acquired from the metastatic mouse model ($5x10^4$ cells; day 10) 10 min post injection of VCAM-MPIO, without blood perfusion. Vessel with partially strong expression of VCAM-1, showing much greater expression of VCAM-1 in some areas of the endothelium, provides a demonstration of VCAM-MPIO specific binding to VCAM-1 expressing endothelium.

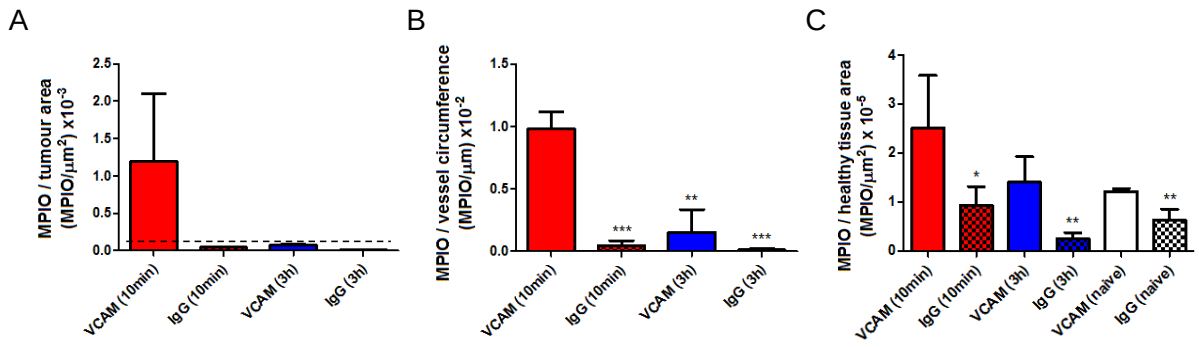



**Figure 3.13. Quantitation of VCAM-MPIO on metastasis model.** Immunohistochemical quantification of MPIO binding in metastasis-bearing or naïve lungs (10 min or 3 h after i.v. injection). Bar graphs represent (A) total number of VCAM- or IgG-MPIO per μm$^2$ tumour area, (B) number of MPIO per μm of vessel circumference and (C) number of MPIO in diseased and/or healthy lung tissue. (A, B) At 10 min post administration VCAM-MPIO showed significant greater retention on VCAM-1 expressing vessels associated with micrometastases compared to IgG-MPIO controls. Similar levels of targeted and control agent retention at 3 h indicates rapid clearance of MPIO from tissue. (C) Non-specific retention was insignificant compared to specific binding.

## 3.4 Discussion

In this chapter I have demonstrated that VCAM-MPIO bind to VCAM-1 expressing vessels in a model of LPS induced pulmonary inflammation. Moreover, I have shown that VCAM-MPIO bind specifically to VCAM-1 expressing endothelium associated with micrometastases in the lungs.

VCAM-1 has been identified as an important vascular marker that can be used as a molecular target for *in vivo* imaging techniques to detect inflammatory responses [187], in cardiovascular disease [189], neurovascular diseases (multiple sclerosis [194, 291], cerebral ischemia [193] and epilepsy [292]) and metastasis in the brain [195]. The intravascular MRI contrast agent, VCAM-MPIO, has been developed to identify VCAM-1 upregulation on the brain vasculature during the early stages of neuropathology using *in vivo* MRI[187, 194, 195]. VCAM-1 has been shown to be upregulated on pulmonary endothelial cells early in the development of metastatic foci in a biphasic manner [290]. On this basis, it was hypothesized that VCAM-MPIO would bind to sites of metastasis in the lungs, and that the potent negative susceptibility effect of the MPIO could be used to detect lung micrometastases by novel bright lung MRI, using hyperpolarized gases. Here I have demonstrated that VCAM-MPIO do indeed bind to inflamed vessels associated with micrometastasis in the lungs, and that, with careful optimisation, a dose and time window can be found with the potential for *in vivo* imaging.

In the first instance, I tested the hypothesis that VCAM-MPIO will bind to VCAM-1 activated pulmonary endothelium in a general inflammation mouse model (LPS induced systemic vascular inflammation). In this proof-of-principal study, I demonstrated specific binding of VCAM-MPIO on VCAM-1 activated lung endothelium, with little or no retention of either VCAM-MPIO in naïve mice or IgG-MPIO in LPS treated mice. These findings

provided support for this initial hypothesis and a basis on which to take the approach forward into the lung metastasis model.

In the second instance, I tested the hypothesis that VCAM-MPIO specifically bind in metastasis-bearing lungs owing to the micrometastasis induced endothelial VCAM-1 expression. In these initial studies the metastatic mouse model (BALB/c / i.v, $5x10^5$ 4T1-GFP / day 7), MPIO concentration dose (4 mg Fe/kg body weight) and time point post-administration of contrast agent (1 h) previously reported [195, 290] were used. However, the outcome of these initial studies raised substantial concerns as to the suitability of this protocol in the current setting. Consequently, I performed a series of experiment in order to optimise the metastatic mouse model (BALB/c / $5x10^4$ 4T1-GFP / day 10), the MPIO concentration dose (1.6 mg/kg) and the time point after contrast agent administration at which the *ex vivo* studies should be performed (10 min). Using this optimised protocol, I demonstrated that VCAM-MPIO specifically bind to VCAM-1 on the pulmonary vasculature associated with micrometastases, with minimal non-specific binding in either metastasis-bearing or naïve mice.

To date there are no reported clinical or pre-clinical *in vivo* methods that can detect lung metastasis at the cross-sectional range of the metastases studied here (mean cross-sectional diameter ± SD, 130 ± 50 μm). On this basis, in the following chapter, I have taken this study on to assess the possibility of detecting specifically bound VCAM-MPIO in pulmonary micrometastasis-bearing mice *in vivo*.

# Chapter 4 – *In vivo* specific targeting of pulmonary metastasis induced VCAM-1 activated endothelium

## 4.1 Introduction

In the previous chapter I demonstrated specific binding of VCAM-MPIO to metastasis induced VCAM-1 expressing pulmonary endothelium. On the basis of those positive results, the initial aim of this chapter was to develop a novel MRI method for detection of lung metastasis, using the iron oxide susceptibility effect of VCAM-MPIO. Lung is undoubtedly the most difficult organ to image with proton MRI, owing to its very low proton density compared to solid tissues (approximately one third of muscle proton density; [293]. Thus, in general no detectable signal is obtained from lung using proton MRI. In order to make use of the negative susceptibility effects of the MPIO, bright lung *in vivo* MRI techniques have been considered, with the hope that the MPIO associated with micrometastases would dephase the signal giving rise to specific contrast effects.

Hyperpolarised (HP) gases are still considered to be a new class of contrast agents since they have only been used for *in vivo* imaging for the last 20 years [294, 295]. HP gases are a different type of contrast agent than gadolinium or iron oxides, which alter the $T_1$ or $T_2$ relaxation times of nearby protons. HP gases are actually the signal source and, because they are in a non-equilibrium state, no polarisation recovery time is needed between RF pulses and fast acquisition sequences can be used. However, HP gases have a finite amount of magnetisation in a given volume, which limits sensitivity in some situations. Furthermore, the HP gas molecules show rapid diffusion in the gas phase and, consequently, hyperpolarisation of the gases has a short half-life limiting image resolution and making conventional spin-echo formation difficult.

Inert HP gases do not pose any toxicity concerns and can be safely used in the clinic. MRI with HP gases can provide regional pulmonary information which is not available with spirometry or plethysmography and, furthermore, structural and functional pulmonary information. Thus, HP gas MRI has been considered as a method that can assist in the management of chronic respiratory diseases like chronic obstructive pulmonary disease (COPD; progressive irreversible airflow limitation), asthma (airway wall inflammation and reversible bronchial obstruction) and cystic fibrosis (lung infection). To this end, pre-clinical development of ventilation techniques has quickly been translated to humans [296-299]. The diffusion properties of the HP gases have also been considered as a basis for HP lung diffusion imaging, under the same MRI diffusion principals as for conventional diffusion MRI [300-303].

With regards to lung metastasis detection, a previous publication from Duke University in 2010 (Branca *et al*, 2010; [304]) reported specific lung metastasis detection with HP gas lung MRI, making use of the negative MR susceptibility effects induced by luteinizing hormone-releasing hormone (LHRH)-targeted nanoparticles. It was this proof-of-principal report that the premise of the current project was based and I hypothesized that if the nanoparticles could cause sufficient reduction in the signal from HP gases, our orders of magnitude larger MPIO should provide a much more potent dephasing effect. Thus, it would be possible to detect the MPIO using HP gas MRI. Over the cause of this project I have collaborated with colleagues at Duke University laboratory in order to test this hypothesis.

For reasons that will be discussed during and at the end of this chapter, it was not possible to induce sufficient negative contrast effects on the HP gas signal at sites of metastasis associated VCAM-MPIO binding, as shown by IHC in Chapter 3. Owing to this setback, two alternative approaches were considered: (i) fluorinated gas and liquid MRI and (ii) radiolabelling VCAM-MPIO for PET detection.

Unlike the HP gases, inert fluorinated gases don't need to be hyperpolarised prior to use for MRI, owing to the high gyromagnetic ratio of fluorine-19 ($^{19}$F) which means there is sufficient thermally polarized signal. Inert fluorinated gases are also highly abundant, making them very inexpensive compared to HP gases. Moreover, fluorinated gases are suitable for clinical translation as they are not toxic. Considering *in vivo* lung MRI with inert fluorinated gases, within a single breath-hold it is possible to acquire several averages owing to the short longitudinal relaxation times and the quality of lung images is comparable to those obtained with HP noble gas MRI. Furthermore, the gas can be mixed with air and, therefore, multi-breath imaging can be considered without specialised ventilation. Consequently, $^{19}$F MRI has gained interest for clinical application [305, 306]. On this basis, it was hypothesised that VCAM-MPIO would dephase the fluorinated gas signal in the metastasis-bearing lungs and I have tested this hypothesis with a preliminary *post mortem* study. Subsequently, fluorinated liquids were considered as an alternative approach. The MRI physics behind imaging of $^{19}$F remains the same for fluorinated gases, but the density of the liquid compared to gas provides significantly more signal for $^{19}$F MRI. Liquid breathing is a very old concept and was first considered in 1989 in pre-term neonates, showing the potential for human liquid ventilation [307]. Pre-clinical research on total and partial liquid ventilation techniques has been reported for various animal models [308, 309], whilst there are on-going clinical trials of partial ventilation [310]. Since liquid ventilation is a realistic *in vivo* application, I have also tested *post mortem* the hypothesis that VCAM-MPIO will dephase the MRI signal from fluorinated liquid in metastasis-bearing lungs.

The premise of the radiolabelling technique was to increase the sensitivity of detection, whilst Sustaining the size of the conjugate and thus, both the binding and clearance characteristics. I hypothesized, therefore, that $^{89}$Zr labelled VCAM-MPIO would enable *in vivo* PET detection of micrometastasis in the lungs.

## 4.2 Methods

### 4.2.1 *In vivo* HP gas lung MRI

All of the hyperpolarized gas work was performed at the Center for *In Vivo* Microscopy, Duke University, Durham, USA, in collaboration with Dr Bastiaan Dierhuy's group. The 4T1-GFP cells and all reagents for contrast agent synthesis were sent from Oxford to Durham 2 months prior to the experiment and the tumour model was tested with preliminary IHC, to confirm comparable sizes of micrometastasis at the experimental time point (day 10) after i.v. tumour cell injection. The synthesis of VCAM- and IgG-MPIO was performed at Durham following the protocol previously described (section 3.2.1) by myself. Cell and animal handling was performed by Dr Simone Degan. On the day of imaging, tracheotomies were performed by Dr Yi Qi and HP gas MRI by PhD student Matt Freeman. Following MRI mice were euthanasised and the lungs excised by myself. I was present for all of the aforementioned processes, but for regulatory reasons was unable to undertake any of the *in vivo* work myself.

#### *4.2.1.1 Animal Preparation*

Mice were prepared following procedures approved by the Duke University Institutional Animal Care and Use Committee. Prior to MRI experiments, animals were anesthetized by intraperitoneal (IP) injection of 75-mg/kg sodium pentobarbital (Nembutal, Lundbeck, Inc., Deerfield, IL) and tracheotomised with an 18-G catheter (Abbocath, Hospira, Inc., Lake Forest, IL) to provide an airtight seal for mechanical ventilation. Anesthesia was maintained with periodic injections of sodium pentobarbital (25 mg/kg) administered via an indwelling 22-G IP catheter. Animals were ventilated (75% $N_2$ and 25% $O_2$) at a rate of 100 breaths/minute on an HP-gas compatible, constant-volume mechanical ventilator [282] using a tidal volume of 0.20 ml. During HP gas MRI acquisition, HP gases replaced the $N_2$ in the breathing gas mixture, while the $O_2$ concentration was held constant. During MRI acquisitions, the ventilation rate was reduced to 75 breaths/minute (140-ms inhalation period, a 360-ms breath-hold and a 300-ms period of passive exhalation) to accommodate a longer mechanical breath-hold.

Whilst in the magnet, the body temperature of the mice was monitored via a rectal thermistor and maintained at ~35°C with warm air flowing through the magnet bore. Airway pressure was monitored using a pressure transducer attached to the ventilator gas delivery lines near the trachea of the mouse. Heart rate was monitored via electrocardiogram readings using custom LabVIEW 8.1 software (National Instruments Corporation, Austin, TX, USA). This software also controlled the timing of the ventilator and triggered the MRI acquisition. Following imaging, mice were euthanized by injection of sodium pentobarbitol overdose (100 μl).

#### *4.2.1.2 HP Gas Production and Delivery*

Isotopically enriched (85% $^{129}$Xe) xenon was hyperpolarized in a 1% Xe, 10% $N_2$, 89% He mixture (Linde Electronics and Specialty Gases Inc., Stewartsville, NJ), by spin exchange optical pumping using a prototype commercial polarizer (model 9800, MITI, Durham, NC) and extracted from the buffer gases in a liquid nitrogen trap [311]. Following cryogenic accumulation, HP $^{129}$Xe (polarization ~10%) was thawed into 150 ml Tedlar bags (Jensen Inert Products, Coral Springs, FL) housed inside a Plexiglas cylinder. This cylinder was then pressurized to 3.5 psig, and HP $^{129}$Xe was delivered to the mice using the custom ventilator, as described previous [282]. $^{3}$He was polarized using the same polarizer, but with the cartridge removed and replaced with a $^{3}$He specific unit. $^{3}$He was polarized overnight at 10 atm to 30%-40% polarization, then cooled, dispensed, and delivered in the same manner as $^{129}$Xe.

#### *4.2.1.3 Imaging*

Ventilation imaging was achieved using a 3D radial sequence (views = 2501, views per breath = 4, TR = 20 ms, flip angle = 30°, matrix = 64×64×64, FOV = 2.5 cm, acquisition BW = 8 kHz), with a non-selective, 500-μs, 3-lobe sinc pulse and 8-kHz excitation bandwidth. The echo time was selected to be 0.384 ms (minimum, for maximum overall signal), 4 ms or 8 ms, to allow for increased detection of local magnetic field inhomogeneities. For $^{3}$He, the scan parameters were views = 10001, views per breath = 10, TR = 15 ms, flip angle = 20°, matrix = 128×128×128, FOV = 2.5 cm and acquisition BW = 31.25 kHz.

### 4.2.2 *Post mortem* $^{19}$F-labelled gas and liquid lung imaging

All of the *post mortem* work was performed in Oxford. Metastasis-bearing mice, as described previously (section 3.2.5), or naïve mice were euthanatized with an i.p. injection of 200 μL of pentobarbital (1:1 v/v with PBS). Mice underwent tracheotomy and a 24-gauge tracheal tube was inserted into the trachea and secured with sutures.

#### *4.2.2.1 Fluorinated gases*

For gases, a low dead volume Y-connector with a switch was connected to the tracheal tube. The gases were loaded in 10 ml syringes and connected to one end of the Y-connector, whilst an empty 10 ml syringe was connected to the other end. Lungs were inflated manually with 1 ml of gases and this was then collected into the empty syringe. The process was repeated 5 times (washing) to ensure the extraction of all air from the lungs. After washing, 1.5 ml of gases was infused into the lungs followed by encapsulation via a tracheal block with suture knot. Finally, mice were fixed in position in the imaging cradle inside a homebuilt 27 mm $^{19}$F birdcage coil (281 MHz) and placed in a 7T magnet. Three fluorinated gases were used:

tetrafluoromethane (FC-14) 99%; perfluoroethane (FC-116) 99%; and perfluorocyclobutane (PFC C-318) 99%. Ultra Short Echo Time (UTE3D) was used for gases, with radial k-space sampling; Matrix = 128 x 256 x 128, FOV = 45 x 45 x 45 mm (0.35 mm isotropic), TR = 4 ms, TE = [10, 1000] us, nt = 64, Texp = 2 h 40 min.

#### *4.2.2.2 Fluorinated liquids*

For liquids, only a single 5 ml syringe was used loaded with 2 ml liquid of choice. After tracheotomy and placement of the tracheal tube, mice were fixed in position inside the cradle and the cradle was positioned in the up right direction, to allow air to move upwards as the liquid was infused. Subsequently, 1 ml of liquid was infused and subsequently removed manually (washing), with care not to damage the lungs, in order to displace the maximum amount of air from the lungs. A final 1.5 ml (from initial 2 ml) of liquid was infused per lung and the trachea sealed with a suture knot. Five different fluorinated liquids were used: tetradecafluorohexane 99%; perfluorohexane 95%; perfluoro-15-crown-5-ether 99%; hexafluorobenzene 99%; and tetradecafluorohexane 99%. Mice were placed in 7T magnet, inside a homebuilt 27 mm $^{19}$F birdcage coil (281MHz). Multi Gradient Echo Multi Slice (MGEMS) was used for liquids, with radial k-space sampling: 2D axial, coronal or sagittal MGEMS, Matrix = 128 x 128; TE = 5 ms; TR = 400 ms; FatSatFrq = -2.5 kHz, FOV = 25.6 x 25.6 mm; THK = 1 mm; nt = 64; Texp = 54min. Also GE3D was used for liquids: Matrix = 128 x 128 x 128; TE = 4, 6, 8 us; TR = 400 ms FOV = 32 x 32 x 32 mm; Texp = 1 h 50 min.

### 4.2.3 [$^{89}$Zr]-DFO-VCAM- or [$^{89}$Zr]-DFO-IgG-MPIO synthesis

Radiolabelling of VCAM- and IgG-MPIO was performed by Dr Bart Cornelissen, Radiopharmaceuticals and Molecular Imaging group, Oxford Institute for Radiation Oncology. To allow radiolabelling with $^{89}$Zr, rat anti-mouse VCAM-1 antibody or rat anit-mouse IgG antibody was dissolved in sodium bicarbonate buffer (0.1 M, pH 8.5), and incubated with the chelator, desferroxamine-*p*-SCN or DFO (1-(4-Isothiocyanatophenyl)-3-[6,17-dihyroxy-7,10,18,21-tetraoxo-27-[N-acetylhydroxylamino)-6,11,17,22-tetraazaheptaeicosane]thiourea; Macrocyclics, Dallas, TX), at 15-fold molar excess, for 1 hour at room temperature. Excess unreacted DFO was removed by size exclusion chromatography (G50 SEC). The product reagents DFO-VCAM or DFO-IgG were subsequently conjugated to MPIO by myself, using the same protocol as described previously (section 2.3.4.1 – its gone to methods). $^{89}Zr^{4+}$ (dissolved in 0.1M oxalic acid; Perkin Elmer, Amsterdam, NL) was rendered to neutral pH using 2 M NaOH. DFO-VCAM-MPIO or DFO-IgG-MPIO were dissolved in HEPES buffer (0.1 M, pH 7.0), and reacted with the appropriate amount of $^{89}$Zr for one hour at room temperature, resulting in $^{89}$Zr-DFO-VCAM-MPIO or $^{89}$Zr-DFO-VCAM-MPIO (Figure 4.1). Unreacted $^{89}$Zr was removed using G50 SEC, and quality control was performed using instant thin layer chromatography (ITLC) eluted with sodium citrate buffer (0.1M, pH 5.0). Radiolabelling yield was routinely >85%. After purification using G50 SEC, radiochemical purity was >96%.

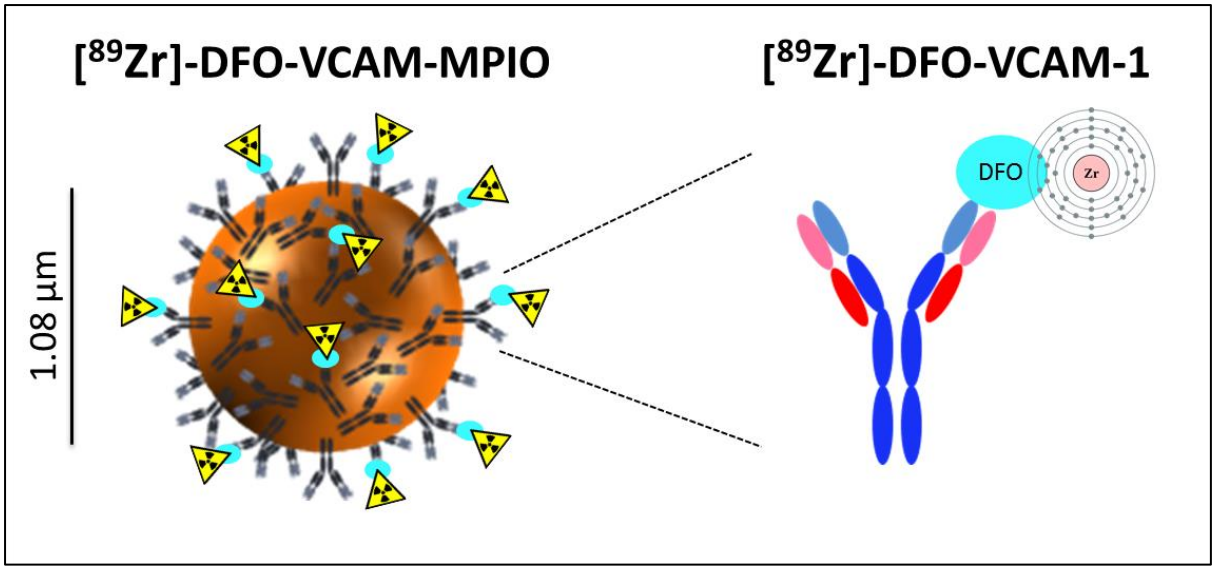



**Figure 4.1. [$^{89}$Zr]-DFO-VCAM-MPIO.** Schematic representation of the [$^{89}$Zr]-DFO-VCAM-MPIO assembly (not in scale).

### 4.2.4 *In vitro* binding of [$^{89}$Zr]-DFO-VCAM-MPIO

To confirm the binding affinity of [$^{89}$Zr]-DFO-VCAM-MPIO or [$^{89}$Zr]-DFO-IgG-MPIO to VCAM-1, competition radioimmunoassays (RIA) were performed with recombinant VCAM-1 (rVCAM-1) or TNF-α stimulated HUVEC cells *in vitro*.

#### *4.2.4.1 Radioimmunoassays with rVCAM-1*

ELISA plates were coated with 3 exponential dilutions of mouse rVCAM-1 (1:1 = 0.5 µg/ml; 50163-M08H, Sino Biological Inc., Beijing, China). Triplicates of 1 nM of [89Zr]-DFO-VCAM-MPIO, [89Zr]-DFO-IgG-MPIO, [89Zr]-DFO-VCAM and [89Zr]-DFO were incubated for 30 minutes at room temperature. The plates were washed and the radioactivity in each well was determined by quantitative autoradiography.

#### *4.2.4.2 Radioimmunoassays with HUVECs*

HUVECs were seeded onto ELISA plates (5x10$^3$/well) and grown to 80% confluency. To stimulate VCAM-1 expression 2/3 of the wells were incubated with 10 ng/ml of human TNF (315-01A, Peprotech, London, UK) for 18 hours. Subsequently, 1 nM of [$^{89}$Zr]-DFO-VCAM-MPIO, [$^{89}$Zr]-DFO-IgG-MPIO, [$^{89}$Zr]-DFO-VCAM or [$^{89}$Zr]-DFO was added to the wells and incubated for 30 minutes.Experiments were carried out in triplicates of TNF-stimulated cells, TNF-stimulated cells with a VCAM-1 blocking step, or naïve cells. Plates were washed and the radioactivity in each well determined by quantitative autoradiography.

### 4.2.5 *Ex vivo* biodistribution of MPIO

In order to minimise the radiation exposure and cover the substantial cohort of animals used in the *ex vivo* biodistribution study, the work was shared between myself and Dr James Knight, Radiopharmaceuticals and Molecular Imaging group. Metastasis-bearing animals or naïve animals were injected i.v. with 1.6 mg/kg of either [$^{89}$Zr]-DFO-VCAM-MPIO or [$^{89}$Zr]-DFO-IgG-MPIO, with 0.5 MBq activity, and terminated 10 minutes later (n=8). For each animal, heart, lungs, liver, spleen, stomach, large intestine, small intestine, pancreas, kidneys and samples of bone, skin and fat were excised, washed in PBS (eliminate blood) and left to dry on a high absorbency paper. The organs as well as blood samples were placed inside 5 ml tubes (75x13 mm, 11729412, Fisher, Loughborough, UK) tubes with pre-measured mass. All tubes were placed in a robotic gamma camera (1470 WIZARD gamma counter, Perkin Elmer) machine overnight to determine the activity per organ. The tubes containing the organs were weighed to calculate the mass of the organ and, subsequently, the % of injected dose per gram of organ was calculated.

### 4.2.6 *Ex vivo* autoradiography

Equivalent groups to these described for the biodistribution study (section 4.2.5), with a single mouse per group, were used for autoradiography. Lungs were excised and treated as previously described (section 3.2.2). After cryo-sectioning, mounted lung sections were placed inside a Cylcone® storage phosphor screen with a phosphor exposure cassette and allowed long exposure (O/N), since this step was performed ~ 3 days post-injection and activity was low. The cassette was loaded onto a Cyclone® Plus storage phosphor system (Perkin Elmer, London, UK) and single images were acquired per phosphor screen with negative contrast (dark) indicating spatial distribution of activity.

### 4.2.7 *In vivo* binding of [$^{89}$Zr]-DFO-VCAM-MPIO

All radiation and animal handling for the *in vivo* study was undertaken by myself, whilst the PET acquisition was performed by Dr Veerle Kersemans, Imaging Core Group, Oxford Institute for Radiation Oncology. Mice were anesthetized with 3% isofluorane mixed with room air, and subsequently anesthesia was maintained with 1-2% isofluorane until termination. Metastasis-bearing mice were injected with either [$^{89}$Zr]-DFO-VCAM-MPIO or [$^{89}$Zr]-DFO-IgG-MPIO (1.6 mg/kg iron concentration and 5 MBq activity per injection; n=4 per group). As further controls, naïve mice were injected with either [$^{89}$Zr]-DFO-VCAM-MPIO or [$^{89}$Zr]-DFO-VCAM (n=4 per group).
PET and CT imaging was performed using the Inveon PET/CT system (Siemens Preclinical Solutions). Throughout each imaging session, mice were maintained at 37 °C and respiration rate was monitored (60-100 respirations/minute). Mice were placed supine, head first, in the imaging cradle and a cannula was inserted into the lateral tail vein. CT based attenuation correction (continuous rotation, 220 degrees, 120 steps, 65 kV, 500 μA, 200ms exposure

time, 3072 x 2048 matrix, binning of 4, 3 bed positions with 28.45% overlap) was performed before each PET emission scan. The latter CT acquisition was also used for anatomical referencing. Both histogramming and image reconstruction was conducted with the Inveon Acquisition Workplace software (IAW, version 1.5). For all compounds, 1-hour whole-body dynamic acquisitions were acquired (Figure 4.2).

Following the attenuation CT-scan, the PET emission data acquisition (3600 s, Zr-89, 3.432 ns timing window, 511 keV photpeak energy level, 350 – 650 keV energy level discrimination) was initiated and the radiotracer injected via the tail vein cannula. Data were histogrammed in 24 time frames (15x 20s, 7x 300s, 2x 600s) with a span of 3 and a ring difference of 79. Global deadtime correction and Fourier rebinning was applied to all data sets.

The dynamic histograms were reconstructed using a 2-dimensional filtered backprojection (2D-FBP) algorithm, a Ramp projection filter, a 0.5/mm Nyquist projection cut-off value, no zoom and a matrix size of 128x128x159 (sagittal x coronal x transversal).

Image analysis was performed using the Inveon Research Workplace software (IRW, version 4.2).

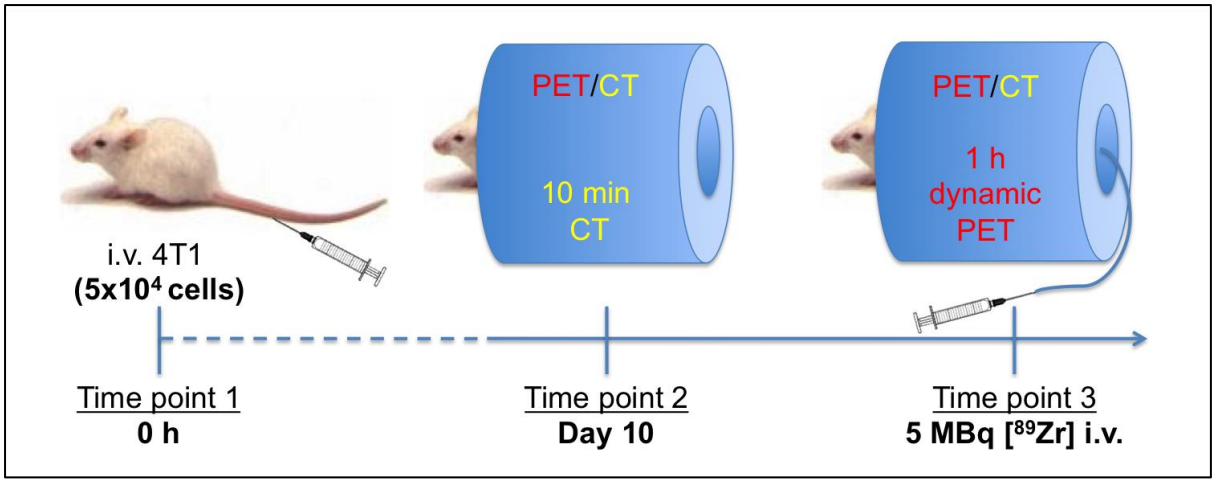



**Figure 4.2. *In vivo* PET protocol**. Schematic representation of the *in vivo* PET/CT imaging protocol time line.

## 4.3 Results

### 4.3.1 HP gases lung MRI

Figure 4.3 shows representative signal intensity projection images from the targeted and control groups, using either HP $^{3}$He or $^{129}$Xe gas. However, all of the results from the *in vivo* HP gas imaging with $^{3}$He and $^{129}$Xe were essentially negative; it was not possible to observe or measure any contrast induced by MPIO located within the lungs. Confirmation of successful i.v. injections was justified from the paired proton images (pre- and post-administration of MPIO), since the presence of MPIO in the circulation results in rapid signal loss in the liver and spleen (Figure 4.4). Subsequently, IHC analysis from tissue acquired from micrometastasis-bearing lungs confirmed the presence of VCAM-MPIO within and around micrometastatic colonies (Figure 4.5). Given the absence of signal reduction it is possible that the cluster size of MPIO was not sufficiently large to induce a detectable signal change. Therefore, further experiments were performed with higher doses of MPIO (x2, x8 and x16). Despite the increase in dose, no visible signal reduction in the lungs was observed.

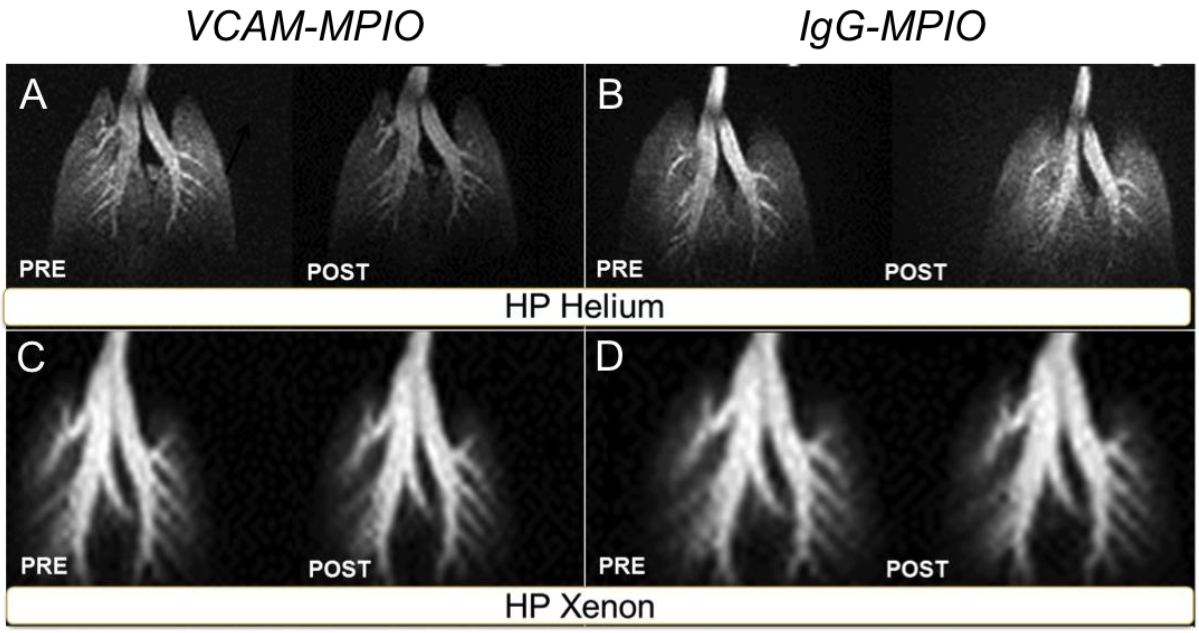



**Figure 4.3. *In vivo* HP gas imaging.** Representative signal intensity projection MRI images from *in vivo* HP $^{3}$He (A-B) or $^{129}$Xe (C-D) lung imaging, from micrometastasis-bearing mice prior to and post-administration of VCAM-MPIO (A, C) or IgG-MPIO (B, D). No visible or measurable reduction in signal intensity was found as result of either VCAM-MPIO or IgG-MPIO on either $^{3}$He or $^{129}$Xe images.

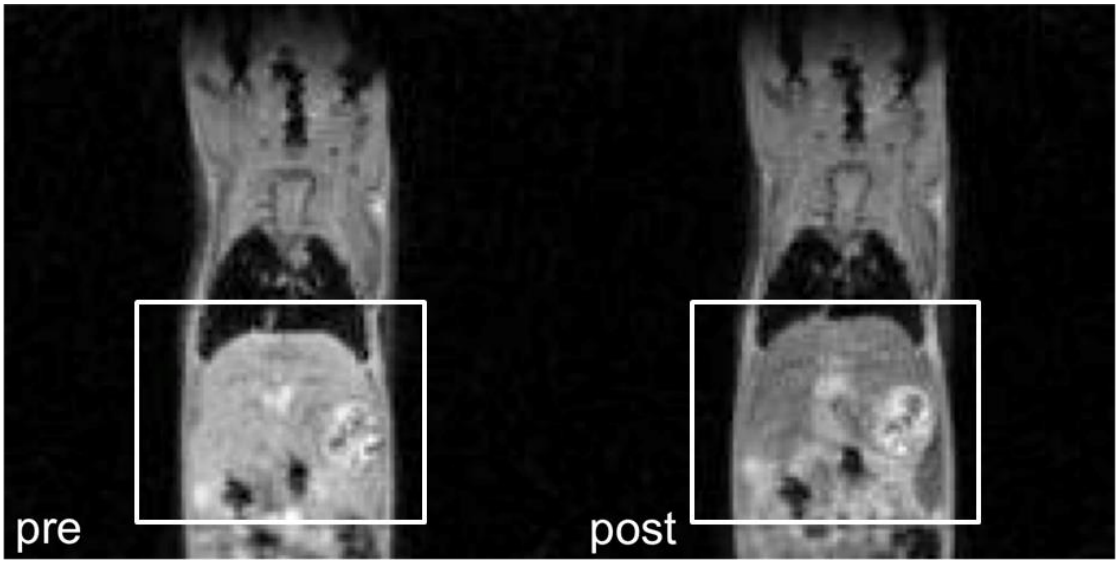



**Figure 4.4. Confirmation of successful administration of contrast agents.** Figure shows $^{1}$H MRI images acquired pre- and post-VCAM-MPIO administration from a metastasis-bearing mouse. Signal loss is seen in both liver and spleen (white boxes) after administration.

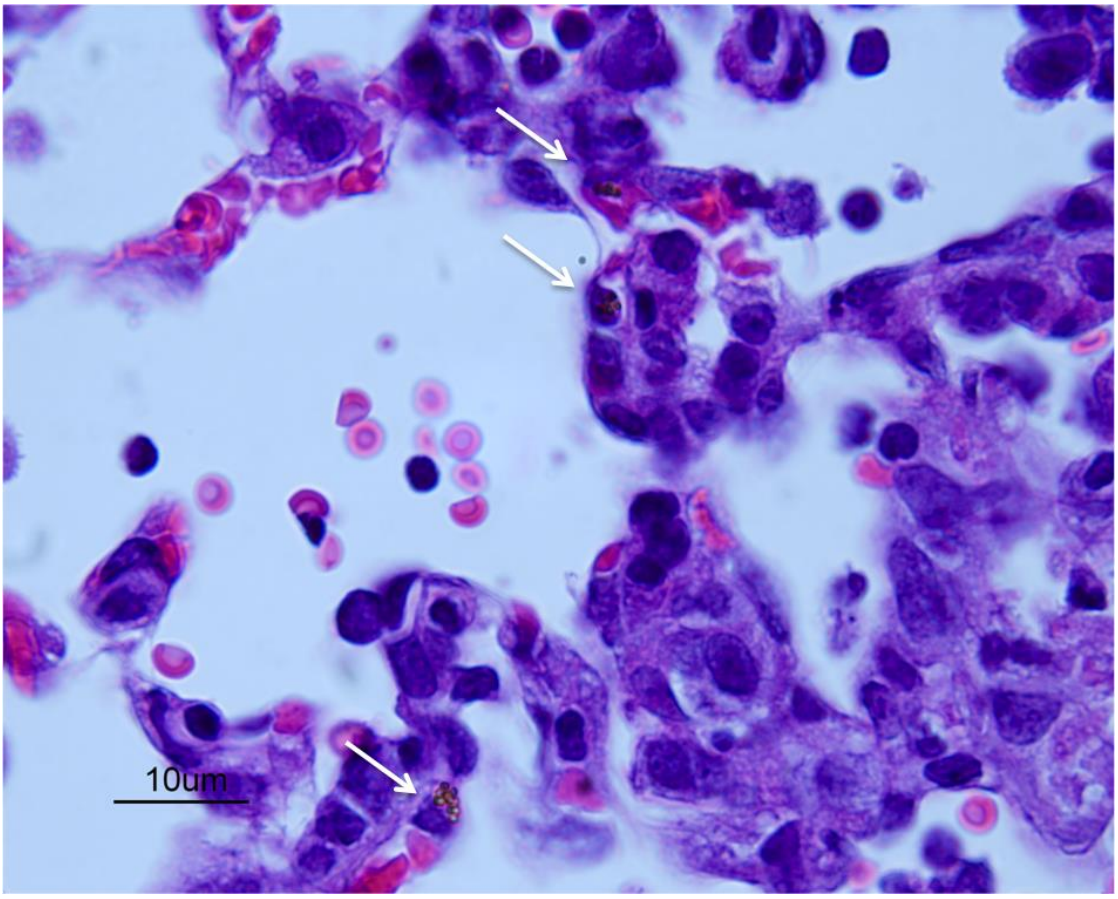



**Figure 4.5. Colocalisation of VCAM-MPIO and micrometastases in lungs**. Bright field micrograph of representative lung micrometastasis stained for nuclei (hematoxylin; blue) and cytoplasm (eosin; red). The presence of VCAM-MPIO (white arrows) associated with micrometastases was confirmed.

### 4.3.2 *Post mortem* imaging of lungs with fluorinated gases and liquids

#### *4.3.2.1 Fluorinated gases*

With the use of stable state gases it has been possible to acquire averages across multiple images and, therefore, high sensitivity lung images. Figure 4.6 shows representative 3D ultra-short time-echo (UTE3D) images from the lungs of a naïve mouse inflated with tetrafluoromethane (FC-14) 99%. Despite achieving reasonable SNR it was not possible to detect signal reductions following administration of VCAM-MPIO and the lung images from metastasis-bearing mice were comparable with images from naïve without VCAM-MPIO administration. In subsequent gas phantom experiments, were a significant amount of MPIO (estimated 10,000- to 100,000-fold higher than the injectable dose) was glued (mixed MPIO with super-glue) in the bottom of 10 ml tube and filled with gases, a detectable reduction in signal was observed. These data suggest that the level of MPIO retention achieved *in vivo* may simply not be great enough to induce a detectable change in signal. Similarly negative results were found using the other two fluorinated gases.

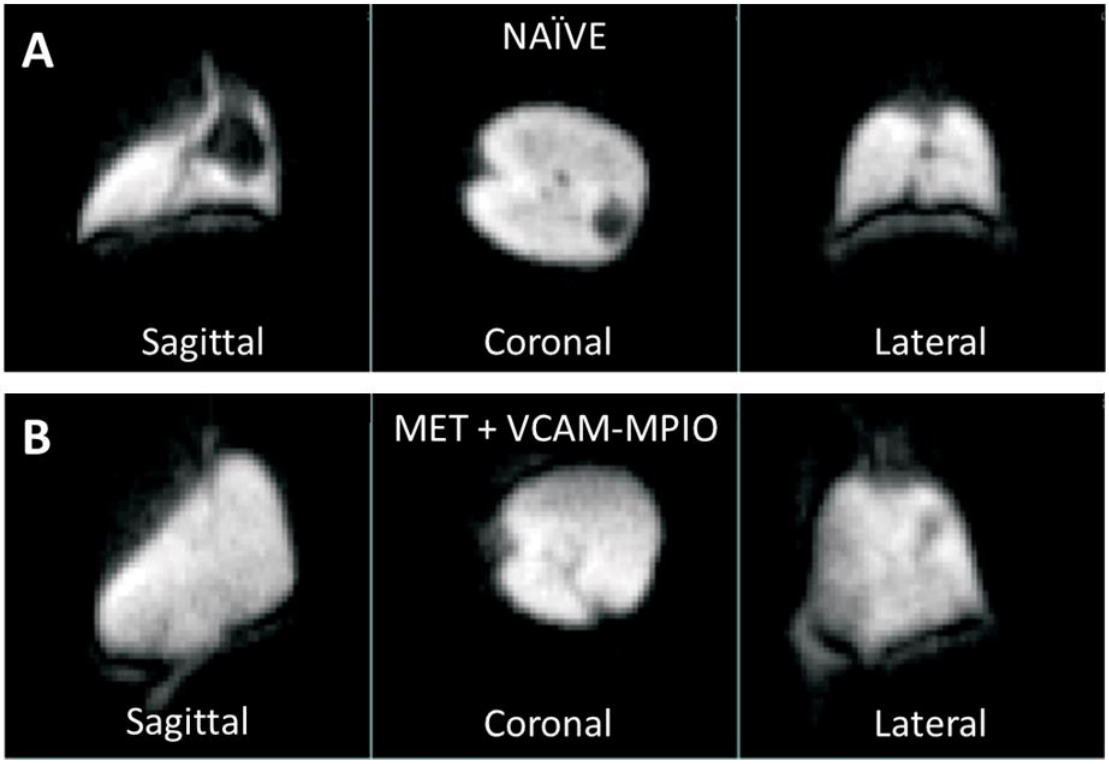



**Figure 4.6. *Post mortem* $^{19}$F gas MRI.** (A) *Post mortem* $^{19}$F MRI images of lungs from naïve mouse inflated with fluorinated gas. Lungs were inflated with tetrafluoromethane (FC-14) 99% and scanned with UTE3D MRI using radial k-space sampling, TE = 10 μs. $T_{exp}$ = 1 h 30 min. (B) Images from a GE3D dataset acquired from micrometastasis-bearing lungs following i.v. injection of VCAM-MPIO. No detectable difference in SNR was evident between the naïve and metastasis-bearing mice injected with VCAM-MPIO.

#### 4.3.2.2 Fluorinated liquids

Liquid inflation of the lungs with fluorinated liquids provided greater lung definition images compared to fluorinated gases. Figure 4.7 shows representative 3D gradient echo (GE3D) of naïve lungs without administration of VCAM-MPIO compared to metastasis-bearing lungs with administration of VCAM-MPIO. Overall, no visible signal reduction was evident to indicate the presence of VCAM-MPIO and the lungs. Since no effect of VCAM-MPIO was evident in metastasis-bearing mice compared to naïve mice, these experiments were not pursued further at that time.

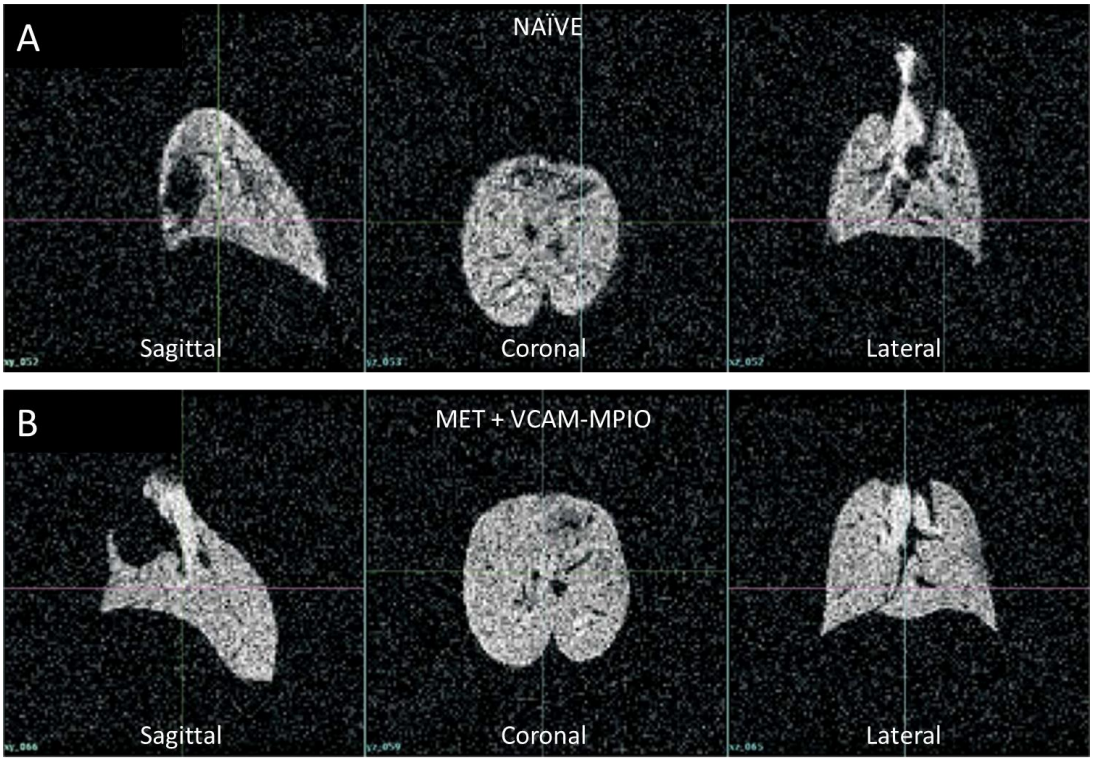



**Figure 4.7. *Post mortem* $^{19}$F liquid MRI**. (A) *Post mortem* $^{19}$F MRI images of lungs from naïve mouse inflated with fluorinated liquid. Lungs were inflated with perfluorohexane 95% and scanned with GE3D MRI using radial k-space sampling, TE = 6 ms, $T_{exp}$ = 110 min. (B) Images from a GE3D dataset acquired from micrometastasis-bearing lungs following i.v. injection of VCAM-MPIO. No detectable difference in SNR was evident between the naïve and metastasis-bearing mice injected with VCAM-MPIO.

### 4.3.3 *In vitro* binding of [$^{89}$Zr]-DFO-VCAM-MPIO

Given the problems experienced with bright lung MRI, the alternative strategy of radiolabelling the VCAM-MPIO was considered, using a radiolabelling linker (DFO) which links the isotope with VCAM-1 antibody. To confirm that the binding characteristics of VCAM-MPIO were not affected by the radiolabelling, radioimmunoassays were performed using radiolabelled VCAM-MPIO, IgG-MPIO (negative control), DFO-VCAM (positive control) and DFO alone (negative control). In initial assays with recombinant VCAM-1 (Figure 4.8 A), [$^{89}$Zr]-DFO-VCAM-MPIO showed significant % binding (% cpm ± SD, 1:1, 29.51 ± 7.03; 1:10, 12.94 ± 3.99; 1:100, 8.72 ± 2.16; $P < 0.0001$) compared to both of the negative controls [$^{89}$Zr]-DFO-IgG-MPIO (% cpm ± SD, 1:1, 10.34 ± 0.57; 1:10, 4.04 ± 0.18; 1:100, 4.48 ± 0.88) and [$^{89}$Zr]-DFO (% cpm ± SD, 1:1, 13.41 ± 1.20; 1:10, 4.61 ± 1.41; 1:100, 3.00 ± 0.18) at all dilutions and also showed consistently % binding compared to the positive control [$^{89}$Zr]-DFO-VCAM (% cpm ± SD; 1:1, 22.78 ± 2.51; 1:10, 7.89 ± 0.78; 1:100, 4.85 ± 0.26). A significant reduction in binding was observed when [$^{89}$Zr]-DFO-VCAM-MPIO binding was blocked by VCAM-1 antibody (% cpm ± SD; 1:1, 14.30 ± 2.28, $P < 0.0001$; 1:10, 7.76 ± 1.58, $P < 0.001$; 1:100, 6.32 ± 0.25, $P < 0.01$). Although binding was significantly reduced by blocking, [$^{89}$Zr]-DFO-VCAM-MPIO still showed significantly greater binding than all of the reagents at 1:1 and 1:10 dilutions ($P < 0.0001$). At the 1:100 dilution [$^{89}$Zr]-DFO-VCAM-MPIO and [$^{89}$Zr]-DFO-IgG-MPIO showed comparable binding.
Subsequently, binding was assessed with TNF stimulated HUVECs (Figure 4.8 B), where [$^{89}$Zr]-DFO-VCAM-MPIO showed significantly higher binding (% cpm ± SD, 14.23 ± 4.43; $P < 0.0001$) compared to both of the negative controls [$^{89}$Zr]-DFO-IgG-MPIO (% cpm ± SD, 4.22 ± 0.92) and [$^{89}$Zr]-DFO (% cpm ± SD, 3.27 ± 0.72) but not the positive control [$^{89}$Zr]-DFO-VCAM. Pre-incubation with the VCAM-1 antibody effectively out-competed the binding of [$^{89}$Zr]-DFO-VCAM-MPIO to TNF-stimulate HUVECs, and [$^{89}$Zr]-DFO-VCAM-MPIO binding was negligible on naïve HUVECs.

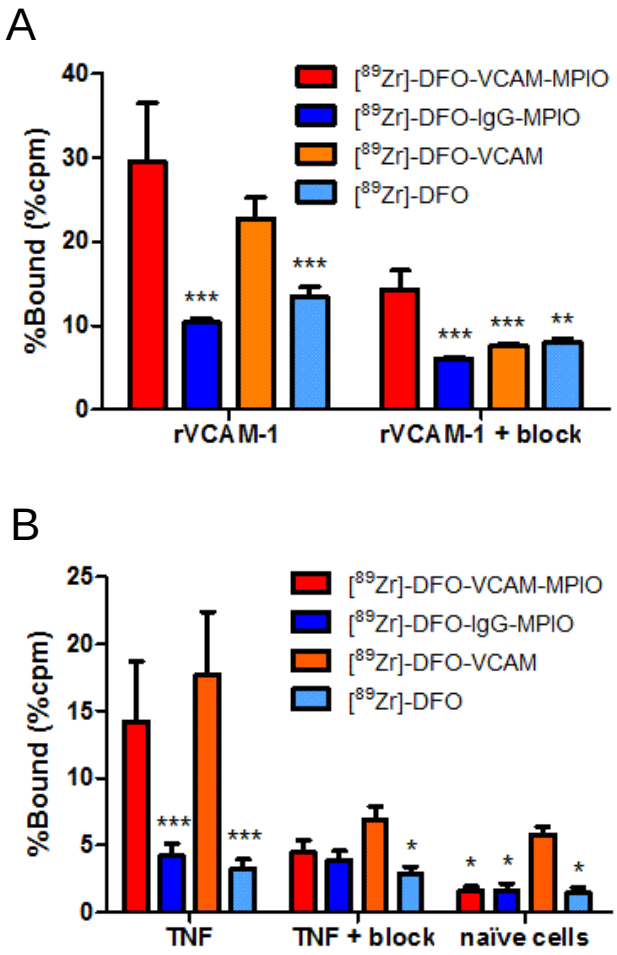



**Figure 4.8. Testing binding specificity of [$^{89}$Zr]-DFO-VCAM-MPIO**. Radioimmunoassay plots showing the % of bound radiolabelled (hot) agents against recombinant VCAM-1 (A) at 3 exponential dilutions (1:1 = 0.5 μg/ml) or TNF-stimulated HUVECs (B) with 30 minutes static incubation, + / − competition with VCAM-1 antibody (blocking). (A) [$^{89}$Zr]-DFO-VCAM-MPIO showed significantly greater % binding compared to both negative controls [$^{89}$Zr]-DFO-IgG-MPIO and [$^{89}$Zr]-DFO at all dilutions ($P<0.0001$). Following blockade with VCAM-1 antibody, [$^{89}$Zr]-DFO-VCAM-MPIO binding was reduced at all dilutions (1:1, $P<0.0001$; 1:10, $P< 0.001$; 1:100, $P<0.01$). (B) [$^{89}$Zr]-DFO-VCAM-MPIO showed significantly greater % binding to TNF-stimulated HUVECs compared to both negative controls [$^{89}$Zr]-DFO-IgG-MPIO and [$^{89}$Zr]-DFO ($P<0.0001$) and binding was reduced with inclusion of a blocking step, and also un-stimulated cells.

### 4.3.4 *In vivo* PET imaging of [$^{89}$Zr]-DFO-VCAM-MPIO

Since the binding characteristics of radiolabelled VCAM-MPIO were not affected by radiolabelling, and having confirmed the binding of VCAM-MPIO to metastasis induced inflamed vasculature *ex vivo*, [$^{89}$Zr]-DFO-VCAM-MPIO was tested *in vivo* in mice with pulmonary micrometastasis. Binding [$^{89}$Zr]-DFO-VCAM-MPIO was compared that of radiolabelled IgG-MPIO and also [$^{89}$Zr]-DFO-VCAM at 10 min post-administration using PET. As additional control, [$^{89}$Zr]-DFO-VCAM-MPIO was injected at naïve mice. Relevant organs were identified and segmented from the co-registered CT scan and the activity uptake curves of each organ plotted over time. Figure 4.9 shows the activity uptake curves for liver, lungs, kidneys and blood from a representative pair of animals injected with the targeted agent (top) and a representative pair of animals injected with the control agent ([$^{89}$Zr]-DFO-IgG-MPIO; bottom). In all animals from all groups, the liver showed an exponential increase in uptake of the agent and to a much higher level than any other organ; uptake plateaued at 5 min post-administration without further significant variations. For n=4, the mean Bq/ml of liver over 50 min for the diseased mice injected with [$^{89}$Zr]-DFO-VCAM-MPIO was 2.65 x $10^6$ ± 2.78 x $10^5$, for [$^{89}$Zr]-DFO-IgG-MPIO was 1.79 x $10^6$ ± 2.52 x $10^5$ and for naïve mice injected with [$^{89}$Zr]-DFO-VCAM-MPIO was 2.61 x $10^6$ ± 3.19 x $10^5$ (Figure 4.10 A-C). The lungs from [$^{89}$Zr]-DFO-VCAM-MPIO injected metastasis bearing animals showed the second highest activity uptake within the group (Bq/ml ± SD, 5.33 x $10^5$ ± 2.84 x $10^5$; Figure 4.10 A), whilst the lungs from [$^{89}$Zr]-DFO-IgG-MPIO injected metastasis bearing animals showed minimal uptake (Bq/ml ± SD, 6.85 x $10^4$ ± 2.01 x $10^4$; Figure 4.10 B) comparable to blood activity levels, as was the case for naïve mice injected with [$^{89}$Zr]-DFO-VCAM-MPIO (Bq/ml ± SD, 9.81 x $10^4$ ± 9.60 x $10^3$; Figure 4.10 C). Kidney and blood activity uptake in all groups was consistently lower than the lung uptake of [$^{89}$Zr]-DFO-VCAM-MPIO metastasis-bearing animals (Figure 4.10 A-C).

Static analysis of lung uptake was performed for two time points, 10 and 50 min post-administration. Lungs from the targeted group showed significant uptake compared to both the [$^{89}$Zr]-DFO-VCAM-MPIO injected naïve animals ($P < 0.0005$) and the diseased animals injected with the control agent ($P < 0.0005$) at both time points (Figure 4.11).

Blood was expected to be free of particles very rapidly, as indicated by previous blood clearance results (see section 3.3.5), thus the uptake curves of the heart were analysed and the half-life of the activity was estimated. The mean half-life for all animals in all groups was comparable with the previously estimated biological clearance of the particles (biological clearance $T_{½}$ PET *vs.* MRI, 36.56 *vs.* 39.90 s; Figure 4.12).

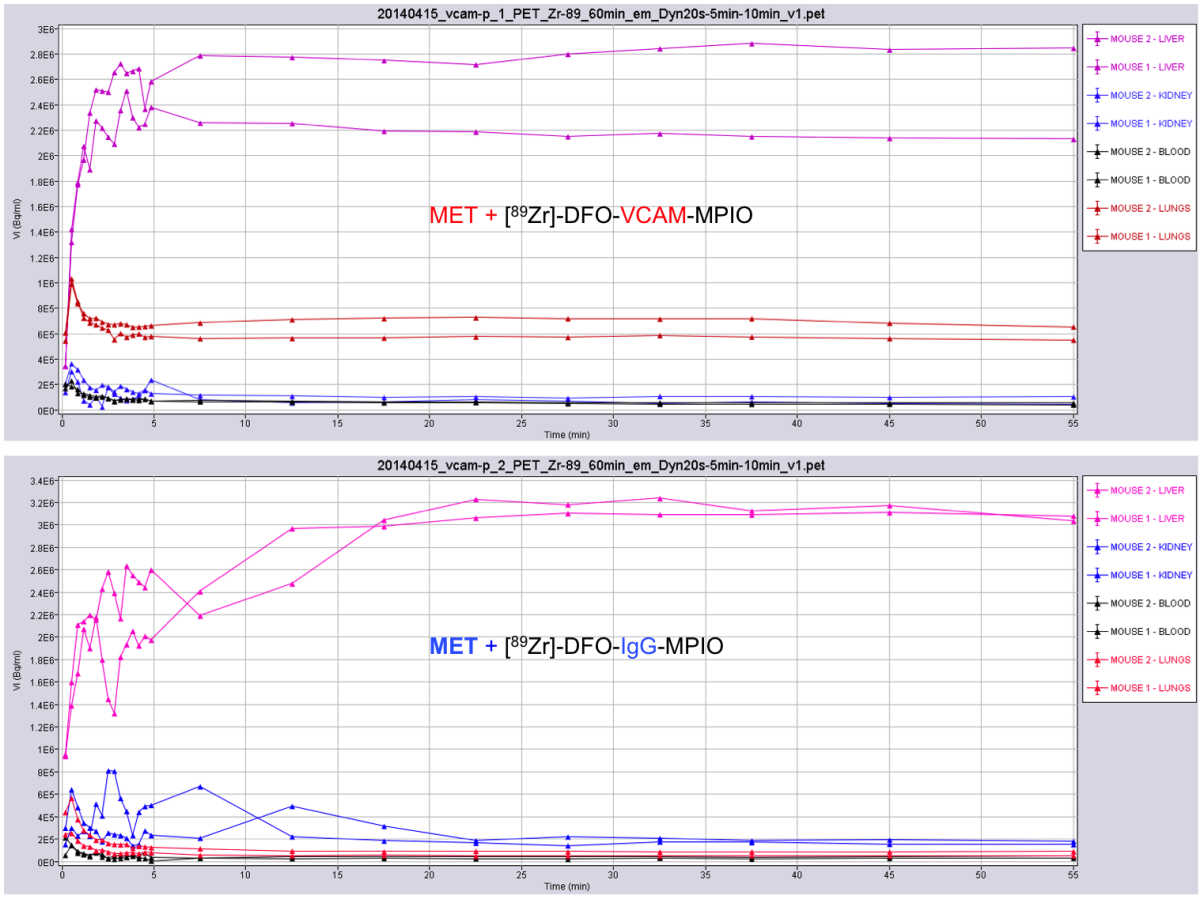



**Figure 4.9. Representative PET dynamic analysis**. Activity uptake curves of [$^{89}$Zr]-DFO-VCAM-MPIO or [$^{89}$Zr]-DFO-IgG-MPIO for lungs (red), liver (pink), blood (black) and kidneys (blue), from metastasis bearing mice (n = 2 per group). Liver shows rapid and high accumulation of radioactivity in both targeted and control groups. For [$^{89}$Zr]-DFO-VCAM-MPIO injected mice, lungs showed higher accumulation of activity compared to the [$^{89}$Zr]-DFO-IgG-MPIO group. Kidneys and blood show minimal uptake in both groups.

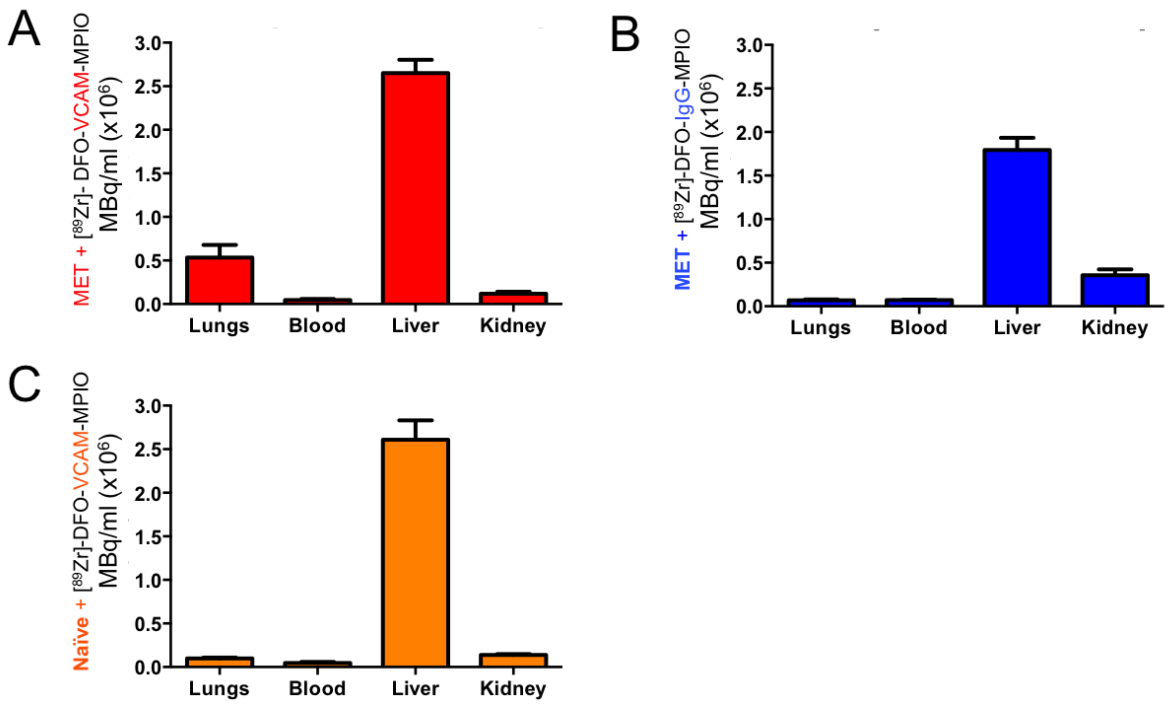



**Figure 4.10. Mean activity uptake of lung, blood, liver and kidney over time**. Mean activity uptake per organ determined from PET dynamic analysis (n = 4). (A-C) Graph showing activity uptake for lung, blood, liver and kidney from diseased mice injected with [$^{89}$Zr]-DFO-VCAM-MPIO (A) or [$^{89}$Zr]-DFO-IgG-MPIO (B), or from naïve mice injected with [$^{89}$Zr]-DFO-VCAM-MPIO (C). Liver showed significantly higher uptake compared to the rest of the organs in all groups ($P < 0.0001$), reflecting the role of the liver in scavenging unbound MPIO from the blood. (A) Lungs from diseased mice injected with the targeted agent showed significantly higher uptake than lungs from diseased mice injected with the control agent (B; $P < 0.0005$) or lungs from naïve mice injected with the targeted agent (C; $P < 0.0005$).

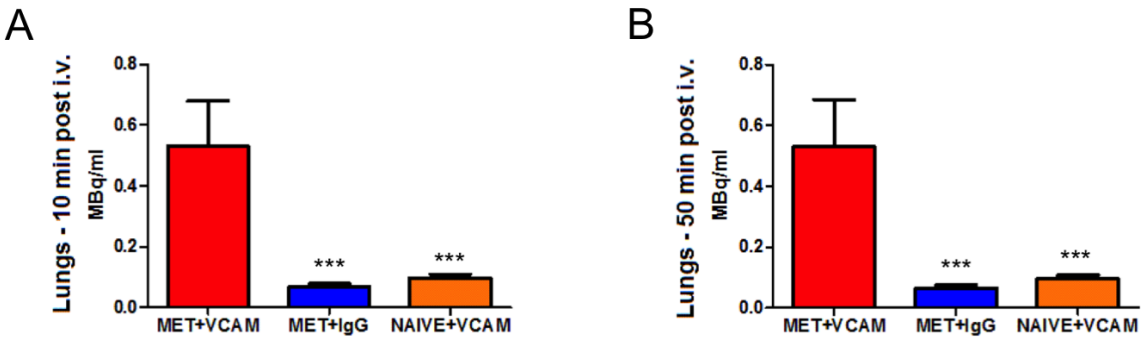



**Figure 4.11. PET static analysis for lungs.** PET static analysis of activity uptake in the lungs at (A) 10 and (B) 50 min post-MPIO administration. [$^{89}$Zr]-DFO-VCAM-MPIO showed significantly greater retention in diseased lungs compared to naïve lungs or to the [$^{89}$Zr]-DFO-IgG-MPIO retention in diseased lungs, at both 10 and 50 min post-administration ($P < 0.0001$).

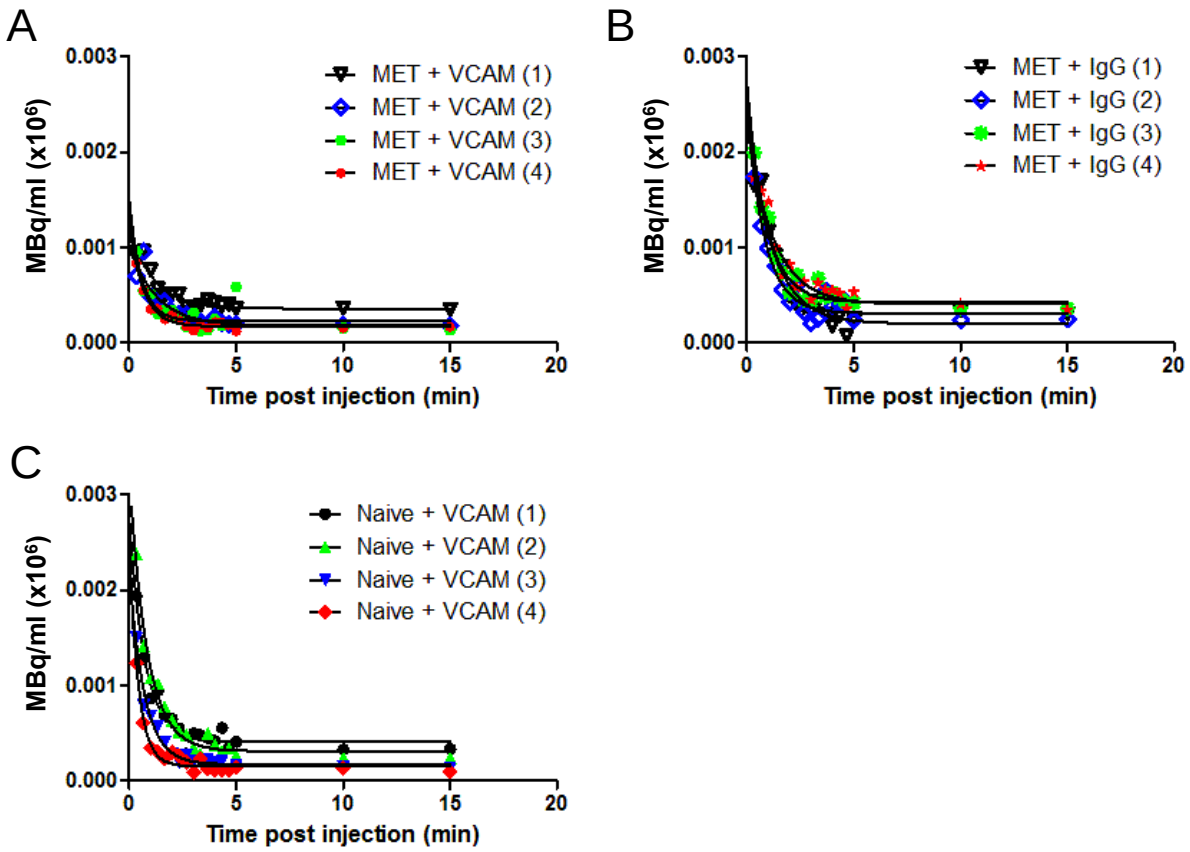



**Figure 4.12. Biological clearance determined from PET**. Activity uptake of segmented heart from (A) diseased and (B) naïve mice injected with [$^{89}$Zr]-DFO-VCAM-MPIO and (C) diseased mice injected with [$^{89}$Zr]-DFO-IgG-MPIO over time (n=4/group). Curves are fitted as single-phase exponential decays. (A-C) The half-life of [$^{89}$Zr]-DFO-VCAM-MPIO in diseased mice circulation is shorter compared to [$^{89}$Zr]-DFO-IgG-MPIO injected in diseased mice (mean ± SD, 38.02 ± 14.48 s *vs.* 43.21 ± 8.31 s) and longer when compared to [$^{89}$Zr]-DFO-VCAM-MPIO naïve mice (mean ± SD, 28.45 ± 7.27 s). Despite the small variations, the half-lives of all groups were statistically comparable (P = ns) and the mean all groups (mean ± SD, 36.56 ± 7.48 s) is in good correlation with the *ex vivo* measurement of biological clearance half-life of these particles from circulation (39.9 s ± 7.48 s; see section 4.3.8).

### 4.3.5 *Ex vivo* Biodistribution of [$^{89}$Zr]-DFO-VCAM-MPIO

In order to acquire more comprehensive biodistribution data for the radiolabelled VCAM-MPIO, a separate study was performed in which either [$^{89}$Zr]-DFO-VCAM-MPIO or [$^{89}$Zr]-DFO-IgG-MPIO was injected into metastasis-bearing or naïve animals (for this section we may also refer to the experimental groups as organ-MET+VCAM, organ-MET+IgG, organ-Naïve+VCAM and organ-Naïve+IgG, respectively). In this study, whole organs (heart, lungs, liver, spleen, stomach, pancreas, kidneys, small and large intestine) and samples of blood, muscle, skin, bone and fat from each mouse were isolated and activity measured using a gamma camera (n=4 per group). Figure 4.13 shows the % injected dose per mass of mouse organ (% ID/g) for all groups.

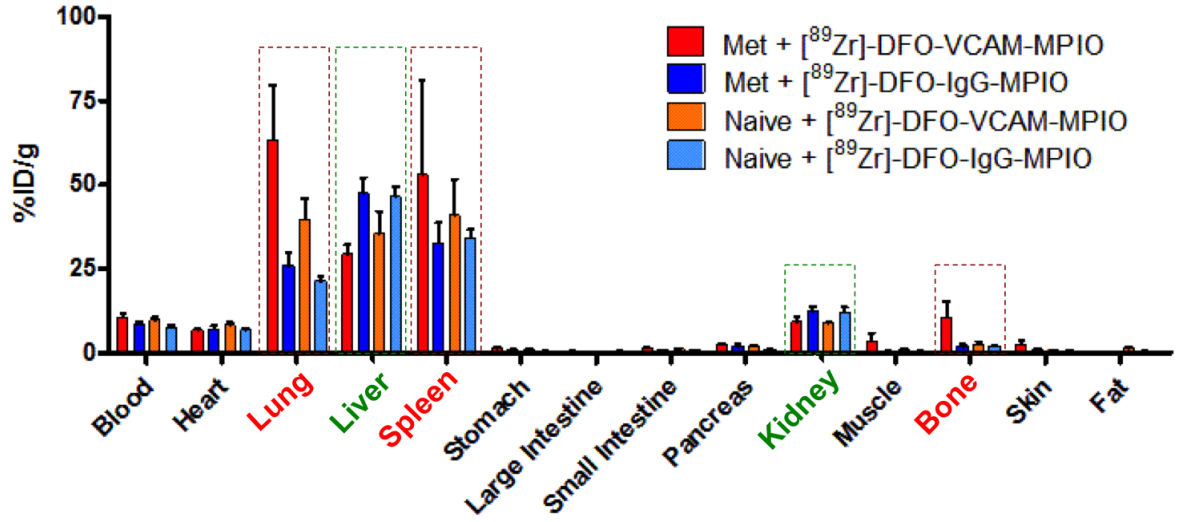



**Figure 4.13. Biodistribution of [$^{89}$Zr]-DFO-VCAM-MPIO.** Bar graph showing average % of injected dose per mass of organ for all groups. For lung, spleen and bone (red), significantly greater retention was found in the MET-VCAM (red) group compared to IgG controls (blue and cyan; $P<0.05$). For same organs, high %ID/g was also seen in the Naïve-VCAM (orange) group, but to a lesser extent than MET-VCAM, likely reflecting basal VCAM-1 expression. Uptake patterns in liver and kidney (green) support their role in scavenging of non-bound particles.

The diseased lungs injected with [$^{89}$Zr]-DFO-VCAM-MPIO yielded the highest % ID/g, out of all of the organs and all groups (lung-MET-VCAM, mean of % ID/g ± SD; 63.37 ± 32.50). One-way Anova in the lung group showed significantly different means ($P < 0.05$) and unpaired t-tests between lungs-MET-VCAM and lung-IgG groups revealed a significant difference only for lung-Naïve+IgG (21.49 ± 3.15, $P < 0.05$) and not for lung-MET+IgG (25.92 ± 8.06; $P = 0.06$). The Naïve+VCAM group also showed a high % ID/g (39.78 ± 12.45), but to a lesser extent than lungs from the MET-VCAM group.

Spleens excised from diseased mice injected with the targeted agent yielded the second highest % ID/g (spleen-MET+VCAM, mean % ID/g ± SD, 53.16 ± 55.91). A high level of VCAM-1 expression in the spleen is expected in the experimental mouse model used, since this is a multi-organ (lung, spleen, bone and brain at later time point) metastasis mouse model. Bone metastases were also indicated by the high % ID/g of the bone-MET-VCAM group (10.66 ± 9.04), which was 3-fold higher than the second highest % ID/g within the bone group (Naïve+VCAM, 2.60 ± 1.64).

From lung, spleen and bone a VCAM-1 positive group-pattern is evident; MET-VCAM showing the highest % ID/g followed by Naïve+VCAM and IgG groups yielding the lowest % ID/g. From liver and kidneys, which are organs known for their role in filtering blood and scavenging of MPIO, a negative VCAM-1 group pattern can be seen; low % ID/g of MET+VCAM and Naïve+VCAM groups and higher % ID/g in the IgG groups. Although the spleen has also been considered to be a contributor to scavenging of MPIO from the blood, the positive VCAM-1 group-pattern observed supports that the presence of metastases in the diseased groups out-weighs the spleen's scavenging role under non-diseased conditions. Nevertheless, the filtering of the MPIO is reflected in the % ID/g from the spleen-IgG groups

(spleen-MET+IgG, 32.73 ± 11.92; spleen-Naïve+IgG, 34.35 ± 5.03), which are the second highest IgG levels of % ID/g from all of the groups and organs.

### 4.3.6 Lung autoradiography

At the end of biodistribution experiment, one extra mouse per group was used for autoradiographic assessment. We may also refer for this section to groups as M-V for metastasis-bearing mice injected with [$^{89}$Zr]-DFO-VCAM-MPIO, M-I for metastasis-bearing mice injected with [$^{89}$Zr]-DFO-IgG-MPIO, N-V and N-I for naïve animals injected with [$^{89}$Zr]-DFO-VCAM-MPIO or [$^{89}$Zr]-DFO-IgG-MPIO, respectively; n=1). 72 h post lung excision, lung sections were placed in a phosphorous plate (5x M-V, 3x N-V, 2x N-I and 2x M-I; Figure 4.14 A) O/N for sufficient radiation yield. Figure 4.14 B shows the radiation yield from the lung sections as appear in Figure 4.14 A. In all M-V sections basal activity was evident across the whole lung, in addition to intense spots in discrete areas of the lungs. Little signal was seen in the M-I and N-I sections, whilst no signal was seen in N-V sections.
Subsequently, the sections were stained for VCAM-1 in order to confirm the source of the dark spots. Figure 4.15 shows representative metastases that correlated with dark spots, on the autoradiography film; strongly VCAM-1-positive vessels are evident in both cases.
The metastatic colony shown in Figure 4.15 A exhibited much stronger VCAM-1 expression on the associated microvasculature than the metastasis shown in Figure 4.15 B. The source of the dark spots on the autoradiographic plates appeared to be primarily the large number of [$^{89}$Zr]-DFO-VCAM-MPIO evident in the larger VCAM-1 positive vessels associated with the metastatic colonies (Figure 4.15 A-B, blown ups) rather than the particles seen actually within the metastasis itself (red arrows), presumably in the capillaries. In many cases the dark spots appeared to correlate with strongly VCAM-1 expressing vessels, as shown in Figure 4.16 A, with no apparently related metastatic colony. However, this may simply be an artefact of the analysis approach, since not all tissue sections were examined and there may be associated metastases through-plane in adjacent parallel sections. A complete correlation analysis was not performed between IHC sections and autoradiography, since the amount of work required for this assessment[3] made it unrealistic within the time frame of completing the thesis. However, it is acknowledged that this analysis would provide a deeper understanding of the retention of [$^{89}$Zr]-DFO-VCAM-MPIO on metastasis associated inflamed vasculature.

[3] Multiple consecutive sections are required for full assessment of the correlation between IHC treated sections and autoradiography, in order to determine if there are micrometastases in the z direction associated with these inflamed vessels. Therefore, a great number of sections across the whole lung (or n=3 mice), would be required for positive correlation between IHC and autoradiography. Owing to the nature of this work, the time required is estimated to be 2 months of dedicated work.

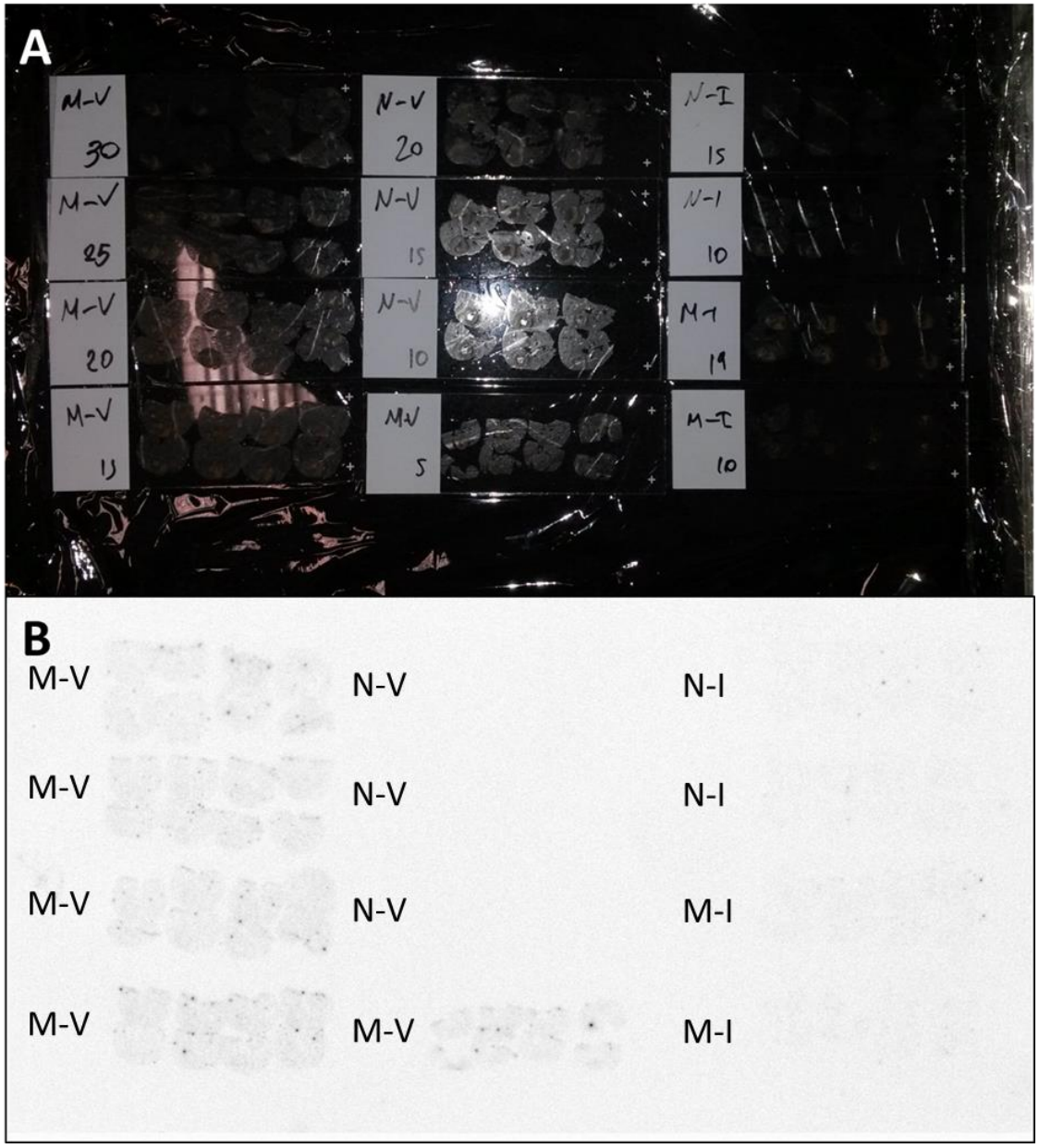



**Figure 4.14. Autoradiography of lung tissue.** (A) Photograph showing the orientation of slides during the autoradiography exposure: 5 slides of metastases bearing lungs + [$^{89}$Zr]-DFO-VCAM-MPIO (M-V), 3 slides naïve lungs + [$^{89}$Zr]-DFO-VCAM-MPIO (N-V), 2 slides of metastases bearing lungs or 2 slides of naïve lungs + [$^{89}$Zr]-DFO-IgG-MPIO (M-I and N-I, respectively). (B) Autoradiography images of lungs data from the slides as shown in (A) O/N. M-V slides showed sparse basal activity in all areas of the lung sections and localized intense signal (dark spots). The rest of the group yield no or minimal activity.

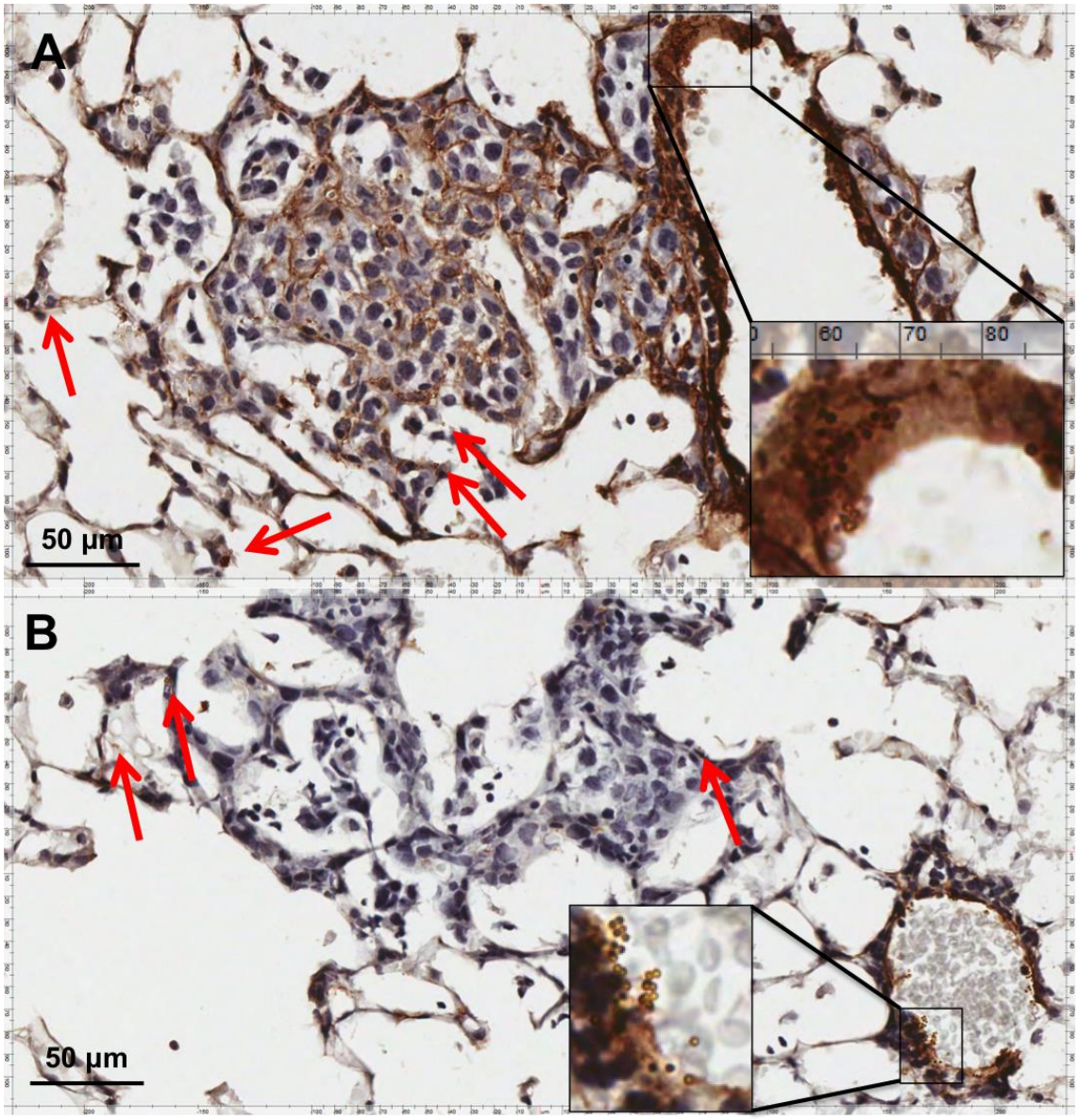



**Figure 4.15. Correlation of [$^{89}$Zr]-DFO-VCAM-MPIO with micrometastasis.** (A-B) Bright field micrographs of immunohistochemically stained for VCAM-1 expression (brown) and nuclei (blue) of lung sections used for autoradiography. The metastases shown in both (A) and (B) correlate with strong signal from the autoradiography. The micrometastasis of (A) has greater cell density and VCAM-1 expression than the micrometastasis shown in (B). Both main vessels in (A) and (B) show the same strength of VCAM-1 expression. The [$^{89}$Zr]-DFO-VCAM-MPIO evident on micrometastasis burden (red arrows) is insignificant compared to the [$^{89}$Zr]-DFO-VCAM-MPIO seen on the metastasis-induced VCAM-1 activated nearby vessels.

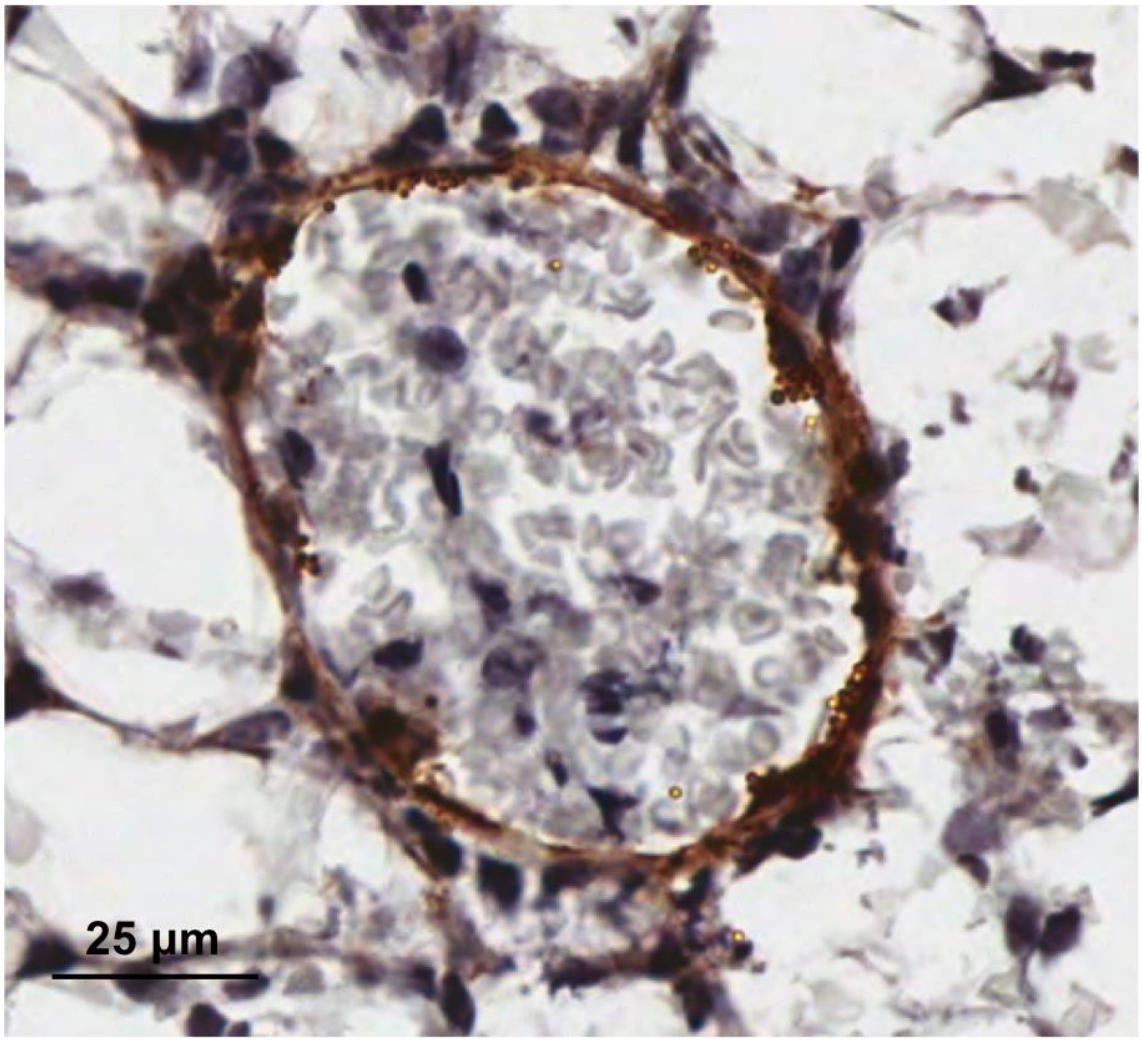



**Figure 4.16. VCAM-1 activated vessel with no apparent metastasis on tissue section.** Bright field micrograph immunohistochemically stained for VCAM-1 expression (brown) and nuclei (blue) lung section. This is a representative vessel that correlates with autoradiography but with no evident micrometastasis association. Great number of [$^{89}$Zr]-DFO-VCAM-MPIO is evident on the inflamed endothelium.

## 4.4 Discussion

To date there are no reported clinical or pre-clinical *in vivo* methods that can detect lung metastases with metastatic cross-sectional range comparable to the size of metastases detected in our work; mean cross section diameter 130 µm. The most widely used conventional CT in the clinic provides 1-2 mm resolution and is the most sensitive lung imaging method to date. The majority of lung metastasis cases are diagnosed from CT and for the most patients the number of metastases is large (poly-metastasis), with metastasis sizes indicting that the disease is well beyond the initiation (extravasation) stage. The ultimate goal of this work was to provide an *in vivo* method that can detect pulmonary micrometastasis much earlier than any other pre-clinical or clinical conventional *in vivo* method, on the

assumption that the earlier the detection of disease the wider the window for therapeutic intervention.

In this work I have demonstrated utility of a micron size iron oxide particle that provides rapid biological clearance from the blood stream, coupled with sufficient and rapid adherence on VCAM-1 activated endothelium, to enable early detection of micrometastasis. Owing to the rapid clearance imaging can happen within a short time frame (10-40 min) after the administration.

In this chapter I have demonstrated the limitations of bright lung MRI for detection of VCAM-MPIO in metastasis-bearing lungs. In contrast, the use of [$^{89}$Zr] radiolabelled VCAM-MPIO enabled quantifiable *in vivo* PET detection of lung micrometastasis early in the development of the disease.

In the first instance I hypothesized that it would be possible to use the potent negative susceptibility effect of the MPIO to detect lung micrometastasis using a novel bright lung MRI approach. However, on completion of the hyperpolarised *in vivo* work it was evident that the number of accumulated MPIO is not sufficient to dephase the HP gas signal to a detectable level. On further consideration of the report published previously by Branca *et al*, I concluded that this may be misleading. In that paper, the authors present compelling data demonstrating that the negative contrast effect on HP $^{3}$He from nanoparticles of iron oxide (NPIO) accumulation in the lymph node is sufficient to perturb the signal in the top lobe of the lung (Figure 4.17). Subsequently, in the second part of that paper the authors present a proof-of principal figure (Branca *et al*, 2010, Figure 4-5), from a single animal, in which the absence of signal in the top cranial lobe of the lung is attributed to the presence of metastasis associated NPIO (Figure 4.18). However, from the studies performed at Duke University in the course of this DPhil, we have been able to demonstrate similar losses of signal in the same cranial lung lobe as a consequence of imperfect inflation (Figure 4.19). We assume that the phenomenon arises from the misplacement of the tracheal tube, which shifts closer to the tracheal junction. The pressure of the gas from the ventilation increases at the junction and there is a possibility that this hinders infusion of the cranial lobe. We would also expect that any dephasing caused by NPIO would have a spherical partial volume effect as seen in Figure 4.17, rather than complete signal loss across the entire lobe. Consequently, with the experience gained in lung inflation and MPIO de-phasing it now seems likely, in looking at Figure 4.18, that in the study of Branca *et al* the whole lobe is lacking in signal as a result of imperfect ventilation of this lobe with HP gas and not owing to metastasis-induced NPIO accumulation.

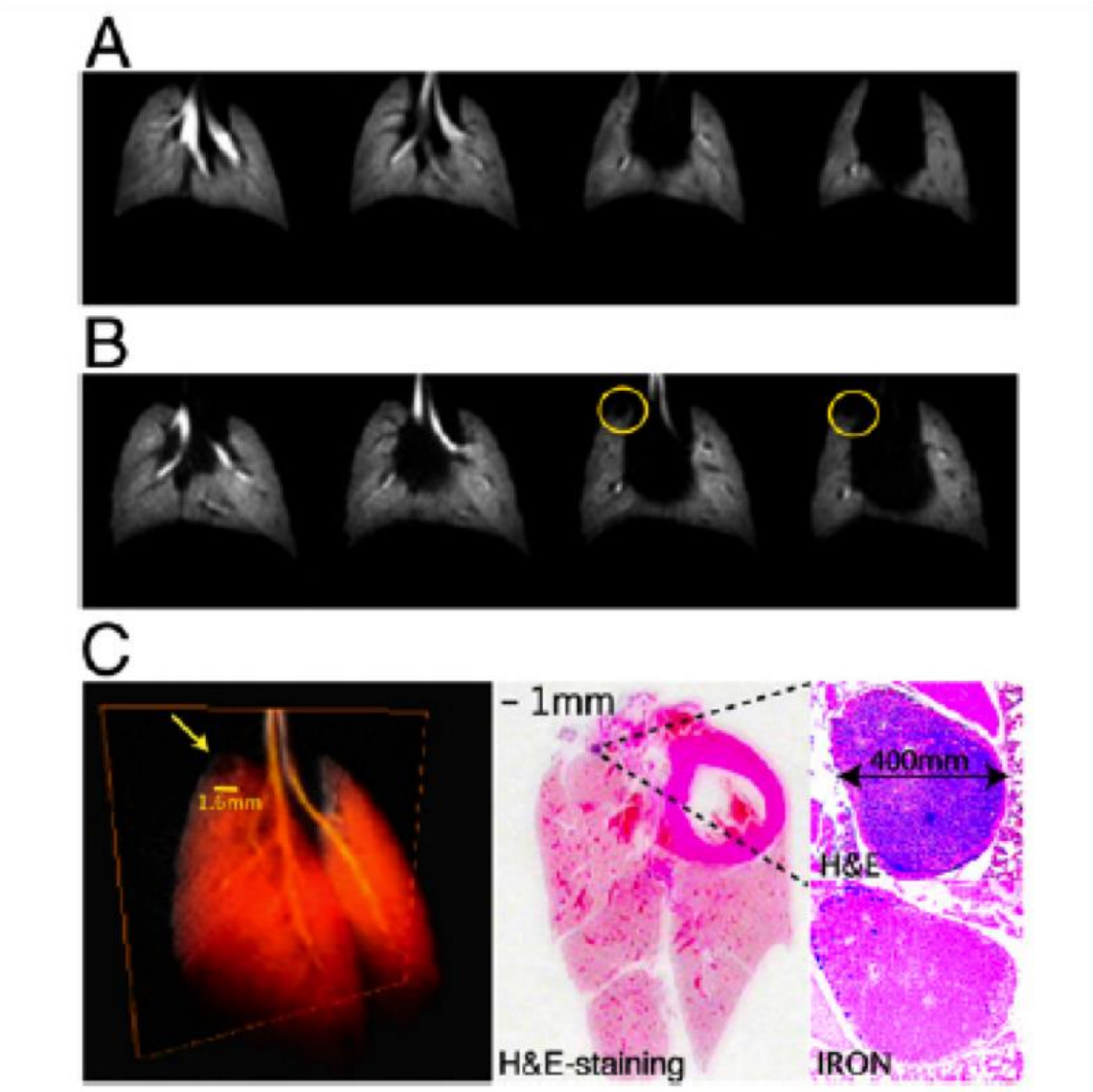



**Figure 4.17. Figure 2 as presented in Branca *et al*, 2010.** (A) HP $^{3}$He in vivo lung imaging of naïve animals, showing 4 sagittal planes. (B) HP $^{3}$He in vivo lung imaging of diseased animals, showing 4 sagittal planes. There is a small de-phasing effect on the top left lobe (yellow circle). (C) 3D representation of the lungs shown at B with indication of the hypointensity effect. On the right are histology micrographs with Prussian blue, showing the lymph node next to the lung lobe that shows the hypointensity.

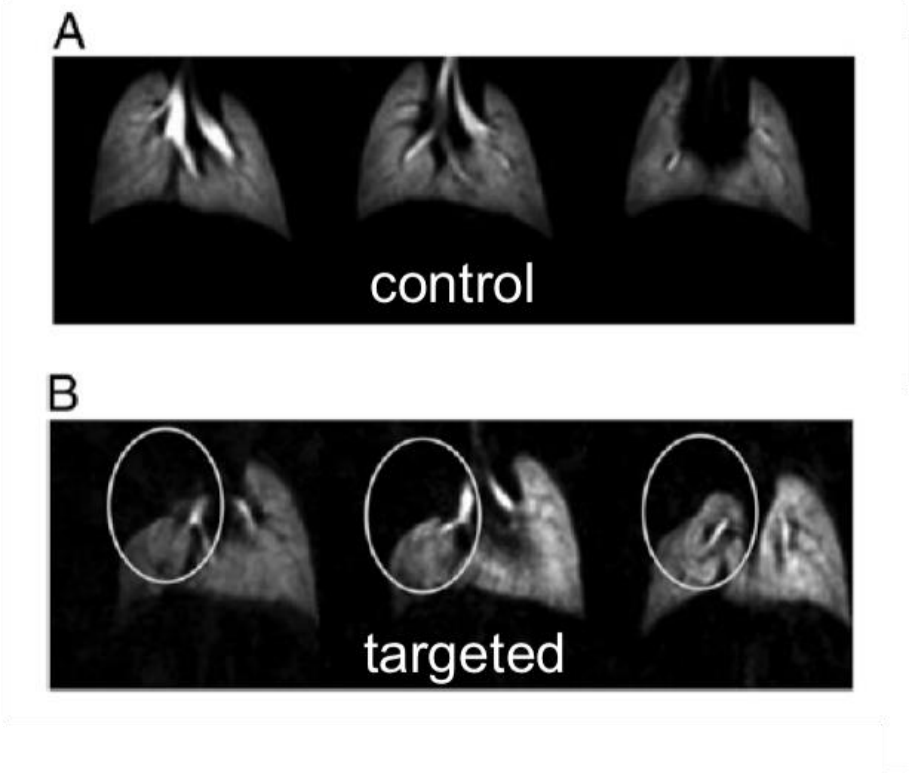



**Figure 4.18. Figure 4 as presented in Branca *et al*, 2010**. (A) HP $^{3}$He in vivo lung imaging of naïve animals, showing 3 sagittal planes. (B) HP $^{3}$He in vivo lung imaging of diseased animals, showing 3 sagittal planes. In this work, the authors claimed that the missing right cranial lobe (white circles) have been caused from the accumulation of NPIO on the micrometastases contained in the lobe.

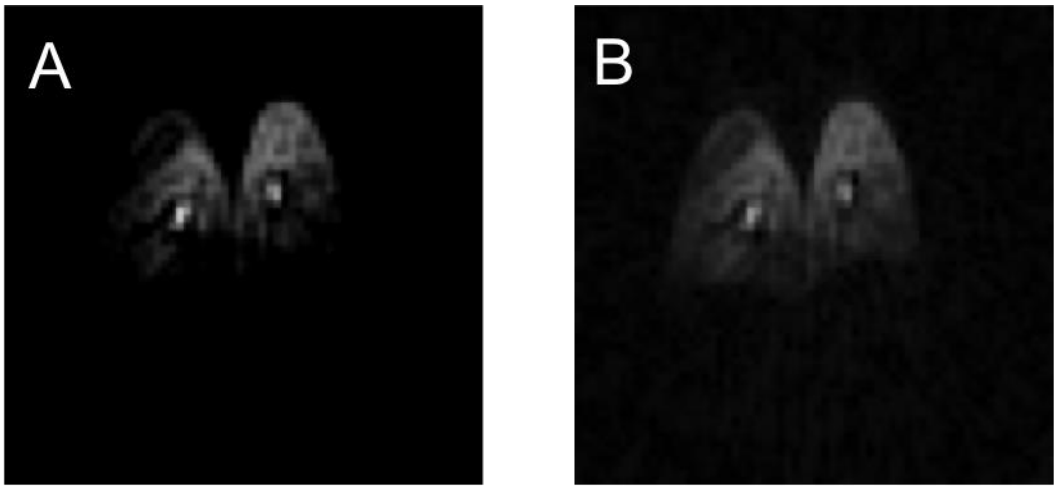



**Figure 4.19. Imperfect HP $^{3}$He ventilation-inflation on the cranial lobe, from a control group.** (A) Single slice of lateral HP gas lung 3D MRI showing negative intensity artefact from imperfect ventilation. (B) A stack image of 9 slices alongside (A) from the same dataset.

In the second instance I hypothesized that alternative bright lung fluorinated MRI would allow detection of the potent negative susceptibility effect of the MPIO. Through our *post mortem* work with fluorinated gases and liquids it was concluded that it is not possible to reduce the signal from fluorinated contrast agents sufficiently for detection at the MPIO concentrations used in our protocol. As demonstrated in the phantom experiments, higher concentrations of MPIO do indeed reduce the signal from fluorinated gases and liquids, but these are concentrations far beyond those required for specific detection of micrometastases in the lungs. Furthermore, although I am convinced that manual inflation of the lungs has been adequate for the proof-of-principal experiments described here, this is not a robust technique for quantification, and a controlled ventilation gas or liquid method would be required for further in-depth investigation of bright lung fluorinated MRI.

Given the limitations encountered with bright lung MRI, I next considered PET as an alternative imaging modality. Owing to the greater sensitivity of PET compared to MRI, I hypothesised that this would be sufficient for enabling detection of even a small number of MPIO. To this end the MRI contrast agent was radiolabelled thus retaining the advantages of MPIO but gaining the sensitivity of PET. The [$^{89}$Zr] radioisotope, is a useful radioisotope owing to its long half-life, which allows for concomitant histological and autoradiographical correlation (fixation and cryo-protection requires 72 h). The proof-of-principal *in vivo* detection of pulmonary micrometastasis presented here, could also be performed using a different positron emitter or gamma emitters for SPECT modality detection.

Following radiolabelling of VCAM-MPIO I tested the binding characteristics of [$^{89}$Zr]-DFO-VCAM-MPIO *in vitro* and demonstrated that the radiolabelling did not affect the previously shown binding specificity in Chapter 3. Subsequently, I tested my hypothesis for PET detection of micrometastasis using [$^{89}$Zr]-DFO-VCAM-MPIO *in vivo* and demonstrated quantifiable, sensitive and specific detection of micrometastatic development in the lungs. Administration of [$^{89}$Zr]-DFO-VCAM-MPIO into mice containing pulmonary metastases allowed for accurate identification of mice with pulmonary micrometastasis. The agent had rapid uptake (< 5 min) in all organs and it was predominantly accumulated in the liver and spleen, providing rapid clearance of the agent from the blood circulation (< 1 min). Micrometastases containing lungs could be identified by volumetric quantitation of radioactivity within the first 10 minutes after administration of the contrast agent. Specific binding of the agent on single micrometastasis could not be visible on PET images, therefore, I cannot exclude the possibility of detecting the volumetric effect of many metastases in the lungs. It is unclear weather a single metastasis of the size reported in this work could provide enough detectable signal.

From autoradiography and concomitant immunohistochemical staining, I confirmed the co-localisation of [$^{89}$Zr]-DFO-VCAM-MPIO in VCAM-1 activated microvasculature of micrometastatic colonies and the radioactivity signal detected by autoradiographic assessment. Similarly, I co-localised specific binding of [$^{89}$Zr]-DFO-VCAM-MPIO to VCAM-1 positive main vessels with no evident micrometastasis association (Figure 4.17). Since only representative sections were assessed for correlation of autoradiography with immunohistochemistry there is no way to know if the VCAM-1 positive main vessels that show high retention of [$^{89}$Zr]-DFO-VCAM-MPIO, with no evident association to micrometastatic colonies, are strongly related with developed micrometastatic colonies in

consecutive sections or are related with an earlier stage of micrometastatic development (invasion). If these highly activated vessels are not related to nearby micrometastasis then I can hypothesize that either there is a systemic pulmonary inflammation due to micrometastases in the lungs or there is a tumour self seeding process that activates the vessels locally. Immunohistochemical observations, does not support the systemic pulmonary hypothesis because distant vessels from apparent micrometastasis (100-200 μm away from the center of micrometastasis) were not VCAM-1 positive. Therefore, given the early upregulation of VCAM-1 in the specified pulmonary metastasis mouse model [290], I cannot exclude the possibility that the method presented in this Chapter could be sensitive enough to detect volumetrically an earlier stage of pulmonary metastasis development (invasion).

Subsequently, I confirmed autoradiographic and immunohistochemical findings with an *ex vivo* biodistribution study, in which I also was able to show [$^{89}$Zr]-DFO-VCAM-MPIO uptake in spleen and bone indicating that these organs also containing micrometastasis, as is known to be the case for this metastatic mouse model. Finally, in the course of this work, to identify a suitable imaging modality for VCAM-MPIO detection in metastatic lung, I have constructed a dual modality PET/MRI probe that has the potential not only to enable rapid PET detection of lung micrometastasis *in vivo*, but also metastases in other organs via $T_2$*-weighted MRI. Considering the positive uptake of [$^{89}$Zr]-DFO-VCAM-MPIO in spleen and bone, I believe that the [$^{89}$Zr]-DFO-VCAM-MPIO within these organs could be detected by $T_2$* weighted MRI, and the parent VCAM-MPIO agent has already been demonstrated to detect micrometastases in brain. The fact that PET can confirm lung detection in a very short time frame makes concomitant MRI assessment a realistic possibility, within a short time frame after PET imaging (~30 min).

A substantial number of cancer patients develop multi-organ metastases and to date whole body PET/CT and SPECT/CT is the standard clinical tool for the assessment of this cases. However, these modalities can only provide anatomical information from the CT and are completely lacking in structural and soft tissue information. Additional MRI in many of these cases is required for the management of treatment, owing to the excellent soft tissue contrast and structural information provided. The newly developed probe I have presented in this work has the potential to allow PET/CT/MRI screening in a single assessment, providing detection of lung metastasis much earlier than conventional PET/CT and possibly multi-organ (spleen, bone and brain) micrometastasis by MRI.

# Chapter 5 – *In vivo* MRI characterisation of angiogenesis in s.c. tumour models

## 5.1 Introduction

In the previous chapter I discussed the fact that there is a commercially available binding peptide sequence for VCAM-1. The VCAM-1 binding peptide VHPKQHRGGSKGC has a significantly lower molecular weight than the full anti-VCAM-1 antibody (1390 and 84,000 Da, respectively). Such peptides have been used as ligands with nano-sized particles, which have a significantly lower weight than MPIO. However, a reasonable concern in using conjugates of peptides with micron-sized particles that the long-term binding characteristics of the contrast agent on the endothelial target could be affected from the significantly large MPIO, from increased mechanical forces. Therefore, in the following paragraphs the affinity of peptides and their potential to be efficient ligands for molecularly targeted imaging with micron-sized particles will be discussed in the context of angiogenesis imaging.

Angiogenesis, the formation of new blood vessels from pre-existing vessels, is required for tumour growth, development and metastasis [312-314] and, consequently, is a target for cancer therapy [315]. Therefore, the ability to localise and quantify angiogenesis has considerable importance for directing treatment selection and monitoring response to therapy.

Expression of the integrin $\alpha_v\beta_3$, also known as vitronectin receptor[316] is characteristic of angiogenesis, in which it plays a key role in endothelial cell proliferation, adhesion, and survival [317]. Whilst expression of $\alpha_v\beta_3$ is particularly strong on activated endothelial cells of angiogenic blood vessels, it is weak on normal, non-angiogenic blood vessels [318]. Moreover, clinical studies have identified $\alpha_v\beta_3$ as a biomarker of malignancy and its expression correlates with tumour grade [319, 320]. Accordingly, $\alpha_v\beta_3$ has become an important target for molecular imaging of angiogenesis [178, 321].

Physiologically, $\alpha_v\beta_3$ mediates cell adhesion to extracellular matrix proteins, such as fibronectin and collagen, by binding to the conserved amino acid sequence Arginine-Glycine-Aspartic Acid (RGD) [322, 323]. The RGD-binding site is located at the interface between the β-propeller domain and the β I-like domain, where amino-acid residues from the two domains interact directly with the RGD peptide [324]. Initial reports of radiolabelled RGD probes for clinical and preclinical PET or SPECT imaging of $\alpha_v\beta_3$ expression were published over a decade ago [325, 326]. Despite this, progress has been relatively slow, most likely as a consequence of the complex multi-step radiochemistry required for many such agents. At the same time, the relatively poor spatial resolution of PET/SPECT imaging remains a hurdle, particularly in assessing tumour vasculature heterogeneity at the micron size scale. In contrast, MRI yields high spatial resolution and excellent soft tissue contrast without the need for ionising radiation. Moreover, MRI also allows for concomitant angiography and perfusion acquisitions. Paramagnetic contrast agents (e.g. containing gadolinium) targeted to endothelial $\alpha_v\beta_3$ via monoclonal antibodies [178] or peptidomimetics [180] have been used

previously to image tumour angiogenesis [327], as have gadolinium-based lipidic nanoparticles encapsulating fluorescent dyes using RGD as a ligand [182, 183]. However, the MRI contrast effect conferred by gadolinium-containing contrast agents is relatively low. Consequently, interest has also extended to ultrasmall superparamagnetic particles of iron oxide (USPIO; diameter < 100 nm), which yield considerably greater contrast effects than gadolinium-based agents. More recently, USPIO conjugated with RGD peptides have been used to target $\alpha_v\beta_3$ integrin expression on tumour cells or on the tumour vasculature [184, 328, 329].

Despite the improved sensitivity of nanoparticles of iron oxides (NPIO < 500 nm) several issues remain including the possibility of non-specific extravasation [184, 328, 329], long blood half-life (reducing specific contrast) and low targeting valency. In contrast, microparticles of iron oxide (MPIO; diameter > 1 μm) have a short half-life in the circulation (< 5 min) [330] together with considerably greater surface area, which can increase binding affinities through multivalency effects [331]. Moreover, the higher iron content of MPIO, compared to NPIO, yields a substantially higher contrast-to-noise ratio per particle, with a dephasing effect approximately 50 times their physical diameter [332]. In addition, whilst NPIO can extravasate from leaky angiogenic vessels, potentially compromising molecular specificity through passive tissue retention, the relatively large MPIO are obligate intravascular agents. Indeed, the potential of MPIO for molecular imaging, has been demonstrated in numerous animal models of human disease [186-195]

Whilst the relatively large size of such microparticles brings many positive characteristics for imaging purposes (above), their buoyancy in flowing blood means that to achieve effective retention at sites of interest, the target-ligand interaction must be, not only specific, but also of high affinity [333].

In this study we have used a cyclic RGD variant [c(RGDyK)] that has been previously generated in order to increase the effective affinity to $\alpha_v\beta_3$ integrin and was subsequently coupled with 2.8 μm outer diameter commercially available MPIO's (Figure 2.2). The contrast agent was provided from Dr Xiaoyuan Chen[4] to Prof Robin Choudhury's laboratory[5] for preliminary *in vitro* testing. The binding characteristics of c(RGDyK)-MPIO to $\alpha_v\beta_3$-expressing endothelial cells were tested under static and flow conditions *in vitro* and quantified prior to this work[6].

[4] Laboratory of Molecular Imaging and Nanomedicine (LOMIN), National Institute of Biomedical Imaging and Bioengineering (NIBIB), National Institutes of Health (NIH), Bethesda, Maryland 20892, United States.

[5] Division of Cardiovascular Medicine, Radcliffe Department of Medicine, University of Oxford, John Radcliffe Hospital, Oxford, OX3 9DU, United Kingdom.

[6] Since to date this work has not been published, the *in vitro* results and methods will be included in this thesis for completion.

The aim of the current study, therefore,was to determine the efficacy of RGD-targeted MPIO for detection of angiogenic tumour vessels *in vivo.* To this end the MRI contrast effects of c(RGDyK)-MPIO were tested and quantified in two separate subcutaneous animal models of colon carcinoma and melanoma derived tumours, respectively.

## 5.2 Materials and Methods

### 5.2.1 RGD-MPIO Synthesis

Cyclic RGD and RAD based peptides [c(RGDyK) / c(RADyK)] (CS Bio, Menlo Park, CA) were coupled to 2.80 µm Dynabeads (M-270 amine, Invitrogen) according to a protocol provided by the manufacturer. Dynabeads (100 µl) were first suspended in phosphate buffered saline (PBS) (pH 7.4). A heterodimer crosslinker, 4-maleimidobutyric acid N-hydroxysuccinimide ester (75 µg), was added to the solution. The mixture was incubated for 30 min at room temperature with slow tilt rotation. After incubation, a magnet was placed to the tube to collect the beads, and the supernatant was removed. The beads were washed twice with PBS and resuspended in 100 µl of PBS. c(RGDyK) / c(RADyK) peptides were thiolated as described previously [334] and the thiolated c(RGDyK) / c(RADyK) (200 µg) was added to the Dynabead solution. The mixture was incubated for 1 h at room temperature with slow tilt rotation. After 1 h, cysteine was added to a final concentration of 5 mM, and the mixture was incubated for another 15 min at room temperature to quench non-reacted groups. The beads were then washed with PBS twice. The final products were resuspended in PBS.

### 5.2.2 Assessment of peptide-loading

Peptide loading of c(RGDyK)-MPIO and c(RADyK)-MPIO was determined by flow cytometry analysis. The aspartic acid residue of the peptide was fluorescently labelled in a two step protocol consisting of the activation of the free carboxylic acid by EDC and further reaction of the activated ester with a fluorophore containing a primary amino group (Alexa Fluor 647 cadaverine). When labelled in such way each RGD unit contains one fluorophore. Quifikit calibration beads were used as reference and labelled with a secondary antibody containing 5 fluorophores per protein. Briefly, 10 µg c(RGDyK)- or c(RADyK)-MPIO were diluted in 1 mL of MES buffer 15 mM pH 6.0, pelleted on a Dynal magnetic separator (Invitrogen, UK) and redispersed in 200 µL EDC (Sigma Aldrich, UK) solution (10 mg/mL) in MES buffer 15 mM pH 6.0. The sample was shaken at 1000 rpm for 10 min, pelleted, washed with cold water and then redispersed in 200 µL of MES buffer 15 mM pH 6.0. Subsequently, 2 µL of Alexa Fluor 647 cadaverine disodium salt (2 mg/mL; Invitrogen, UK) was added. The sample was shaken for 24 h, pelleted in a magnet, washed 3 times with 1 mL of PBS + 0.1 % tween 20 and redispersed in 400 µL of PBS. Qifikit calibration beads (Dako, UK), used as a reference, were prepared according to the manufacturer's protocol, but substituting the provided fluorescently-conjugated antibody with Alexa Fluor 647 goat anti-

mouse IgG (H+L) (Invitrogen, UK). Flow cytometry experiments were performed on a BD FACScalibur flow cytometer using channel FL4.

### 5.2.3 RGD-MPIO binding in vitro

In order to assess $\alpha_v\beta_3$-integrin expression, human umbilical vein endothelial cells (HUVEC)-C were seeded onto glass coverslips in 12-well plates to a final density of 4 x $10^5$ per well, in Media 199 supplemented with 10% fetal calf serum, penicillin and streptomycin (100 µg/ml). HUVEC-C cells were treated with PBS control or 100 µM S-nitroso-n-acetylpenicillamine (SNAP) (Alexis Corp., San Diego, CA, USA) for 20 h at 37 °C to induce endothelial $\alpha_v\beta_3$-integrin expression [335]. Cells were then fixed with 4% PFA, washed, and stored in PBS. Coverslips were blocked with 3% bovine serum albumin (BSA) in PBS with 0.01% Tween-20 for 60 min at room temperature. Following blocking, coverslips were incubated with antibodies against one of: either $\alpha_v\beta_3$-integrin (Clone 21 / CD51. BD Bioscience Oxford, UK); VCAM (Clone 1G11B1, Abcam, Cambridge UK) or PECAM-1 (Clone 9g11 R&D Systems). Following overnight incubation, cells were washed and then incubated with goat anti-mouse AlexaFluor 488 (for VCAM-1 and PECAM-1) or AlexaFluor 594 (for $\alpha_v\beta_3$-integrin) in the dark for 30 min at 37 °C. Finally, coverslips were washed and counterstained with 4',6-diamidino-2-phenylindole (DAPI) and mounted onto glass slides and stored in the dark at 4°C. In order to quantify immunofluorescence, automated colour based segmentation was applied to coverslips stained for $\alpha_v\beta_3$-integrin, using ImagePro Plus (Media Cybernetics, Rockville, Maryland, USA).

Following blocking, coverslips were incubated with antibodies against one of: either $\alpha_v\beta_3$-integrin (Clone 21 / CD51. BD Bioscience Oxford, UK); VCAM (Clone 1G11B1, Abcam, Cambridge UK) or PECAM-1 (Clone 9g11 R&D Systems). Following overnight incubation, cells were washed and then incubated with goat anti-mouse AlexaFluor 488 (for VCAM-1 and PECAM-1) or AlexaFluor 594 (for $\alpha_v\beta_3$-integrin) in the dark for 30 min at 37 °C. Finally, coverslips were washed and counterstained with 4',6-diamidino-2-phenylindole (DAPI) and mounted onto glass slides and stored in the dark at 4°C. In order to quantify immunofluorescence, automated colour based segmentation was applied to coverslips stained for $\alpha_v\beta_3$-integrin, using ImagePro Plus (Media Cybernetics, Rockville, Maryland, USA).

### 5.2.4 Animal tumour models

Female, C57Bl/6 mice (n = 26; Charles River, UK) were housed in ventilated cages with a 12-hour light / dark cycle and controlled temperature (20-22°C), fed normal chow and given water *ad libitum*. 7-10 week old mice were anesthetised with 2-3% isoflurane (IsoFlo) in $O_2$ and injected subcutaneously in the right upper flank with either 5 x $10^4$ B16F10 mouse melanoma cells (n = 10), or 5 x $10^4$ MC-38 mouse colon carcinoma cells (n = 16) in 100 µl sterile PBS. Tumours were allowed to grow for either 21 days to achieve tumour volumes < 400 $mm^3$ (n =20), or 28 days for tumour volumes > 400 $mm^3$ (n = 6). All experiments were approved by the UK Home Office.

### 5.2.5 In vivo experimental protocol

For imaging, mice were anaesthetised with 2-3% isoflurane in room air and a tail vein cannulated for contrast agent administration. Anaesthesia was maintained with 1-2% isoflurane in room air thereafter. Core temperature was monitored and maintained at 36 °C with a homeothermic system (Harvard Instruments, Edenbridge, Kent, UK). Respiratory gating was achieved using a pressure balloon, placed in contact with the chest, that was interfaced to a signal processing unit (MP150 unit, Biopac Inc, California, USA) and trigger control unit (DTU200, Biopac Inc).
For each animal, a $T_2$*-weighted 3D dataset was acquired prior to contrast agent administration and again 30 min after injection. After the initial acquisition, the coil was removed from the magnetic field with the cradle at fixed position, while anesthesia and monitoring was maintained. The contrast agent was administered intravenously while the mice remained within the coil to enable co-registration of pre- and post-contrast images. Mice were injected with 100 µl of either c(RGDyK)-MPIO or the control c(RADyK)-MPIO at a concentration of 4 mg Fe/kg body weight. Dynamic contrast enhanced (DCE) MRI was performed at the end of each imaging protocol with 30 µl gadolinium-DTPA (Omniscan; 0.5 mmol/ml) injected intravenously during the scan (Figure 5.1).

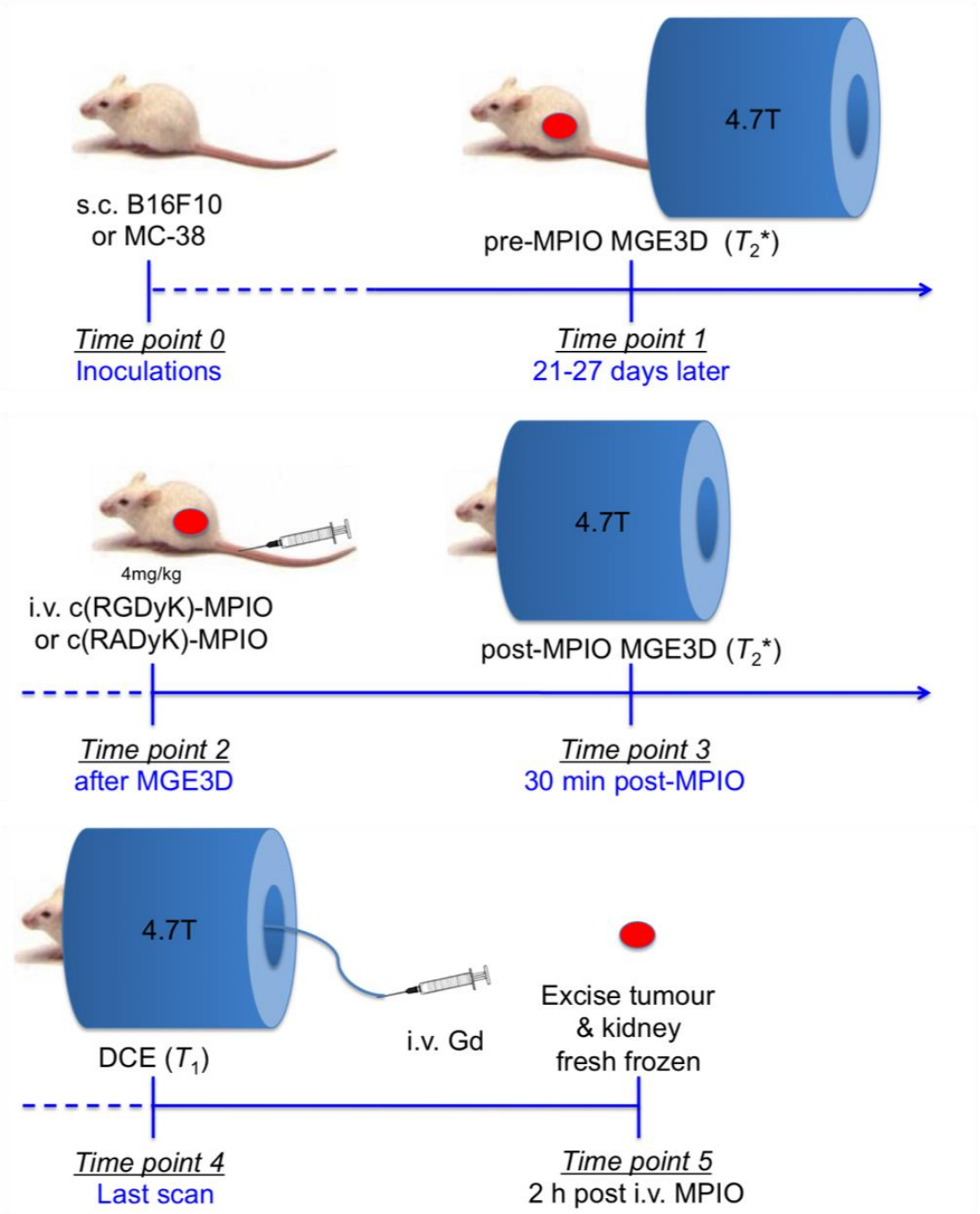



**Figure 5.1. Schematic diagram of the *in vivo* experimental MRI protocol.** Timeline of *in vivo* experimental protocol from tumour inoculation to tumour excision.

### 5.2.6 In vivo Magnetic Resonance Imaging

All MRI data were acquired using a 4.7 T horizontal bore magnet (Agilent Technologies, Santa Clara, CA, USA) using a 25 mm quadrature birdcage coil (Rapid Biomedical, Wurzburgy, Germany). For detection of MPIO, a respiratory-gated, fat-suppressed, 3D multi-gradient echo, $T_2$*-weighted acquisition was performed with TE = 3.33, 7.82, 12.31 and 16.8 ms; TR = 40ms; nominal flip angle = 16°; field of view (FOV) 54 x 27 x 27 mm giving an isotropic resolution of 150 μm. For DCE MRI, a respiratory-gated 3D gradient echo, $T_1$-weighted acquisition was performed with TE = 0.55 ms, TR = 1.1 ms, nominal flip angle = 5°, FOV = 54 x 27 x 27 giving an isotropic spatial resolution of *ca.* 412 μm in a scan time of *ca.* 10 s/frame. 100 frames were acquired with contrast agent infused (Omniscan, 30 μL) over the duration of frame 11/100. Respiratory gating to eliminate residual motion artefacts, whilst maintaining constant $T_1$-weighting throughout the scans, was achieved by only acquiring data during the respiratory plateau period [283]. $B_1$ inhomogeneity was corrected for using a respiratory-gated implementation of the Actual Flip angle Imaging technique [284] performed with TE = 0.59, TR = 20, 100 ms, nominal flip angle = 60°, covering the same FOV as the DCE scan, but at half the resolution in each of the phase encode directions, to give a spatial resolution of *ca*. 400 x 800 x 800 μm in a scan time of approximately 4 min. $T_1$ was estimated using the same scan parameters as for the DCE acquisition, but with an array of flip angles (1-6°) in a scan time of approximately 1 min. Both $B_1$ correction and $T_1$ mapping were performed prior to the DCE scan to avoid confounding arising from gadolinium washout.

### 5.2.7 MRI data analysis

#### *5.2.7.1 Static $T_2$*-Weighted dataset*

5.2.7.1.a Hypointensity Volumes

To calculate the volumes of MPIO-induced hypointensities an automated computational method was used to determine hypointensities based on local contrast levels (Hamilton A., DPhil Thesis 2013, Oxford University). To this end, the signal intensity of each individual voxel was statistically compared with the intensity distribution of all surrounding voxels within a 5x5x5 (voxel) volume, to determine whether it was significantly lower than the average local signal intensity. To segment true MPIO-induced hypointensities in this way, a threshold value was set at a fraction of the local mean (FLM) signal intensity. The optimal FLM was found to be dependent on tumour type, owing to differences in the global signal intensity distributions; where there are more natural hypointense regions within the tumour (e.g. melanoma) these will be delineated incorrectly with a higher FLM. By assessing a range of FLM values it was possible to determine optimal FLM values that did not return regions of natural hypointenisty (i.e. observed in the pre-injection datasets). On this basis, FLM values of 0.45 for the melanoma model and 0.65 for the colorectal model were found to be optimal.

Below these thresholds voxels were designated as MPIO-induced hypointensities (Figure 5.2). A margin parameter (2 voxel radius excluded in all directions) was applied at the edge of the segmented tumour volumes in order to minimise false counts due to minor segmentation errors. Any independent hypointensity volumes larger than 20 voxels were excluded from the analysis as these reflected pre-existing tumour local inhomogeneities (i.e. present in pre-contrast images), although optimization of the FLM minimised inclusion of such regions in the segmented datasets (Figure 5.3). 3D reconstructions of MPIO induced hypointensities were created using 3D Slicer 4.3.1 (2013) (http://www.slicer.org). Pairwise statistical comparisons were made between pre- and post-contrast datasets using paired t tests. Unpaired t tests were used to compare between groups (Figure 5.4 A-B).

#### 5.2.7.1.b Mean Intensities

To calculate the mean tumour intensities, the 3D segmented volumes averaged over the 4 echoes (as described above 5.3.7.1.b) were used. All voxel gray intensity values were averaged to a single mean per tumour and further normalized over the tumour volume. Pairwise statistical comparisons were made between pre- and post-contrast datasets using paired t tests. Unpaired t tests were used to compare between groups (Figure 5.4 A, C).

#### 5.2.7.1.c $T_2$* relaxation times

All $T_2$*-weighted datasets were processed with ITK-Snap v2.4.0 (http://www.itksnap.org) [285] tumour volumes were segmented manually and further analysis of datasets was performed using MATLAB v7.11.0.584 (2010b) (Mathworks, Cambridge, UK). $T_2$* relaxation times, for each independent voxel within the tumour volume, were calculated by fitting a $T_2$* curve across the 4 echo times. Values were subsequently averaged across the entire tumour volume to yield a single mean $T_2$* relaxation rate per tumour. Pairwise statistical comparisons were made between pre- and post-contrast datasets using paired t tests. Unpaired t tests were used to compare between groups (Figure 5.4 A, D).

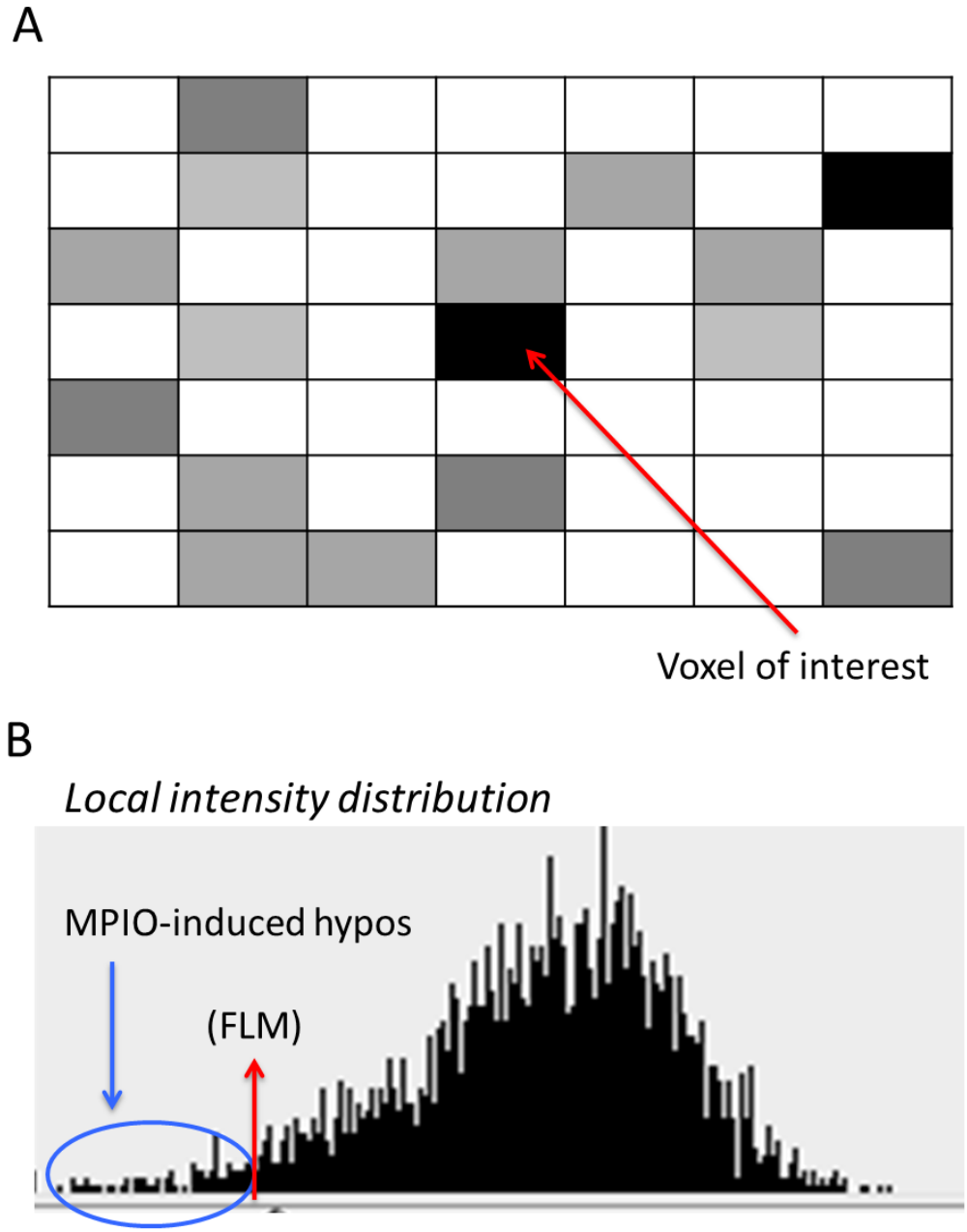



**Figure 5.2. Methodology of estimating MPIO-induced hypointense voxel.** (A) Schematic representation of 2D spatial, where each square represents voxels with unit resolution, and the voxel of interest in located in the middle (arrow). (B) Local intensity distribution of the neighboring voxels in radius of 5 voxels away from the voxel of interest.

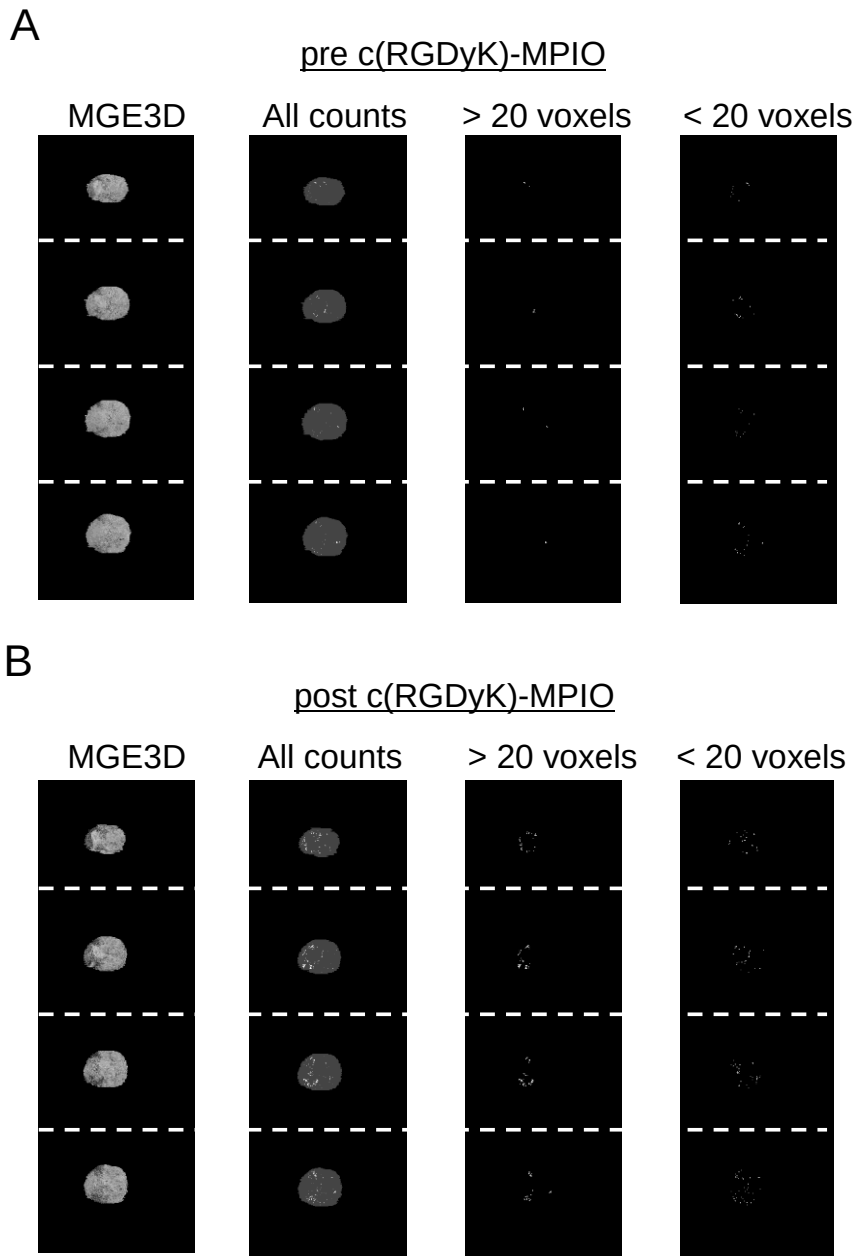



**Figure 5.3. Categorization and interpretation of positive hypointensce volumes.** (A-B) 2D lateral representative montages of the segmented colorectal tumour from the MGE3D, and the categorized computed equivalents; before (A.1-A.4) and after (B.1-B.2) administration of c(RGDyK)-MPIO; (A.1, B.1) MGE3D 2D lateral montage, (A.2, B.2) all detected hypointense voxels with segmented tumour margin, (A.3, B.3) only counts with volume > 20 voxels (excluded form analysis) and (A.4, B.4) ony counts with volume < 20 voxels (included in the analysis).

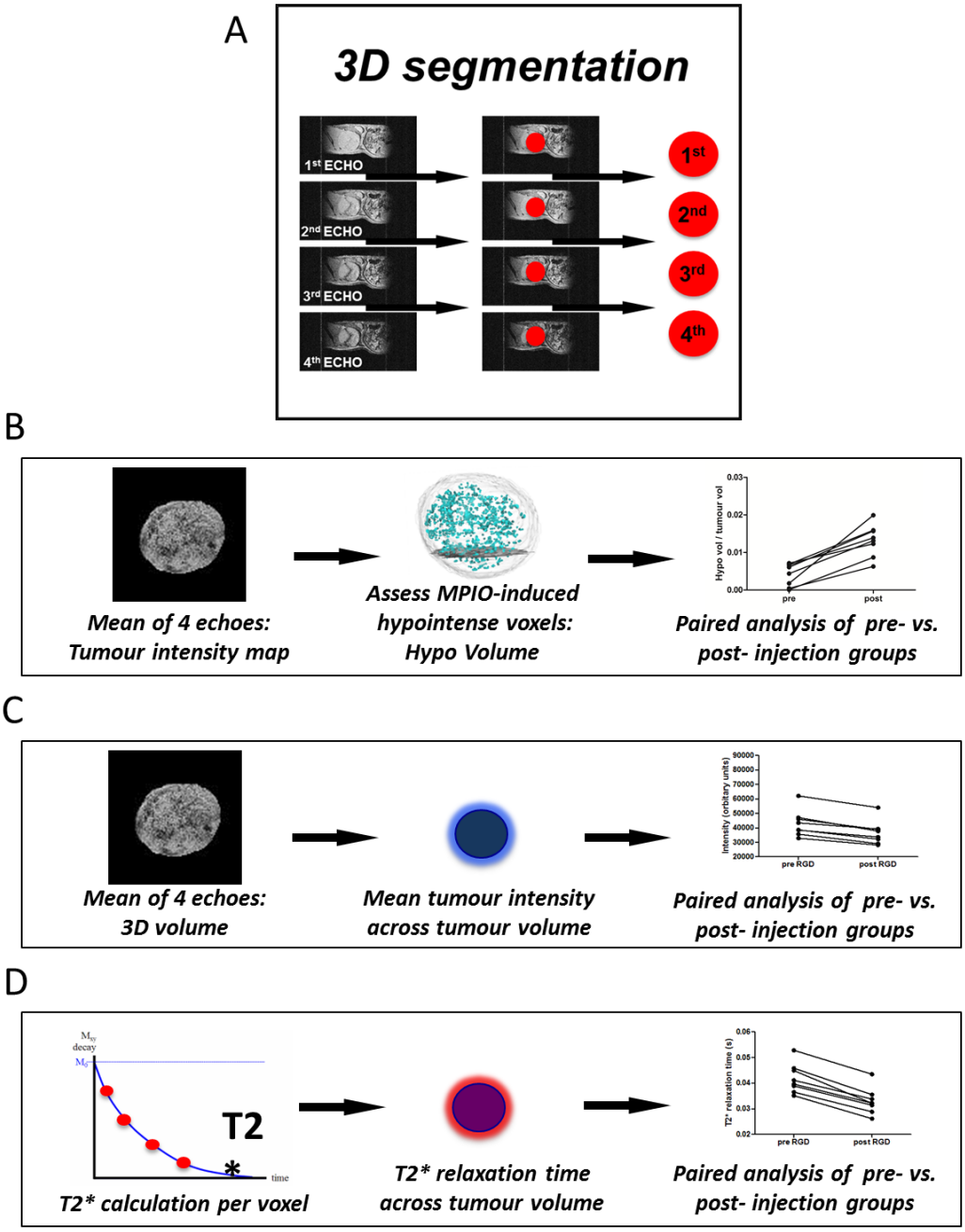



**Figure 5.4. Schematic diagrams of MRI analysis methodology. (**A) Representative lateral image of MGE3D dataset at 4 different echo times and the associated segmentation. (B) Methodology of hypointensity volumetric analysis. (C) Methodology of mean tumour intensity analysis. (D) Methodology of $T_2$* relaxation time analysis.

#### *5.2.7.2 DCE MRI*

The DCE datasets were manually segmented for tumour volumes and adequate muscle volume. Areas under the curve of intensity signal of the enhanced tumour voxels over time were estimated from 100 $T_1$-weighted images. Tumour and muscle tissue sections were segmented manually using ITK-Snap [285]. Pharmacokinetic analysis was performed with the kind help of Dr Danny Allen using the reference region model [336-338] implemented in MATLAB v7.11.0.584 (2010b).

### 5.2.8 Histological analysis

Immediately after imaging, mice were killed by exsanguination and perfused with 20 ml of sterile heparinised PBS via the right cardiac ventricle within 30 min. Tumours, kidneys and livers were dissected, embedded in optimum cutting temperature compound (OCT-Tissue Tek, VWR International Ltd, Lutterworth, UK) and frozen with isopentane and dry ice. The tissues were stored at -80 °C until cryosectioning. Tissues were sectioned at 10 µm thickness for further histological assessment.

Excluding the outermost 300 µm of each tumour, series of 30 x 10 µm sections were taken from 3 equidistant representative regions of the tumour. (Figure 5.5 A) Sections were stained for CD-31 (platelet endothelial cell adhesion molecule-1, anti-PECAM-1, ab28364, Abcam, Cambridge, UK). Frozen sections were thawed for 20 min at room temperature and, subsequently, fixed for 10 min with pre-chilled 100% ethanol at 4 °C. Slides were quenched with 1% v/v of 30% w/v hydrogen peroxide in methanol (Sigma Aldrich, Gillingham, UK) and blocked with 1% normal goat serum in PBS (Vector Laboratories) for 1 h. Sections were incubated with primary antibody (ab28364, Abcam) at 4 °C overnight, then washed with PBS containing 0.01% Tween-20 (Sigma Aldrich) and incubated with a biotinylated goat polyclonal to chicken IgG secondary antibody (1:1,000; Abcam) for 1 h. Slides were washed and then incubated in Vectorstain Elite ABC kit (1:1:100; Vector Laboratories) for 45 min. The peroxidase was visualised using 3,3′-diaminobenzidine (DAB; Sigma Aldrich). Sections were counterstained with cresyl violet (Sigma Aldrich).

Slides were further scanned with Leica Biosystem ScanScope CS2 (Aperio, ePathology Solutions, Milton Keynes, UK) from which high magnification images were acquired and further analysed with Image Scope (ePathology Solutions). For each tumour section, all vessels were manually segmented and MPIO, which are visible at high magnification, were manually counted (Figure 5.5 B-C). The vessel densities of the tumours, the MPIO density within each tumour and the adherence of MPIO per unit vessel circumference were calculated. Group-wise differences in these parameters were assessed statistically using unpaired t tests.

Expression of $\alpha_v\beta_3$ integrin on the tumour vasculature was evaluated by immunofluorescence, and co-localisation of $\alpha_v$ and $\beta_3$ subunits was determined. Frozen sections were thawed for 10 min at room temperature and, subsequently, fixed or 10 min with pre-chilled 100% ethanol at 4 °C. Sections were quenched with 1% v/v of 30% w/v hydrogen peroxide in PBS,

streptavidin- and biotin-blocked (SP-2002, Vector Laboratories) and then incubated with Tris-NaCl blocking buffer (TNB, PerkinElmer, MA, USA). Sections were incubated overnight at 4 °C with the following primary antibodies: Rabbit anti-Integrin beta3A [CD61] antibody (EPR2417Y, Milipore, MA, USA) and Rat anti-Mouse Monoclonal anti-ITGAV/Integrin Alpha V/CD51 Antibody (LS-C57970, LifeSpan Biosciences, WA, USA). Sections were washed with PBS and, subsequently, incubated with the appropriate secondary antibody, biotonylated anti-rat (BA-4001, Vector Laboratories) in TNB for 30 min at room temperature. Sections were washed with PBS, incubated with streptavidin-HRP (PerkinElmer, 1:200) in TNB for 30 min, washed and incubated for 8 min in the dark with TSA-biotin (PerkinElmer; 1:100) in amplification buffer (PerkinElmer). Subsequently, slides were washed and incubated with a streptavidin-Alexa Fluor 488 (Invitrogen, Paisley, UK; 1:100) for 30 min. To detect the other fluorophore, a Texas Red-conjugated secondary antibody was added at the same time as streptavidin-Alexa Fluor 488. Slides were cover-slipped using Vectashield mounting medium (Vector Laboratories).

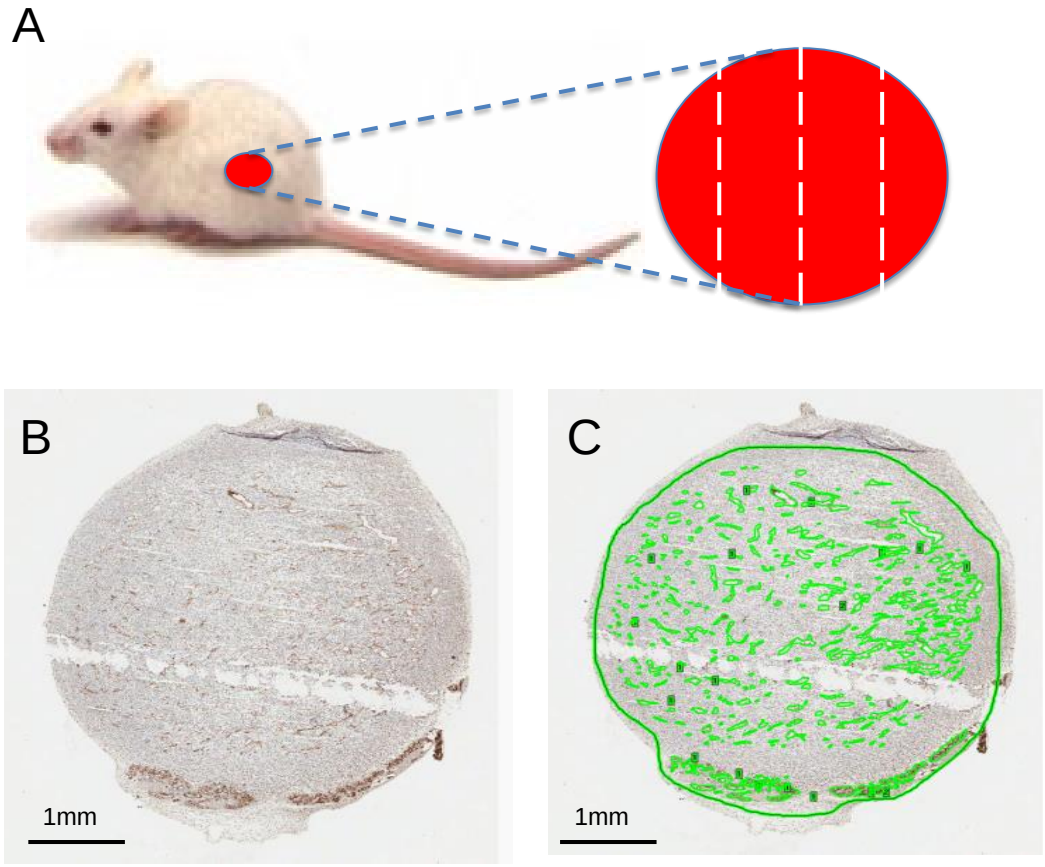



**Figure 5.5. Schematic diagram of IHC analysis. (**A) Tumour volumes were sectioned and equidistant representative slices across the tumour volume were chosen for IHC assessment (white dashed lines). (B) Representative section of colorectal derived tumour, stained for CD31. (C) Segmentation of tumour and tumour vessel area (green lines) and scoring of bound MPIO per vessel, under high magnification light microscopy.

### 5.2.9 Biological blood clearance protocol

For the iron oxide biological clearance experiments, 7-9 week old female CD1 mice (Charles River, UK) were injected intravenously via a tail vein with (i) 2.8 μm MPIO (n = 10), or (ii) 1.08 μm MPIO (n = 9), or (iii) ~20 nm nanoparticles (NPIO; n = 15); 4 mg of iron per kg of body mass weight in all cases. Dextran-coated NPIO (20.5 ± 8.9 nm diameter) were synthesised in-house by Dr Francisco Perez-Balderas, and since the synthetic protocol has not been, to date, it is included in this Thesis for completion (see 5.2.10). The NPIO biological clearance study was performed by Dr James Larkin as part of a separate study, but is include here, for comparison with MPIO clearance rates.
Blood samples from naïve mice were used to assess relaxivity of normal blood (n = 8). For the MPIO experiments, mice were anesthetised with 2-3% isoflurane in $O_2$ and at different time points after administration of MPIO underwent a thoracotomy, followed by cutting of the inferior vena cava and aorta below the lungs to allow the blood to pool inside the thoracic cavity. Blood was collected with a syringe containing 5 μl of heparin sodium (25,000 I.U./ml, Wockhardt, UK). For early time points, surgery was performed prior to injection of particles, leaving the diaphragm intact. Time points studied were: 10, 20, 30, 40, 50, 60, 90 (except 1.08 μm), 120, 180 and 240 s after MPIO injection (n = 1 per time point). For the NPIO experiments, blood was collected by cardiac puncture under terminal anaesthesia at different time points after administration of NPIO. A maximum amount of 5 μl heparin sodium was used per sample. Time points studied were: 60, 120, 240, 600 and 1440 min after MPIO injection (n = 3 per time point).

### 5.2.10 Determination of blood relaxivity

Blood samples were oxygenated by incubation with $O_2$ gas in a sealed tube on a rolling platform for 5 min. Samples were set into agar by mixing blood and 1% agarose solution in PBS, both at 40.5 °C, at a 1:1 ratio, to a final volume of 300 μl, in a 500 μl microcentrifuge tube. Set samples were stored at 4 °C. $T_2$ relaxivity measurements were made at 4.7 T, within 24 h, using an array of 100 μs hard 90° and 180° pulses, TR = 1000 ms, 2000 complex points and 8 averages. Blood half-life was determined from the fitted one phase decay curves, constrained to plateau at the average naive blood sample values (baseline).

### 5.2.11 Synthesis of dextran coated NPIO

1 L volume 3 neck round flask was charged with 6.75 g of $FeCl_3 \cdot 6H_2O$ (Sigma Aldrich, UK), 75 g of dextran 10 Pharmacological grade (Pharmacosmos, batch Nr. HR210) and 100 ml of water. The sample was stirred using an overhead stirrer at 300 rpm for 15 min until complete dissolution of the solids, and deoxygenated thoroughly by repeated cycles of vacuum assisted by sonication and argon flushing. After the first deoxygenation cycle, 3.0 g of $FeCl_2 \cdot 4H_2O$ (Sigma Aldrich, UK) in 25 ml of water was added and the solution was deoxygenated by the above procedure (4 times). While being stirred at 600 rpm, 20 ml of 30% $NH_4OH$ (Sigma

Aldrich, UK) was added at a rate of 168 ml/h. The reaction was heated to 80 ºC and then stirred at this temperature for 1 hour. The solution was cooled and dialyzed against water in a Spectra/Por 2 membrane (MWCO 6-8000) for 21 hours against 5 litter of water with water changes after 2 and 4 h.
Particle size was measured by dynamic light scattering in a Zetasizer Nano ZS (Malvern, UK). Briefly, 20 µl of particles were dispersed in 700 µl of water, the sample was shaken for 15 min and placed in polystyrene cuvette. Size measurement was performed in triplicate at 25 °C and results were analysed using the general purpose analysis model provided by the instrument software. The product particle size was 20.5 ± 8.9 nm with a PdI of 0.188.

## 5.3 Results

### 5.3.1 In vitro binding studies

Both c(RGDyK)-MPIO and c(RADyK)-MPIO were successfully synthesised, and peptide loading calculated to be *ca.* 2,000 ligands per $\mu m^2$; c(RGDyK)-MPIO 202,632 and c(RADyK)-MPIO 211,407 ligands per MPIO, respectively. Primarily, c(RGDyK)-MPIO needed to be assessed as for its specificity to $\alpha_v\beta_3$ expressing endothelial cells *in vitro.* Endothelial cells stimulated with SNAP showed $\alpha_v\beta_3$-integrin expression detected immunohistochemically, while $\alpha_v\beta_3$-integrin was largely absent from cells incubated with PBS. Quantification of positively immunostained areas showed that expression of $\alpha_v\beta_3$-integrin was 39-fold greater in SNAP stimulated HUVEC-C cells (5.80 ± 0.60 $mm^2$) *vs.* cells incubated with PBS (0.15 ± 0.08 $mm^2$, $P < 0.001$). Both SNAP- and PBS-stimulated cells showed similar staining for PECAM-1 (5.10 ± 0.46 $mm^2$ *vs.* 4.93 ± 0.44 $mm^2$; P = n.s.). Under static conditions, in SNAP stimulated cells, c(RGDyK)-MPIO binding (167.00 ± 16.70 MPIO) was 14-fold greater than cells incubated with PBS (12.20 ± 3.00 MPIO, n = 2, 10 fields of view per coverslip, $P < 0.001$) (Figure 5.6 A,B). Unconjugated MPIO showed sparse binding to both SNAP-stimulated and PBS-stimulated HUVEC-C (Figure 5.6 C-D).
c(RGDyK)-MPIO retention under flow conditions (1 dyne $cm^{-2}$) in SNAP stimulated cells (13.2 ± 1.9 MPIO) was 44-fold greater than retention in PBS-treated cells (0.3 ± 0.2 MPIO, $P < 0.001$), 3.8-fold greater than unconjugated MPIO in SNAP-stimulated cells (3.5 ± 0.9 MPIO, $P < 0.001$) and 4-fold greater than c(RGDyK)-MPIO retention in cells treated with soluble (blocking) RGD-peptide following SNAP stimulation and prior to MPIO administration (3.3 ± 0.9 MPIO, $P < 0.001$; Figure 5.6 E). c(RGDyK)-MPIO incubation in cells treated with the irrelevant RAD-peptide following SNAP stimulation (11.0 ± 1.3 MPIO) MPIO was 3.3-fold greater than cells undergoing similar conditions but treated with soluble RGD-peptide prior to MPIO administration (n = 2, 10 fields of view per coverslip, 400x magnification, $P < 0.001$; Figure 5.6 E). c(RGDyK)-MPIO retention at shear rate of 0.25 dyne $cm^{-2}$ (19.07 ± 3.08 MPIO) was 1.6-fold greater than c(RGDyK)-MPIO retention at a 1.0 dyne $cm^{-2}$ (12.3 ± 2.6 MPIO, $P < 0.001$) and 12.3-fold greater than c(RGDyK)-MPIO binding at 5.0 dyne $cm^{-2}$ in SNAP stimulated cells (0.37 ± 0.57 MPIO, n = 3, 10 fields of view, 400x magnification; Figure 5.6 F; $P < 0.001$).

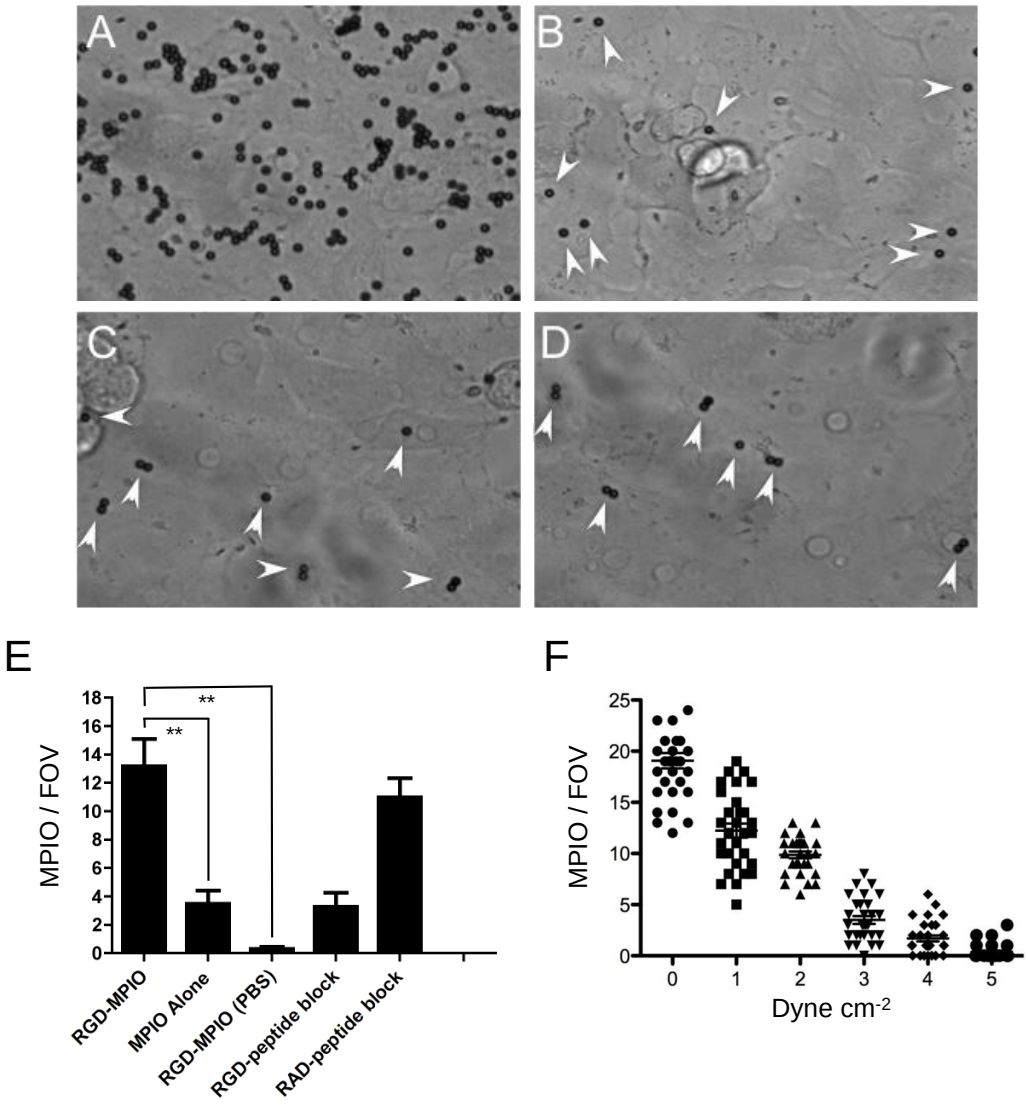



**Figure 5.6. *In vitro* c(RGDyK)-MPIO binding on $\alpha_v\beta_3$ activated HUVECs.** (A-E). *In vitro* binding experiments for c(RGDyK)-MPIO. c(RGDyK)-MPIO binding to HUVEC-C following incubation with either SNAP (A) or PBS (C). (D) Binding of unconjugated MPIO to SNAP stimulated HUVEC-C was significantly lower than that of c(RGDyK)-MPIO (white arrows). (E) Graph to show binding of c(RGDyK)-MPIO or unconjugated MPIO to HUVEC-C under static conditions , with or without blocking peptide (n = 2, 10 fields of view per coverslip, 40X magnification, $P < 0.001$). (F) c(RGDyK)-MPIO binding experiments under shear stress conditions. Graph to show comparison of c(RGDyK)-MPIO retention at different shear rates (n = 3 per condition, 10 fields of view, 40X magnification).

### 5.3.2 Biological clearance of micro- and nano sized iron oxide particles from blood circulation

As described in Chapter 3 (section 3.2.5), unbound circulating iron oxides in the blood circulation, during *in vivo* MRI acquisition, can cause significant undesired contrast effects. Having previously estimate the biological clearance for the 1 μm MPIO's compared to NPIO's from the blood circulation, we wanted here to investigate if a particle within the micrometer range but ~3 times larger has different clearance rate. Here we also present the previous data from Chapter 3 (section 3.3.5) for 1 μm MPIO for easier and direct comparison and furthermore clearance data from NPIO. Clearance of iron oxide micro- and nanoparticles from the blood circulation was determined for 2.8 μm, 1.08 μm and 25 nm iron oxide particles. The initial relaxivity (10 sec sample) for blood containing the 2.8 μm MPIO was approximately 1.5 times higher than for the 1.08 μm MPIO, $1/T_2$ = 74.6 *vs.* 30.3 $s^{-1}$, respectively (Figure 5.7 A). Although the iron content by mass of the 2.8 μm MPIO is less than that of the 1.08 μm MPIO (14% *vs.* 26%), the total amount of iron per particle is still greater in the larger MPIO. This, together with the size of the particles, will confer a greater dephasing effect per particle, given that both particles are porous polymers containing evenly distributed iron oxide cores of the same range (6-12 nm) [339] (Figure 5.8 A,B). Although this will be partially offset by the lower number of 2.8 μm MPIO injected to maintain the constant 4 mg / kg dose (5.5 x $10^7$ *vs.* 5 x $10^8$), the greater initial relaxivity of the 2.8 μm MPIO is expected. Despite these differences in relaxivity, the half-lives of the 2.8 and 1.08 μm MPIO were very similar; 34.9 and 39.9 seconds, respectively (Figure 5.7 A). In contrast, the half-life of the 25 nm NPIO in the blood was considerably longer (2.6 h) than those of the MPIO (Figure 5.7 B). The validity of the method for estimation of the half-lives of MPIO was tested by measuring the linearity of the $T_2$ relaxation rates with increasing concentration of iron, using 2.8 μm MPIO (Figure 5.7 C)

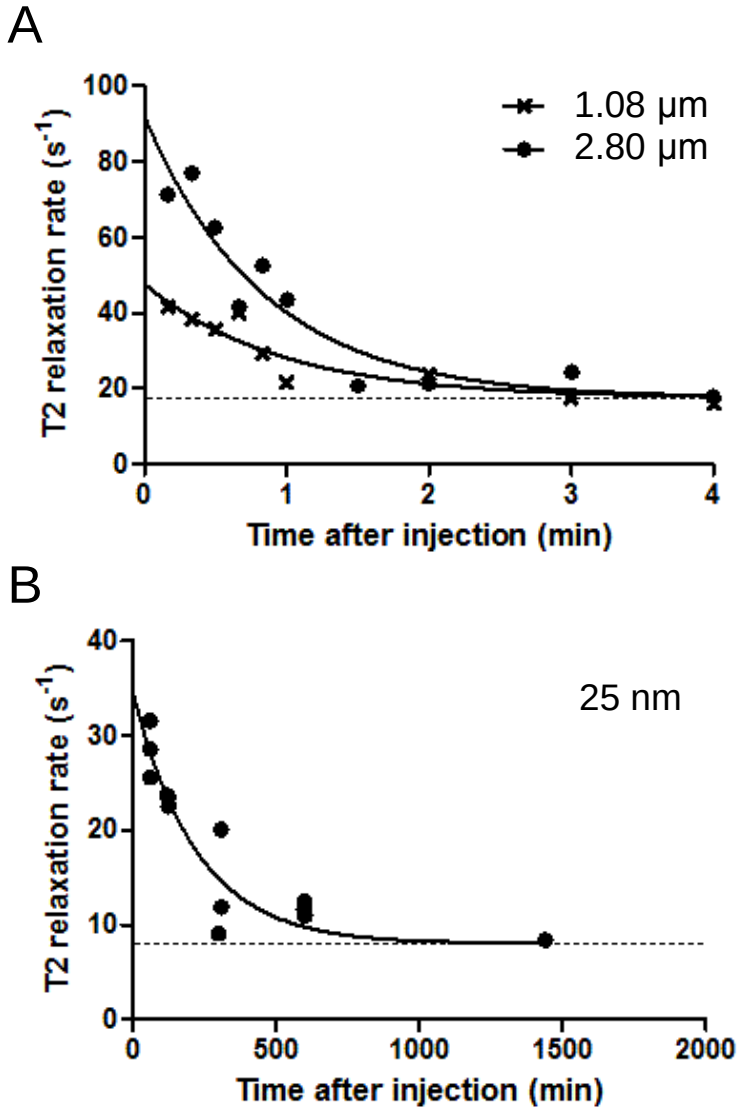



**Figure 5.7. Biological clearance of unbound MPIO *vs.* unbound NPIO from the blood circulation.** (A,B) Graphs showing decay curves for biological clearance of injected iron oxide micro- and nanoparticles from the circulation, at a constant dose of 4mg of iron per kg of body weight. (A) Comparison between 1.08 and 2.80 µm MPIO. Graph shows $T_2$ relaxivity values of blood samples at different time points after administration of either 1.08 or 2.80 µm MPIO. The clearance half-life for 2.80 µm MPIO was calculated to be 34.91 s (K = 0.019 $s^{-1}$, Y0 = 92.18 Hz) and 39.86 s for 1.08 µm MPIO (K = 0.017 $s^{-1}$, Y0 = 47.80 Hz). (B) Graph showing $T_2$ relaxivity values of blood samples at different time points after administration of 25 nm NPIO. The clearance half-life for 25 nm NPIO was calculated to be 153.70 min (K = 0.0045 $min^{-1}$, Y0 = 34.69 Hz). Curves are fitted as one phase exponential decay constrained to plateau at the average naïve blood sample values (baseline; dashed lines).

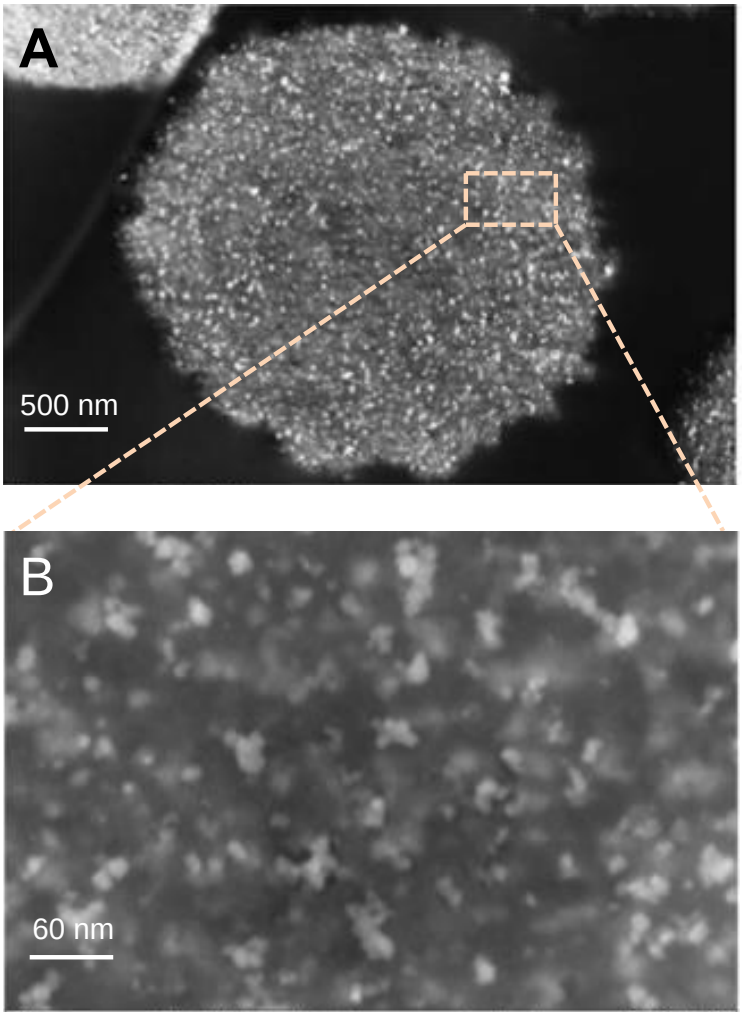



**Figure 5.8. MPIO structure.** (A) Scanning electron microscope micrograph of a M280 bead at two different magnifications. MPIO are composed from a sponge-like structure that impregnates clusters of 6-12 nm iron oxide. (B) Magnified area, showing distribution of NPIO clusters inside the MPIO's sponge-like structure (bright spots). Figure was adapted from Fonnum *et al*, 2005).

### 5.3.3 Quantification of c(RGDyK)-MPIO binding in vivo

#### *5.3.3.1 Hypointensity volumes*

Intravenous administration of c(RGDyK)-MPIO to mice bearing either melanoma or colorectal carcinoma derived subcutaneous tumours induced new signal hypointensities within the tumours on $T_2$*-weighted images compared to pre-contrast images (Figure 5.9 A-D, Figure 5.10 A-D). Paired analysis of the ratios of hypointensity volume to total tumour volume, between pre- and post-contrast administration datasets, showed a significant increase following c(RGDyK)-MPIO injection in both the melanoma (pre- *vs.* post-c(RGDyK)-MPIO, 0.010 ± 0.005 *vs.* 0.020 ± 0.003, $P < 0.05$; Figure 5.9 E) and colorectal models (pre- *vs.* post-c(RGDyK)-MPIO, 0.004 ± 0.003 *vs.* 0.013 ± 0.004, $P < 0.0005$; Figure 5.10 E). No significant increase in hypointense volume was seen following administration of the control

c(RADyK)-MPIO for the melanoma group (Figure 5.9 F). In contrast, the colorectal group showed a significant increase in the volume of MPIO-induced hypointensity (as a fraction of total tumour volume) following administration of the control c(RADyK)-MPIO (pre- *vs.* post-c(RADyK)-MPIO, 0.004 ± 0.003 *vs.* 0.009 ± 0.004, $P < 0.005$; Figure 5.10 F), but to a lesser extent than with c(RGDyK)-MPIO. Unpaired analysis between the melanoma model injected with c(RGDyK)-MPIO and c(RADyK)-MPIO did not show significance difference between groups; ratio of hypointensity volume to total tumour volume (post - pre) = 0.010 ± 0.006 *vs*. 0.003 ± 0.003 ($P = 0.051$; Figure 5.9 G). In contrast, colorectal model injected with targeted and control agent confirmed the significant difference between groups; ratio of hypointensity volume to total tumour volume (post - pre) = 0.009 ± 0.004 *vs*. 0.004 ± 0.003 ($P < 0.05$; Figure 5.10 G). Spatial distribution differences and shift in retention of c(RGDyK)-MPIO *vs.* c(RADyK)-MPIO) can be visible on 3D reconstructions of hypointensity volumes; representative melanoma derived tumours, Figure 5.11 A-D; colorectal derived tumours; Figure 5.12 A-D).

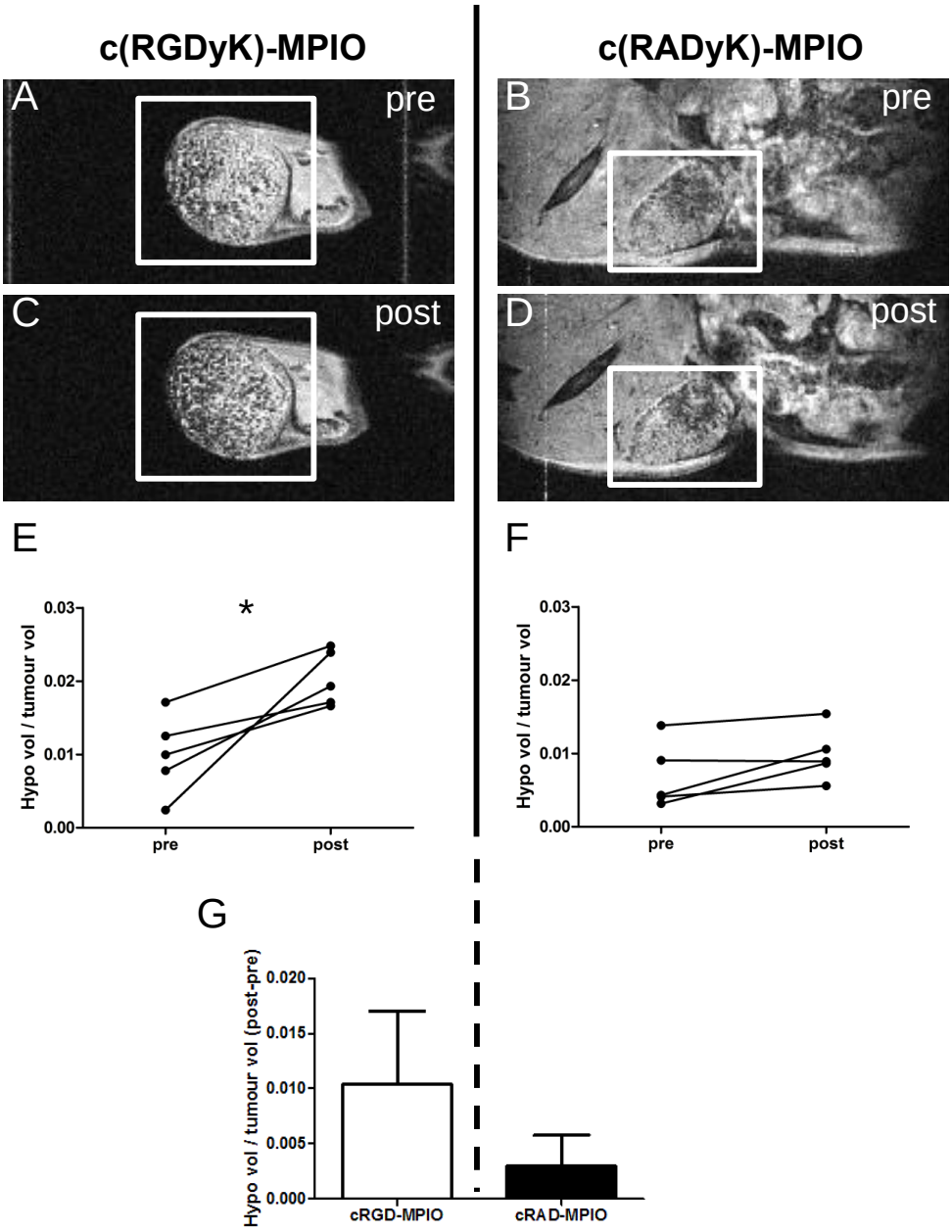



**Figure 5.9. Hypointensity volume ratio results for melanoma derived tumours.** (A-D) Selected images from a 3D gradient echo dataset from the B16F10 (melanoma) subcutaneous tumour model, averaged over the 4 echoes. Images acquired pre- (A) and (B) and post- (C) and (D) injection of c(RGDyK)-MPIO or c(RADyK)-MPIO, respectively. (E-F) Graphs showing paired analysis of hypointensity volumes from c(RGDyK)-MPIO (E) and c(RADyK)-MPIO (F) treated animals. Data are expressed as a ratio of the volume of MPIO-induced hypoinintensity *vs.* the total tumour volume. (G). Graph showing unpaired comparison of the hypointense volume ratios for c(RGDyK)-MPIO *vs.* c(RADyK)-MPIO injected melanoma derived tumours. *P < 0.05.

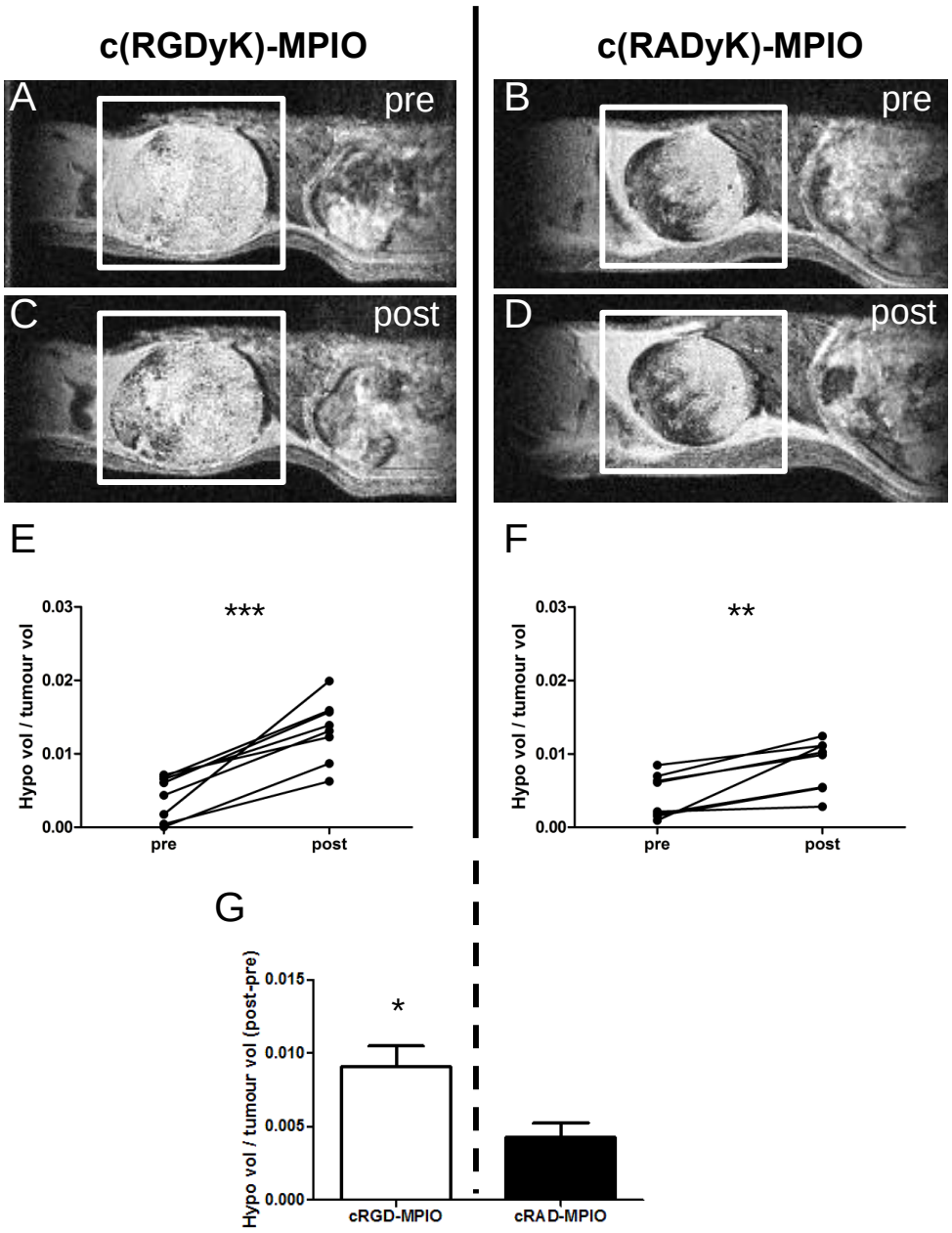



**Figure 5.10. Hypointensity volume ratio results for colorectal derived tumours.** (A-D) Selected images from a 3D gradient echo dataset from the MC38 (colorectal) subcutaneous tumour model, averaged over the 4 echoes. Images acquired pre- (A) and (B) and post- (C) and (D) injection of c(RGDyK)-MPIO or c(RADyK)-MPIO, respectively. (E-F) Graphs showing paired analysis of hypointensity volumes from c(RGDyK)-MPIO (E) and c(RADyK)-MPIO (F) treated animals. Data are expressed as a ratio of the volume of MPIO-induced hypoinintensity *vs.* the total tumour volume. (G) Graph showing unpaired comparison of the hypointense volume ratios for c(RGDyK)-MPIO *vs.* c(RADyK)-MPIO injected colorectal derived tumours. $^{**}P < 0.005$, $^{***}P < 0.0005$.

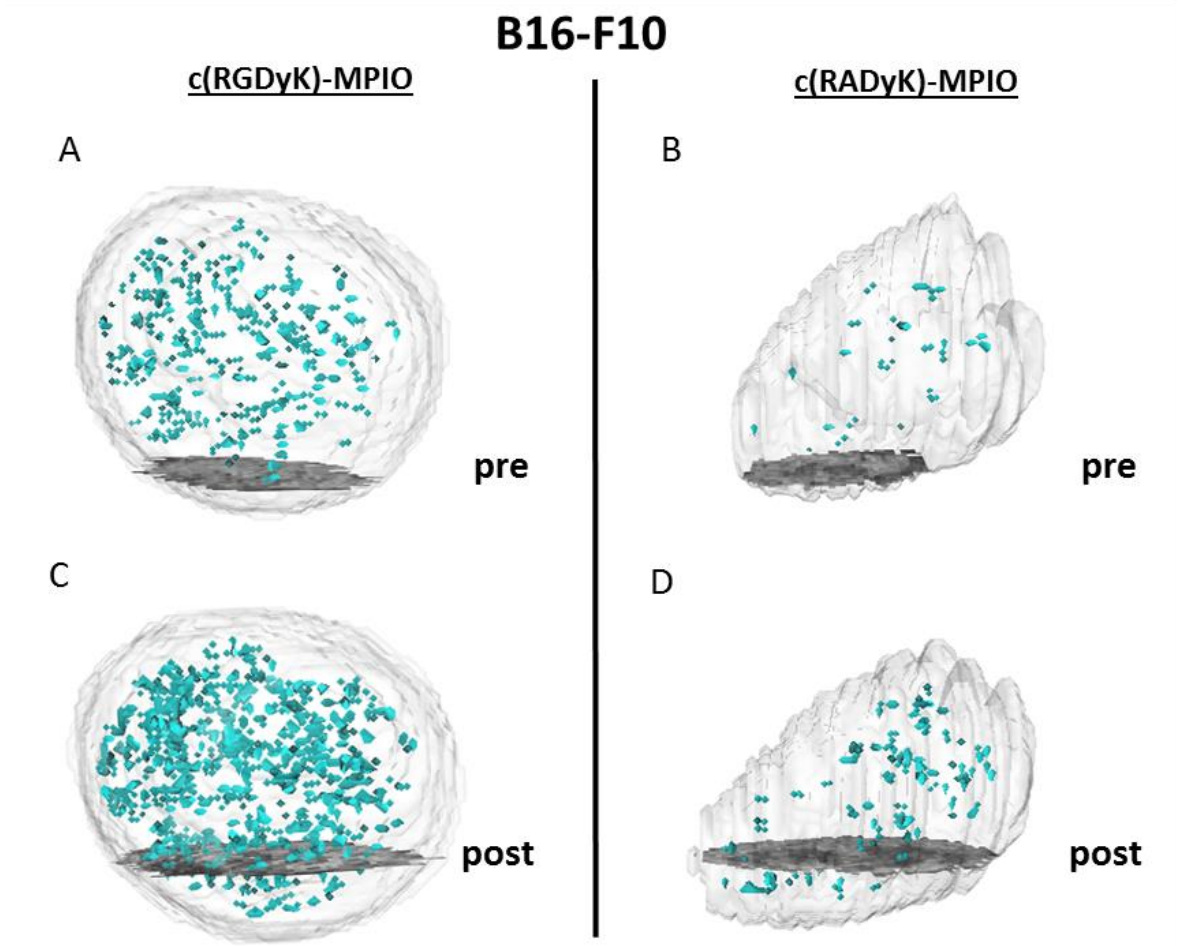



**Figure 5.11. 3D reconstructions of hypointesity volumes of the melanoma derived tumours.** (A-D) 3D representation of hypointensity volumes (cyan) within the representation of the 3D segmented tumour volume (gray), of the previously presented melanoma derived tumours (Figure 10 A-D). (A) and (B) shows 3D reconstructions of datasets before administration of c(RGDyK)-MPIO or c(RADyK)-MPIO, respectively. (C) and (D) showing the paired 3D hypointensity volume reconstruction after administration of c(RGDyK)-MPIO or c(RADyK)-MPIO, respectively.

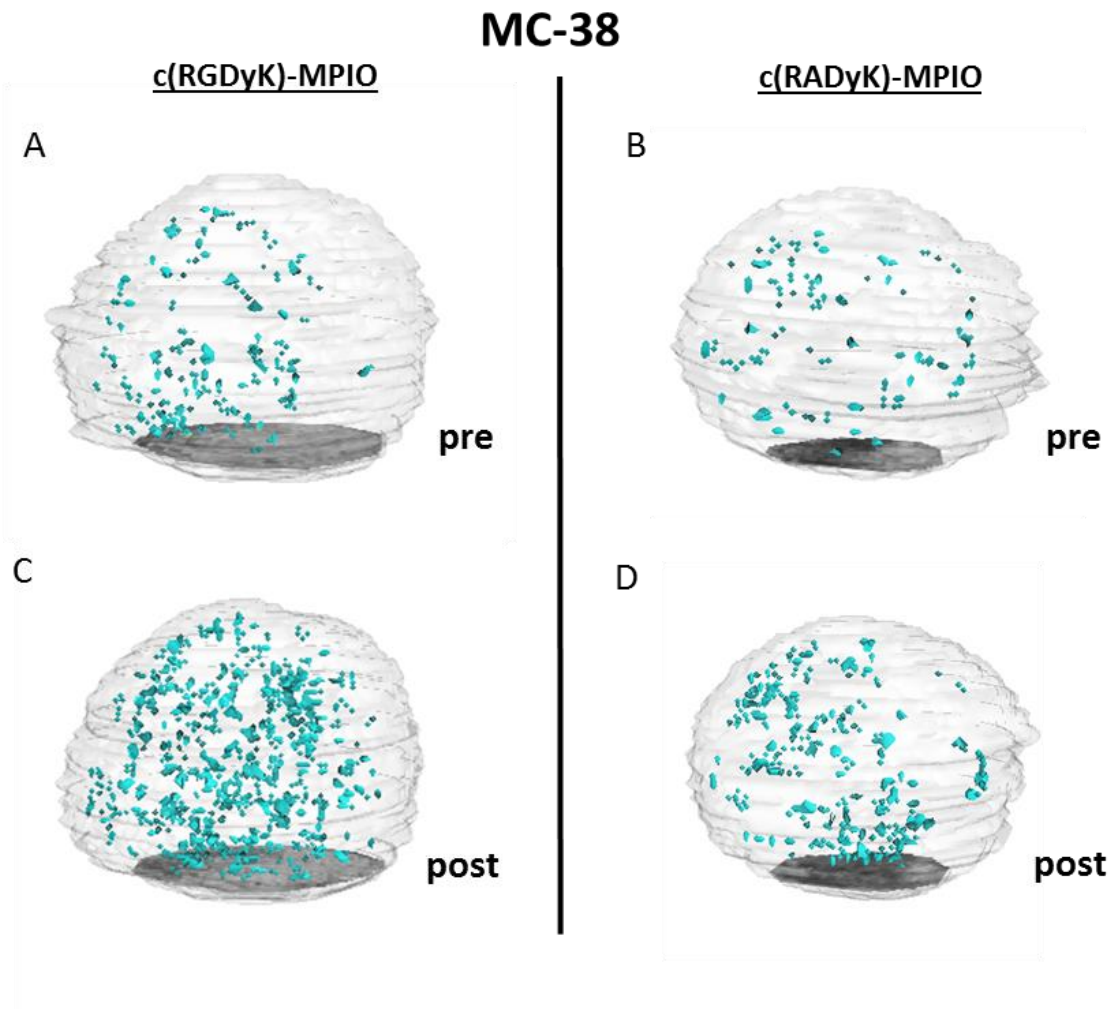



**Figure 5.12. 3D reconstructions of hypointesity volumes of the colorectal derived tumours.** (A-D) 3D representation of hypointensity volumes (cyan) within the representation of the 3D segmented tumour volume (gray), of the previously presented melanoma derived tumours (Figure 11 A-D). (A) and (B) shows 3D reconstructions of datasets before administration of c(RGDyK)-MPIO or c(RADyK)-MPIO, respectively. (C) and (D) showing the paired 3D hypointensity volume reconstructions after administration of c(RGDyK)-MPIO or c(RADyK)-MPIO, respectively.

#### *5.3.3.2 Mean tumour intensity*

Since the volumetric analysis method is measuring the contrast effect per unit area, we have also considered whether a more straightforward global measurement of the effect of MPIO binding could promote sufficient information to be useful. To this end, changes in signal intensity levels owing to c(RGDyK)-MPIO binding were assessed. Mean tumour intensities across the whole tumour were calculated for both the melanoma (Figure 5.13 A-B, E) and colorectal (Figure 5.13 C-D, F) groups. Administration of c(RGDyK)-MPIO in mice bearing subcutaneous melanoma derived tumours significantly reduced the mean tumour intensities (pre- *vs.* post-c(RGDyK)-MPIO, arbitrary units (a.u.), 40295 ± 30948 *vs.* 31532 ± 25727 a.u.; $P < 0.05$; Figure 5.13 A). No significant change in mean tumour intensities was seen after administration of the control contrast agent in the melanoma-derived tumours. (pre- *vs.* post-c(RADyK)-MPIO, 35476 ± 9335 *vs.* 33560 ± 10223 a.u.; Figure 5.13 B). Similarly, in the colorectal derived tumours mean tumour intensities were significantly reduced (pre- *vs*. post-c(RGDyK)-MPIO, 43000 ± 9182 *vs.* 36563 ± 8236 a.u.; $P < 0.0001$; Figure 5.13 C). However, the c(RADyK)-MPIO injected mice also showed a significant, but lesser reduction in mean tumour intensities from pre- to post-contrast datasets (42862 ± 9764 *vs*. 39625 ± 9029 a.u.; $P < 0.05$; Figure 5.13 D). The reduction in mean tumour intensities in the c(RGDyK)-MPIO group was significantly greater than in the c(RADyK)-MPIO group ($P < 0.05$; Figure 5.13 E). The reduction in mean tumour intensities in the c(RGDyK)-MPIO group was significantly greater than in the c(RADyK)-MPIO group ($P < 0.01$; Figure 5.13 F).

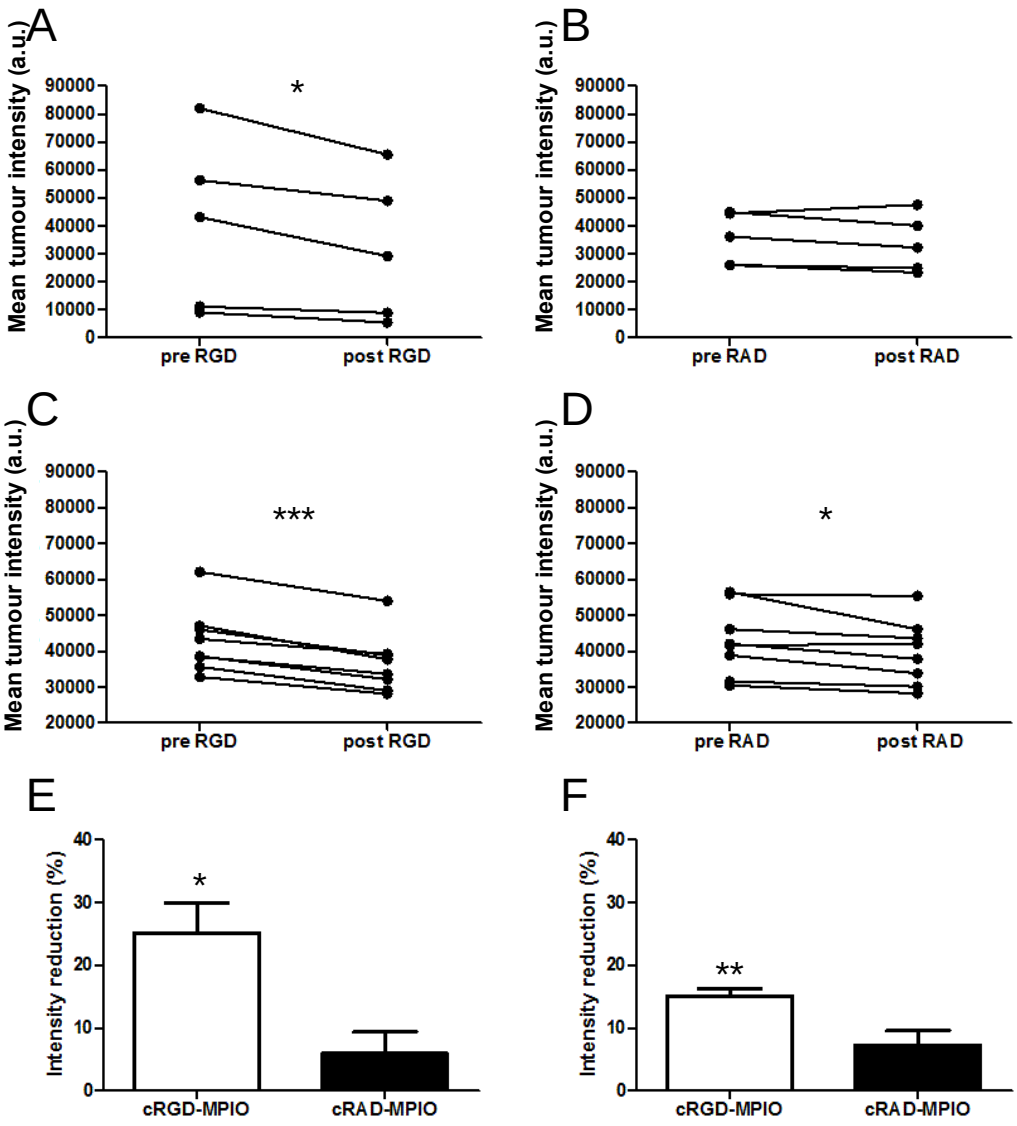



**Figure 5.13. Mean tumour intensity results for both subcutaneous mouse models.** (A) Graph showing paired analysis of averaged tumour intensities between pre- and post- c(RGDyK)-MPIO treatment in the B16F10 (melanoma) model. (B) Graph showing paired analysis of averaged tumour intensities between pre- and post-c(RADyK)-MPIO treatment in the B16F10 model. (C) Graph showing paired analysis of averaged tumour intensities between pre- and post-c(RGDyK)-MPIO treatment in the MC-38 (colorectal) model. (D) Graph showing paired analysis of averaged tumour intensities between pre- and post-c(RADyK)-MPIO treatment in the MC-38 model. (E,F) Graphs showing percentage reduction of tumour intensities following administration of either targeted [c(RGDyK)-MPIO] or control [c(RADyK)-MPIO] contrast agent for B16F10 (E) or MC-38 (F) models. *P < 0.05, **P < 0.01, ***P < 0.0001.

#### *5.3.3.3 $T_2$* relaxation times*

Given inherent issues with signal intensity measurements (see Discussion), we have further considered absolute measurements of mean $T_2$* relaxation rates across the whole tumour (Figure 5.14). In accord with the analysis of both segmented hypointensities (see 5.3.3.1) and mean tumour intensities (see 5.3.3.2), administration of c(RGDyK)-MPIO significantly reduced the mean tumour $T_2$* relaxation time in mice bearing subcutaneous melanoma derived group (pre- *vs.* post-c(RGDyK)-MPIO, 0.025 ± 0.004 *vs.* 0.019 ± 0.004 s; $P < 0.005$; Figure 5.14 B). No significant shortening in $T_2$* relaxation times was seen after administration of the control contrast agent in the melanoma derived tumours. (pre- *vs.* post-c(RADyK)-MPIO, 0.025 ± 0.002 *vs.* 0.024 ± 0.002 s; Figure 5.14 C). Similarly, in the colorectal derived tumours mean tumour $T_2$* relaxation time was significantly reduced (pre-*vs*. post-c(RGDyK)-MPIO, 0.042 ± 0.006 *vs.* 0.033 ± 0.005 s; $P < 0.000005$; Figure 5.14 D). However, in this group, the c(RADyK)-MPIO injected tumours also showed a significant, but lesser reduction in $T_2$* relaxation time from pre- to post-contrast datasets (0.041 ± 0.009 *vs.* 0.037 ± 0.008 s; $P < 0.005$; Figure 5.14 E). In the melanoma derived tumours the reduction in $T_2$* relaxation time in the c(RGDyK)-MPIO injected group was significantly greater than in the c(RADyK)-MPIO injected group ($P < 0.001$; Figure 5.14 F). Similarly, in the colorectal derived tumours, the reduction in $T_2$* relaxation times in the c(RGDyK)-MPIO group was significantly greater than in the c(RADyK)-MPIO group ($P < 0.0001$; Figure 5.14 G).

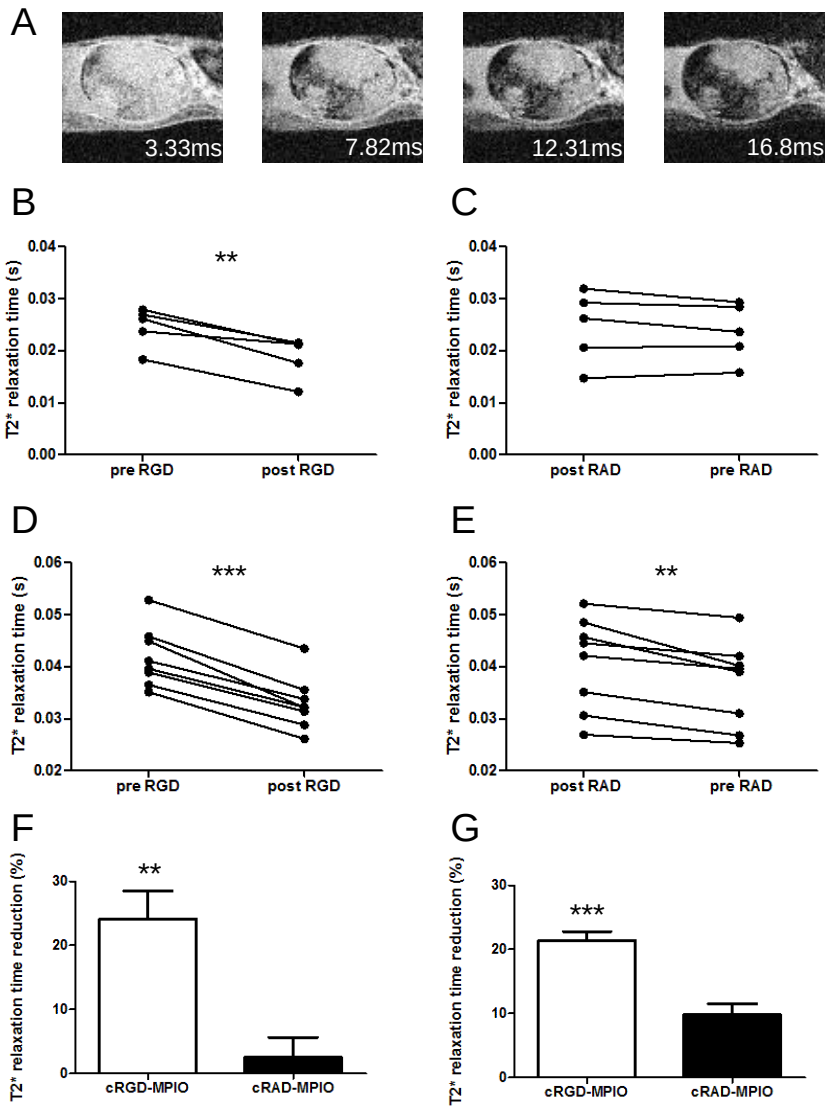



**Figure 5.14. Mean tumour $T_2$* relaxation times for both subcutaneous mouse models.** (A) Selected slice from a 3D gradient echo dataset from MC38 (colorectal) subcutaneous tumour model showing all 4 echoes (echo times shown for each image) acquired post- c(RGDyK)-MPIO administration. (B) Graph showing paired analysis of tumour $T_2$* relaxation times between pre- and post- c(RGDyK)-MPIO treatment in the B16F10 model. (C) Graph showing paired analysis of tumour $T_2$* relaxation times between pre- and post-c(RADyK)-MPIO treatment in the B16F10 model. (D) Graph showing paired analysis of tumour $T_2$* relaxation times between pre- and post- c(RGDyK)-MPIO treatment in the MC-38 model. (E) Graph showing paired analysis of tumour $T_2$* relaxation times between pre- and post-c(RADyK)-MPIO treatment in the MC-38 model. (F,G) Graphs showing percentage reduction in $T_2$* relaxation times following administration of either targeted (c(RGDyK)-MPIO) or control (c(RADyK)-MPIO) contrast agent for B16F10 (F) or MC-38 (G) models. **P < 0.005, ***P < 0.0005.

#### *5.3.3.4 Size grouping for colorectal model*

Initially, experiments were planned to be n = 5 per group (targeted and control), for both models. However, owing to inconsistency in tumour growth rate, some animals were found to have significantly larger tumours than the rest of the cohort. Given that differences in tumour perfusion would be expected in different size tumours, and the potential confound this could introduce to the above analysis, we investigate this issue further in one of the models. Since the MC-38 (colorectal) model had demonstrated the greater size variability and also a higher degree of no-specific c(RADyK)-MPIO retention, 3 additional animals were added to the colorectal group only, in order to create two size limited subgroups: tumours volumes < 400 $mm^3$ (n=5 per group), and tumours volumes > 400 $mm^3$ (n=3 per group) (Figure 5.15).

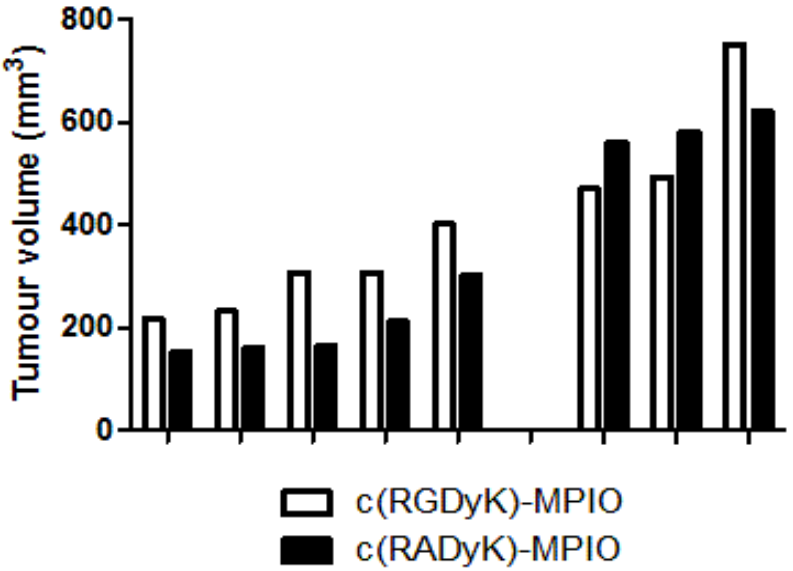



**Figure 5.15. Subcutaneous tumour volumes.** Colorectal derived tumour volumes treated with c(RGDyK)- or c(RADyK)-MPIO.

##### 5.3.3.4.a Hypointensity volumes

In accord with the analysis of segmented hypointensities across the whole group (see 5.3.3.1), paired analysis of the ratios of hypointensity volume to total tumour volume, between pre- and post-contrast administration datasets, showed a significant increase following c(RGDyK)-MPIO injection in both the smaller volume tumours (pre- vs. post-c(RGDyK)-MPIO, 0.003 ± 0.003 *vs.* 0.013 ± 0.006, $P < 0.05$; Figure 5.16 A) and larger size tumours (pre- vs. post- c(RGDyK)-MPIO, 0.006 ± 0.002 *vs.* 0.014 ± 0.002, $P < 0.05$; Figure 5.16 C). No significant increase in hypointense volume was seen following administration of the control c(RADyK)-MPIO for the smaller size group (Figure 5.16 B). In contrast, the large size tumour group showed a significant increase in the volume of MPIO-induced

hypointensity (as a fraction of total tumour volume) following administration of the control c(RADyK)-MPIO (pre- *vs.* post-c(RADyK)-MPIO, 0.005 ± 0.003 *vs.* 0.009 ± 0.003, $P < 0.05$; Figure 5.16 D), but to a lesser extent than with c(RGDyK)-MPIO. Unpaired analysis between the c(RGDyK)-MPIO and c(RADyK)-MPIO treated groups showed no significant differences, for both the small and large volume tumour groups (Figure 5.16 E,F).

#### 5.3.3.4.b Mean tumour intensity

In accord with the analysis of mean tumour intensities for the entire group (see 5.3.3.2), paired analysis between pre- and post-contrast administration datasets, showed a significant decrease in mean tumour intensities following c(RGDyK)-MPIO injection in both the smaller volume tumours (pre- vs. post-c(RGDyK)-MPIO, arbitrary units, 45920 ± 9743 *vs.* 39320 ± 8703, $P < 0.005$; Figure 5.17 A) and larger volume tumours (pre- vs. post-c(RGDyK)-MPIO, arrbitrary units, 38133 ± 6955 *vs.* 31967 ± 5934, $P < 0.05$; Figure 5.17 C). Administration of the control c(RADyK)-MPIO did not result in a significant reduction in mean tumour intensities in either sub-group (Figure 5.17 B and D). Interestingly, unpaired analysis between c(RGDyK)-MPIO and c(RADyK)-MPIO treated groups did reveal significant differences between the percentage of mean tumour intensity only in the large volume tumour group ($P < 0.005$; Figure 5.17 E,F).

#### 5.3.3.4.c $T_2$* relaxation times

In accord with the analysis of $T_2$* relaxation times for the whole group (see 5.3.3.3), paired analysis between pre- and post-contrast administration datasets, showed a significant decrease in $T_2$* relaxation times following c(RGDyK)-MPIO injection in both the smaller volume tumours (pre- vs. post-c(RGDyK)-MPIO, 0.044 ± 0.007 *vs.* 0.033 ± 0.006 s, $P < 0.0005$; Figure 5.18. A) and larger volume tumours (pre- vs. post- c(RGDyK)-MPIO, 0.039 ± 0.002 *vs.* 0.031 ± 0.003 s, $P < 0.0005$; Figure 5.18 C). Administration of the control c(RADyK)-MPIO also significantly reduce the $T_2$* relaxation times in both sub-groups ($P < 0.05$; Figure 5.18 B, D), but to a lesser extent following c(RGDyK)-MPIO. Unpaired analysis between c(RGDyK)-MPIO and c(RADyK)-MPIO treated groups confirmed the significant difference between the percentage reduction in $T_2$* for both sub-groups ($P < 0.01$; Figure 5.18 E,F).

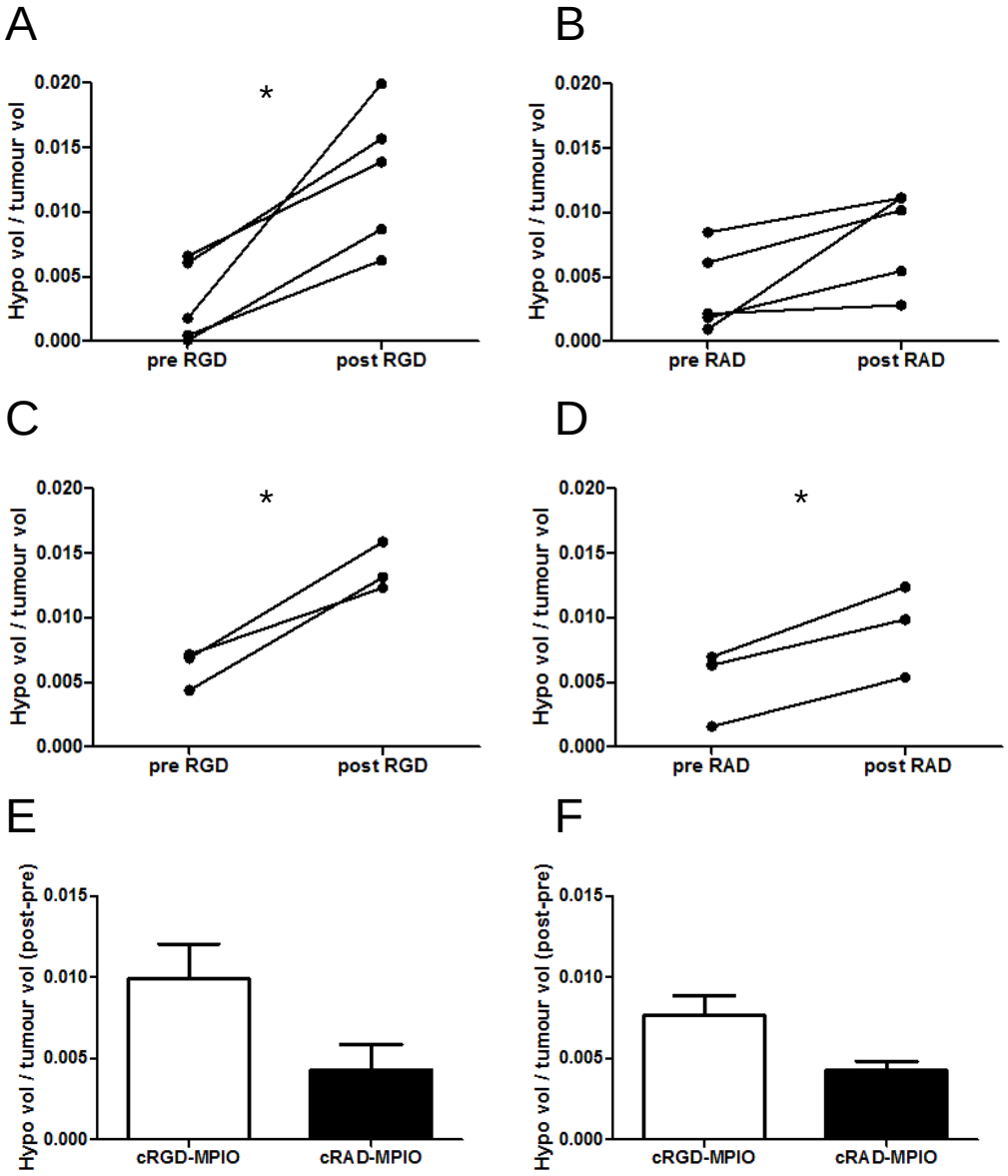



**Figure 5.16. Hypointensity volume ratios for size restricted sub-groups of colorectal derived tumours.** (A,B) Graphs showing paired analysis of tumour hypointensity volumes either between pre- and post-c(RGDyK)-MPIO (A) or pre- and post-c(RADyK)-MPIO (B) treatment in the MC-38 model, for tumour volumes < 400mm$^3$. (C,D) Graphs showing paired analysis of tumour hypointensity either between pre- and post-c(RGDyK)-MPIO (C) or pre- and post-c(RADyK)-MPIO (D) treatment in the MC-38 model, for tumour volumes > 400mm$^3$. (E,F) Graphs showing comparison of hypointensity volume differences (post - pre) between administration of targeted (c(RGDyK)-MPIO) or control (c(RADyK)-MPIO) contrast agent, for size group of tumour volumes < 400mm$^3$ (E) or tumour volumes > 400mm$^3$ (F). *P < 0.05.

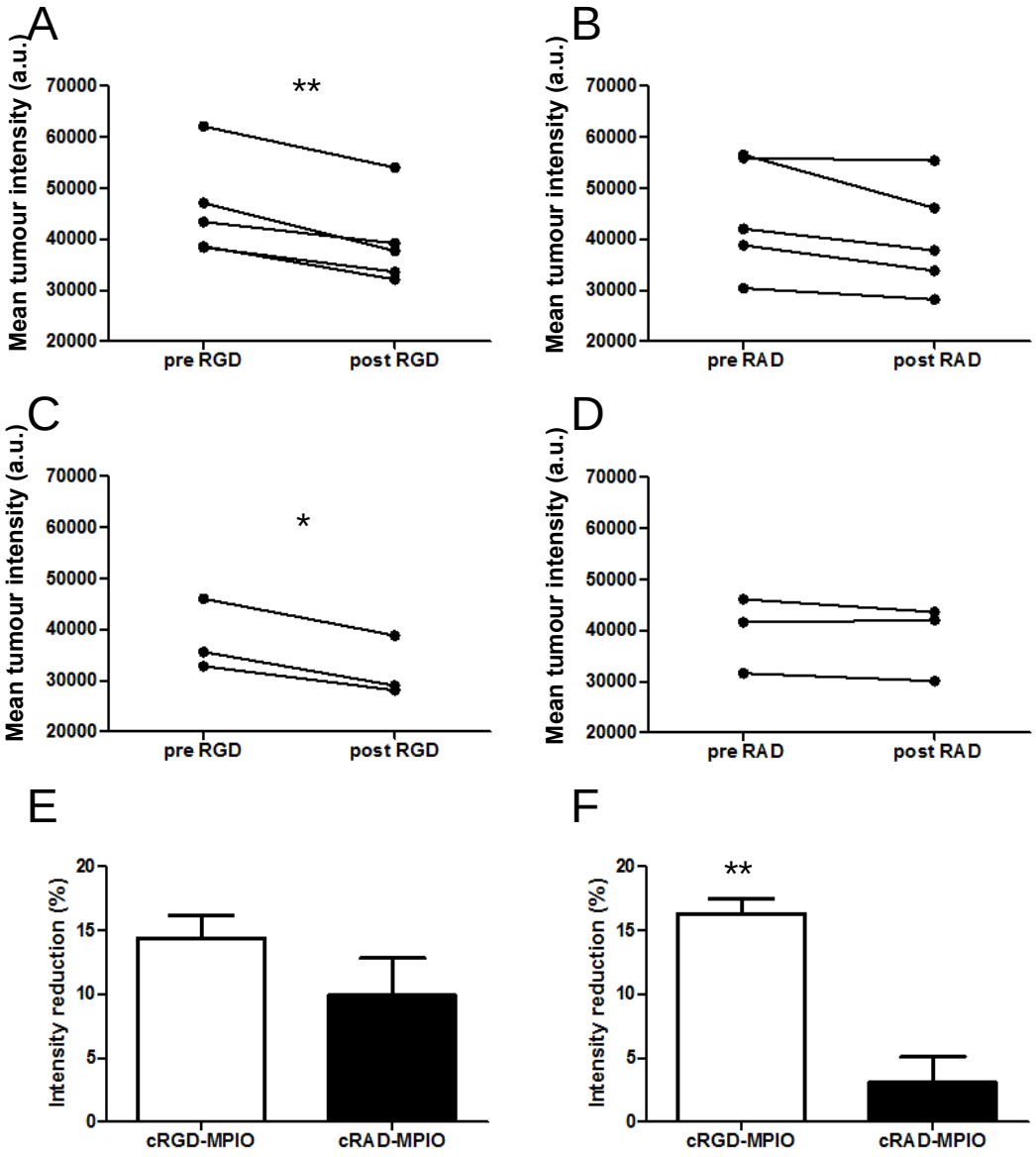



**Figure 5.17. Mean tumour intensities for size restricted sub-groups of colorectal derived tumours.** (A,B) Graphs showing paired analysis of mean tumour intensities either between pre- and post-c(RGDyK)-MPIO (A) or pre- and post-c(RADyK)-MPIO (B) treatment in the MC-38 model, for tumour volumes < 400mm$^3$. (C,D) Graphs showing paired analysis of mean tumour intensities either between pre- and post-c(RGDyK)-MPIO (C) or pre- and post-c(RADyK)-MPIO (D) treatment in the MC-38 model, for tumour volumes > 400mm$^3$. (E,F) Graphs showing percentage reduction in mean tumour intensities following administration of either targeted (c(RGDyK)-MPIO) or control (c(RADyK)-MPIO) contrast agent for group with tumour volumes < 400mm$^3$ (E) or tumour volumes > 400mm$^3$ (F). *P < 0.05, **P < 0.005.

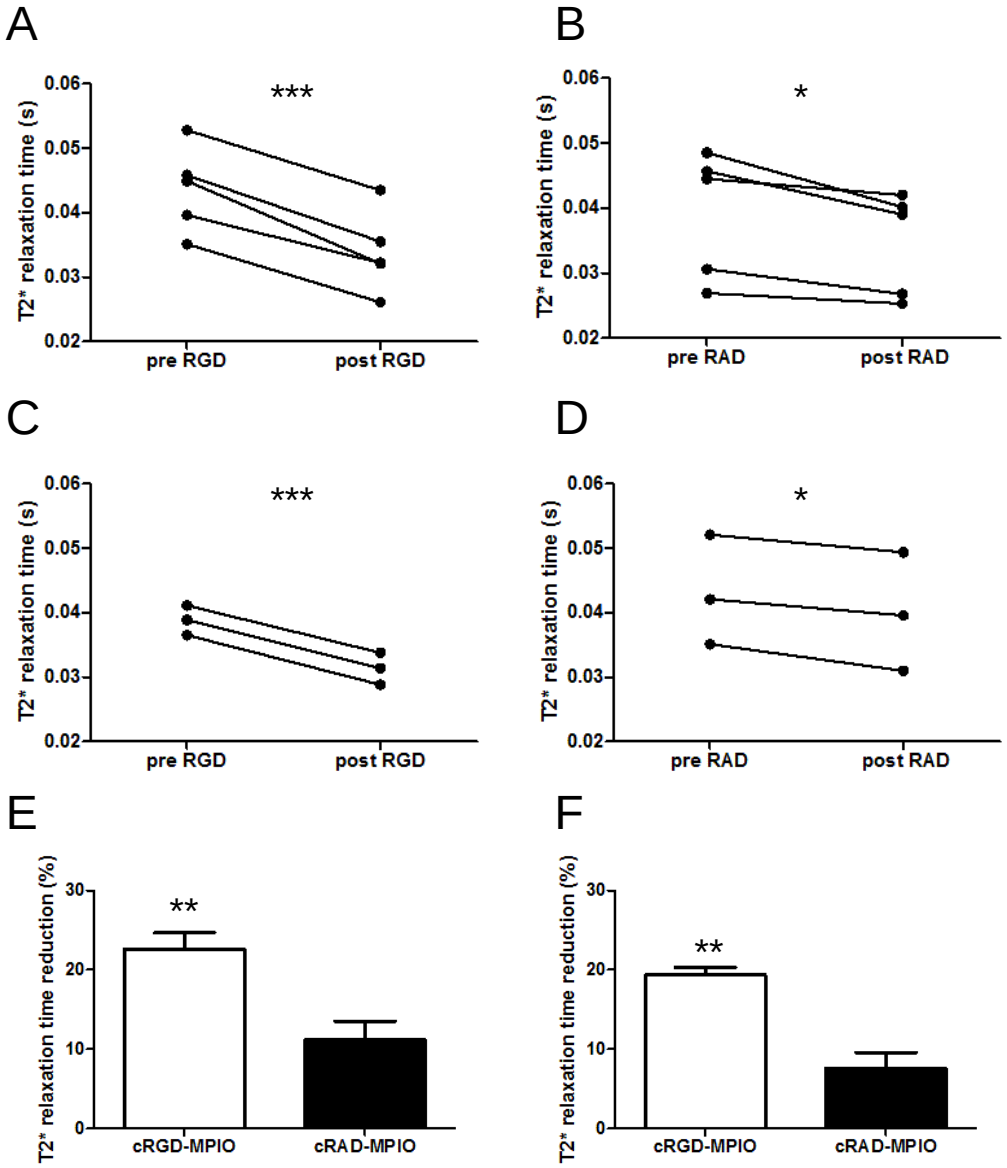



**Figure 5.18. Mean tumour $T_2$* relaxation times for size restricted sub-groups of colorectal derived tumours.** (A,B) Graphs showing paired analysis of tumour $T_2$* relaxation times either between pre- and post-c(RGDyK)-MPIO (A) or pre- and post-c(RADyK)-MPIO (B) treatment in the MC-38 model, for tumour volumes < 400mm$^3$. (C,D) Graphs showing paired analysis of tumour $T_2$* relaxation times either between pre- and post-c(RGDyK)-MPIO (C) or pre- and post-c(RADyK)-MPIO (D) treatment in the MC-38 model, for tumour volumes > 400mm$^3$. (E,F) Graphs showing percentage reduction in $T_2$* relaxation times following administration of either targeted (c(RGDyK)-MPIO) or control (c(RADyK)-MPIO) contrast agent for group with tumour volumes < 400mm$^3$ (E) or tumour volumes > 400mm$^3$ (F). *P < 0.05, **P < 0.01, ***P < 0.0005.

### 5.3.4 DCE MRI

The blood perfusion of the tumour is strongly associated with the spatial distribution and accessibility of the injected MPIO across the whole tumour. Previously, we described a static contrast-enhanced MR imaging approach, which does not provide information over time (static imaging). Thus, although the retention of MPIO's will be dependent of perfusion the method is not perfusion-sensitive. In order to assess the level of perfusion of the tumour volumes over time we implemented a gadolinium dynamic contrast enhanced (DCE) MRI. Figure 5.19 shows representative slices across the DCE dataset from the largest (Figure 5.19 A) and the smallest (Figure 5.19 B) colorectal derived tumours. Gadolinium enhancement over time is evident in both, but is noticeably faster in the smaller tumour (Figure 5.19 B). Correspondingly, linear regression analysis of the tumour area under the curve (AUC) against tumour volume shows significant negative correlation with tumour volume ($R^2 = 0.7272$; $P < 0.05$; Figure 5.19 C). In contrast, linear correlation of the muscle AUC against tumour volume shows positive correlation ($R^2 = 0.6899$; $P < 0.05$; Figure 5.19 D). These results indicate that as the tumour volumes increase in size, the tumours become less well perfused; therefore, more contrast agent will circulate on the muscle area. Since, there are variations in the Gd bolus and differences in perfusion from animal to animal, the ratios of tumour-to-muscle AUC were assessed against tumour volume also. Tumour-to-muscle AUC revealed a significant negative correlation ($R^2 = 0.6716$; $P < 0.05$; Figure 5.19 E). These correlations indicating an inverse relationship between contrast agent uptake and tumour size. A negative correlation was also observed between volume transfer coefficient ($K^{trans}$) and tumour volume ($R^2 = 0.8097$; $P < 0.05$; Figure 5.19 F). $K^{trans}$ ($min^{-1}$) is the volume transfer constant, which expresses the rate of the unit volume of contrast agent (gadolinium) being transferred from the plasma to extravascular extracellular space (EES). This owns to either normal capillary permeability or abnormal leakiness of the tumour vasculature. Thus, $K^{trans}$ is directly proportional to how efficient a tumour is perfused and decreases with tumour size.

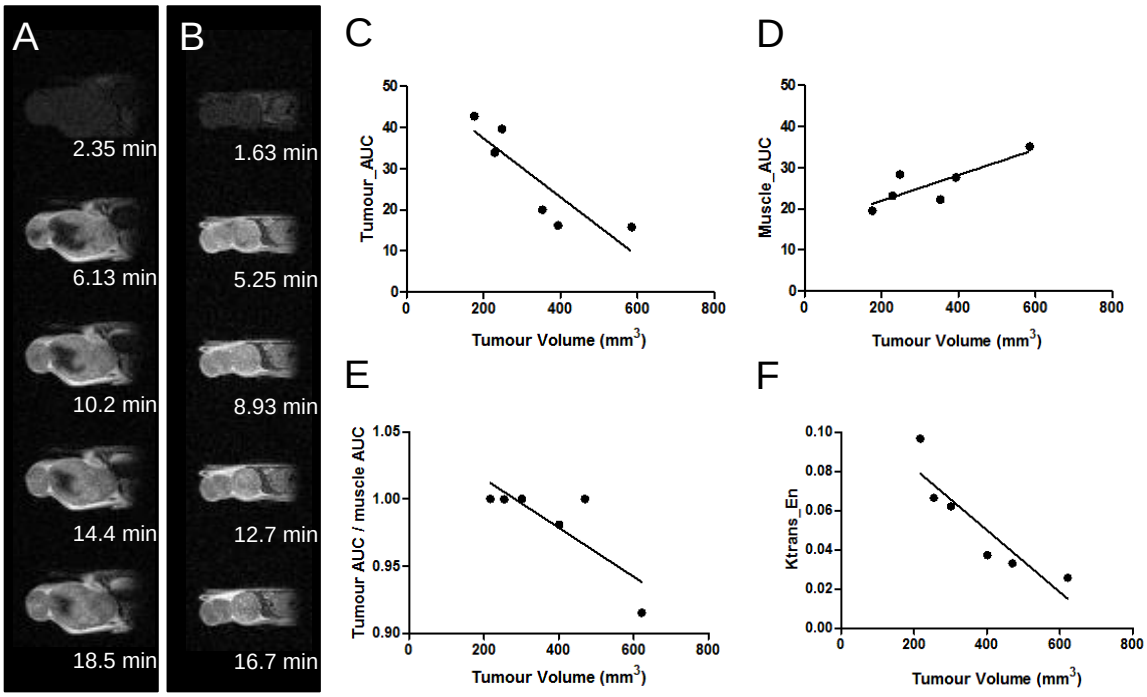



**Figure 5.19. DCE MRI results and their correlations with tumour volume, for colorectal derived tumours.** (A,B) Representative slice from 3D DCE MRI dataset, showing gadolinium enhancement over time, from (A) the largest colorectal tumour (621 $mm^3$) and (B) the smallest colorectal tumour (219 $mm^3$). (C-F) Linear regression analysis of the DCE data parameters with respect to the size of the tumour; (C) Tumour AUC for intensity signal against tumour volume, demonstrating a negative correlation with increasing tumour volume ($R^2 = 0.7272$; $P < 0.05$); (D) Muscle AUC of intensity signal against tumour volume, demonstrating a positive correlation with increasing tumour volume ($R^2 = 0.6899$; $P < 0.05$); (E) Tumour-to-muscle AUC revealed a negative correlation ($R^2 = 0.6716$; $P < 0.05$); (F) Mean tumour $K_{trans}$ rate constant parameter against tumour volume, indicating a strong negative correlation with increasing tumour volume ($R^2 = 0.8097$; $P < 0.05$).

### 5.3.5 Comparison of MPIO analysis with DCE MRI

The volumes of hypointensity measured in the cohort of colorectal tumour animals injected with c(RGDyK)-MPIO (see 5.3.3.1) showed a positive correlation with increasing tumour size ($R^2 = 0.05752$, $P < 0.05$; Figure 5.20 A). Interestingly, administration of c(RADyK)-MPIO on colorectal derived tumours also showed positive correlation of the same degree ($R^2 = 0.05837$, $P < 0.05$; Figure 5.20 B). This evidence indicates that specific and non-specific retention of MPIO will increase as the tumour volume increases, in the colorectal derived tumours. No significant correlation was found between the reduction of either mean intensities or $T_2$* relaxation times (pre-post) and tumour volumes, for both c(RGDyK)-MPIO or c(RADyK)-MPIO injected colorectal derived tumours (Figure 5.20 C-F). Moreover, these results indicate that although the retention, as we have seen previously, will increase as the tumour volume increases, the dephasing effect of the MPIO, as measured here globally, will be independent of tumour size.

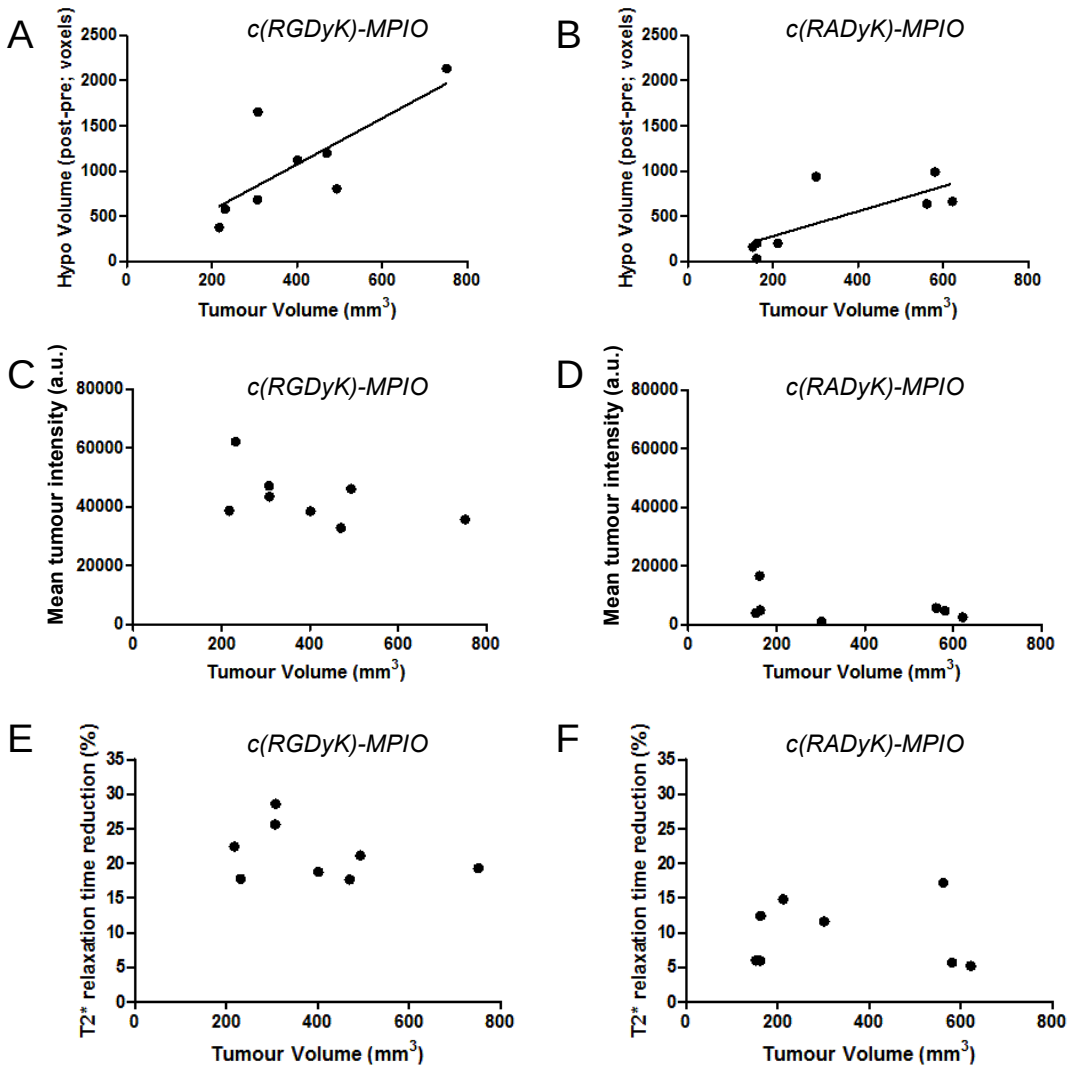



**Figure 5.20. Correlation of MRI analyses with tumour volume, for the colorectal derived tumours.** (A-B) Linear regression analysis of (A) c(RGDyK)-MPIO- or (B) c(RADyK)-MPIO-induced hypointense volumes (post – pre) against tumour volume, demonstrating a positive correlation with increasing tumour volume ($R^2$ = 0.05752, $R^2$ = 0.05837; $P < 0.05$). (C-D) Linear regression analysis of (C) c(RGDyK)-MPIO- or (D) c(RADyK)-MPIO-induced mean intensity reductions (pre - post) against tumour volume, indicating no relationship with increasing tumoru size. (E-F) Linear regression analysis of (E) c(RGDyK)-MPIO- or (F) c(RADyK)-MPIO-induced $T_2$* relaxation time reductions (pre - post) against tumour volume, indicating no relationship with increasing tumour size.

### 5.3.6 Immunohistochemistry (IHC) and immunofluorescence (IMF)

In order to confirm $\alpha_v\beta_3$ expression on tumour vasculature and specific binding of c(RGDyK)-MPIO onto $\alpha_v\beta_3$ expressing vessels, and furthermore, validate the quantitative MRI results, we have assess the tumour tissues histologically.

#### *5.3.6.1 Quantitative assessment of IHC and IMF*

Tumour tissue from both models was stained with Alexa Fluor 488 (green) for $\alpha_v$ and Texas Red for $\beta_3$ with a DAPI (blue) nuclear counterstain, in order to confirm specific binding of c(RGDyK)-MPIO to $\alpha_v\beta_3$ expressing endothelium. As shown in Figure 5.21 for melanoma (A-C) and colorectal (E-G) tumours, respectively, expression of $\alpha_v$ and $\beta_3$ co-localised on blood vessels. At the same time, the MPIO were detectable in the red channel owing to autofluorescence at this wavelength and could be seen to also co-localise to regions of $\alpha_V$ and $\beta_3$ expression (Figures 5.21 C and G; arrows). The MPIO were also clearly visualized in the equivalent phase contrast images (Figures 5.21 D and H; arrows). MPIO were also clearly detectable as brown spheres under bright field microscopy (Figures 5.21 I and J; arrows).

#### *5.3.6.2 Quantitation of MPIO binding from IHC*

Quantitative analysis of MPIO binding indicated significant differences in MPIO density per $\mu m^2$ tumour area between c(RGDyK)-MPIO and c(RADyK)-MPIO injected animals, for both melanoma tissue ($16.81 \pm 4.81$ *vs*. $1.21 \pm 0.84$; $P < 0.05$; Figure 5.22 A) and colorectal tissue ($18.34 \pm 0.42$ *vs*. $4.75 \pm 1.25$; $P < 0.0005$; Figure 5.22 B). Interestingly, the average area per vessel in the melanoma derived tumours was significantly greater than that of the colorectal tumours, with a mean vessel cross-sectional area of 2444 $\mu m^2$ compared to 1219 $\mu m^2$ ($P < 0.0001$; Figure 5.22 C). This greater vessel area was also reflected in the 10-fold higher c(RGDyK)-MPIO retention in the melanoma tumours, despite a lower vessel density (per unit tumour area) in the melanoma tumours than in the colorectal tumours ($P < 0.0001$; Figure 5.22 D). Vessel density analysis within groups showed little variation, and no significant change with tumour volume (Figure 5.22 E and F).

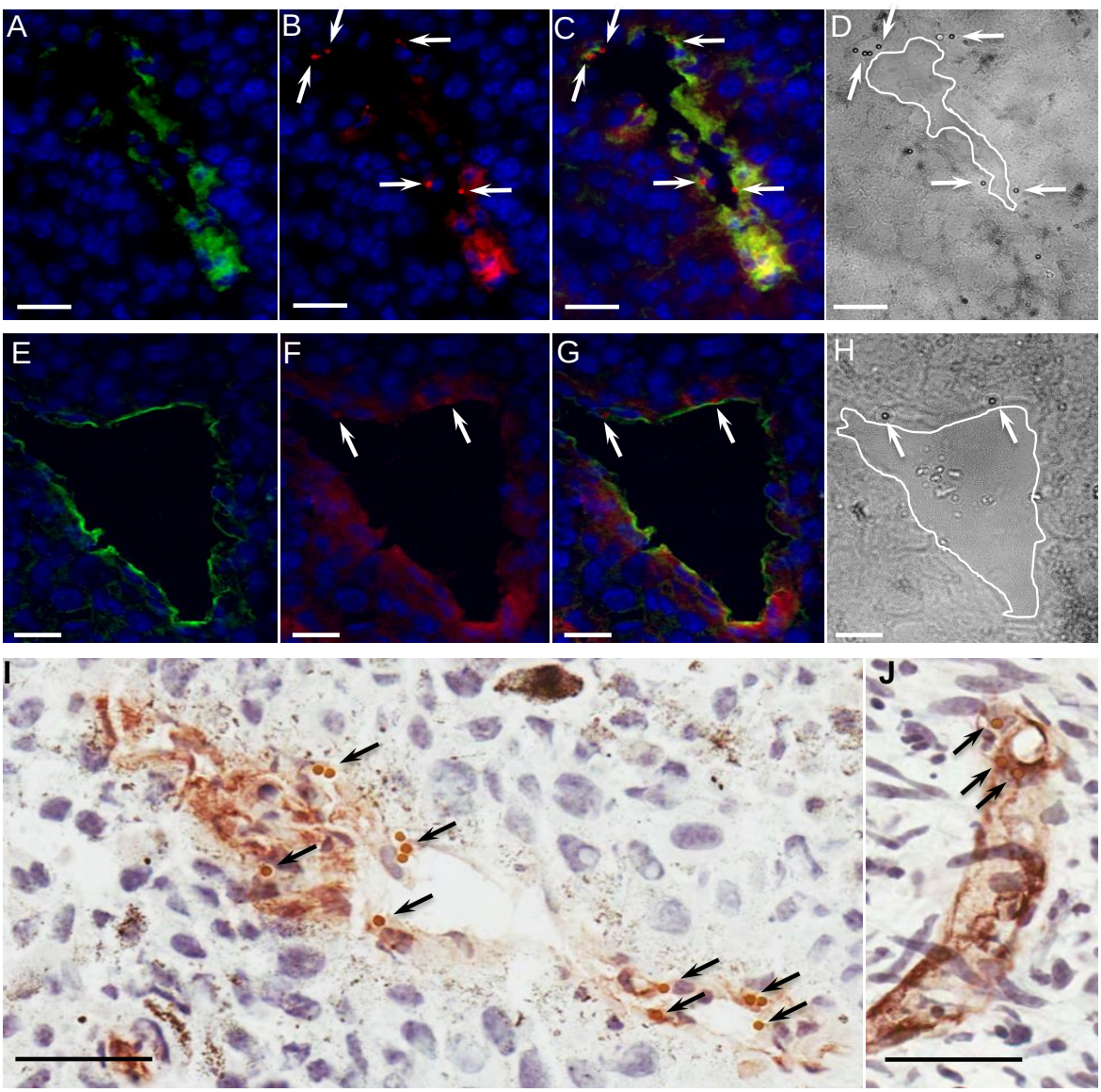



**Figure 5.21. Demonstration of specific binding of c(RGD)-MPIO on tumour vasculature, by IF and IHC.** Epifluorescence micrographs of (A-C) tissue from subcutaneous B16F10 (melanoma), or (E-G) MC-38 (colorectal) derived tumour stained for $\alpha_v$ (green) and $\beta_3$ (red) with a dpaiand nuclei counterstain with DAPI (blue). Expression of both $\alpha_v$ (A,E) and $\beta_3$ (B,F) clearly localized to vascular structures, and colocalised (yellow), with each other (C,G) in both tumour types. (D,H) Equivalent phase contrast micrographs in which c(RGDyK)-MPIO are clearly visible (arrows). (B,C,F,G,) c(RGDyK)-MPIO may also appear as red under this protocol (arrows). (I,J) Immunohistochemical micrographs from B16F10 (I) and MC38 (J) tumours showing vessels (CD31) stained brown and clearly detectable bound c(RGDyK)-MPI (arrows).

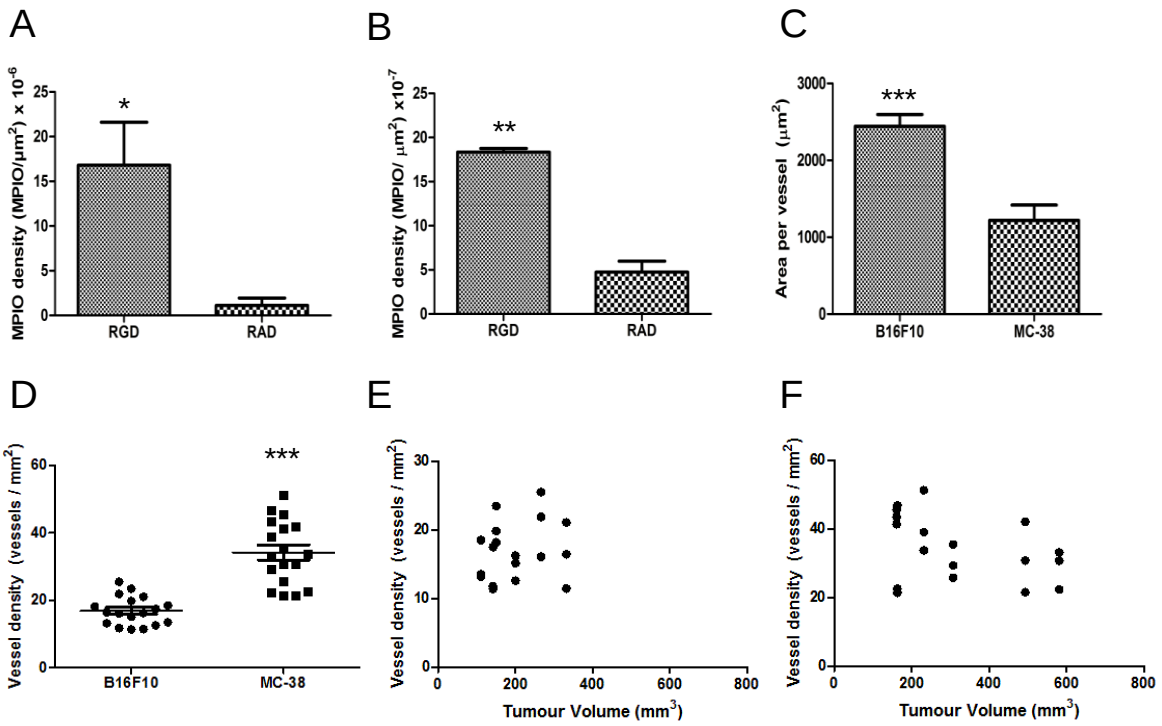



**Figure 5.22. Quantitation of specific binding of c(RGD)-MPIO on tumour vasculature, assessed from IHC treated sections.** (A,B) Quantitation of MPIO density per $\mu m^2$ tumour area for both c(RGDyK)-MPIO and c(RADyK)-MPIO treated groups in the B16F10 (melanoma; A) and MC38 (colorectal; B) models. (C) Graph showing quantitation of total vessel area per tumour. (D) Vertical scatter plot represent the number of vessels per $mm^2$ tumour area for both B16F10 and MC38 tumours, assessed immunohistochemically (n=6 per group, 3X field of view). Vessel density was significantly greater in the MC38 tumours than in the B16F10 tumours. Some spread in the vessel density was apparent, particularly within the MC38 cohort, and so the relationship with tumour volume was assessed (E,F). However, no significant correlations were found between tumour vessel density and increasing tumour volume, again indicating that tumour vascularity per unit tumour area remained largely constant across the range of tumour sizes studied (in accord with the $T_2$* analysis in Figure 5.20 F). *P < 0.05; **P < 0.005; ***P < 0.0001.

## 5.4 Discussion

Angiogenesis is of critical importance in the pathogenesis of cancer. Imaging processes associated with angiogenesis provide opportunities both for early tumor detection and for effective choice of specific treatments. Here, we have taken a cyclic RGD moiety, designed to have high affinity for the angiogenesis marker $\alpha_v\beta_3$, conjugated to microparticles of iron oxide and have demonstrated potent and quantifiable contrast effects *in vivo* owing to specific retention of c(RGDyK)-MPIO in two different mouse tumour models.

### 5.4.1 Comparison of MPIO based agents with NPIO or smaller molecules

Targeting the integrin $\alpha_v\beta_3$ with *in vivo* imaging agents has been attempted in a number of different approaches. Thus, the novelty of the approach described here lies, not in the targeting of $\alpha_v\beta_3$, by particles, but in the delivery of particles that are orders of magnitude larger than the nanoparticles that have more usually been used for this application. In an imaging context, the substantially enhanced payload of iron oxide delivers conspicuous, quantifiable contrast effects, which are aided by the rapid clearance of unbound blood phase MPIO, leading to excellent target to background contrast. Clearly, the ability to deliver large cargo loads also opens possibilities for therapeutic purposes.

Alternative widely used MRI contrast agents are based on paramagnetic gadolinium, in which the Gd(III) ion is chelated to low molecular weight ligands, such as diethylene triamine pentacetate acid (DTPA). However, binding of only a few gadolinium complexes to molecular targets cannot usually provide a sufficiently high contrast-to-noise ratio for robust detection. In order to enhance the detection sensitivity, Gd(III) complexes are very often loaded onto nanocarriers [178]. For instance, cross-linked liposomes with a high payload of gadolinium (containing 30% of Gd[III] chelate-labelled lipid) and a mean size of 300–350 nm were conjugated with an anti-integrin $\alpha_v\beta_3$ antibody [178]. After intravenous administration into rabbits with squamous cell carcinoma, regions of tumour angiogenesis were detectable by MRI. Other endeavours for improving MRI sensitivity for tumour angiogenesis imaging include developing Gd(III)-containing micelles, liposomes, or high-density lipoprotein-like nanoparticles. While these other approaches have used much smaller particles, one limitation that has been identified is the tendency for passive extravasation and accumulation, thereby diminishing molecular specificity, as found in tumour xenograft models implanted with non–small cell lung cancer cells [185]. In contrast, we have previously shown that MPIO are not internalised by either endothelial cells or peripheral immune cells (e.g. macrophages) during the period between injection and imaging [186]. A further limitation of nano-scale particles is their relatively long blood-half life, which greatly reduces the binding-specific contrast at short time frames after administration. As it has been demonstrated in this Thesis, the half-life of micron-sized particles in the blood is considerably shorter (< 1 min), thus yielding substantial benefits for detection of binding-specific contrast changes.

These features are important advantages of microparticles over nanoparticles for potential clinical application, together with the greater targeting ligand valency that can be achieved.

Towards clinical application we have developed a new class of biodegradable iron oxide microparticle in which 60nm nanoparticles are linked together to form larger (approx. 600 nm) particles using peptide bonds that are selectively susceptible to cleavage by macrophage enzymes [340].

### 5.4.2 Binding characteristics

Micron sized particles of iron oxide have proved successful in imaging molecules differentially expressed on vascular endothelial cells in disease states across a variety of clinically relevant pathologies [186-195]. In earlier work, to enhance target affinity, leukocyte mimetic strategies have been developed, in which dual targeting of antibodies, e.g. recognizing VCAM-1 and P-selectin, markedly improved target-MPIO binding [186, 195]. These molecules are regulated at sites of vascular inflammation, where they mediate the binding of mononuclear leukocytes prior to their migration across the vessel wall. Systematic evaluation of a variety of ligands under variable flow conditions demonstrated that dual antibody targeting provided superior binding compared with either antibody individually *in vitro* [341]. Since, the integrin $\alpha_v\beta_3$ comprises two subunits, this rises the possibility of a similar dual targeting approach to increase MPIO-target affinity. However, although antibodies can be generated against each subunit, the spatial relationship of MPIO surface mounted antibodies and cell membrane-associated $\alpha_v\beta_3$ and sub-units would not be predictable. In order to enhance binding, therefore, an alternative approach was adopted, in which the cognate ligand RGD was mounted on the surface of MPIO in a multivalent configuration. The binding affinity of c(RGDyK) to $\alpha_v\beta_3$ has previously been described in comparison to c(RGDyK)-functionalised quantum dots (QD) [342]. Owing to the polyvalent presentation of the c(RGDyK) on the MPIO, we believe that the $IC_{50}$ of the functionalised particle will be in the low nanomolar range. Variable shear rate flow chamber experiments, calculated in R.C.'s laboratory, demonstrated that c(RGDyK)-MPIO bound at low shears equivalent to what might be expected in small vessels and veins. In the current study, *in vivo* administration of c(RGDyK)-MPIO enabled molecular imaging of integrin $\alpha_v\beta_3$ on tumour neovasculature. Retention was specific, as confirmed by enhanced binding of c(RGDyK)-MPIO compared with c(RADyK)-MPIO.

### 5.4.3 MPIO induced contrast effect

MPIO's have a dephasing effect that far exceeds their physical size, approximately 50 times their physical diameter [332]. Therefore, the 2.8 μm will extend for a volume of approximately 150 μm, in diameter. The resolution of the MGE3D datasets where chosen to be approximate to the sphere of influence of a single MPIO, which is more than the half of a volume of single voxel at 150 μm resolution datasets; sphere to cube ratio is 51% (Figure 5.23). However, the contrast effect is 'negative' (i.e. low signal), which can present challenges to distinguish MPIO from features of tissue heterogeneity. In the current study both tumour models showed intrinsic $T_2$*-weighted inhomogeneities, although to varying

degrees, reflecting differences in tumour growth and cell density. For this reason, it was necessary to obtain pre- and post-contrast MR acquisitions to enable distinction between pre-existing and MPIO-specific hypointensities. However, the injectable medium with MPIO when inside a strong magnetic field, experience strong magnetic forces and the particles tent to aggregate. Therefore, the injections of the contrast agent were administered outside the magnet room, by removing the fixed coil-cradle-mouse complex (see 5.2.4). Despite preserving the same positioning of the mice in the coil, acquisition of pre- and post-contrast datasets were not possible to be registered with voxel to voxel accuracy, neither it was possible for the sample shimming to be identical in the pre- and post-contrast agent scans. Thus, direct subtraction of images is not possible and alternative analytical approaches are required. To this end independent analysis of pre- and post-contrast datasets was performed and paired statistical analysis used to assess MPIO-induced changes. In order to validate the observed MPIO-induced contrast effects, given the aforementioned limitations, 3 separate data analysis approaches for the quantification of $T_2$*-weighted datasets were implemented. The aim was to determine whether these analysis approaches yielded comparable and/or complementary information, and at the same time insight as to their suitability for quantification.

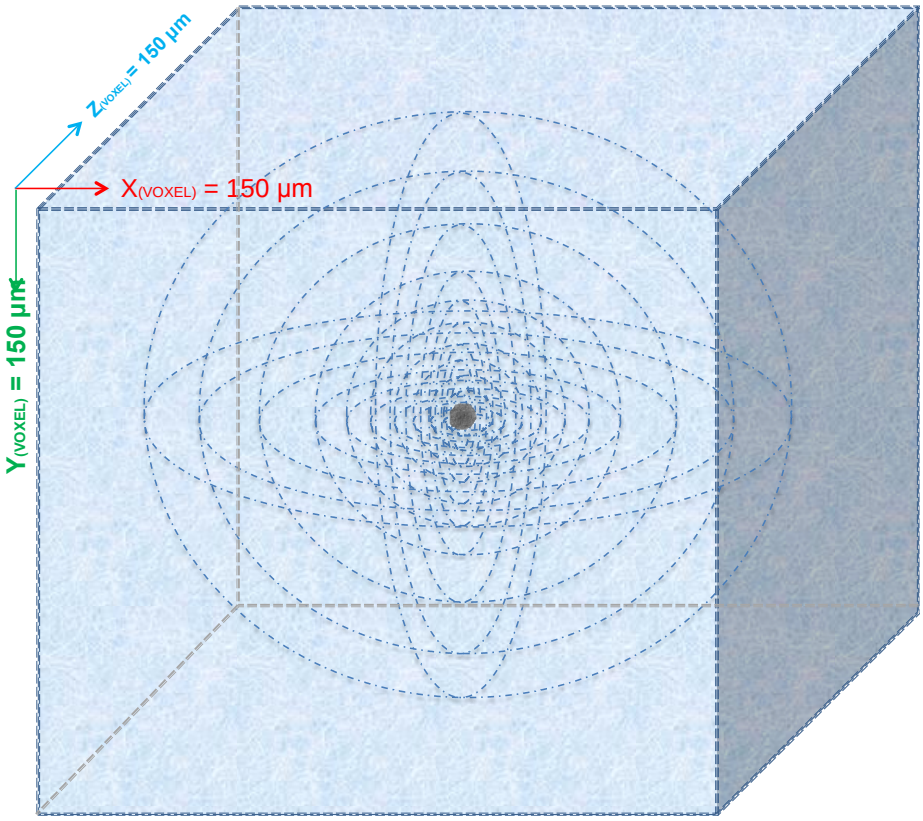



**Figure 5.23. Schematic representation of the dephasing magnitude of a single MPIO, within a cube of water based molecule.** MPIO with 2.8µm diameter are expected to have a sphere of dephasing influence with a radius of 75µm. This will be equal to approximately the 51% volume ration with a single voxels of 150 µm unit resolution.

### 5.4.4 Quantitative analyses

#### *5.4.4.1 Hypointensity volumes*

The volumetric analysis of MPIO-induced hypointensitites identifies individual voxels that are darker than their local surrounding voxels. This automated method was originally developed for much more homogeneous tissues (brain) compared to the subcutaneous tumours in this study and for a single post-contrast dataset. The results of this method have been compared previously with a manual, semi-automated approach and yielded outstanding accuracy between the two (Hamilton A., DPhil Thesis 2013, Oxford University). However, the concept of paired datasets (pre- and post-contrast agent administration) required modifications to certain parameters to work reliably and accurately in the current subcutaneous tumours.

Analysis of pre-contrast datasets yielded hypointensity volumes correlating to natural imhomogeneities in the tumours, since MPIO are absent. Since the natural inhomogeneities are tumour type dependent, the thresholding parameter (FLM) had to be optimised separately for each tumour type in order to minimise the non-MPIO related positive detection (i.e. the natural darkened areas). However, within each tumour group good consistency was evident in

the effectiveness of the optimised FLM for that tumour type. Subsequently, analysis of the post-contrast datasets using the optimal FLM enables identification of the MPIO-induced hypointensity volumes as well as hypointensities associated with natural inhomogeneities. By subtracting the hypointensity volumes of the pre-treatment from the post-treatment datasets, effects due to non-MPIO causes are eliminated.
However, there are three potential caveats to this method:

a) From the volumetric analysis we exclude positive events (voxels) that are geometrically related (connected) and are more than 20 voxels volume, as they considered to most likely arise from natural inhomogeneities. As a result, there is a possibility that two average size positive events (e.g. 10 voxel volume, which is included in the analysis) identified in the pre-contrast treatment datasets, which are separated by one voxel, could be joined to a combined large positive event (excluded from the analysis) if MPIO are present in the separating voxel in the post- contrast datasets (Figure 5.24). Thus, the MPIO positive voxel will be excluded from the analysis and the two middle size areas also, leading to potential underestimation of MPIO-induced hypointensities.

b) In accord to the same line of thinking, an MPIO-induced event of a single voxel, which is located within a hypointense region, thus geometrically related to a large positive event (excluded from analysis), will not be included in the analysis (Figure 5.25). Again, there is a potential of MPIO-induced hypointensities to be underestimated.

c) The size of the particles is significantly less than the voxel size (2.8 μm *vs.*150 μm). This means that each voxel could contain up to 12500 MPIO, volumetrically. If we accept this hypothesis as an example, then this voxel should result in much greater dephasing effect than a voxel that contains only few MPIO. However, this method anaysis does not distinguish the density of MPIO per voxel, simply returning either positive or negative detection event per voxel. (Figure 5.26). Thus, the sensitivity of this approach to MPIO density is limited by the image resolution and information is consequently lost.

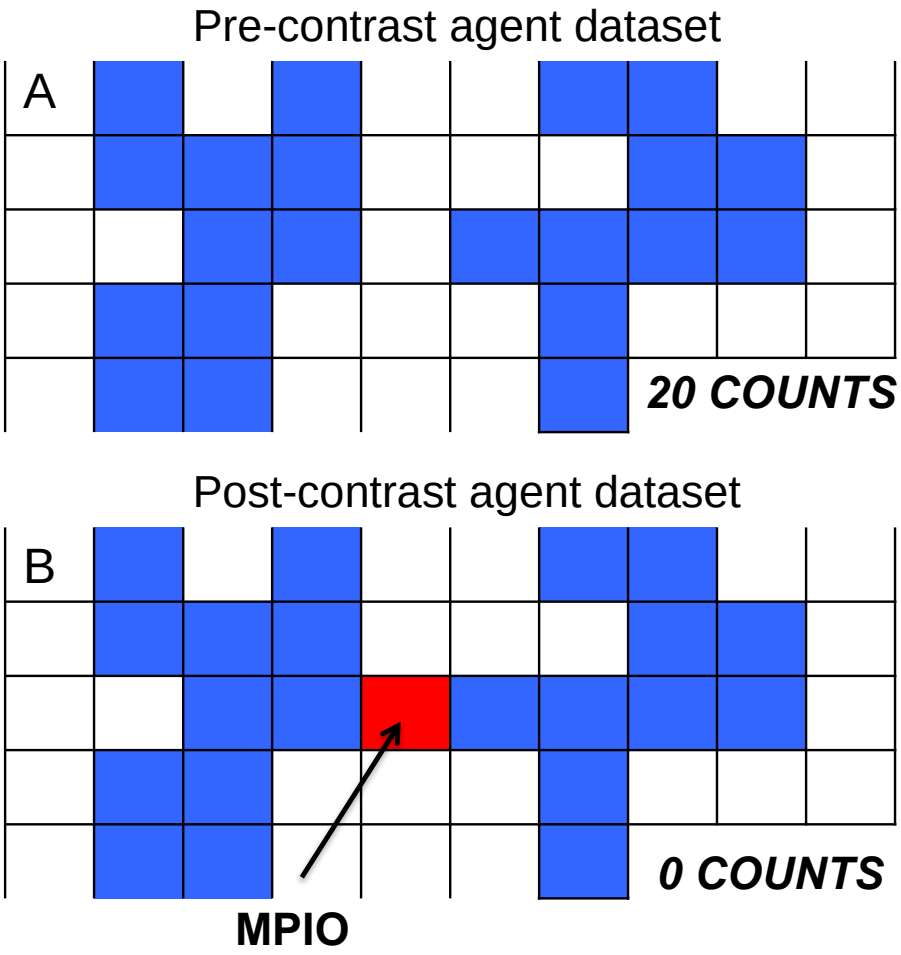



**Figure 5.24. 1st theoretical example of underestimated MPIO-induced hypointensities in the volumetric analysis.** (A) Two volumes (blue) of 10 voxels, one voxel distant form each other, are detected by the hypointensity analysis on the dataset prior to MPIO administration. These 2x 10-voxel volumes, fall within the acceptable volume threshold (< 20 voxels), and thus, will be counted as a total 20 voxel volume, that will be finally subtracted from the total hypointensity volume of the post-MPIO administration dataset analysis. (B) An MPIO-induced hypointensity (red) in the voxel that geometrically separates the 2x 10-voxels volumes, will join them to a large 21 voxels volume. This volume will be larger than the volume threshold and will be excluded for the total volume. Therefore, the 20 voxel volume of the pre-MPIO scan (A) will be subtracted from the total volume of the post-MPIO hypointensity volume (B), although it has not been included in this final volume.

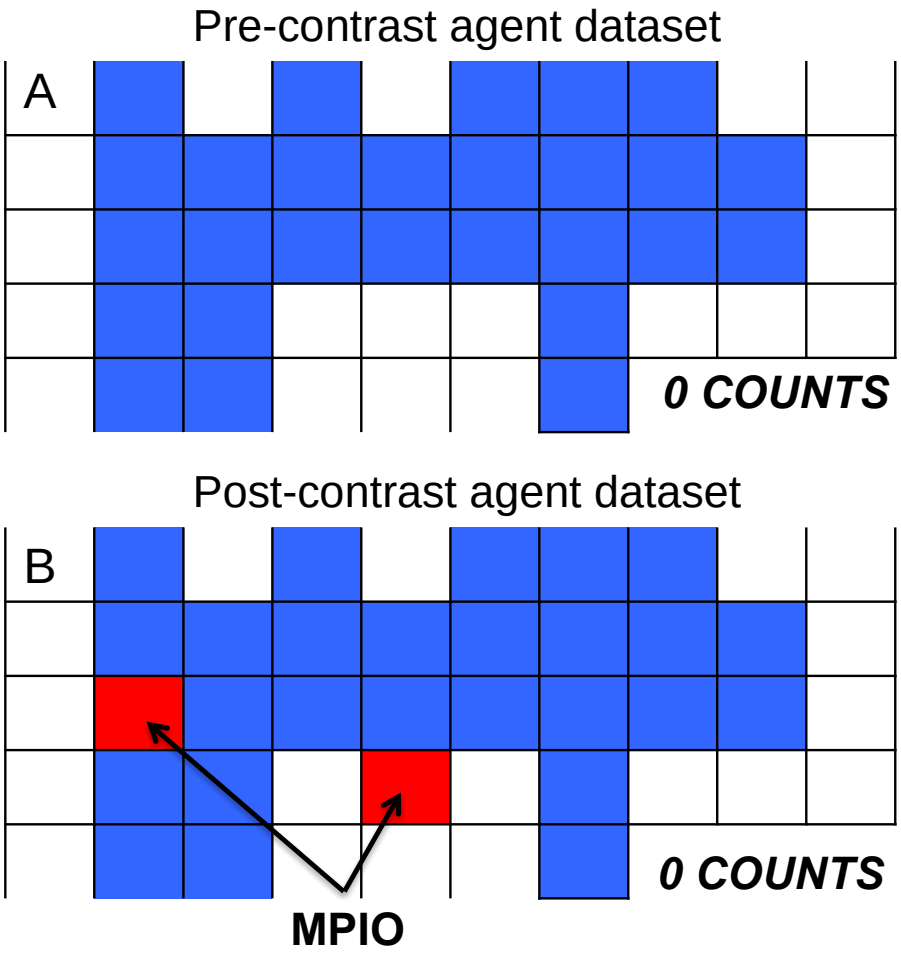



**Figure 5.25. 2nd theoretical example of underestimated MPIO-induced hypointensities in the volumetric analysis.** (A) Positive detected volume (blue) of > 20 voxels volume, in the pre-MPIO dataset. This volume will be excluded from the analysis as it falls above the volume threshold. (B) After administration of MPIO, two MPIO (red) are located; a) inside the previously > 20 voxel detected hypointense volume (red square right), and b) in a voxel geometrically connected to the previously > 20 voxel detected hypointense volume (red square right). These two MPIO, or either case individually, if identified in the post–MPIO dataset, will be excluded from the analysis as a part of a volume above the volume threshold. Therefore, the MPIO will remain undetected in this case.

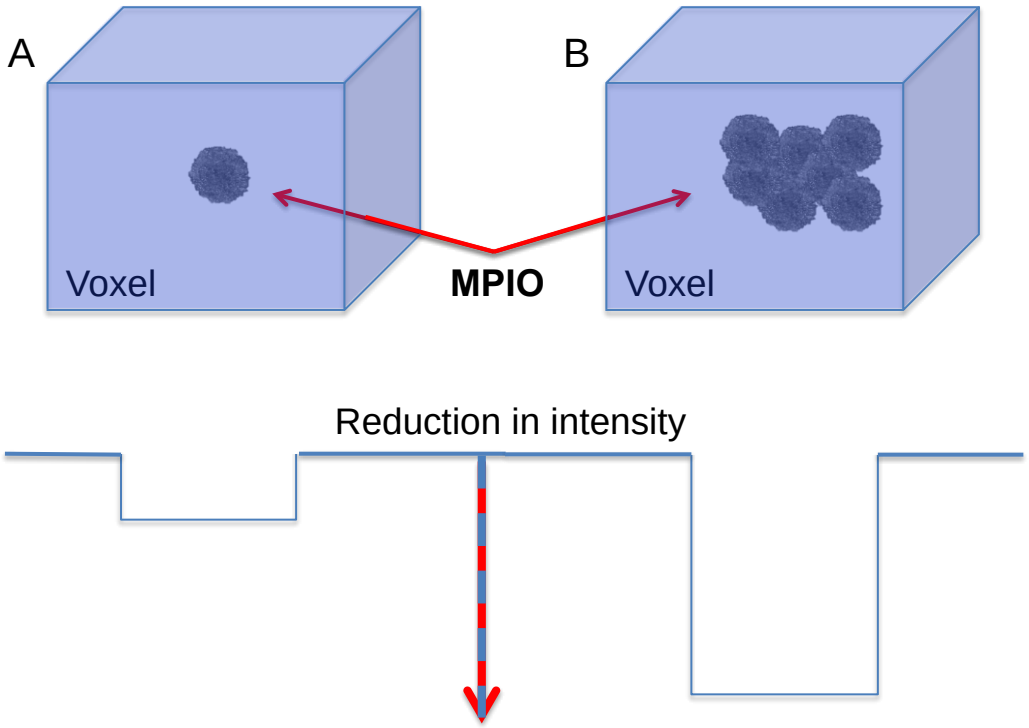



**Figure 5.26. Schematic diagram illustrating the relationship between MPIO density and signal intensity reduction.** (A) Prepresentation of a single spartial resolution unit (voxel) that encloses 1x MPIO. (B) Prepresentation of a single spartial resolution unit (voxel) that encloses 7x MPIO. Underneath each voxel there is an intensity reduction dip that represents by how much the signals of the voxels should be reduced. As the MPIO density per voxel will increase the voxel intensity will decrease.

### *5.4.4.2 Mean tumour intensities and $T_2$* relaxation times*

Given the aforementioned theoretical limitations of the volumetric analysis, we have implemented aiming to determine whether these analyses yielded comparable and/or complementary information to the more complex volumetric image segmentation approach. Mean intensity and $T_2$* analysis, both account for the present of a multiple MPIO in the same voxel. However, the $T_2$* relaxation time estimations it is assumed to be more accurate measurement, less prone to shimming differences and pre existing hypointensities, related with inhomogeneities. Although mean tumour intensity implementation included the effects of intrinsic tumour inhomogeneities the pre- and post-contrast values allowed assessment of the reduction in intensity by MPIO retention. As described previously (see 5.3.3.4.b-c), both approaches also confirmed the specific binding of c(RGDyK)-MPIO, compared to c(RADyK)-MPIO, by a greater shortening of global mean tumour intensity and $T_2$* relaxivity in both models.

#### *5.4.4.3 Comparison of MRI quantitation methods*

The results of all three methods, as described (Figure 5.27, 5.28 and 5.29), have confirmed specific binding with comparable statistical significances. The melanoma derived tumours, with more severe inhomogeneities than the colorectal derived tumours showed greater within group variability in both the volumetric analysis and mean tumour intensity quantitacation. Consequently, the specific binding showed lower statistical significance than was found in the $T_2$* relaxation time quantitation. In contrast, the colorectal group showed much lower within group varaibility in all three quantitation methods, with excellent agreement between the outputs. This agreement between methods was even more apparent in the size restricted analysis of the colorectal model, where statistical significance for the paired analysis of $T_2$* relaxation time in the cRGD-MPIO treated group was higher than the other two methods for both small and large volume tumour groups. Furthermore, $T_2$* relaxation rate it was the only method showed significant difference between the targeted [c(RDGyK-MPIO] and control [cRADyK-MPIO] groups, in both volume sub-groups; hypointensity volumes did not show significant difference between the targeted and control groups for either volume limited sub-group and mean tumour intensityanalysis only showed significant difference in the large volume group. Herein, the $T_2$* relaxation rate measurement is proved to be more sensitive than the other two methods. However, as we have seen from the correlations of the methods with tumour volume, the implementation of the mean intensity and $T_2$* relaxation rate analysis provide information on the global MPIO-induced changes while the volumetric hypointensitiy analysis implementation on the local MPIO-induced changes. These data suggest that the relaxivity analysis method may be more sensitive to non-specific retention of MPIO that are too dispersed to detect with the thresholded volumetric analysis.

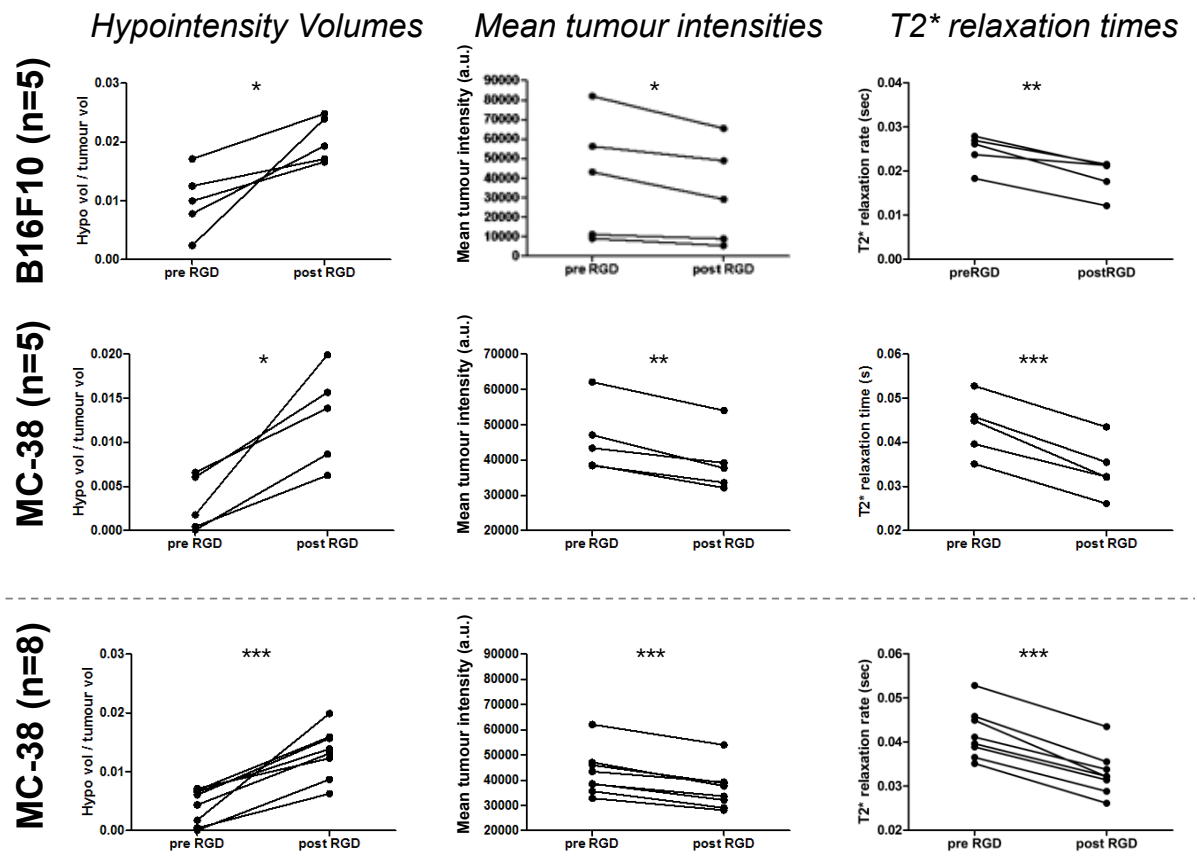



**Figure 5.27. Outline of all paired analyses for c(RGDyK)-MPIO treated groups, for all implemented MRI analyses.** Each column represent a different MRI dataset analysis; (from left to right) Hypo-volumes, Mean Intensity volumes, $T_2$* relaxation rate. The first row represent the melanoma derived tumours (n=5) injected with c(RGDyK)-MPIO, and the second the equivalent results from colorectal derived tumours (small size, n=5). The 3$^{rd}$ row shows the whole cohort of colorectal derived tumours injected with c(RGDyK)-MPIO (n=8).

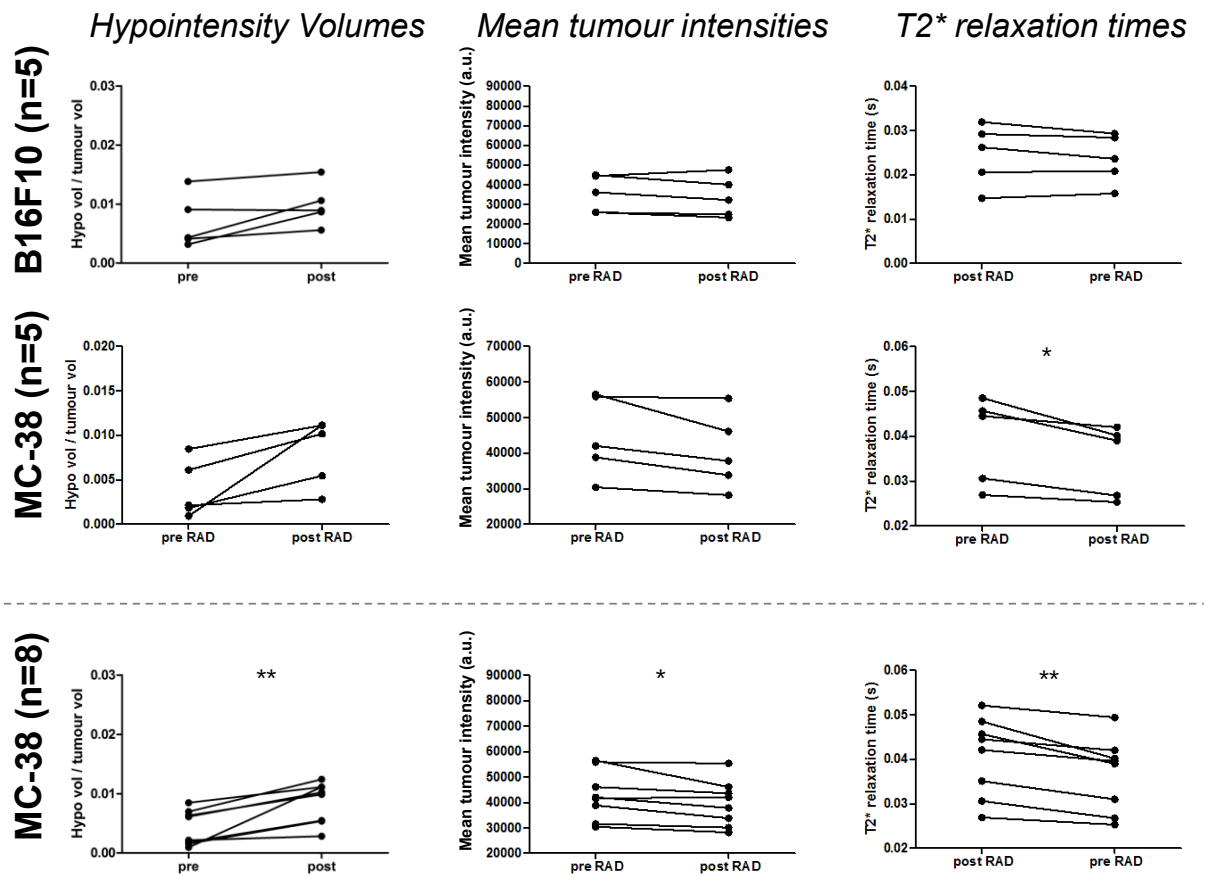



**Figure 5.28. Outline of all paired analyses for c(RADyK)-MPIO treated groups, for all implemented MRI analyses.** Each column represent a different MRI dataset analysis; (from left to right) Hypo-volumes, Mean Intensity volumes, $T_2$* relaxation rate. The first row represent the melanoma derived tumours (n=5) injected with c(RADyK)-MPIO, and the second the equivalent results from colorectal derived tumours (small size, n=5). The 3rd row shows the whole cohort of colorectal derived tumours injected with c(RADyK)-MPIO (n=8).

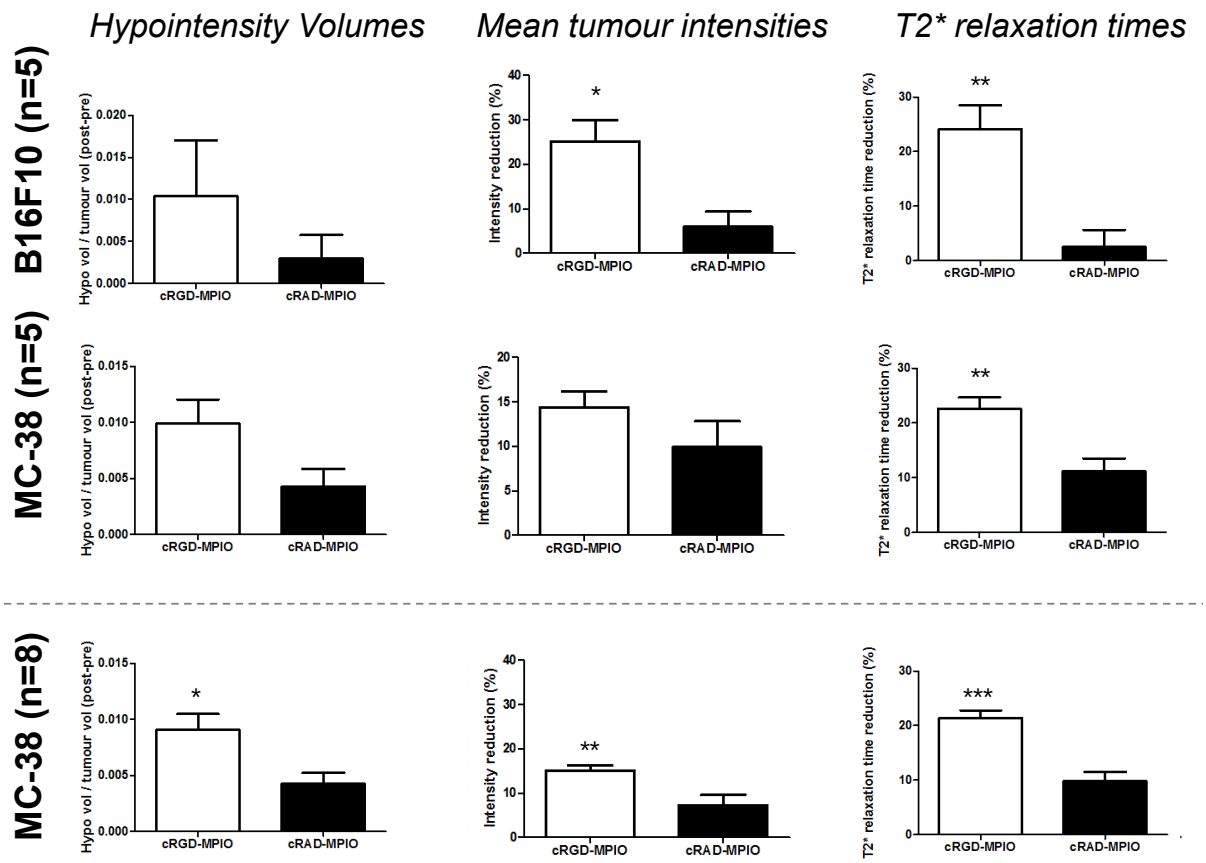



**Figure 5.29. Outline of all un-paired analyses for c(RGDyK)-MPIO treated groups, for all implemented MRI analyses.** Each column represent a different MRI dataset analysis; (from left to right) Hypo-volumes, Mean Intensity volumes, $T_2$* relaxation rate. The first row represent the melanoma derived tumours (n=5) injected with c(RGDyK)-MPIO, and the second the equivalent results from colorectal derived tumours (small size, n=5). The 3$^{rd}$ row shows comparison of c(RGDyK)-MPIO and c(RADyK)-MPIO treated groups for the whole cohort of colorectal animals (n=8).

### *5.4.4.4 Comparison of MRI with IHC quantitation*

Importantly, all MRI quantitative analysis methods correlated well with histological quantitation of the c(RGDyK)-MPIO binding, for both tumour models. The two subcutaneous tumour models showed slightly different patterns of c(RGDyK)-MPIO retention, in accord with the spatial distribution of their vasculature. The melanoma-derived tumours, with double the mean vessel area of the colorectal-derived tumours, showed largely constant c(RGDyK)-MPIO induced hypointensities across the tumour volume, with the exception of a small poorly-vascularised rim region that did not show c(RGDyK)-MPIO retention. In contrast, the colorectal-derived tumours tended to show greater heterogeneity in c(RGDyK)-MPIO induced hypointensities across the tumour volume. These findings are in accord with other reports in the literature of the binding distribution of angiogenesis-targeted $^{19}$F- and Gd-based nanoparticles in experimental tumour models, in which patterns of particle and vessel distribution vary according to tumour type and site [343-346].

All three MRI quantitative methods reflected the same pattern in the analysis between targeted and control groups; in the melanoma group the differences between the c(RGDyK)-MPIO and c(RADyK)-MPIO were consistently greater compared to the colorectal group, however, the differences between targeted and control groups were more significant for the colorectal group.

#### *5.4.4.5 Control peptide c(RADyK)*

Interestingly, administration of the control contrast agent showed significant retention of MPIO in the colorectal model, but not in the melanoma model. This finding may reflect the smaller average vessel diameter in the colorectal derived tumours, since the probability of the MPIO's to be scavenged from the microvasculature should increase as vessel cross sectional area decreases. Notably, the $T_2$* relaxation time quantitation of control contrast agent confirmed significant reduction in both small and large size tumours, although a significant effect was only observed in the larger volume tumours for the volumetric analysis. These observations suggest two possibilities – firstly that as the tumours grow bigger more non-specific MPIO retention occurred owing to compromise of vascular perfusion and potentially agent "pooling" in the tumours, or secondly that there is some non-specific binding of the RAD-MPIO. With respect to the latter point, the control peptide [c(RADyK)] is not an isotype control and has been derived from the RAD-based peptide, by substitution of alanine (Ala = A) for glycine (Gly = G). The use of this contrl was based on data indicating that such substitution significantly reduces the affinity of the peptide for $\alpha_v\beta_3$. Nevertheless, this peptide will still show some affinity for $\alpha_v\beta_3$ [347] and therefore this may explain the non-specific retention.

### 5.4.5 Concomitant DCE

Finally, it is important to note that the molecular MRI approaches described here, are compatible within the same imaging session with other MRI-based measurement of tumour vascularity and permeability. Interestingly, whilst DCE measures of vascular perfusion and permeability showed a negative relationship with increasing tumour volume, volumetric analysis of c(RGDyK)-MPIO binding showed a positive correlation with tumour volume. The former likely reflects slow blood flow through the poorly perfused central tumour regions (as can be seen in the DCE images) which, nevertheless, does not appear to alter the ability of the c(RGDyK)-MPIO to bind effectively within these vessels. No correlation was found between the percent reduction in global tumour $T_2$* relaxation time and increasing tumour volume, indicating that this measure was independent of tumour size. This finding suggests that the average vascularity per unit tumour volume did not change markedly with increasing tumour size (across the range studied), as confirmed histologically. Taken together, the molecular MRI data (volume and $T_2$* relaxation) indicate that vascularity increases linearly with tumour growth over the size range studied. It is possible that this relationship will change once substantial necrosis develops within the core of the tumour, leading to either vessel

destruction and reduced MPIO access and binding, and/or pooling of contrast agent owing to greater compromise of vascular perfusion through intact vessels. Nevertheless, over the tumour size range studied, our data indicate that despite some reduction in tumour perfusion with tumour growth, the c(RGDyK)-MPIO are able to reach their targets and provide a reliable biomarker of intact tumour vessels. Thus, the molecular approach described here may provide a more accurate measure of vessel number, whilst the complementary DCE data provide information on vascular perfusion and permeability. Together, these methods may enable more effective patient stratification for specific therapies and provide useful biomarkers of efficacy in therapeutic trials.

## 5.5 Conclusions

Alternative, widely used MRI contrast agents are based on paramagnetic gadolinium, in which the Gd(III) ion is chelated to low molecular weight ligands, such as diethylenetriaminepentacetic acid (DTPA). However, binding of only a few gadolinium complexes to molecular targets cannot provide a sufficiently high contrast-to-noise ratio for robust detection. In order to enhance the detection sensitivity, Gd(III) complexes are very often loaded onto nanocarriers [178, 179]. For instance, cross-linked liposomes with a high payload of gadolinium (containing 30 % Gd[III] chelate-labelled lipid) and a mean size of 250-350 nm have been conjugated with an anti-$\alpha_v\beta_3$ antibody or specific peptomimetic [178, 179]. After 2 hours of intravenous administration into rabbits with squamous cell carcinoma, regions of tumour angiogenesis were detectable by MRI. Work in mice-bearing subcutaneous tumours using similar paramagnetic nanocarriers conjugated to anti-integrin αvβ3 peptidomimetic was able to characterise the angiogenic phenotype in early melanoma [180], whilst $\alpha_5\beta_1(\alpha_v\beta_3)$-targeted nanocarriers have enabled 3D maps of angiogenesis in xenographs to be constructed [181]. Again, to enable sufficient contrast accumulation, MRI assessments were performed 2 h post-administration of the contrast agent, owing to the limited binding efficiency at earlier time points. Other endeavours for improving MRI sensitivity for tumour angiogenesis imaging include developing Gd(III)-containing micelles, liposomes, or high-density lipoprotein-like nanoparticles. Work in mice bearing subcutaneous tumours with RGD-liposomes have been able to reduce the time of MRI assessment post-administration to 35 minutes, with sufficient $T_1$-W contrast to characterise angiogenesis [182, 183]. In that work, there was evidence that unbound nanoparticles had extravasated from the vasculature [182, 183], but this was considered insignificant for $T_1$-W imaging of the nanoparticles, owing to the relatively small contrast effect of the Gd. However, extravasation of an equivalent number of USPIO would cause significant non-specific contrast on $T_2$-W imaging. For example, specific targeting of tumour angiogenesis has been demonstrated using RGD-USPIO conjugates (< 100 nm) [184], in squamous cell carcinoma-bearing subcutaneous xenographs. One limitation that was identified, was the tendency for passive extravasation and accumulation, thereby diminishing molecular specificity, as also found in tumour xenograft models implanted with non–small cell lung cancer cells [185]. In contrast, we have previously shown that MPIO are not internalised by either endothelial cells or peripheral immune cells (e.g. macrophages) during the period between injection and imaging [186].

A further limitation of nano-scale particles is their relatively long blood half-life, which increases background contrast effects and greatly reduces the binding-specific contrast at short time frames after administration. As demonstrated here, the half-life of micron-sized particles in the blood is considerably shorter (< 1min). We have previously demonstrated that this clearance occurs primarily through the liver and spleen, with minimal retention in non-target organs (e.g. kidney, lungs, brain), but cannot exclude a role of complement in this process. In common with previously described molecular imaging approaches [186-195], we show empirically that specific MPIO binding to target is sufficient to attain effective contrast. In imaging vascular inflammation using a particle targeting vascular cell adhesion molecule-1 (VCAM-1) we have previously shown that specific binding has occurred within 20 minutes of administration and that this was maintained at a constant level for at least 60 minutes [188]. If reproduced in humans, these characteristics would be ideal for clinical application.

In conclusion, we present a polyvalent c(RGDyK)-MPIO that binds specifically to the integrin $\alpha_v\beta_3$ in tumour neo-vessels. Unbound MPIO are cleared rapidly from circulation. The result is a marked and quantifiable contrast effect that is evident both on $T_2$* weighted images as intensely low signal volumes and through automated quantitative pan-tumour $T_2$* relaxivity analysis. Recently developed biodegradable MPIO make clinical translation a realistic possibility, thereby enabling integrated molecular, anatomical and perfusion tumour imaging with MRI.

# Chapter 6 – Discussion

It has become increasingly apparent over the past few years in the field of cancer research that molecularly sensitive imaging will provide essential insight into the mechanisms that dictate cancer development and progression. *In vivo* molecular imaging provides a strategy to target important molecular markers that play a role in the hallmarks of cancer. The application of molecular imaging using established molecular markers can provide a tool for diagnosis, or management of treatment. In this thesis, I have focused on the diagnostic application of molecular imaging and have shown, firstly, that early detection of pulmonary metastasis is possible by targeting the endothelial inflammation marker VCAM-1 and, secondly, that characterisation of angiogenesis can be improved by targeting $\alpha_v\beta_3$.

## 6.1 MPIO *vs.* NPIO

The work of this thesis has encompassed two major imaging projects, both of which have used microparticles of iron oxide (MPIO). The size of the MPIO has been the key element behind the *in vivo* pharmacokinetics of these particles, which enables rapid imaging without background noise arising from circulating unbound MPIO. The rapid clearance of these micron-sized particles from the blood circulation provides a clinically practical time window for molecular imaging application, in comparison to the widely used nanoparticles of iron oxide (NPIO), which have a much longer circulating half-life. Furthermore, MPIO deliver a substantially greater payload of iron oxide to a single molecular biomarker than NPIO, thus providing potent contrast on MRI.

## 6.2 Pulmonary micrometastasis detection

Currently, the primary problem with tumour metastasis is undoubtedly the lack of early detection of the metastatic process; invasion and micrometastasis formation. Consequently, detection and therapy in the clinic often occurs beyond the point of effective therapeutic intervention. The mechanism and steps involved in metastatic development are not fully understood yet, and arguably the most efficient stage of detection would be prior to cell invasion (CTCs) or as early as single cell invasion. However, although progress is being made in this respect, this remains a substantial challenge. Perhaps a more tractable problem is the lack of metastatic clinical staging, where significant advantages might be gained if improvements could be made. Currently, patients are clinically classified and staged as a single group, M1 patients, irrespective of whether they have just a single metastatic colony or many metastatic colonies and they receive the same cancer metastasis treatment. This approach of one-therapy fits-all in metastasis patients is clearly a consequence of the lack of

metastatic staging, which is largely due to the lack of clinical detection methods that can characterise the disease at early stages after tumour cell invasion.
The work described here was based on previous studies in the group demonstrating that in mouse models brain metastasis can be detected much earlier than conventional clinical methods allow and at a time when therapeutic intervention may be considerably more effective [195]. On the basis of this previous work and the work of this thesis, we believe that our imaging approach can provide a sensitive tool for metastatic staging and, consequently, help to improve cancer metastasis treatment.
In this thesis I have presented proof-of-principal experiments for pre-clinical pulmonary volumetric micrometastasis detection in mice, sensitive to metastases at a size smaller than any other method reported to date. If translated into the clinic this approach will open a therapeutic window for lung metastasis treatment that is currently not available, allowing prompt and effective clinical intervention. The volume of mouse lung is 3000-fold smaller than human lung and, therefore, I hypothesize that the translation of our pulmonary micrometastasis PET detection approach could be translated into the clinic with remarkable sensitivity for metastases detection in human lungs, which might allow for single micrometastasis localisation. Concerning clinical translation, one limitation of our approach, as presented in this thesis, is undoubtedly the toxicity of the commercially available MPIO. To this end, considerable work is underway towards the development of micron-sized multimeric biodegradable MPIO (Perez-Balderas, under review, *Nat. Med*.) which make the possibility of clinical translation more realistic. At the same time, the group has produced a new fully humanised anti-human VCAM-1 antibody for clinical application. Another limitation of our imaging approach, concerning molecularly targeted clinical pulmonary detection of micrometastasis by targeting VCAM-1, is that the inflammatory protein VCAM-1 is involved in chronic inflammation pathology. Therefore, respiratory diseases such as asthma and COPD [348] or smoking [349] can increase the expression of VCAM-1 in the lungs. Consequently, the method might not be suitable for certain type of patients; thus, the levels of VCAM-1 expression on these cases must be carefully evaluated.

## 6.3 Detection of multi-organ micrometastasis

As described in Chapter 4, the initial aim of this project was the detection of pulmonary micrometastasis with MRI using hyperpolarised gases, which has not proved possible. Remarkably, this set back was the driving force behind the development of a multimodality imaging probe. Consequently, in this work I have provided evidence to support the concept that our newly developed PET/MRI probe has the potential for PET/MRI multi-organ micrometastasis detection. In recent years, considerable effort has been devoted to the development of multimodality probes aiming to combine the various quality characteristics of each modality, in order to form a more accurate imaging representation of disease. Here I present a probe with the potential to be used for pulmonary micrometastases detection via whole body PET/CT followed by $T_2$*-weighted whole body and/or brain MRI, providing this way exceptional structural, anatomical and soft tissue information. I hypothesise that in a clinical whole body PET imaging there is a possibility that micrometastitic lessions in the

bones could also be detected. However, the strong radioactive signal from the accumulation of the particles in the liver will limit the possibility to identify any micrometastases in the spleen. Concerning $T_2$*-weighted whole body MRI, one limitation is that spleen has significantly short $T_2$ values and the visualisation of MPIO could be very challenging. Concerning detection of micrometastasis in the bones with whole body MRI it must be noted that for whole body scan with convenient resolution the time of the acquisition must be significantly prolonged. Therefore, a more realistic approach would be to amin detection of micrometastases in lungs and bones with PET/CT followed by brain micrometastasis detection by MRI.
A substantial number of patients develop metastasis in multiple organs, with brain, bone and lungs being responsible for the greatest percentage of metastatic incidences. The described detection approach has the potential to screen for metastasis in multiple organs with either combined or sequential PET and MRI.

## 6.4 Characterisation of angiogenesis in subcutaneous tumours

The second part of this thesis has focused on the detection of newly formed vessels in subcutaneous tumours. To this end, I have targeted a well-established molecular marker of angiogenesis, the cell transmembrane integrin $\alpha_v\beta_3$, and the ligand used for targeting $\alpha_v\beta_3$ was based on an extensively studied peptide ligand, RGD, with high specificity to $\alpha_v\beta_3$. This ligand was synthesised into a cyclic pentapeptide variant c(RGDyK) with the aim of increasing its affinity to $\alpha_v\beta_3$.
In these studies, I demonstrated that the chemical affinity of the peptide, compared to a protein, does not pose limitations in targeting molecular markers when it is loaded on MPIO, compared to previously used NPIO, owing likely to the considerably greater targeting valency. I have further demonstrated that this contrast agent provides potent and quantifiable negative contrast effects within a very short time post-administration, in two mouse subcutaneous models. This detection ability was evident in both small and large tumours, highlighting the potential to target the early stages of angiogenesis.
In this study, I assessed 3 different analysis methods for quantitation of the contrast effects observed – there is no perfect measurement. However, all three analyses showed comparable results, providing confirmation of the validity of the individual quantitative analysis results. I have also shown that volumetric representation of the negative contrast is possible and can provide spatial information with regards to the heterogeneity of tumour vasculature. This may prove extremely useful in assessing the likely success of specific therapeutic strategies, where the degree of vascularity may have a profound effect.
By acquiring concomitant DCE imaging I have concluded that the molecularly targeted approach is complementary to the previously used angiogenesis characterisation with gadolinium infusion. The two imaging approaches can be performed within 1 h post-administration of the c(RGDyK)-MPIO and the one does not affect the results of the other, since they are performed with different relaxation parameters. DCE can be easily implemented at the end of the MPIO imaging protocol and can certainly provide additional

and valuable information as to the functionality of the tumour vasculature, whilst c(RGDyK)-MPIO can provide static spatial information on the degree of tumour angiogenesis.

## 6.5 Future directions

### 6.5.1 Micrometastasis detection targeting VCAM-1

With a view to strengthening the work presented herein for pulmonary micrometastasis detection, a next step would be to use spontaneous tumour-mouse models. It would be interesting also to test the method in a pulmonary orthotopic mouse model. A further important control experiment would be to block VCAM-1 expression in lungs by injection of an anti-VCAM-1 antibody prior to administration of the contrast agent, to confirm specific binding to VCAM-1. Although, it should be noted that this experiment has been performed previously in the brain setting [187].

In this work I have provided evidence for the potential of our approach for multi-organ PET/MRI detection. One straightforward proof-of-principal study to test this concept would be to conduct the lung metastasis imaging followed by MRI for detection of bone and spleen metastases, using the exact same tumour-mouse model. This approach, as discussed previously (section 6.3), might be limited by resolution which could be compromised with prolong acquisition. As for the brain, it has been shown previously that detection of micrometastasis is possible [195] but the tumour-mouse model used in the work of this thesis does not yield brain metastases at the time point studied (day 10 post 50,000 4T1-GFP i.v.). Therefore, our tumour-mouse model could be modified to also induce micrometastasis in the brain, possibly by performing intracerebral injection of the same type of tumour cells at an appropriate time point (1-5 days post i.v. of 4T1-GFP). Alternatively, intracardial injection of cells, which is known to induce brain metastasis, may also induce sufficient lung metastases for these purposes.

Alternative molecular imaging approaches could be also considered. The pharmacokinetics of the micron-sized particles have been proven to be suitable for the successful operation of our method, therefore, in order to achieve the same targeting efficiency, the alternative molecularly targeted probes should have an equivalent size to MPIO. To date there are no reported gold microparticles (GMP) in the literature. Given the compatibility of GNP for clinical imaging it would be interesting to target pulmonary micrometastasis using VCAM-GMP. However, given the resolution limitation of the CT, single GMP would not be detected, and therefore, it is not certain if micrometastases will have enough particles to allow sufficient attenuation of X-rays. Consequently, the method could be sensitive for the detection of some pulmonary lesions with high accumulation of GMP and insensitive for micrometastasis with low accumulation of GMP. However, the technique might provide a solution to the spleen micrometastasis detection that it would be challenging with either PET or MRI.

Concerning the limitation of the toxicity of MPIO used in this method, an alternative probe could be constructed using microbubbles. Radiolabelled anti-VCAM can be conjugated to

microbubbles of 1 μm size and used for pulmonary PET or SPECT imaging. Pinhole-SPECT could also be employed, that has higher resolution (submillimetre), which could potentially allow for detection of single pulmonary micrometastasis.

### 6.5.2 Angiogenesis detection targeting $\alpha_v\beta_3$

Concerning the quantitative analysis, one thing that wasn't considered in this thesis was analysis of the $T_2$* relaxation time data as a volumetric output, using the 3D $T_2$* maps of the tumour samples. This analysis is not very difficult with the current data, but as the project evolved it was assumed not to be essential for the conclusions of the proof-of-principal study. Nevertheless, it would be very interesting to compare the $T_2$* and hypointensity volumetric analyses.
An important future direction for this project would be to compare different sizes of iron oxide particles using the same targeting ligand, thus, 1 μm MPIO and 20 or 60 nm NPIO conjugated to c(RGDyK) in order to confirm the superior contrast achieved with MPIO *vs.* NPIO. At the same time, different cyclic RGD peptides could be compared to the one used in this thesis, in order to verify the most effective targeting ligand.

## 6.6 Concluding remarks

The lack of both early detection and staging in lung metastasis is clearly reflected in the mortality rates from metastasis incidence in the lungs, which have not improved over the past century. The work presented in this thesis suggests that early detection of lung metastasis is possible, and this could have a huge impact on lung metastasis treatment if it can be translated into clinic. At the same time, the molecular imaging approach for assessing tumour angiogenesis presented here, has the potential to substantially improve treatment strategies with anti-angiogenic therapy. Numerous anti-angiogenic treatments are currently in clinical trial and the translation of this new and sensitive approach to angiogenesis monitoring may play a critical role in the success of treatment planning.

# Bibliography

1. Cancer Research UK. All cancers combined key facts. 29/4/14; Available at: http://www.cancerresearchuk.org/cancer-info/cancerstats/keyfacts/Allcancerscombined/. Accessed 07/26, 2014.

2. Cancer Research UK. Worldwide cancer key facts. 14/02/14; Available at: http://www.cancerresearchuk.org/cancer-info/cancerstats/keyfacts/worldwide/. Accessed 07/29, 2014.

3. Cancer Research UK. Worldwide cancer incidence statistics. 14/01/14; Available at: http://www.cancerresearchuk.org/cancer-info/cancerstats/incidence/commoncancers/. Accessed 07/26, 2014.

4. Cancer Research UK. Cancer incidence for common cancers. 14/01/14; Available at: http://www.cancerresearchuk.org/cancer-info/cancerstats/incidence/commoncancers/. Accessed 07/26, 2014.

5. Cancer Research UK, Men's Health Forum and NCIN. Cancer statistics report - The excess burden of cancer in men in UK. 2013; Available at: http://www.cancerresearchuk.org/cancer-info/cancerstats/inequalities/#The. Accessed 07/26, 2014.

6. Cancer Research UK. Cancer mortality for all cancer combined. 14/12/13; Available at: http://www.cancerresearchuk.org/cancer-info/cancerstats/mortality/all-cancers-combined/. Accessed 07/26, 2014.

7. Cancer Research UK. Worldwide cancer mortality statistics. 14/02/14; Available at: http://www.cancerresearchuk.org/cancer-info/cancerstats/world/mortality/. Accessed 07/26, 2014.

8. Mehlen P, Puisieux A. Metastasis: a question of life or death. Nat Rev Cancer 2006 Jun;6(6):449-458.

9. Bianconi E, Piovesan A, Facchin F, Beraudi A, Casadei R, Frabetti F, et al. An estimation of the number of cells in the human body. Ann Hum Biol 2013 Nov-Dec;40(6):463-471.

10. Alberts B, Johnson A, Lewis J, et al,e t a l, Alberts B. Molecular biology of the cell. New York: Garland Science; 2002.

11. Loeb LA. Mutator phenotype may be required for multistage carcinogenesis. Cancer Res 1991 Jun 15;51(12):3075-3079.

12. Loeb LA. A mutator phenotype in cancer. Cancer Res 2001 Apr 15;61(8):3230-3239.

13. Cairns J. Cancer and the immortal strand hypothesis. Genetics 2006 Nov;174(3):1069-1072.

14. Furth J, Kahn MC, Breedis C. The Transmission of Leukemia of Mice with a Single Cell. The American Journal of Cancer 1937 October 01;31(2):276-282.

15. Fidler IJ, Kripke ML. Metastasis results from preexisting variant cells within a malignant tumor. Science 1977 Aug 26;197(4306):893-895.

16. Heppner GH. Tumor heterogeneity. Cancer Res 1984 Jun;44(6):2259-2265.

17. Dexter DL, Kowalski HM, Blazar BA, Fligiel Z, Vogel R, Heppner GH. Heterogeneity of tumor cells from a single mouse mammary tumor. Cancer Res 1978 Oct;38(10):3174-3181.

18. Fidler IJ, Hart IR. Biological diversity in metastatic neoplasms: origins and implications. Science 1982 Sep 10;217(4564):998-1003.

19. Nicolson GL. Generation of phenotypic diversity and progression in metastatic tumor cells. Cancer Metastasis Rev 1984;3(1):25-42.

20. Marusyk A, Polyak K. Tumor heterogeneity: causes and consequences. Biochim Biophys Acta 2010 Jan;1805(1):105-117.

21. Meacham CE, Morrison SJ. Tumour heterogeneity and cancer cell plasticity. Nature 2013 Sep 19;501(7467):328-337.

22. BRUCE WR, VAN DER GAAG H. A Quantitative Assay for the Number of Murine Lymphoma Cells Capable of Proliferation in Vivo. Nature 1963 Jul 6;199:79-80.

23. PIERCE GB,Jr, DIXON FJ,Jr, VERNEY EL. Teratocarcinogenic and tissue-forming potentials of the cell types comprising neoplastic embryoid bodies. Lab Invest 1960 Nov-Dec;9:583-602.

24. Lapidot T, Sirard C, Vormoor J, Murdoch B, Hoang T, Caceres-Cortes J, et al. A cell initiating human acute myeloid leukaemia after transplantation into SCID mice. Nature 1994 Feb 17;367(6464):645-648.

25. Al-Hajj M, Wicha MS, Benito-Hernandez A, Morrison SJ, Clarke MF. Prospective identification of tumorigenic breast cancer cells. Proc Natl Acad Sci U S A 2003 Apr 1;100(7):3983-3988.

26. Hill RP. Identifying cancer stem cells in solid tumors: case not proven. Cancer Res 2006 Feb 15;66(4):1891-5; discussion 1890.

27. Mintz B, Illmensee K. Normal genetically mosaic mice produced from malignant teratocarcinoma cells. Proc Natl Acad Sci U S A 1975 Sep;72(9):3585-3589.

28. Park CC, Bissell MJ, Barcellos-Hoff MH. The influence of the microenvironment on the malignant phenotype. Mol Med Today 2000 Aug;6(8):324-329.

29. Dvorak HF. Tumors: wounds that do not heal. Similarities between tumor stroma generation and wound healing. N Engl J Med 1986 Dec 25;315(26):1650-1659.

30. Nagy JA, Shih SC, Wong WH, Dvorak AM, Dvorak HF. Chapter 3. The adenoviral vector angiogenesis/lymphangiogenesis assay. Methods Enzymol 2008;444:43-64.

31. Egeblad M, Nakasone ES, Werb Z. Tumors as organs: complex tissues that interface with the entire organism. Dev Cell 2010 Jun 15;18(6):884-901.

32. Folkman J. Tumor angiogenesis: therapeutic implications. N Engl J Med 1971 Nov 18;285(21):1182-1186.

33. Hanahan D, Coussens LM. Accessories to the crime: functions of cells recruited to the tumor microenvironment. Cancer Cell 2012 Mar 20;21(3):309-322.

34. Leu AJ, Berk DA, Lymboussaki A, Alitalo K, Jain RK. Absence of functional lymphatics within a murine sarcoma: a molecular and functional evaluation. Cancer Res 2000 Aug 15;60(16):4324-4327.

35. Risau W, Flamme I. Vasculogenesis. Annu Rev Cell Dev Biol 1995;11:73-91.

36. Dvorak HF. Rous-Whipple Award Lecture. How tumors make bad blood vessels and stroma. Am J Pathol 2003 Jun;162(6):1747-1757.

37. Nagy JA, Dvorak AM, Dvorak HF. VEGF-A and the induction of pathological angiogenesis. Annu Rev Pathol 2007;2:251-275.

38. Denekamp J. Endothelial cell proliferation as a novel approach to targeting tumour therapy. Br J Cancer 1982 Jan;45(1):136-139.

39. Denekamp J, Hobson B. Endothelial-cell proliferation in experimental tumours. Br J Cancer 1982 Nov;46(5):711-720.

40. Alitalo K, Tammela T, Petrova TV. Lymphangiogenesis in development and human disease. Nature 2005 Dec 15;438(7070):946-953.

41. Hanahan D, Weinberg RA. The hallmarks of cancer. Cell 2000 Jan 7;100(1):57-70.

42. Hanahan D, Weinberg RA. Hallmarks of cancer: the next generation. Cell 2011 Mar 4;144(5):646-674.

43. Greenblatt M, Shubi P. Tumor angiogenesis: transfilter diffusion studies in the hamster by the transparent chamber technique. J Natl Cancer Inst 1968 Jul;41(1):111-124.

44. Folkman J, Merler E, Abernathy C, Williams G. Isolation of a tumor factor responsible for angiogenesis. J Exp Med 1971 Feb 1;133(2):275-288.

45. Folkman J, Hanahan D. Switch to the angiogenic phenotype during tumorigenesis. Princess Takamatsu Symp 1991;22:339-347.

46. Sakurai T, Kudo M. Signaling pathways governing tumor angiogenesis. Oncology 2011;81 Suppl 1:24-29.

47. Ferrara N, Gerber HP, LeCouter J. The biology of VEGF and its receptors. Nat Med 2003 Jun;9(6):669-676.

48. Kim KJ, Li B, Winer J, Armanini M, Gillett N, Phillips HS, et al. Inhibition of vascular endothelial growth factor-induced angiogenesis suppresses tumour growth in vivo. Nature 1993 Apr 29;362(6423):841-844.

49. Ferrara N, Hillan KJ, Gerber HP, Novotny W. Discovery and development of bevacizumab, an anti-VEGF antibody for treating cancer. Nat Rev Drug Discov 2004 May;3(5):391-400.

50. Fokas E, McKenna WG, Muschel RJ. The impact of tumor microenvironment on cancer treatment and its modulation by direct and indirect antivascular strategies. Cancer Metastasis Rev 2012 Dec;31(3-4):823-842.

51. Sitohy B, Nagy JA, Dvorak HF. Anti-VEGF/VEGFR therapy for cancer: reassessing the target. Cancer Res 2012 Apr 15;72(8):1909-1914.

52. Blankenberg FG, Backer MV, Levashova Z, Patel V, Backer JM. In vivo tumor angiogenesis imaging with site-specific labeled (99m)Tc-HYNIC-VEGF. Eur J Nucl Med Mol Imaging 2006 Jul;33(7):841-848.

53. Collingridge DR, Carroll VA, Glaser M, Aboagye EO, Osman S, Hutchinson OC, et al. The development of [(124)I]iodinated-VG76e: a novel tracer for imaging vascular endothelial growth factor in vivo using positron emission tomography. Cancer Res 2002 Oct 15;62(20):5912-5919.

54. Wang H, Cai W, Chen K, Li ZB, Kashefi A, He L, et al. A new PET tracer specific for vascular endothelial growth factor receptor 2. Eur J Nucl Med Mol Imaging 2007 Dec;34(12):2001-2010.

55. Nagengast WB, de Vries EG, Hospers GA, Mulder NH, de Jong JR, Hollema H, et al. In vivo VEGF imaging with radiolabeled bevacizumab in a human ovarian tumor xenograft. J Nucl Med 2007 Aug;48(8):1313-1319.

56. Chen K, Cai W, Li ZB, Wang H, Chen X. Quantitative PET imaging of VEGF receptor expression. Mol Imaging Biol 2009 Jan-Feb;11(1):15-22.

57. Nagengast WB, Lub-de Hooge MN, Oosting SF, den Dunnen WF, Warnders FJ, Brouwers AH, et al. VEGF-PET imaging is a noninvasive biomarker showing differential changes in the tumor during sunitinib treatment. Cancer Res 2011 Jan 1;71(1):143-153.

58. Tamkun JW, DeSimone DW, Fonda D, Patel RS, Buck C, Horwitz AF, et al. Structure of integrin, a glycoprotein involved in the transmembrane linkage between fibronectin and actin. Cell 1986 Jul 18;46(2):271-282.

59. Humphries MJ. Integrin structure. Biochem Soc Trans 2000;28(4):311-339.

60. Parise LV, Lee J, Juliano RL. New aspects of integrin signaling in cancer. Semin Cancer Biol 2000 Dec;10(6):407-414.

61. Berman AE, Kozlova NI. Integrins: structure and functions. Membr Cell Biol 2000;13(2):207-244.

62. Hynes RO. Integrins: bidirectional, allosteric signaling machines. Cell 2002 Sep 20;110(6):673-687.

63. Yamada KM, Geiger B. Molecular interactions in cell adhesion complexes. Curr Opin Cell Biol 1997 Feb;9(1):76-85.

64. Guo W, Giancotti FG. Integrin signalling during tumour progression. Nat Rev Mol Cell Biol 2004 Oct;5(10):816-826.

65. Miyata S, Koshikawa N, Yasumitsu H, Miyazaki K. Trypsin stimulates integrin alpha(5)beta(1)-dependent adhesion to fibronectin and proliferation of human gastric carcinoma cells through activation of proteinase-activated receptor-2. J Biol Chem 2000 Feb 18;275(7):4592-4598.

66. Hollenbeck ST, Itoh H, Louie O, Faries PL, Liu B, Kent KC. Type I collagen synergistically enhances PDGF-induced smooth muscle cell proliferation through pp60src-dependent crosstalk between the alpha2beta1 integrin and PDGFbeta receptor. Biochem Biophys Res Commun 2004 Dec 3;325(1):328-337.

67. Hedin U, Roy J, Tran PK. Control of smooth muscle cell proliferation in vascular disease. Curr Opin Lipidol 2004 Oct;15(5):559-565.

68. Zhou X, Murphy FR, Gehdu N, Zhang J, Iredale JP, Benyon RC. Engagement of alphavbeta3 integrin regulates proliferation and apoptosis of hepatic stellate cells. J Biol Chem 2004 Jun 4;279(23):23996-24006.

69. Hirsch E, Iglesias A, Potocnik AJ, Hartmann U, Fassler R. Impaired migration but not differentiation of haematopoietic stem cells in the absence of beta1 integrins. Nature 1996 Mar 14;380(6570):171-175.

70. Sakai T, Zhang Q, Fassler R, Mosher DF. Modulation of beta1A integrin functions by tyrosine residues in the beta1 cytoplasmic domain. J Cell Biol 1998 Apr 20;141(2):527-538.

71. Fujiwara H, Kikkawa Y, Sanzen N, Sekiguchi K. Purification and characterization of human laminin-8. Laminin-8 stimulates cell adhesion and migration through alpha3beta1 and alpha6beta1 integrins. J Biol Chem 2001 May 18;276(20):17550-17558.

72. Paulhe F, Racaud-Sultan C, Ragab A, Albiges-Rizo C, Chap H, Iberg N, et al. Differential regulation of phosphoinositide metabolism by alphaVbeta3 and alphaVbeta5 integrins upon smooth muscle cell migration. J Biol Chem 2001 Nov 9;276(45):41832-41840.

73. Takanami I. Increased expression of integrin-linked kinase is associated with shorter survival in non-small cell lung cancer. BMC Cancer 2005 Jan 5;5:1.

74. Guo HB, Lee I, Bryan BT, Pierce M. Deletion of mouse embryo fibroblast N-acetylglucosaminyltransferase V stimulates alpha5beta1 integrin expression mediated by the protein kinase C signaling pathway. J Biol Chem 2005 Mar 4;280(9):8332-8342.

75. Enserink JM, Price LS, Methi T, Mahic M, Sonnenberg A, Bos JL, et al. The cAMP-Epac-Rap1 pathway regulates cell spreading and cell adhesion to laminin-5 through the alpha3beta1 integrin but not the alpha6beta4 integrin. J Biol Chem 2004 Oct 22;279(43):44889-44896.

76. Chung J, Mercurio AM. Contributions of the alpha6 integrins to breast carcinoma survival and progression. Mol Cells 2004 Apr 30;17(2):203-209.

77. Felding-Habermann B, Fransvea E, O'Toole TE, Manzuk L, Faha B, Hensler M. Involvement of tumor cell integrin alpha v beta 3 in hematogenous metastasis of human melanoma cells. Clin Exp Metastasis 2002;19(5):427-436.

78. Gladson CL, Hancock S, Arnold MM, Faye-Petersen OM, Castleberry RP, Kelly DR. Stage-specific expression of integrin alphaVbeta3 in neuroblastic tumors. Am J Pathol 1996 May;148(5):1423-1434.

79. Zheng DQ, Woodard AS, Fornaro M, Tallini G, Languino LR. Prostatic carcinoma cell migration via alpha(v)beta3 integrin is modulated by a focal adhesion kinase pathway. Cancer Res 1999 Apr 1;59(7):1655-1664.

80. Zheng DQ, Woodard AS, Tallini G, Languino LR. Substrate specificity of alpha(v)beta(3) integrin-mediated cell migration and phosphatidylinositol 3-kinase/AKT pathway activation. J Biol Chem 2000 Aug 11;275(32):24565-24574.

81. Lu X, Lu D, Scully M, Kakkar V. The role of integrins in cancer and the development of anti-integrin therapeutic agents for cancer therapy. Perspect Medicin Chem 2008 Apr 10;2:57-73.

82. Pytela R, Pierschbacher MD, Ruoslahti E. A 125/115-kDa cell surface receptor specific for vitronectin interacts with the arginine-glycine-aspartic acid adhesion sequence derived from fibronectin. Proc Natl Acad Sci U S A 1985 Sep;82(17):5766-5770.

83. Gardner JM, Hynes RO. Interaction of fibronectin with its receptor on platelets. Cell 1985 Sep;42(2):439-448.

84. Horton MA. The alpha v beta 3 integrin "vitronectin receptor". Int J Biochem Cell Biol 1997 May;29(5):721-725.

85. Friedlander M, Brooks PC, Shaffer RW, Kincaid CM, Varner JA, Cheresh DA. Definition of two angiogenic pathways by distinct alpha v integrins. Science 1995 Dec 1;270(5241):1500-1502.

86. Brooks PC, Clark RA, Cheresh DA. Requirement of vascular integrin alpha v beta 3 for angiogenesis. Science 1994 Apr 22;264(5158):569-571.

87. Karczewski J, Knudsen KA, Smith L, Murphy A, Rothman VL, Tuszynski GP. The interaction of thrombospondin with platelet glycoprotein GPIIb-IIIa. J Biol Chem 1989 Dec 15;264(35):21322-21326.

88. Joshi P, Chung CY, Aukhil I, Erickson HP. Endothelial cells adhere to the RGD domain and the fibrinogen-like terminal knob of tenascin. J Cell Sci 1993 Sep;106 ( Pt 1)(Pt 1):389-400.

89. Ruggeri ZM, De Marco L, Gatti L, Bader R, Montgomery RR. Platelets have more than one binding site for von Willebrand factor. J Clin Invest 1983 Jul;72(1):1-12.

90. Davis GE. Affinity of integrins for damaged extracellular matrix: alpha v beta 3 binds to denatured collagen type I through RGD sites. Biochem Biophys Res Commun 1992 Feb 14;182(3):1025-1031.

91. Schnapp LM, Breuss JM, Ramos DM, Sheppard D, Pytela R. Sequence and tissue distribution of the human integrin alpha 8 subunit: a beta 1-associated alpha subunit expressed in smooth muscle cells. J Cell Sci 1995 Feb;108 ( Pt 2)(Pt 2):537-544.

92. Kimura N, Toyoshima T, Kojima T, Shimane M. Entactin-2: a new member of basement membrane protein with high homology to entactin/nidogen. Exp Cell Res 1998 May 25;241(1):36-45.

93. Xiong JP, Stehle T, Diefenbach B, Zhang R, Dunker R, Scott DL, et al. Crystal structure of the extracellular segment of integrin alpha Vbeta3. Science 2001 Oct 12;294(5541):339-345.

94. Xiong JP, Stehle T, Zhang R, Joachimiak A, Frech M, Goodman SL, et al. Crystal structure of the extracellular segment of integrin alpha Vbeta3 in complex with an Arg-Gly-Asp ligand. Science 2002 Apr 5;296(5565):151-155.

95. Keski-Oja J, Mosher DF, Vaheri A. Cross-linking of a major fibroblast surface-associated glycoprotein (fibronectin) catalyzed by blood coagulation factor XIII. Cell 1976 Sep;9(1):29-35.

96. Kuusela P, Ruoslahti E, Engvall E, Vaheri A. Immunological interspecies cross-reactions of fibroblast surface antigen (fibronectin). Immunochemistry 1976 Aug;13(8):639-642.

97. Yamada KM, Olden K. Fibronectins--adhesive glycoproteins of cell surface and blood. Nature 1978 Sep 21;275(5677):179-184.

98. Pierschbacher MD, Hayman EG, Ruoslahti E. Location of the cell-attachment site in fibronectin with monoclonal antibodies and proteolytic fragments of the molecule. Cell 1981 Oct;26(2 Pt 2):259-267.

99. Pierschbacher MD, Ruoslahti E, Sundelin J, Lind P, Peterson PA. The cell attachment domain of fibronectin. Determination of the primary structure. J Biol Chem 1982 Aug 25;257(16):9593-9597.

100. Pierschbacher M, Hayman EG, Ruoslahti E. Synthetic peptide with cell attachment activity of fibronectin. Proc Natl Acad Sci U S A 1983 Mar;80(5):1224-1227.

101. Pierschbacher MD, Ruoslahti E. Cell attachment activity of fibronectin can be duplicated by small synthetic fragments of the molecule. Nature 1984 May 3-9;309(5963):30-33.

102. Plow EF, Pierschbacher MD, Ruoslahti E, Marguerie GA, Ginsberg MH. The effect of Arg-Gly-Asp-containing peptides on fibrinogen and von Willebrand factor binding to platelets. Proc Natl Acad Sci U S A 1985 Dec;82(23):8057-8061.

103. Pytela R, Pierschbacher MD, Ginsberg MH, Plow EF, Ruoslahti E. Platelet membrane glycoprotein IIb/IIIa: member of a family of Arg-Gly-Asp--specific adhesion receptors. Science 1986 Mar 28;231(4745):1559-1562.

104. Pytela R, Pierschbacher MD, Argraves S, Suzuki S, Ruoslahti E. Arginine-glycine-aspartic acid adhesion receptors. Methods Enzymol 1987;144:475-489.

105. Barnes D, Wolfe R, Serrero G, McClure D, Sato G. Effects of a serum spreading factor on growth and morphology of cells in serum-free medium. J Supramol Struct 1980;14(1):47-63.

106. Whateley JG, Knox P. Isolation of a serum component that stimulates the spreading of cells in culture. Biochem J 1980 Feb 1;185(2):349-354.

107. Hayman EG, Pierschbacher MD, Ohgren Y, Ruoslahti E. Serum spreading factor (vitronectin) is present at the cell surface and in tissues. Proc Natl Acad Sci U S A 1983 Jul;80(13):4003-4007.

108. Suzuki S, Pierschbacher MD, Hayman EG, Nguyen K, Ohgren Y, Ruoslahti E. Domain structure of vitronectin. Alignment of active sites. J Biol Chem 1984 Dec 25;259(24):15307-15314.

109. Hayman EG, Pierschbacher MD, Suzuki S, Ruoslahti E. Vitronectin--a major cell attachment-promoting protein in fetal bovine serum. Exp Cell Res 1985 Oct;160(2):245-258.

110. Smith JW, Cheresh DA. Integrin (alpha v beta 3)-ligand interaction. Identification of a heterodimeric RGD binding site on the vitronectin receptor. J Biol Chem 1990 Feb 5;265(4):2168-2172.

111. Saiki I, Murata J, Makabe T, Nishi N, Tokura S, Azuma I. Inhibition of tumor angiogenesis by a synthetic cell-adhesive polypeptide containing the Arg-Gly-Asp (RGD) sequence of fibronectin, poly(RGD). Jpn J Cancer Res 1990 Jun-Jul;81(6-7):668-675.

112. Samanen J, Ali F, Romoff T, Calvo R, Sorenson E, Vasko J, et al. Development of a small RGD peptide fibrinogen receptor antagonist with potent antiaggregatory activity in vitro. J Med Chem 1991 Oct;34(10):3114-3125.

113. Gurrath M, Muller G, Kessler H, Aumailley M, Timpl R. Conformation/activity studies of rationally designed potent anti-adhesive RGD peptides. Eur J Biochem 1992 Dec 15;210(3):911-921.

114. Koivunen E, Gay DA, Ruoslahti E. Selection of peptides binding to the alpha 5 beta 1 integrin from phage display library. J Biol Chem 1993 Sep 25;268(27):20205-20210.

115. Scarborough RM, Naughton MA, Teng W, Rose JW, Phillips DR, Nannizzi L, et al. Design of potent and specific integrin antagonists. Peptide antagonists with high specificity for glycoprotein IIb-IIIa. J Biol Chem 1993 Jan 15;268(2):1066-1073.

116. Nowlin DM, Gorcsan F, Moscinski M, Chiang SL, Lobl TJ, Cardarelli PM. A novel cyclic pentapeptide inhibits alpha 4 beta 1 and alpha 5 beta 1 integrin-mediated cell adhesion. J Biol Chem 1993 Sep 25;268(27):20352-20359.

117. Pfaff M, Tangemann K, Muller B, Gurrath M, Muller G, Kessler H, et al. Selective recognition of cyclic RGD peptides of NMR defined conformation by alpha IIb beta 3, alpha V beta 3, and alpha 5 beta 1 integrins. J Biol Chem 1994 Aug 12;269(32):20233-20238.

118. Aumailley M, Gurrath M, Muller G, Calvete J, Timpl R, Kessler H. Arg-Gly-Asp constrained within cyclic pentapeptides. Strong and selective inhibitors of cell adhesion to vitronectin and laminin fragment P1. FEBS Lett 1991 Oct 7;291(1):50-54.

119. Burgess K, Lim D, Mousa SA. Synthesis and solution conformation of cyclo[RGDRGD]: a cyclic peptide with selectivity for the alpha V beta 3 receptor. J Med Chem 1996 Oct 25;39(22):4520-4526.

120. Bach AC, Eyermann CJ, Gross JD, Bower MJ, Harlow RL, Weber PC, et al. Structural studies of a family of high affinity ligands for GPIIb/IIIa. J Am Chem Soc 1994;116(8):3207-3219.

121. Dechantsreiter MA, Planker E, Matha B, Lohof E, Holzemann G, Jonczyk A, et al. N-Methylated cyclic RGD peptides as highly active and selective alpha(V)beta(3) integrin antagonists. J Med Chem 1999 Aug 12;42(16):3033-3040.

122. Mas-Moruno C, Beck JG, Doedens L, Frank AO, Marinelli L, Cosconati S, et al. Increasing alphavbeta3 selectivity of the anti-angiogenic drug cilengitide by N-methylation. Angew Chem Int Ed Engl 2011 Sep 26;50(40):9496-9500.

123. Smith JW. Cilengitide Merck. Curr Opin Investig Drugs 2003 Jun;4(6):741-745.

124. Friess H, Langrehr JM, Oettle H, Raedle J, Niedergethmann M, Dittrich C, et al. A randomized multi-center phase II trial of the angiogenesis inhibitor Cilengitide (EMD 121974) and gemcitabine compared with gemcitabine alone in advanced unresectable pancreatic cancer. BMC Cancer 2006 Dec 11;6:285.

125. Nabors LB, Mikkelsen T, Rosenfeld SS, Hochberg F, Akella NS, Fisher JD, et al. Phase I and correlative biology study of cilengitide in patients with recurrent malignant glioma. J Clin Oncol 2007 May 1;25(13):1651-1657.

126. Hariharan S, Gustafson D, Holden S, McConkey D, Davis D, Morrow M, et al. Assessment of the biological and pharmacological effects of the alpha nu beta3 and alpha nu

beta5 integrin receptor antagonist, cilengitide (EMD 121974), in patients with advanced solid tumors. Ann Oncol 2007 Aug;18(8):1400-1407.

127. Hirano Y, Okuno M, Hayashi T, Goto K, Nakajima A. Cell-attachment activities of surface immobilized oligopeptides RGD, RGDS, RGDV, RGDT, and YIGSR toward five cell lines. J Biomater Sci Polym Ed 1993;4(3):235-243.

128. Haubner R. Structural and Functional Aspects of RGD-Containing Cyclic Pentapeptides as Highly Potent and Selective Integrin avß3 Antagonists. J Am Chem Soc 1996;118(32):7461-7472.

129. Recamier JC. Recherches sur le traitement du cancer sur la com- pression methodique simple ou combinee et sur l'histoire generale de la meme maladie. 1829;2nd.

130. Paget S. The distribution of secondary growths in cancer of the breast. The Lancet 1889;133(3421):571-573.

131. Virchow R. Cellular pathology. As based upon physiological and pathological histology. Lecture XVI--Atheromatous affection of arteries. 1858. Nutr Rev 1989 Jan;47(1):23-25.

132. Ewing J. Neoplastic Diseases. W.B. Saunders 1928(6th).

133. Proctor JW. Rat sarcoma model supports both "soil seed" and "mechanical" theories of metastatic spread. Br J Cancer 1976 Dec;34(6):651-654.

134. Hart IR, Fidler IJ. Role of organ selectivity in the determination of metastatic patterns of B16 melanoma. Cancer Res 1980 Jul;40(7):2281-2287.

135. Poste G, Fidler IJ. The pathogenesis of cancer metastasis. Nature 1980 Jan 10;283(5743):139-146.

136. Chambers AF, Groom AC, MacDonald IC. Dissemination and growth of cancer cells in metastatic sites. Nat Rev Cancer 2002 Aug;2(8):563-572.

137. Fidler IJ. Selection of successive tumour lines for metastasis. Nat New Biol 1973 Apr 4;242(118):148-149.

138. Luzzi KJ, MacDonald IC, Schmidt EE, Kerkvliet N, Morris VL, Chambers AF, et al. Multistep nature of metastatic inefficiency: dormancy of solitary cells after successful extravasation and limited survival of early micrometastases. Am J Pathol 1998 Sep;153(3):865-873.

139. Podsypanina K, Du YC, Jechlinger M, Beverly LJ, Hambardzumyan D, Varmus H. Seeding and propagation of untransformed mouse mammary cells in the lung. Science 2008 Sep 26;321(5897):1841-1844.

140. Husemann Y, Geigl JB, Schubert F, Musiani P, Meyer M, Burghart E, et al. Systemic spread is an early step in breast cancer. Cancer Cell 2008 Jan;13(1):58-68.

141. Talmadge JE. Clonal selection of metastasis within the life history of a tumor. Cancer Res 2007 Dec 15;67(24):11471-11475.

142. Kaplan RN, Riba RD, Zacharoulis S, Bramley AH, Vincent L, Costa C, et al. VEGFR1-positive haematopoietic bone marrow progenitors initiate the pre-metastatic niche. Nature 2005 Dec 8;438(7069):820-827.

143. Yakubenko VP, Lobb RR, Plow EF, Ugarova TP. Differential induction of gelatinase B (MMP-9) and gelatinase A (MMP-2) in T lymphocytes upon alpha(4)beta(1)-mediated adhesion to VCAM-1 and the CS-1 peptide of fibronectin. Exp Cell Res 2000 Oct 10;260(1):73-84.

144. Hiratsuka S, Nakamura K, Iwai S, Murakami M, Itoh T, Kijima H, et al. MMP9 induction by vascular endothelial growth factor receptor-1 is involved in lung-specific metastasis. Cancer Cell 2002 Oct;2(4):289-300.

145. Dawson MR, Duda DG, Fukumura D, Jain RK. VEGFR1-activity-independent metastasis formation. Nature 2009 Sep 17;461(7262):E4; discussion E5.

146. Kaplan N. Kaplan et al. reply to doi: 10.1038/nature08254**Database: Database:** . Nature 2009;461:E5-E6.

147. Hanahan D, Folkman J. Patterns and emerging mechanisms of the angiogenic switch during tumorigenesis. Cell 1996 Aug 9;86(3):353-364.

148. Dutrochet H. Recherches anatomiques et physiologiques sur la structure intime des animaux et des végetaux, et sur leur motilité. 1-233 ed. Paris; 1824.

149. Wagner R. 1839 in Elläuterungstafeln zur Physiologie und Entwicklungsgeschichte. Leopold Voss, Leipzig 1839.

150. Butcher EC. Leukocyte-endothelial cell recognition: three (or more) steps to specificity and diversity. Cell 1991 Dec 20;67(6):1033-1036.

151. Springer TA. Traffic signals for lymphocyte recirculation and leukocyte emigration: the multistep paradigm. Cell 1994 Jan 28;76(2):301-314.

152. Kinashi T. Intracellular signalling controlling integrin activation in lymphocytes. Nat Rev Immunol 2005 Jul;5(7):546-559.

153. Laudanna C, Kim JY, Constantin G, Butcher E. Rapid leukocyte integrin activation by chemokines. Immunol Rev 2002 Aug;186:37-46.

154. Ley K, Laudanna C, Cybulsky MI, Nourshargh S. Getting to the site of inflammation: the leukocyte adhesion cascade updated. Nat Rev Immunol 2007 Sep;7(9):678-689.

155. Kansas GS. Selectins and their ligands: current concepts and controversies. Blood 1996 Nov 1;88(9):3259-3287.

156. McEver RP, Cummings RD. Role of PSGL-1 binding to selectins in leukocyte recruitment. J Clin Invest 1997 Dec 1;100(11 Suppl):S97-103.

157. Berlin C, Bargatze RF, Campbell JJ, von Andrian UH, Szabo MC, Hasslen SR, et al. Alpha 4 Integrins Mediate Lymphocyte Attachment and Rolling Under Physiologic Flow. Cell 1995 Feb 10;80(3):413-422.

158. Salas A, Shimaoka M, Kogan AN, Harwood C, von Andrian UH, Springer TA. Rolling adhesion through an extended conformation of integrin alphaLbeta2 and relation to alpha I and beta I-like domain interaction. Immunity 2004 Apr;20(4):393-406.

159. Campbell JJ, Qin S, Bacon KB, Mackay CR, Butcher EC. Biology of chemokine and classical chemoattractant receptors: differential requirements for adhesion-triggering versus chemotactic responses in lymphoid cells. J Cell Biol 1996 Jul;134(1):255-266.

160. Campbell JJ, Hedrick J, Zlotnik A, Siani MA, Thompson DA, Butcher EC. Chemokines and the arrest of lymphocytes rolling under flow conditions. Science 1998 Jan 16;279(5349):381-384.

161. Bidard FC, Pierga JY, Soria JC, Thiery JP. Translating metastasis-related biomarkers to the clinic--progress and pitfalls. Nat Rev Clin Oncol 2013 Mar;10(3):169-179.

162. Pantel K, Alix-Panabieres C, Riethdorf S. Cancer micrometastases. Nat Rev Clin Oncol 2009 Jun;6(6):339-351.

163. Rahbari NN, Aigner M, Thorlund K, Mollberg N, Motschall E, Jensen K, et al. Meta-analysis shows that detection of circulating tumor cells indicates poor prognosis in patients with colorectal cancer. Gastroenterology 2010 May;138(5):1714-1726.

164. Lucci A, Hall CS, Lodhi AK, Bhattacharyya A, Anderson AE, Xiao L, et al. Circulating tumour cells in non-metastatic breast cancer: a prospective study. Lancet Oncol 2012 Jul;13(7):688-695.

165. Miller MC, Doyle GV, Terstappen LW. Significance of Circulating Tumor Cells Detected by the CellSearch System in Patients with Metastatic Breast Colorectal and Prostate Cancer. J Oncol 2010;2010:617421.

166. Pierga JY, Hajage D, Bachelot T, Delaloge S, Brain E, Campone M, et al. High independent prognostic and predictive value of circulating tumor cells compared with serum

tumor markers in a large prospective trial in first-line chemotherapy for metastatic breast cancer patients. Ann Oncol 2012 Mar;23(3):618-624.

167. Gao D, Nolan DJ, Mellick AS, Bambino K, McDonnell K, Mittal V. Endothelial progenitor cells control the angiogenic switch in mouse lung metastasis. Science 2008 Jan 11;319(5860):195-198.

168. Riethdorf S, Wikman H, Pantel K. Review: Biological relevance of disseminated tumor cells in cancer patients. Int J Cancer 2008 Nov 1;123(9):1991-2006.

169. Uhr JW, Pantel K. Controversies in clinical cancer dormancy. Proc Natl Acad Sci U S A 2011 Jul 26;108(30):12396-12400.

170. Hayers DF.Breast cancer staging. 2009; 7th edition.

171. Weissleder R, Bogdanov A,Jr, Tung CH, Weinmann HJ. Size optimization of synthetic graft copolymers for in vivo angiogenesis imaging. Bioconjug Chem 2001 Mar-Apr;12(2):213-219.

172. Tournier H, Hyacinthe R, Schneider M. Gadolinium-containing mixed micelle formulations: a new class of blood pool MRI/MRA contrast agents. Acad Radiol 2002 May;9 Suppl 1:S20-8.

173. Storrs RW, Tropper FD, Li HY, Song CK, Sipkins DA, Kuniyoshi JK, et al. Paramagnetic polymerized liposomes as new recirculating MR contrast agents. J Magn Reson Imaging 1995 Nov-Dec;5(6):719-724.

174. Kobayashi H, Brechbiel MW. Dendrimer-based macromolecular MRI contrast agents: characteristics and application. Mol Imaging 2003 Jan;2(1):1-10.

175. Enochs WS, Harsh G, Hochberg F, Weissleder R. Improved delineation of human brain tumors on MR images using a long-circulating, superparamagnetic iron oxide agent. J Magn Reson Imaging 1999 Feb;9(2):228-232.

176. Harisinghani MG, Barentsz J, Hahn PF, Deserno WM, Tabatabaei S, van de Kaa CH, et al. Noninvasive detection of clinically occult lymph-node metastases in prostate cancer. N Engl J Med 2003 Jun 19;348(25):2491-2499.

177. Miller JC, Pien HH, Sahani D, Sorensen AG, Thrall JH. Imaging angiogenesis: applications and potential for drug development. J Natl Cancer Inst 2005 Feb 2;97(3):172-187.

178. Sipkins DA, Cheresh DA, Kazemi MR, Nevin LM, Bednarski MD, Li KC. Detection of tumor angiogenesis in vivo by alphaVbeta3-targeted magnetic resonance imaging. Nat Med 1998 May;4(5):623-626.

179. Winter PM, Caruthers SD, Kassner A, Harris TD, Chinen LK, Allen JS, et al. Molecular imaging of angiogenesis in nascent Vx-2 rabbit tumors using a novel alpha(nu)beta3-targeted nanoparticle and 1.5 tesla magnetic resonance imaging. Cancer Res 2003 Sep 15;63(18):5838-5843.

180. Schmieder AH, Winter PM, Caruthers SD, Harris TD, Williams TA, Allen JS, et al. Molecular MR imaging of melanoma angiogenesis with alphanubeta3-targeted paramagnetic nanoparticles. Magn Reson Med 2005 Mar;53(3):621-627.

181. Schmieder AH, Caruthers SD, Zhang H, Williams TA, Robertson JD, Wickline SA, et al. Three-dimensional MR mapping of angiogenesis with alpha5beta1(alpha nu beta3)-targeted theranostic nanoparticles in the MDA-MB-435 xenograft mouse model. FASEB J 2008 Dec;22(12):4179-4189.

182. Mulder WJ, Strijkers GJ, Habets JW, Bleeker EJ, van der Schaft DW, Storm G, et al. MR molecular imaging and fluorescence microscopy for identification of activated tumor endothelium using a bimodal lipidic nanoparticle. FASEB J 2005 Dec;19(14):2008-2010.

183. Mulder WJ, van der Schaft DW, Hautvast PA, Strijkers GJ, Koning GA, Storm G, et al. Early in vivo assessment of angiostatic therapy efficacy by molecular MRI. FASEB J 2007 Feb;21(2):378-383.

184. Zhang C, Jugold M, Woenne EC, Lammers T, Morgenstern B, Mueller MM, et al. Specific targeting of tumor angiogenesis by RGD-conjugated ultrasmall superparamagnetic iron oxide particles using a clinical 1.5-T magnetic resonance scanner. Cancer Res 2007 Feb 15;67(4):1555-1562.

185. Jiang T, Zhang C, Zheng X, Xu X, Xie X, Liu H, et al. Noninvasively characterizing the different alphavbeta3 expression patterns in lung cancers with RGD-USPIO using a clinical 3.0T MR scanner. Int J Nanomedicine 2009;4:241-249.

186. Akhtar AM, Schneider JE, Chapman SJ, Jefferson A, Digby JE, Mankia K, et al. In vivo quantification of VCAM-1 expression in renal ischemia reperfusion injury using non-invasive magnetic resonance molecular imaging. PLoS One 2010 Sep 21;5(9):e12800.

187. McAteer MA, Sibson NR, von Zur Muhlen C, Schneider JE, Lowe AS, Warrick N, et al. In vivo magnetic resonance imaging of acute brain inflammation using microparticles of iron oxide. Nat Med 2007 Oct;13(10):1253-1258.

188. McAteer MA, Mankia K, Ruparelia N, Jefferson A, Nugent HB, Stork LA, et al. A leukocyte-mimetic magnetic resonance imaging contrast agent homes rapidly to activated endothelium and tracks with atherosclerotic lesion macrophage content. Arterioscler Thromb Vasc Biol 2012 Jun;32(6):1427-1435.

189. McAteer MA, Schneider JE, Ali ZA, Warrick N, Bursill CA, von zur Muhlen C, et al. Magnetic resonance imaging of endothelial adhesion molecules in mouse atherosclerosis using dual-targeted microparticles of iron oxide. Arterioscler Thromb Vasc Biol 2008 Jan;28(1):77-83.

190. von Zur Muhlen C, Sibson NR, Peter K, Campbell SJ, Wilainam P, Grau GE, et al. A contrast agent recognizing activated platelets reveals murine cerebral malaria pathology undetectable by conventional MRI. J Clin Invest 2008 Mar;118(3):1198-1207.

191. von zur Muhlen C, von Elverfeldt D, Moeller JA, Choudhury RP, Paul D, Hagemeyer CE, et al. Magnetic resonance imaging contrast agent targeted toward activated platelets allows in vivo detection of thrombosis and monitoring of thrombolysis. Circulation 2008 Jul 15;118(3):258-267.

192. Serres S, Anthony DC, Jiang Y, Broom KA, Campbell SJ, Tyler DJ, et al. Systemic inflammatory response reactivates immune-mediated lesions in rat brain. J Neurosci 2009 Apr 15;29(15):4820-4828.

193. Hoyte LC, Brooks KJ, Nagel S, Akhtar A, Chen R, Mardiguian S, et al. Molecular magnetic resonance imaging of acute vascular cell adhesion molecule-1 expression in a mouse model of cerebral ischemia. J Cereb Blood Flow Metab 2010 Jun;30(6):1178-1187.

194. Serres S, Mardiguian S, Campbell SJ, McAteer MA, Akhtar A, Krapitchev A, et al. VCAM-1-targeted magnetic resonance imaging reveals subclinical disease in a mouse model of multiple sclerosis. FASEB J 2011 Dec;25(12):4415-4422.

195. Serres S, Soto MS, Hamilton A, McAteer MA, Carbonell WS, Robson MD, et al. Molecular MRI enables early and sensitive detection of brain metastases. Proc Natl Acad Sci U S A 2012 Apr 24;109(17):6674-6679.

196. Yankeelov TE, Lepage M, Chakravarthy A, Broome EE, Niermann KJ, Kelley MC, et al. Integration of quantitative DCE-MRI and ADC mapping to monitor treatment response in human breast cancer: initial results. Magn Reson Imaging 2007 Jan;25(1):1-13.

197. Bauerle T, Komljenovic D, Merz M, Berger MR, Goodman SL, Semmler W. Cilengitide inhibits progression of experimental breast cancer bone metastases as imaged noninvasively using VCT, MRI and DCE-MRI in a longitudinal in vivo study. Int J Cancer 2011 May 15;128(10):2453-2462.

198. Bauerle T, Komljenovic D, Semmler W. Monitoring molecular, functional and morphologic aspects of bone metastases using non-invasive imaging. Curr Pharm Biotechnol 2012 Mar;13(4):584-594.

199. Heijmen L, Verstappen MC, Ter Voert EE, Punt CJ, Oyen WJ, de Geus-Oei LF, et al. Tumour response prediction by diffusion-weighted MR imaging: ready for clinical use? Crit Rev Oncol Hematol 2012 Aug;83(2):194-207.

200. Moffat BA, Chenevert TL, Lawrence TS, Meyer CR, Johnson TD, Dong Q, et al. Functional diffusion map: a noninvasive MRI biomarker for early stratification of clinical brain tumor response. Proc Natl Acad Sci U S A 2005 Apr 12;102(15):5524-5529.

201. Gambhir SS. Molecular imaging of cancer with positron emission tomography. Nature Reviews Cancer 2002;2(9):683-693.

202. Jones T. The role of positron emission tomography within the spectrum of medical imaging. Eur J Nucl Med 1996;23(2):207-211.

203. Phelps ME. PET: the merging of biology and imaging into molecular imaging. Journal of Nuclear Medicine 2000;41(4):661-681.

204. Franc BL, Acton PD, Mari C, Hasegawa BH. Small-animal SPECT and SPECT/CT: important tools for preclinical investigation. J Nucl Med 2008 Oct;49(10):1651-1663.

205. Goorden MC, Beekman FJ. High-resolution tomography of positron emitters with clustered pinhole SPECT. Phys Med Biol 2010;55(5):1265.

206. Wilson CB, Lammertsma AA, McKenzie CG, Sikora K, Jones T. Measurements of blood flow and exchanging water space in breast tumors using positron emission tomography: a rapid and noninvasive dynamic method. Cancer Res 1992 Mar 15;52(6):1592-1597.

207. Tseng J, Dunnwald LK, Schubert EK, Link JM, Minoshima S, Muzi M, et al. 18F-FDG kinetics in locally advanced breast cancer: correlation with tumor blood flow and changes in response to neoadjuvant chemotherapy. J Nucl Med 2004 Nov;45(11):1829-1837.

208. Chen X, Hou Y, Tohme M, Park R, Khankaldyyan V, Gonzales-Gomez I, et al. Pegylated Arg-Gly-Asp peptide: 64Cu labeling and PET imaging of brain tumor alphavbeta3-integrin expression. J Nucl Med 2004 Oct;45(10):1776-1783.

209. Levashova Z, Backer M, Backer JM, Blankenberg FG. Direct site-specific labeling of the Cys-tag moiety in scVEGF with technetium 99m. Bioconjug Chem 2008;19(5):1049-1054.

210. Almutairi A, Rossin R, Shokeen M, Hagooly A, Ananth A, Capoccia B, et al. Biodegradable dendritic positron-emitting nanoprobes for the noninvasive imaging of angiogenesis. Proc Natl Acad Sci U S A 2009 Jan 20;106(3):685-690.

211. Chen K, Cai W, Li Z, Wang H, Chen X. Quantitative PET imaging of VEGF receptor expression. Molecular Imaging and Biology 2009;11(1):15-22.

212. Presta LG, Chen H, O'Connor SJ, Chisholm V, Meng YG, Krummen L, et al. Humanization of an anti-vascular endothelial growth factor monoclonal antibody for the therapy of solid tumors and other disorders. Cancer Res 1997 Oct 15;57(20):4593-4599.

213. Nagengast WB, de Korte MA, Oude Munnink TH, Timmer-Bosscha H, den Dunnen WF, Hollema H, et al. 89Zr-bevacizumab PET of early antiangiogenic tumor response to treatment with HSP90 inhibitor NVP-AUY922. J Nucl Med 2010 May;51(5):761-767.

214. Gaykema SB, Brouwers AH, Lub-de Hooge MN, Pleijhuis RG, Timmer-Bosscha H, Pot L, et al. 89Zr-bevacizumab PET imaging in primary breast cancer. J Nucl Med 2013 Jul;54(7):1014-1018.

215. Paudyal B, Paudyal P, Oriuchi N, Hanaoka H, Tominaga H, Endo K. Positron emission tomography imaging and biodistribution of vascular endothelial growth factor with 64Cu-labeled bevacizumab in colorectal cancer xenografts. Cancer science 2011;102(1):117-121.

216. Zhang Y, Hong H, Engle JW, Yang Y, Barnhart TE, Cai W. Positron Emission Tomography and Near-Infrared Fluorescence Imaging of Vascular Endothelial Growth Factor with Dual-Labeled Bevacizumab. Am J Nucl Med Mol Imaging 2012 Jan 1;2(1):1-13.

217. Christoforidis JB, Carlton MM, Knopp MV, Hinkle GH. PET/CT imaging of I-124-radiolabeled bevacizumab and ranibizumab after intravitreal injection in a rabbit model. Invest Ophthalmol Vis Sci 2011 Jul 29;52(8):5899-5903.

218. Nagengast WB, de Vries EG, Hospers GA, Mulder NH, de Jong JR, Hollema H, et al. In vivo VEGF imaging with radiolabeled bevacizumab in a human ovarian tumor xenograft. J Nucl Med 2007 Aug;48(8):1313-1319.

219. Stollman TH, Scheer MG, Leenders WP, Verrijp KC, Soede AC, Oyen WJ, et al. Specific imaging of VEGF- A expression with radiolabeled anti- VEGF monoclonal antibody. International Journal of Cancer 2008;122(10):2310-2314.

220. Stollman TH, Scheer MG, Franssen GM, Verrijp KN, Oyen WJ, Ruers TJ, et al. Tumor accumulation of radiolabeled bevacizumab due to targeting of cell-and matrix-associated VEGF-A isoforms. Cancer Biotherapy and Radiopharmaceuticals 2009;24(2):195-200.

221. Nagengast WB, Lub-de Hooge MN, van Straten EM, Kruijff S, Brouwers AH, den Dunnen WF, et al. VEGF-SPECT with 111 In-bevacizumab in stage III/IV melanoma patients. Eur J Cancer 2011;47(10):1595-1602.

222. Beer AJ, Grosu AL, Carlsen J, Kolk A, Sarbia M, Stangier I, et al. 18F]galacto-RGD positron emission tomography for imaging of alphavbeta3 expression on the neovasculature

in patients with squamous cell carcinoma of the head and neck. Clin Cancer Res 2007 Nov 15;13(22 Pt 1):6610-6616.

223. Indrevoll B, Kindberg GM, Solbakken M, Bjurgert E, Johansen JH, Karlsen H, et al. NC-100717: a versatile RGD peptide scaffold for angiogenesis imaging. Bioorg Med Chem Lett 2006 Dec 15;16(24):6190-6193.

224. Bach-Gansmo T, Danielsson R, Saracco A, Wilczek B, Bogsrud TV, Fangberget A, et al. Integrin receptor imaging of breast cancer: a proof-of-concept study to evaluate 99mTc-NC100692. J Nucl Med 2006 Sep;47(9):1434-1439.

225. Bach- Gansmo T, Bogsrud TV, Skretting A. Integrin scintimammography using a dedicated breast imaging, solid- state γ- camera and 99mTc- labelled NC100692. Clinical physiology and functional imaging 2008;28(4):235-239.

226. Alzaraa A, Gravante G, Chung WY, Al-Leswas D, Morgan B, Dennison A, et al. Contrast-enhanced ultrasound in the preoperative, intraoperative and postoperative assessment of liver lesions. Hepatol Res 2013 Aug;43(8):809-819.

227. Kaul S. Myocardial contrast echocardiography: a 25-year retrospective. Circulation 2008 Jul 15;118(3):291-308.

228. Piedra M, Allroggen A, Lindner JR. Molecular imaging with targeted contrast ultrasound. Cerebrovasc Dis 2009;27 Suppl 2:66-74.

229. Lindner JR. Molecular imaging with contrast ultrasound and targeted microbubbles. J Nucl Cardiol 2004 Mar-Apr;11(2):215-221.

230. Dayton PA, Rychak JJ. Molecular ultrasound imaging using microbubble contrast agents. Front Biosci 2007 Sep 1;12:5124-5142.

231. Stieger SM, Dayton PA, Borden MA, Caskey CF, Griffey SM, Wisner ER, et al. Imaging of angiogenesis using Cadence contrast pulse sequencing and targeted contrast agents. Contrast Media Mol Imaging 2008 Jan-Feb;3(1):9-18.

232. Ellegala DB, Leong-Poi H, Carpenter JE, Klibanov AL, Kaul S, Shaffrey ME, et al. Imaging tumor angiogenesis with contrast ultrasound and microbubbles targeted to alpha(v)beta3. Circulation 2003 Jul 22;108(3):336-341.

233. Leong-Poi H, Christiansen J, Klibanov AL, Kaul S, Lindner JR. Noninvasive assessment of angiogenesis by ultrasound and microbubbles targeted to alpha(v)-integrins. Circulation 2003 Jan 28;107(3):455-460.

234. Klibanov AL, Rasche PT, Hughes MS, Wojdyla JK, Galen KP, Wible JH,Jr, et al. Detection of individual microbubbles of an ultrasound contrast agent: fundamental and pulse inversion imaging. Acad Radiol 2002 Aug;9 Suppl 2:S279-81.

235. Paganelli G, Chinol M, Maggiolo M, Sidoli A, Corti A, Baroni S, et al. The three-step pretargeting approach reduces the human anti-mouse antibody response in patients submitted to radioimmunoscintigraphy and radioimmunotherapy. Eur J Nucl Med 1997 Mar;24(3):350-351.

236. Breitz HB, Weiden PL, Beaumier PL, Axworthy DB, Seiler C, Su FM, et al. Clinical optimization of pretargeted radioimmunotherapy with antibody-streptavidin conjugate and 90Y-DOTA-biotin. J Nucl Med 2000 Jan;41(1):131-140.

237. Anderson CR, Hu X, Zhang H, Tlaxca J, Decleves AE, Houghtaling R, et al. Ultrasound molecular imaging of tumor angiogenesis with an integrin targeted microbubble contrast agent. Invest Radiol 2011 Apr;46(4):215-224.

238. Streeter JE, Gessner RC, Tsuruta J, Feingold S, Dayton PA. Assessment of molecular imaging of angiogenesis with three-dimensional ultrasonography. Mol Imaging 2011 Dec;10(6):460-468.

239. Wang H, Kaneko OF, Tian L, Hristov D, Willmann JK. Three-Dimensional Ultrasound Molecular Imaging of Angiogenesis in Colon Cancer Using a Clinical Matrix Array Ultrasound Transducer. Invest Radiol 2015 Jan 8.

240. Kalender WA. The use of flat-panel detectors for CT imaging. Radiologe 2003 May;43(5):379-387.

241. Kalender WA, Kyriakou Y. Flat-detector computed tomography (FD-CT). Eur Radiol 2007 Nov;17(11):2767-2779.

242. Kiessling F, Greschus S, Lichy MP, Bock M, Fink C, Vosseler S, et al. Volumetric computed tomography (VCT): a new technology for noninvasive, high-resolution monitoring of tumor angiogenesis. Nat Med 2004 Oct;10(10):1133-1138.

243. Greschus S, Kiessling F, Lichy MP, Moll J, Mueller MM, Savai R, et al. Potential applications of flat-panel volumetric CT in morphologic and functional small animal imaging. Neoplasia 2005 Aug;7(8):730-740.

244. Weichert JP, Lee FT,Jr, Chosy SG, Longino MA, Kuhlman JE, Heisey DM, et al. Combined hepatocyte-selective and blood-pool contrast agents for the CT detection of experimental liver tumors in rabbits. Radiology 2000 Sep;216(3):865-871.

245. Idee JM, Port M, Robert P, Raynal I, Prigent P, Dencausse A, et al. Preclinical profile of the monodisperse iodinated macromolecular blood pool agent P743. Invest Radiol 2001 Jan;36(1):41-49.

246. Kao CY, Hoffman EA, Beck KC, Bellamkonda RV, Annapragada AV. Long-residence-time nano-scale liposomal iohexol for X-ray-based blood pool imaging. Acad Radiol 2003 May;10(5):475-483.

247. Ford NL, Thornton MM, Holdsworth DW. Fundamental image quality limits for microcomputed tomography in small animals. Med Phys 2003 Nov;30(11):2869-2877.

248. Huang X, Jain PK, El-Sayed IH, El-Sayed MA. Gold nanoparticles: interesting optical properties and recent applications in cancer diagnostics and therapy. Nanomedicine (Lond) 2007 Oct;2(5):681-693.

249. Popovtzer R, Agrawal A, Kotov NA, Popovtzer A, Balter J, Carey TE, et al. Targeted gold nanoparticles enable molecular CT imaging of cancer. Nano Lett 2008 Dec;8(12):4593-4596.

250. Zhang XD, Wu HY, Wu D, Wang YY, Chang JH, Zhai ZB, et al. Toxicologic effects of gold nanoparticles in vivo by different administration routes. Int J Nanomedicine 2010 Oct 5;5:771-781.

251. Reuveni T, Motiei M, Romman Z, Popovtzer A, Popovtzer R. Targeted gold nanoparticles enable molecular CT imaging of cancer: an in vivo study. Int J Nanomedicine 2011;6:2859-2864.

252. Ghaghada KB, Badea CT, Karumbaiah L, Fettig N, Bellamkonda RV, Johnson GA, et al. Evaluation of tumor microenvironment in an animal model using a nanoparticle contrast agent in computed tomography imaging. Acad Radiol 2011 Jan;18(1):20-30.

253. Hainfeld JF, O'Connor MJ, Dilmanian FA, Slatkin DN, Adams DJ, Smilowitz HM. Micro-CT enables microlocalisation and quantification of Her2-targeted gold nanoparticles within tumour regions. Br J Radiol 2011 Jun;84(1002):526-533.

254. Curry T, Kopelman R, Shilo M, Popovtzer R. Multifunctional theranostic gold nanoparticles for targeted CT imaging and photothermal therapy. Contrast media & molecular imaging 2014;9(1):53-61.

255. Vilchis-Juárez A, Ferro-Flores G, Santos-Cuevas C, Morales-Avila E, Ocampo-García B, Díaz-Nieto L, et al. Molecular targeting radiotherapy with cyclo-RGDFK (C) peptides conjugated to 177Lu-labeled gold nanoparticles in tumor-bearing mice. Journal of biomedical nanotechnology 2014;10(3):393-404.

256. Nagrath S, Sequist LV, Maheswaran S, Bell DW, Irimia D, Ulkus L, et al. Isolation of rare circulating tumour cells in cancer patients by microchip technology. Nature 2007;450(7173):1235-1239.

257. Miles FL, Pruitt FL, van Golen KL, Cooper CR. Stepping out of the flow: capillary extravasation in cancer metastasis. Clin Exp Metastasis 2008;25(4):305-324.

258. Vilalta M, Rafat M, Giaccia AJ, Graves EE. Recruitment of Circulating Breast Cancer Cells Is Stimulated by Radiotherapy. Cell reports 2014;8(2):402-409.

259. Klauber-DeMore N, Van Zee KJ, Linkov I, Borgen PI, Gerald WL. Biological behavior of human breast cancer micrometastases. Clin Cancer Res 2001 Aug;7(8):2434-2439.

260. Torabi M, Aquino SL, Harisinghani MG. Current concepts in lymph node imaging. J Nucl Med 2004 Sep;45(9):1509-1518.

261. Schmidt-Hansen M, Baldwin DR, Hasler E, Zamora J, Abraira V, Roque I Figuls M. PET-CT for assessing mediastinal lymph node involvement in patients with suspected resectable non-small cell lung cancer. Cochrane Database Syst Rev 2014 Nov 13;11:CD009519.

262. Madeddu G, Spanu A. Use of tomographic nuclear medicine procedures, SPECT and pinhole SPECT, with cationic lipophilic radiotracers for the evaluation of axillary lymph node status in breast cancer patients. European journal of nuclear medicine and molecular imaging 2004;31(1):S23-S34.

263. Scheer MG, Stollman TH, Boerman OC, Verrijp K, Sweep FC, Leenders WP, et al. Imaging liver metastases of colorectal cancer patients with radiolabelled bevacizumab: lack of correlation with VEGF-A expression. Eur J Cancer 2008;44(13):1835-1840.

264. Axelsson R, Bach-Gansmo T, Castell-Conesa J, McParland BJ, Study Group. An open-label, multicenter, phase 2a study to assess the feasibility of imaging metastases in late-stage cancer patients with the alpha v beta 3-selective angiogenesis imaging agent 99mTc-NC100692. Acta Radiol 2010 Feb;51(1):40-46.

265. Weissleder R, Elizondo G, Wittenberg J, Rabito CA, Bengele HH, Josephson L. Ultrasmall superparamagnetic iron oxide: characterization of a new class of contrast agents for MR imaging. Radiology 1990 May;175(2):489-493.

266. Weissleder R, Elizondo G, Wittenberg J, Lee AS, Josephson L, Brady TJ. Ultrasmall superparamagnetic iron oxide: an intravenous contrast agent for assessing lymph nodes with MR imaging. Radiology 1990 May;175(2):494-498.

267. Anzai Y. Superparamagnetic iron oxide nanoparticles: nodal metastases and beyond. Top Magn Reson Imaging 2004 Apr;15(2):103-111.

268. Guimaraes AR, Tabatabei S, Dahl D, McDougal WS, Weissleder R, Harisinghani MG. Pilot study evaluating use of lymphotrophic nanoparticle-enhanced magnetic resonance imaging for assessing lymph nodes in renal cell cancer. Urology 2008 Apr;71(4):708-712.

269. Harisinghani MG, Saksena M, Ross RW, Tabatabaei S, Dahl D, McDougal S, et al. A pilot study of lymphotrophic nanoparticle-enhanced magnetic resonance imaging technique in early stage testicular cancer: a new method for noninvasive lymph node evaluation. Urology 2005;66(5):1066-1071.

270. Serres S. Molecular MRI enables early and sensitive detection of brain metastases. Proc Natl Acad Sci U S A 2012;109(17):6674.

271. Hosseinzadeh K, Schwarz SD. Endorectal diffusion- weighted imaging in prostate cancer to differentiate malignant and benign peripheral zone tissue. Journal of Magnetic Resonance Imaging 2004;20(4):654-661.

272. Guo Y, Cai Y, Cai Z, Gao Y, An N, Ma L, et al. Differentiation of clinically benign and malignant breast lesions using diffusion- weighted imaging. Journal of magnetic resonance imaging 2002;16(2):172-178.

273. Schmidt GP, Baur-Melnyk A, Herzog P, Schmid R, Tiling R, Schmidt M, et al. High-resolution whole-body magnetic resonance image tumor staging with the use of parallel imaging versus dual-modality positron emission tomography–computed tomography: experience on a 32-channel system. Invest Radiol 2005;40(12):743-753.

274. Schlemmer H, Schäfer J, Pfannenberg C, Radny P, Korchidi S, Müller-Horvat C, et al. Fast whole-body assessment of metastatic disease using a novel magnetic resonance imaging system: initial experiences. Invest Radiol 2005;40(2):64-71.

275. Budde MD, Gold E, Jordan EK, Frank JA. Differential microstructure and physiology of brain and bone metastases in a rat breast cancer model by diffusion and dynamic contrast enhanced MRI. Clin Exp Metastasis 2012;29(1):51-62.

276. Leenders W, Küsters B, Pikkemaat J, Wesseling P, Ruiter D, Heerschap A, et al. Vascular endothelial growth factor- A determines detectability of experimental melanoma brain metastasis in GD- DTPA- enhanced MRI. International journal of cancer 2003;105(4):437-443.

277. Schmidt GP, Schoenberg SO, Schmid R, Stahl R, Tiling R, Becker CR, et al. Screening for bone metastases: whole-body MRI using a 32-channel system versus dual-modality PET-CT. Eur Radiol 2007;17(4):939-949.

278. Engelhard K, Hollenbach H, Wohlfart K, Von Imhoff E, Fellner F. Comparison of whole-body MRI with automatic moving table technique and bone scintigraphy for screening for bone metastases in patients with breast cancer. Eur Radiol 2004;14(1):99-105.

279. Steinborn MM, Heuck AF, Tiling R, Bruegel M, Gauger L, Reiser MF. Whole-body bone marrow MRI in patients with metastatic disease to the skeletal system. J Comput Assist Tomogr 1999;23(1):123-129.

280. Aslakson CJ, Miller FR. Selective events in the metastatic process defined by analysis of the sequential dissemination of subpopulations of a mouse mammary tumor. Cancer Res 1992 Mar 15;52(6):1399-1405.

281. Cormack BP, Valdivia RH, Falkow S. FACS-optimized mutants of the green fluorescent protein (GFP). Gene 1996;173(1 Spec No):33-38.

282. Nouls J, Fanarjian M, Hedlund L, Driehuys B. A Constant-Volume Ventilator and Gas Recapture System for Hyperpolarized Gas MRI of Mouse and Rat Lungs. Concepts Magn Reson Part B Magn Reson Eng 2011 Apr;39B(2):78-88.

283. Cassidy PJ, Schneider JE, Grieve SM, Lygate C, Neubauer S, Clarke K. Assessment of motion gating strategies for mouse magnetic resonance at high magnetic fields. J Magn Reson Imaging 2004 Feb;19(2):229-237.

284. Yarnykh VL. Actual flip-angle imaging in the pulsed steady state: a method for rapid three-dimensional mapping of the transmitted radiofrequency field. Magn Reson Med 2007 Jan;57(1):192-200.

285. Yushkevich PA, Piven J, Hazlett HC, Smith RG, Ho S, Gee JC, et al. User-guided 3D active contour segmentation of anatomical structures: significantly improved efficiency and reliability. Neuroimage 2006 Jul 1;31(3):1116-1128.

286. Miles FL, Pruitt FL, van Golen KL, Cooper CR. Stepping out of the flow: capillary extravasation in cancer metastasis. Clin Exp Metastasis 2008;25(4):305-324.

287. Okahara H, Yagita H, Miyake K, Okumura K. Involvement of very late activation antigen 4 (VLA-4) and vascular cell adhesion molecule 1 (VCAM-1) in tumor necrosis factor alpha enhancement of experimental metastasis. Cancer Res 1994 Jun 15;54(12):3233-3236.

288. Klemke M, Weschenfelder T, Konstandin MH, Samstag Y. High affinity interaction of integrin alpha4beta1 (VLA-4) and vascular cell adhesion molecule 1 (VCAM-1) enhances migration of human melanoma cells across activated endothelial cell layers. J Cell Physiol 2007 Aug;212(2):368-374.

289. Soto MS, Serres S, Anthony DC, Sibson NR. Functional role of endothelial adhesion molecules in the early stages of brain metastasis. Neuro Oncol 2014 Apr;16(4):540-551.

290. Ferjancic S, Gil-Bernabe AM, Hill SA, Allen PD, Richardson P, Sparey T, et al. VCAM-1 and VAP-1 recruit myeloid cells that promote pulmonary metastasis in mice. Blood 2013 Apr 18;121(16):3289-3297.

291. Mardiguian S, Serres S, Ladds E, Campbell SJ, Wilainam P, McFadyen C, et al. Anti-IL-17A treatment reduces clinical score and VCAM-1 expression detected by in vivo magnetic resonance imaging in chronic relapsing EAE ABH mice. Am J Pathol 2013 Jun;182(6):2071-2081.

292. Duffy BA, Choy M, Riegler J, Wells JA, Anthony DC, Scott RC, et al. Imaging seizure-induced inflammation using an antibody targeted iron oxide contrast agent. Neuroimage 2012 Apr 2;60(2):1149-1155.

293. Hatabu H, Alsop DC, Listerud J, Bonnet M, Gefter WB. T2* and proton density measurement of normal human lung parenchyma using submillisecond echo time gradient echo magnetic resonance imaging. Eur J Radiol 1999 Mar;29(3):245-252.

294. Alberts B, Johnson A, Lewis J, et al editor. Molecular Biology of the Cell. 4th Edition ed. New York: Garland Science; 2002.

295. Black RD, Middleton HL, Cates GD, Cofer GP, Driehuys B, Happer W, et al. In vivo He-3 MR images of guinea pig lungs. Radiology 1996 Jun;199(3):867-870.

296. Kauczor HU, Hofmann D, Kreitner KF, Nilgens H, Surkau R, Heil W, et al. Normal and abnormal pulmonary ventilation: visualization at hyperpolarized He-3 MR imaging. Radiology 1996 Nov;201(2):564-568.

297. Kauczor HU, Ebert M, Kreitner KF, Grossmann T, Nilgens H, Hofmann D, et al. The helium-3 MRT of pulmonary ventilation: the initial clinical applications. Rofo 1997 Mar;166(3):192-198.

298. McAdams HP, Palmer SM, Donnelly LF, Charles HC, Tapson VF, MacFall JR. Hyperpolarized 3He-enhanced MR imaging of lung transplant recipients: preliminary results. AJR Am J Roentgenol 1999 Oct;173(4):955-959.

299. Altes TA, Powers PL, Knight-Scott J, Rakes G, Platts-Mills TA, de Lange EE, et al. Hyperpolarized 3He MR lung ventilation imaging in asthmatics: preliminary findings. J Magn Reson Imaging 2001 Mar;13(3):378-384.

300. Saam BT, Yablonskiy DA, Kodibagkar VD, Leawoods JC, Gierada DS, Cooper JD, et al. MR imaging of diffusion of (3)He gas in healthy and diseased lungs. Magn Reson Med 2000 Aug;44(2):174-179.

301. Salerno M, de Lange EE, Altes TA, Truwit JD, Brookeman JR, Mugler JP,3rd. Emphysema: hyperpolarized helium 3 diffusion MR imaging of the lungs compared with spirometric indexes--initial experience. Radiology 2002 Jan;222(1):252-260.

302. Yablonskiy DA, Sukstanskii AL, Leawoods JC, Gierada DS, Bretthorst GL, Lefrak SS, et al. Quantitative in vivo assessment of lung microstructure at the alveolar level with hyperpolarized 3He diffusion MRI. Proc Natl Acad Sci U S A 2002 Mar 5;99(5):3111-3116.

303. Swift AJ, Wild JM, Fichele S, Woodhouse N, Fleming S, Waterhouse J, et al. Emphysematous changes and normal variation in smokers and COPD patients using diffusion 3He MRI. Eur J Radiol 2005 Jun;54(3):352-358.

304. Branca RT. Molecular MRI for sensitive and specific detection of lung metastases. Proc Natl Acad Sci U S A 2010;107(8):3693.

305. Halaweish AF, Moon RE, Foster WM, Soher BJ, McAdams HP, MacFall JR, et al. Perfluoropropane gas as a magnetic resonance lung imaging contrast agent in humans. Chest 2013 Oct;144(4):1300-1310.

306. Couch MJ, Ball IK, Li T, Fox MS, Littlefield SL, Biman B, et al. Pulmonary ultrashort echo time 19F MR imaging with inhaled fluorinated gas mixtures in healthy volunteers: feasibility. Radiology 2013 Dec;269(3):903-909.

307. Greenspan JS, Wolfson MR, Rubenstein SD, Shaffer TH. Liquid ventilation of human preterm neonates. J Pediatr 1990 Jul;117(1 Pt 1):106-111.

308. Kaisers U, Kelly KP, Busch T. Liquid ventilation. Br J Anaesth 2003 Jul;91(1):143-151.

309. Tawfic QA, Kausalya R. Liquid ventilation. Oman Med J 2011 Jan;26(1):4-9.

310. Valls-I-Soler A, Alvarez FJ, Gastiasoro E. Liquid ventilation: from experimental use to clinical application. Biol Neonate 2001 May;80 Suppl 1:29-33.

311. Driehuys B, Cates G, Miron E, Sauer K, Walter D, Happer W. High- volume production of laser- polarized 129Xe. Appl Phys Lett 1996;69(12):1668-1670.

312. Folkman J. The role of angiogenesis in tumor growth. Semin Cancer Biol 1992 Apr;3(2):65-71.

313. Folkman J. Angiogenesis in cancer, vascular, rheumatoid and other disease. Nat Med 1995 Jan;1(1):27-31.

314. Weinstat-Saslow D, Steeg PS. Angiogenesis and colonization in the tumor metastatic process: basic and applied advances. FASEB J 1994 Apr 1;8(6):401-407.

315. Kerbel RS. Antiangiogenic therapy: a universal chemosensitization strategy for cancer? Science 2006 May 26;312(5777):1171-1175.

316. Horton MA. The alpha v beta 3 integrin "vitronectin receptor". Int J Biochem Cell Biol 1997 May;29(5):721-725.

317. Drake CJ, Cheresh DA, Little CD. An antagonist of integrin alpha v beta 3 prevents maturation of blood vessels during embryonic neovascularization. J Cell Sci 1995 Jul;108 ( Pt 7)(Pt 7):2655-2661.

318. Griffioen AW, Molema G. Angiogenesis: potentials for pharmacologic intervention in the treatment of cancer, cardiovascular diseases, and chronic inflammation. Pharmacol Rev 2000 Jun;52(2):237-268.

319. Brooks PC, Montgomery AM, Rosenfeld M, Reisfeld RA, Hu T, Klier G, et al. Integrin alpha v beta 3 antagonists promote tumor regression by inducing apoptosis of angiogenic blood vessels. Cell 1994 Dec 30;79(7):1157-1164.

320. Gladson CL. Expression of integrin αvβ3 in small blood vessels of glioblastoma tumors. Journal of Neuropathology & Experimental Neurology 1996;55:1143-1149.

321. Cai W, Chen X. Multimodality molecular imaging of tumor angiogenesis. J Nucl Med 2008 Jun;49 Suppl 2:113S-28S.

322. Buck CA, Horwitz AF. Cell surface receptors for extracellular matrix molecules. Annu Rev Cell Biol 1987;3:179-205.

323. Ruoslahti E, Pierschbacher MD. Arg-Gly-Asp: a versatile cell recognition signal. Cell 1986 Feb 28;44(4):517-518.

324. Xiong JP, Stehle T, Zhang R, Joachimiak A, Frech M, Goodman SL, et al. Crystal structure of the extracellular segment of integrin alpha Vbeta3 in complex with an Arg-Gly-Asp ligand. Science 2002 Apr 5;296(5565):151-155.

325. Haubner R, Wester HJ, Burkhart F, Senekowitsch-Schmidtke R, Weber W, Goodman SL, et al. Glycosylated RGD-containing peptides: tracer for tumor targeting and angiogenesis imaging with improved biokinetics. J Nucl Med 2001 Feb;42(2):326-336.

326. Sivolapenko GB, Skarlos D, Pectasides D, Stathopoulou E, Milonakis A, Sirmalis G, et al. Imaging of metastatic melanoma utilising a technetium-99m labelled RGD-containing synthetic peptide. Eur J Nucl Med 1998 Oct;25(10):1383-1389.

327. Kiessling F, Morgenstern B, Zhang C. Contrast agents and applications to assess tumor angiogenesis in vivo by magnetic resonance imaging. Curr Med Chem 2007;14(1):77-91.

328. Montet X, Montet-Abou K, Reynolds F, Weissleder R, Josephson L. Nanoparticle imaging of integrins on tumor cells. Neoplasia 2006 Mar;8(3):214-222.

329. Persigehl T, Matuszewski L, Kessler T, Wall A, Meier N, Ebert W, et al. Prediction of antiangiogenic treatment efficacy by iron oxide enhanced parametric magnetic resonance imaging. Invest Radiol 2007 Dec;42(12):791-796.

330. Yang Y, Yang Y, Yanasak N, Schumacher A, Hu TC. Temporal and noninvasive monitoring of inflammatory-cell infiltration to myocardial infarction sites using micrometer-sized iron oxide particles. Magn Reson Med 2010 Jan;63(1):33-40.

331. Weissleder R, Kelly K, Sun EY, Shtatland T, Josephson L. Cell-specific targeting of nanoparticles by multivalent attachment of small molecules. Nat Biotechnol 2005 Nov;23(11):1418-1423.

332. Shapiro EM, Skrtic S, Sharer K, Hill JM, Dunbar CE, Koretsky AP. MRI detection of single particles for cellular imaging. Proc Natl Acad Sci U S A 2004 Jul 27;101(30):10901-10906.

333. Jefferson A, Wijesurendra RS, McAteer MA, Digby JE, Douglas G, Bannister T, et al. Molecular imaging with optical coherence tomography using ligand-conjugated microparticles that detect activated endothelial cells: rational design through target quantification. Atherosclerosis 2011 Dec;219(2):579-587.

334. Cai W, Shin DW, Chen K, Gheysens O, Cao Q, Wang SX, et al. Peptide-labeled near-infrared quantum dots for imaging tumor vasculature in living subjects. Nano Lett 2006 Apr;6(4):669-676.

335. Lee PC, Kibbe MR, Schuchert MJ, Stolz DB, Watkins SC, Griffith BP, et al. Nitric oxide induces angiogenesis and upregulates alpha(v)beta(3) integrin expression on endothelial cells. Microvasc Res 2000 Nov;60(3):269-280.

336. Yankeelov TE, Luci JJ, Lepage M, Li R, Debusk L, Lin PC, et al. Quantitative pharmacokinetic analysis of DCE-MRI data without an arterial input function: a reference region model. Magn Reson Imaging 2005 May;23(4):519-529.

337. Yankeelov TE, DeBusk LM, Billheimer DD, Luci JJ, Lin PC, Price RR, et al. Repeatability of a reference region model for analysis of murine DCE-MRI data at 7T. J Magn Reson Imaging 2006 Nov;24(5):1140-1147.

338. Yankeelov TE, Luci JJ, DeBusk LM, Lin PC, Gore JC. Incorporating the effects of transcytolemmal water exchange in a reference region model for DCE-MRI analysis: theory, simulations, and experimental results. Magn Reson Med 2008 Feb;59(2):326-335.

339. Fonnum G, Johansson C, Molteberg A, Mørup S, Aksnes E. Characterisation of Dynabeads< sup>® by magnetization measurements and Mössbauer spectroscopy. J Magn Magn Mater 2005;293(1):41-47.

340. Multimeric iron oxide micro particles: Novel high sensitivity and biodegradable mri contrast agents. Intl. Soc. Mag. Reson. Med; 2010.

341. Xie J, Chen K, Lee HY, Xu C, Hsu AR, Peng S, et al. Ultrasmall c(RGDyK)-coated Fe3O4 nanoparticles and their specific targeting to integrin alpha(v)beta3-rich tumor cells. J Am Chem Soc 2008 Jun 18;130(24):7542-7543.

342. Cai W, Chen X. Preparation of peptide-conjugated quantum dots for tumor vasculature-targeted imaging. Nat Protoc 2008;3(1):89-96.

343. Huo T, Du X, Zhang S, Liu X, Li X. Gd-EDDA/HYNIC-RGD as an MR molecular probe imaging integrin alphanubeta3 receptor-expressed tumor-MR molecular imaging of angiogenesis. Eur J Radiol 2010 Feb;73(2):420-427.

344. Kiessling F, Farhan N, Lichy MP, Vosseler S, Heilmann M, Krix M, et al. Dynamic contrast-enhanced magnetic resonance imaging rapidly indicates vessel regression in human squamous cell carcinomas grown in nude mice caused by VEGF receptor 2 blockade with DC101. Neoplasia 2004 May-Jun;6(3):213-223.

345. Park JA, Lee JJ, Jung JC, Yu DY, Oh C, Ha S, et al. Gd-DOTA conjugate of RGD as a potential tumor-targeting MRI contrast agent. Chembiochem 2008 Nov 24;9(17):2811-2813.

346. Giraudeau C, Geffroy F, Meriaux S, Boumezbeur F, Robert P, Port M, et al. 19F molecular MR imaging for detection of brain tumor angiogenesis: in vivo validation using targeted PFOB nanoparticles. Angiogenesis 2013 Jan;16(1):171-179.

347. Pfaff M, Tangemann K, Muller B, Gurrath M, Muller G, Kessler H, et al. Selective recognition of cyclic RGD peptides of NMR defined conformation by alpha IIb beta 3, alpha V beta 3, and alpha 5 beta 1 integrins. J Biol Chem 1994 Aug 12;269(32):20233-20238.

348. Lee IT, Yang CM. Inflammatory signalings involved in airway and pulmonary diseases. Mediators Inflamm 2013;2013:791231.

349. Pan F, Yang T, Chen X, Chen Y, Gao G, Liu Y, et al. Impact of female cigarette smoking on circulating B cells in vivo: the suppressed ICOSLG, TCF3, and VCAM1 gene functional network may inhibit normal cell function. Immunogenetics 2010;62(4):237-251.

# Abbreviations

| | |
|---|---|
| ° | Unit of degrees |
| °C | Degrees centrigrade |
| 4T1 | Mouse breast cancer cell line |
| α | Alpha integrin subunit |
| Å | Angstrom |
| A | Ampere |
| a.u. | Arbitrary units |
| ABC | Avidin biotin complex |
| ADC | Apparent diffusion coefficient |
| Ala | Alanine |
| ANOVA | Analysis of variance |
| Arg | Arginine |
| Asp | Aspartic acid |
| AUC | Area under the curve |
| β | Beta integrin subunit |
| B16F10 | Mouse melanoma cell line |
| BALB/c | Bagg albino mouse strain |
| BMDC | Bone marrow derived cells |
| BW | Band width |
| c | Centi- or Cyclic |
| C | Carbon |
| *ca.* | Approximately |
| c(RGDyK)-MPIO | 2.8 μm MPIO coated with multiple RGDyK peptides |
| c(RADyK)-MPIO | 2.8 μm MPIO coated with multiple RADyK peptides |
| c(RADyK) | cyclic Arginine Alanine Aspartic acid D-Tyrosine Lysine |
| c(RADfV) | cyclic Arginine Alanine Aspartic acid D-Phenylalanine Lysine |
| c(RGDyK) | cyclic Arginine Glysine Aspartic acid D-Tyrosine Lysine |
| c(RGDfV) | cyclic Arginine Glysine Aspartic acid D-Phenylalanine Lysine |
| C57BL/6 | Black 6 mouse strain |
| CAM | Cell adhesion molecule |
| CD1 | White albino mouse strain |
| COPD | Progressive irreversible airflow limitation |
| $CO_2$ | Carbon dioxide |
| CSC | Cancer stem cell |
| CT | Computed tomography |
| CTC | Circulating tumour cells |
| D | Three dimensional |
| DAB | Diaminobenzidine 3-(4,5-dimethylthiazol-2-yl)-2,5- |

| | |
|---|---|
| | diphenyltetrazolium bromide |
| DAPI | 4’,6-diamidino-2-phenylindole |
| DCE | Dynamic contrast enhanced |
| DFO | (1-(4-Isothiocyanatophenyl)-3-81[6,17-dihyroxy-7,10, 18,21-tetraoxo-27-[N-acetylhydroxylamino)-6,11,17,22-tetraazaheptaeicosane]thiourea |
| DMEM | Dulbecco's modified Eagle's medium |
| DNA | Deoxyribonucleic acid |
| DPX | Distyrene plasticiser xylene |
| DTC | Disseminated↲ tumour cells |
| DTPA | Diethylene triamine pentaacetic acid |
| DW | Diffusion weighted |
| EC | Endothelial cell |
| ECM | Extracellular matrix |
| EDTA | Ethylenediaminetetraacetic acid |
| EES | extravascular extracellular space |
| ELISA | Enzyme-linked immunosorbent assay |
| F | Fluorine |
| FA | Flip angle |
| FBP | Field backprojection |
| FBS | Feta bovine serum |
| Fe | Iron |
| FDG | Fludeoxyglucose |
| FGF | Fibroblast growth factor |
| FLM | Fraction of local mean |
| FOV | Field of view |
| g | Grams or Gravitational force |
| G | Gauge (needle) |
| Gd | Gadolinium |
| $Gd^{3+}$ | Gadolinium ion |
| GFP | Green fluorescent protein |
| Gly | Glysine |
| $H_2O_2$ | Hydrogen peroxide |
| h | Hour |
| $^{1}H$ | Proton |
| $^{2}H$ | Deuterium |
| $^{3}He$ | Helium |
| HRP | Horseradish peroxidase |
| HCl | Hydrochloric acid |
| HUVEC | Human unbiliant vascular endothelial cells |
| Hz | Hertz |
| I | Iodine |
| IC50 | Inhibitory concentration 50% |

| | |
|---|---|
| ICAM-1 | Intercellular adhesion molecule 1 |
| ID | Injected dose |
| IF | Immunofluorescence |
| IgG | Immunoglobulin G |
| IgG-MPIO | 1 μm MPIO coated with multiple IgG antibodies |
| IHC | Immunohistochemistry |
| In | Indium |
| ITKSnap | Medical image software |
| K | Kilo- |
| $K^{trans}$ | Transfer constant |
| L | Litre |
| LHRH | Luteinizing hormone- releasing hormone |
| LPS | Lipolysaccharides |
| Lys | Lysine |
| M | Molar |
| M0 | No detected metastasis |
| M1 | Detected metastasis |
| m | Milli or Metre |
| MATLAB | Matrix laboratory |
| MAdCAM-1 | Human mucosal addressin cell adhesion molecule-1 |
| MET | Metastasis |
| MMP | Matrix metalloproteinases |
| MPIO | Microparticles of iron oxide |
| Bq | Bequerel |
| min | Minute |
| MRI | Magnetic resonance imaging |
| MC-38 | Mouse colorectal carcinoma cells line |
| MCM | Melanoma cell condition media |
| N | Nitrogen |
| n | Nano- or Number of subjects |
| NMR | Nuclear magnetic resonance o.d. Outer diameter |
| NPIO | Nanoparticles of iron oxide |
| $O_2$ | Oxygen |
| p | pico |
| P | Probability value |
| PBS | Phosphate buffered saline |
| PBST | Phosphate buffered saline Tween-20 |
| PDGF | Platelet-derived growth factor |
| PET | Positron emission tomography |
| PECAM | Platelet endothelial cell adhesion molecule |
| PFA | Paraformaldehyde |
| pH | Power of hydrogen |

| | |
|---|---|
| Phe | Phenylalanine |
| PSGL | P-selectin glycoprotein ligand |
| $R^2$ | Coefficient of determination |
| RAD | Arginine Alanine Asprtic acid |
| RF | Radiofrequency |
| RGD | Arginine Glysine Aspartic acid |
| ROI | Region of interest |
| rpm | Revolutions per minute |
| rVCAM | Recombinant vascular cell adhesion molecule |
| s | Second |
| SD | Standard deviation |
| SEM | Standard error of the mean |
| SNAP | S-nitroso-n-acetylpenicillamine |
| SPECT | Single photon emission computed tomography |
| SPIO | Superparamagnetic particles of iron oxide |
| T | Tesla |
| $T_1$ | Time constant, $M_z$ recovers the 63% of its equilibrium value |
| $T_2$ | Time constant, $M_{xy}$ drops to 37% of its original magnitude |
| $T_2$* | Time constant, T2 dependency of the inhomogeneities |
| TAF | Tumour angiogenesis factor |
| Tc | Technetium |
| TE | Echo time |
| TGF | Transforming growth factor |
| TNB | Tris-NaCl blocking buffer |
| TR | Repetition time |
| U | Unit |
| US | Ultrasonography or Ultrasound |
| USPIO | Ultrasmall particles of iron oxide |
| µ | Micro- |
| V | Voltage or Volume |
| v/v | Volume percentage |
| Val | Valine |
| VCAM-1 | Vascular cell adhesion molecule-1 |
| VCAM-MPIO | 1 µm MPIO coated with multiple VCAM-1 antibodies |
| VLA | Very late antigen |
| VEGF | Vascular endothelial growth factor |
| VEGFR | Vascular endothelial growth factor receptor |
| *vs.* | Versus |
| W | Weighted |
| WB | Whole body |
| Xe | Xenon |
| Zr | Zirconium |